NANOSTRUCTURING ON SOLID SURFACES USING LOW ENERGY ATOMIC AND CLUSTER IONS

by

Pintu Barman

Enrolment No.: PHYS05201604020

Saha Institute of Nuclear Physics, Kolkata

A thesis submitted to the
Board of Studies in Physical Sciences

In partial fulfillment of requirements
for the Degree of

DOCTOR OF PHILOSOPHY
of
HOMI BHABHA NATIONAL INSTITUTE

June, 2021

Homi Bhabha National Institute
Recommendations of the Viva Voce Committee

As members of the Viva Voce Committee, we certify that we have read the dissertation prepared by **Pintu Barman** entitled "***Nanostructuring on solid surfaces using low energy atomic and cluster ions***" and recommend that it may be accepted as fulfilling the thesis requirement for the award of Degree of Doctor of Philosophy.

Tapas Kumar Chini Date : 11. 08. 21

Chairman - **Prof. Tapas Kumar Chini**

Supratic Chakraborty Date : 11.08.21.

Guide / Convener - **Prof. Supratic Chakraborty**

Chandi Charan Dey Date : 11.08.21

Member 1 - **Prof. Chandi Charan Dey**

Date :

Member 2 - **Prof. Biswarup Satpati**

Biswarup Satpati Date : 11.08.21

Member 3 - **Prof. Prasanta Karmakar**

Prasanta Karmakar Date : 11.08.2021

External Examiner - **Prof. Aloke Kanjilal**

Final approval and acceptance of this thesis is contingent upon the candidate's submission of the final copies of the thesis to HBNI.

I hereby certify that I have read this thesis prepared under my direction and recommend that it may be accepted as fulfilling the thesis requirement.

Date : 11.08.21.
Place : SINP

Supratic Chakraborty
Signature of Guide

STATEMENT BY AUTHOR

This dissertation has been submitted in partial fulfillment of requirements for an advanced degree at Homi Bhabha National Institute (HBNI) and is deposited in the Library to be made available to borrowers under rules of the HBNI.

Brief quotations from this dissertation are allowable without special permission, provided that accurate acknowledgement of source is made. Requests for permission for extended quotation from or reproduction of this manuscript in whole or in part may be granted by the Competent Authority of HBNI when in his or her judgment the proposed use of the material is in the interests of scholarship. In all other instances, however, permission must be obtained from the author.

Pintu Barman
11.08.21

Pintu Barman

DECLARATION

I, hereby declare that the research works presented in the thesis have been carried out by me. The work is original in nature and has not been submitted earlier as a whole or in part for a degree / diploma at this or any other Institution / University.

Pintu Barman
11.08.21

Pintu Barman

List of Publications related to this thesis

In peer reviewed Journals:

1. *"Interaction of size-selected Ag-clusters on Au-films: a composition study with in-situ XPS analysis at an elevated temperature"*
   Pintu Barman, Anindita Deka and Satyaranjan Bhattacharyya
   J. Phys. D: Appl. Phys. **54** (2021) 275301.

2. *"Surface scaling behaviour of size-selected Ag-nanocluster film growing under subsequent shadowing process"*
   Pintu Barman, Anindita Deka, Shyamal Mondal, Debasree Chowdhury and Satyaranjan Bhattacharyya
   J. Phys. D: Appl. Phys. **53** (2020) 325302.

3. *"Growth dynamics of copper thin film deposited bysoft-landing of size selected nanoclusters ,"*
   Shyamal Mondal, Debasree Chowdhury, **Pintu Barman** and Satyaranjan Bhattacharyya
   Eur. Phys. J. D **71** (2017) 327.

In conference proceedings:

1. *"Evolution from mono-dispersed to mound-like structures of size-selected Ag-nanocluster films"* **Pintu Barman**, Anindita Deka and Satyaranjan Bhattacharyya
   AIP Conference Proceedings **2265** (2020) 030249.

2. *"Thermal diffusion driven island formation and fragmentation of size-selected Ag-nanocluster films"*
   Pintu Barman, Anindita Deka, Shyamal Mondal, Debasree Chowdhury and Satyaranjan Bhattacharyya
   AIP Conference Proceedings **2115** (2019) 030306.

Submitted manuscripts:

1. *"Wettability transition on fractal surface developed by size-selected Ag-nanoclusters"*, **Pintu Barman**, Anindita Deka, Supratic Chakraborty and Satyaranjan Bhattacharyya

2. *"Scaling aspects of the surface morphology for size-selected Ag-nanocluster films"*, **Pintu Barman**, Anindita Deka, Supratic Chakraborty and Satyaranjan Bhattacharyya

List of Publications not related to this thesis

1. *"Transition of nano-ripple to nano-hillock pattern on ion bombarded Si with an enhanced hydrophobicity"*
   Anindita Deka, **Pintu Barman**, M.K. Mukhopadhyay and Satyaranjan Bhattacharyya
   Surf. Interfaces **25** (2021) 101242.

2. *"Evolution of ion-induced nano-dot patterns on silicon surface in presence of seeding materials"*
   Anindita Deka, **Pintu Barman**, Gourab Bhattacharjee and Satyaranjan Bhattacharyya
   Appl. Surf. Sci. **526** (2020) 146645.

3. *"Pattern formation on ion-irradiated Si surface at energies where sputtering is negligible"*
   A. Lopez-Cazalilla, D. Chowdhury, A. Ilinov, S. Mondal, **P. Barman**, S.R. Bhattacharyya, D. Ghose, F. Djurabekova, K. Nordlund and S. Norris
   J. Appl. Phys. **123** (2018) 235108.

4. *"Formation of Non-equilibrium Alloys Through Nanocluster Deposition: The $Ag_{0.3}Al_{0.7}$ Supersaturated Alloy"*
   S. Pramanik, J. Ghosh, **P. Barman**, S.R. Bhattacharyya, M.K. Mukhopadhyay, D.K. Chanda and A. Datta
   J. Phys.: Conf. Ser. **1921** (2021) 012108.

Pintu Barman 11.08.21

Pintu Barman

DEDICATED TO

My Family

ACKNOWLEDGEMENTS

First and foremost, I would like to thank my Ph.D supervisors Prof. Supratic Chakraborty and Prof. Satyaranjan Bhattacharyya for their guidance in my research work. I am deeply indebted to Prof. Satyaranjan Bhattacharyya for his encouragements and valuable discussions as well as suggestions in the research field from the very beginning of my PhD journey. My heartily thanks to my lab-mate cum best friend Mrs. Anindita Deka for her constant support in every stage of my PhD journey and her tremendous help to successfully complete my research work. I also like to thank my former labmate Dr. Shyamal Mondal for his help during some of my initial experiments in the laboratory.

I would like to express my sincere gratitude to the doctoral committee members namely Prof. Tapas Kumar Chini (Chairman), Prof. Chandicharan Dey, Dr. Biswarup Satpati and Dr. Prasanta Karmakar for giving their valuable time to evaluate the progress of my PhD work.

I would like to thank the scientific support staff Mr. Debraj Dey, Mr. Sudipta Barman and Mr. Avijit Das for their technical supports. I would also like to thank Surface Physics and Material Science divisional office staff, Mukul Da and Gobordhan Da for their help in various non-academic affairs.

I would like to thank some of my seniors namely, Dr. Safiul Alam Mollick, Dr. Sourav Das, Dr. Tapas Ghosh, Dr. Achyut Maity and Dr. Ashim Roy for their help and encouragements at the initial stage of my PhD journey. I also sincerely thank one of my friends Mr. Dipak Mazumder.

It would be incomplete without thanking my family members. I would like to thank my mother, my father and my elder brother for their constant help, supports and encouragements throughout my PhD tenure.

Finally, I would like to acknowledge University Grant Commission, India for the financial support during my PhD tenure.

Pintu Barman

11.08.21

Pintu Barman

Contents

List of Figures

List of Tables

Chapter 6

Summary and future scope

In this chapter, the overall thesis works along with the important findings are summarized.

6.1 Summary

The main goal of this thesis is to understand the growth mechanism of metal nanoclusters on Si substrate under various experimental conditions and the influence of interfacial growth over different film properties such as morphological, optical and wetting properties. In order to study their growth behaviour on the substrate, metal nanoclusters were grown within a gas-aggregation nanocluster source and then deposited their size-selected beam on a Si substrate. Apart from the growth behaviour study, an attempt is also made to prepare bimetallic Ag-Au nanoparticles using two-step synthesis method to study their microscopic and spectroscopic properties. The chapter-wise significant findings are described in the thesis as stated below-

In Chapter 1, a brief introduction of nanoclusters, their types and formation mechanism as well as their importance in various fields of research are discussed. Apart from that a detailed explanation of cluster-surface interaction and their role in various types of growth processes are discussed.

In Chapter 2, production of metal nanoclusters and their optimization inside a magnetron based nanocluster source are discussed. Along with that a detailed explanation of various microscopic and spectroscopic tools used for the characterization of nanoclusters are discussed.

In Chapter 3, the growth dynamics of size-selected Cu and Ag nanoclusters is studied on Si substrates. To study the dynamics of surface growth, experiments were carried out at different deposition times. Various surface statistical parameters of the deposited films were analyzed using the AFM micrographs of the films. From the study, it is found that at initial stage of film formation, deposited metallic clusters are randomly distributed over the substrate where the probability of agglomeration

and diffusion of clusters are very low. After a certain time of deposition, the growth of another layer takes place over the pre-existed first layer. Therefore, a change in rms roughness of the films is observed. Experimentally obtained growth exponent (β) exhibits two steps of evolved surface where the first one is associated with sub-monolayer accumulation of the nanoclusters and second one is associated with the multi-monolayer growth. The first growth step is found to follow the Kardaar-Parisi-Zhang model. The most important achievement of this research is to find a second growth step with a higher growth exponent mostly dominated by the shadowing effect. The shadowing effect comes into play when deposition occurred at non-normal incidence. In this process, the pre-existed cluster aggregates act as taller surface which captured most of the incoming clusters and prevent them from reaching the lower lying surface areas or valleys. Although the shadowing effect is dominant in the second growth step, the probability of occurrence of re-emission also exists and as a consequence we find the value of growth exponent(β) slightly lower than unity.

In Chapter 4, the evolution of surface morphology of cluster deposited films as a function of incident ion current has been observed. The knowledge of evolution of the surface morphology for nanocluster-deposited surface has tremendous importance for the development of nanopaticle-based devices. An important issue of surface roughening by depositing size-selected Ag-nanoclusters on planner Si substrates for different ion beam currents is addressed here. It is found that with the increase in ion beam current the Ag cluster aggregates on the surface are enhanced by increasing their size and shape as well. Initially cluster aggregates form small nano-dot structures that evolve into mound-like structure at higher ion currents. Upon analyzing the size-distribution histograms, it is found that the size distribution is bi-modal in nature up to a certain ion beam current which turns out to be mono-modal for higher ion beam current. The upper average size is found to be increased monotonically with ion beam current. The character of the film growth were analysed by AFM measurements using

which we have estimated some of the important surface statistical parameters such as interface width, autocorrelation function, Hurst exponent and fractal dimension. The interface width of the films increases very rapidly with the evolution of the films. The lateral correlation length (ξ) of the films increases with ion beam current. The fractal dimension value of the films also increases with ion beam current suggesting formation of locally jagged surface at higher ion current. From the compositional analysis of the films it is found that the total concentration of silver on the surface increases monotonically with ion beam current. The presence of metallic silver is observed for all the Ag-cluster aggregate films. The water contact angle (CA) study reveals that there is a transition in wettability from hydrophilic to hydrophobic nature of the film with the increase in ion current. The increased amount of silver on the surface with increased ion current may be one of the possible reasons for the change in wettability of the films. Moreover, one of the surface morphological parameter namely, fractal dimension may be another contributory factor influencing the wetting property of the films. It is also observed that the surface developed for highest ion current only satisfies the Wenzel's model.

In Chapter 5, the behaviour of different cluster properties are investigated by varying the deposition temperature of the films. The study shows that the average Ag-cluster aggregate size over the untreated Si substrate increases with the increase in annealing time. But the average cluster size is found to be decreased when the clusters deposited on thermally treated Si substrate was further annealed for longer time. Considering the above morphological variation with annealing temperature and time an attempt is made to synthesize the bimetallic Ag-Au nanoparticles on Si substrate. The bimetallic Ag-Au nanoparticles were prepared by two-step synthesis methods where size-selected Ag-nanocluster with diameter of 5 nm was deposited on an as-prepared Au-film and annealed at an elevated temperature of $\sim 300\ ^{o}$C upto an annealing time of 5 hours. From the morphological investigation of the films, it

is found that the size of bimetallic nanoparticles over the Si film decreases with the increase in annealing time that may be due to diffusion of Ag and Au over Si surface. It is also found that the obtained bimetallic nanoparticles are uniformly distributed over the surface with a narrow size distribution. The composition of these bimetallic nanoparticles were investigated by in-situ XPS measurements. It reveals that after 5 hours of annealing the compositional ratio of Ag to Au on the bimetallic nanoparticles is found as $\sim$ 3:1. It is also observed that the core level Ag 3d and Au 4f peaks shifted towards higher binding energy with increasing annealing time indicate a decrease in size of the bimetallic Ag-Au nanoparticles with annealing time. The analysis of core level O 1s peaks shows that a small fraction of silver of the bimetallic nanoparticles gets oxidized whereas no trace of oxidation of gold is observed. Moreover, metal silicide peaks in the high resolution XPS spectra are not observed at any stages of annealing.

6.2 Future scope

Controlling the size of the nanoclusters during their synthesis is one of the important factors for the fabrication of various nanoparticle-based devices. Production of size-selected nanoclusters has a wide variety of applications due to their unique behaviour as compared to their bulk counterparts. Considering the research observations and conclusion of this thesis, there are several research directions that may be pursued in future. A few of research activities to be pursued in future are the following:

- Study on the size-effect of silver cluster on its surface plasmonic properties and utilize the properties for enhancing the efficiency of the solar cell.
- Study on the surface enhanced Raman scattering (SERS) of Ag nanoclusters of

a particular size and use the property for the fabrication of sensor-based devices.

- Study on the optical properties of bimetallic Ag-Au nanoparticles by tuning its compositions for various device applications.
- Study on modification of the target material(s) for the production of multimetallic nanoclusters in a single step with controlled size, shape and composition.

Chapter 6

Summary and future scope

In this chapter, the overall thesis works along with the important findings are summarized.

6.1 Summary

The main goal of this thesis is to understand the growth mechanism of metal nanoclusters on Si substrate under various experimental conditions and the influence of interfacial growth over different film properties such as morphological, optical and wetting properties. In order to study their growth behaviour on the substrate, metal nanoclusters were grown within a gas-aggregation nanocluster source and then deposited their size-selected beam on a Si substrate. Apart from the growth behaviour study, an attempt is also made to prepare bimetallic Ag-Au nanoparticles using two-step synthesis method to study their microscopic and spectroscopic properties. The chapter-wise significant findings are described in the thesis as stated below-

In Chapter 1, a brief introduction of nanoclusters, their types and formation mechanism as well as their importance in various fields of research are discussed. Apart from that a detailed explanation of cluster-surface interaction and their role in various types of growth processes are discussed.

In Chapter 2, production of metal nanoclusters and their optimization inside a magnetron based nanocluster source are discussed. Along with that a detailed explanation of various microscopic and spectroscopic tools used for the characterization of nanoclusters are discussed.

In Chapter 3, the growth dynamics of size-selected Cu and Ag nanoclusters is studied on Si substrates. To study the dynamics of surface growth, experiments were carried out at different deposition times. Various surface statistical parameters of the deposited films were analyzed using the AFM micrographs of the films. From the study, it is found that at initial stage of film formation, deposited metallic clusters are randomly distributed over the substrate where the probability of agglomeration

and diffusion of clusters are very low. After a certain time of deposition, the growth of another layer takes place over the pre-existed first layer. Therefore, a change in rms roughness of the films is observed. Experimentally obtained growth exponent (β) exhibits two steps of evolved surface where the first one is associated with sub-monolayer accumulation of the nanoclusters and second one is associated with the multi-monolayer growth. The first growth step is found to follow the Kardaar-Parisi-Zhang model. The most important achievement of this research is to find a second growth step with a higher growth exponent mostly dominated by the shadowing effect. The shadowing effect comes into play when deposition occurred at non-normal incidence. In this process, the pre-existed cluster aggregates act as taller surface which captured most of the incoming clusters and prevent them from reaching the lower lying surface areas or valleys. Although the shadowing effect is dominant in the second growth step, the probability of occurrence of re-emission also exists and as a consequence we find the value of growth exponent(β) slightly lower than unity.

In Chapter 4, the evolution of surface morphology of cluster deposited films as a function of incident ion current has been observed. The knowledge of evolution of the surface morphology for nanocluster-deposited surface has tremendous importance for the development of nanopaticle-based devices. An important issue of surface roughening by depositing size-selected Ag-nanoclusters on planner Si substrates for different ion beam currents is addressed here. It is found that with the increase in ion beam current the Ag cluster aggregates on the surface are enhanced by increasing their size and shape as well. Initially cluster aggregates form small nano-dot structures that evolve into mound-like structure at higher ion currents. Upon analyzing the size-distribution histograms, it is found that the size distribution is bi-modal in nature up to a certain ion beam current which turns out to be mono-modal for higher ion beam current. The upper average size is found to be increased monotonically with ion beam current. The character of the film growth were analysed by AFM measurements using

which we have estimated some of the important surface statistical parameters such as interface width, autocorrelation function, Hurst exponent and fractal dimension. The interface width of the films increases very rapidly with the evolution of the films. The lateral correlation length (ξ) of the films increases with ion beam current. The fractal dimension value of the films also increases with ion beam current suggesting formation of locally jagged surface at higher ion current. From the compositional analysis of the films it is found that the total concentration of silver on the surface increases monotonically with ion beam current. The presence of metallic silver is observed for all the Ag-cluster aggregate films. The water contact angle (CA) study reveals that there is a transition in wettability from hydrophilic to hydrophobic nature of the film with the increase in ion current. The increased amount of silver on the surface with increased ion current may be one of the possible reasons for the change in wettability of the films. Moreover, one of the surface morphological parameter namely, fractal dimension may be another contributory factor influencing the wetting property of the films. It is also observed that the surface developed for highest ion current only satisfies the Wenzel's model.

In Chapter 5, the behaviour of different cluster properties are investigated by varying the deposition temperature of the films. The study shows that the average Ag-cluster aggregate size over the untreated Si substrate increases with the increase in annealing time. But the average cluster size is found to be decreased when the clusters deposited on thermally treated Si substrate was further annealed for longer time. Considering the above morphological variation with annealing temperature and time an attempt is made to synthesize the bimetallic Ag-Au nanoparticles on Si substrate. The bimetallic Ag-Au nanoparticles were prepared by two-step synthesis methods where size-selected Ag-nanocluster with diameter of 5 nm was deposited on an as-prepared Au-film and annealed at an elevated temperature of $\sim 300\ ^{o}$C upto an annealing time of 5 hours. From the morphological investigation of the films, it

is found that the size of bimetallic nanoparticles over the Si film decreases with the increase in annealing time that may be due to diffusion of Ag and Au over Si surface. It is also found that the obtained bimetallic nanoparticles are uniformly distributed over the surface with a narrow size distribution. The composition of these bimetallic nanoparticles were investigated by in-situ XPS measurements. It reveals that after 5 hours of annealing the compositional ratio of Ag to Au on the bimetallic nanoparticles is found as $\sim$ 3:1. It is also observed that the core level Ag 3d and Au 4f peaks shifted towards higher binding energy with increasing annealing time indicate a decrease in size of the bimetallic Ag-Au nanoparticles with annealing time. The analysis of core level O 1s peaks shows that a small fraction of silver of the bimetallic nanoparticles gets oxidized whereas no trace of oxidation of gold is observed. Moreover, metal silicide peaks in the high resolution XPS spectra are not observed at any stages of annealing.

6.2 Future scope

Controlling the size of the nanoclusters during their synthesis is one of the important factors for the fabrication of various nanoparticle-based devices. Production of size-selected nanoclusters has a wide variety of applications due to their unique behaviour as compared to their bulk counterparts. Considering the research observations and conclusion of this thesis, there are several research directions that may be pursued in future. A few of research activities to be pursued in future are the following:

- Study on the size-effect of silver cluster on its surface plasmonic properties and utilize the properties for enhancing the efficiency of the solar cell.
- Study on the surface enhanced Raman scattering (SERS) of Ag nanoclusters of

a particular size and use the property for the fabrication of sensor-based devices.

- Study on the optical properties of bimetallic Ag-Au nanoparticles by tuning its compositions for various device applications.
- Study on modification of the target material(s) for the production of multi-metallic nanoclusters in a single step with controlled size, shape and composition.

Chapter 1

General Introduction

In this chapter, a brief introduction of nanoclusters and their importance in various fields of nanotechnology are discussed. A theoretical overview on formation of nanoclusters also is given. Moreover, the interaction of cluster beam with solid surface at different energy ranges and post deposition phenomena on the substrates are discussed.

1.1 Introduction

"*There's plenty of room at the bottom*" is one of the well known lectures and articles by Richard Feynman [1] where he motivated the researchers to construct a new field of study by developing devices and machines using the smallest component of particles such as atoms. The field of nanoscience and nanotechnology is being pursued to study the behaviour of particles of nanometer dimensions and their applications to various devices using this visionary document. The study of cluster physics is a relatively new area of research in the field of nanotechnology grown rapidly during last two decades. At the very beginning, cluster plays a vital role as a component in building devices for variety of applications in the field of electronics, magnetic, optical, mechanical etc. Metal nanoparticles were used for a long time even without knowing the proper science behind their applications. Use of metal nanoparticles to colour the pigments in strained glass windows by the artisans in the medieval period may be considered as a representative example. Another example is the Roman Lycurgus cup where metal nanoparticles were embedded so as to illuminate it with different coloures depending on the direction of illumination. Clusters are considered to be a building block of an application because they change their inherent properties dramatically depending upon their size, shape and compositions. A brief introduction of nanoclusters and their importances in various research directions are given in the next section.

1.2 A Brief introduction to Nanoclusters and their applications

Clusters are aggregates of atoms or molecules of a countable number within a range of 2-10^n where the maximum value of n can be upto 6 or 7. If the constituent particles of a cluster are of the same species, it is termed as homo-atomic (homo-molecular). On the other hand, if different species constitute a cluster, it is then termed as hetero-atomic (hetero-molecular) cluster. Since cluster size lies between atomic and bulk states, clusters are often considered as a bridge between the two due to their intermediate status [2]. The properties of clusters and their aggregates are quite different from their bulk counterparts that bring particular interest to the researchers and motivate them to carry out research on clusters. A large number of atoms or molecules constituting the surface of a cluster have higher surface to volume ratio. Various thermodynamic properties of metallic nanoclusters differ from the bulk and are found to be dependent on cluster size. As the size of the clusters decreases down to nanometer range some of the thermodynamic properties such as melting point, surface tension and heat capacity etc deviates from bulk values. Since majority of atoms in a metallic nanocluster are found on the surface, the clusters exhibit the size-dependent thermodynamic properties due to the influence of surface effects. In a nanocluster, the surface atoms have lower coordination number than that of metal atoms in the bulk and, therefore, less stable. As a result, smaller metal nanoclusters are thermodynamically unstable as compared to bigger clusters due to their larger surface to volume ratio. Apart from the surface effects, structural influence of a nanocluster also attributes towards the size dependent thermodynamic activity. In this regard, their cumulative contribution can be considered for the size dependent thermodynamic properties of nanoclusters. In order to find out the size-dependent thermal stability of a metal nanocluster, the knowledge of interfacial surface energy of the nanocluster is essential. Recently, one of the researchers Wolf [3] found that nanoparticles having size less than 2 nm are thermodynamically unstable and predicted to get oxidized to form the corresponding metal oxide. The study on cluster physics provides an insight information on the uses of clusters as a building block of a new material for future applications. Nanoclusters can be grown/deposited

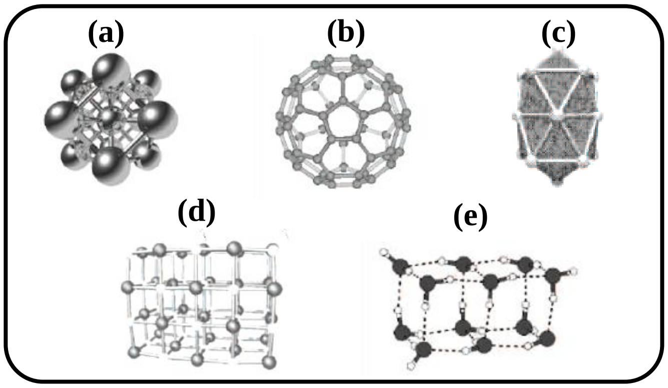

Figure. 1.1: *A Schematic of bond formation of (a) Metal clusters, (b) Semiconductor clusters, (c) Rare gas clusters, (d) Ionic clusters and (e) Molecular clusters.*

using various techniques either on a surface or in embedded form depending on the nature of applications. Use of cluster beam may be considered as a technique to grow/deposit cluster on a substrate for the preparation of clustered films.

1.2.1 Classifications of Clusters

Clusters can be formed by most of the elements of the periodic table. Even the rare gases form clusters. Clusters can be sub-divided into various groups such as metal clusters, semiconductor clusters, rare-gas clusters, molecular clusters, ionic clusters etc. depending on the nature of the atomic bonds in the clusters. A schematic of formation of various types of clusters is shown in figure 1.1.

1.2.1.1 Metal clusters

Metal elements from different blocks of the periodic table produce metal clusters by formation of various bonds. S-block elements (alkali and alkaline earth metals) utilize delocalized and non-directional metallic bonds between s-orbitals to produce metallic cluster; sp-block metals e.g. aluminum produces metal clusters by forming covalent bonds between the s and p orbitals; transition metals use d orbitals for the bond formation in a cluster. Metal clusters may be formed either by single element or multi elements. Alloyed clusters are produced by two or more elements of different metals.

1.2.1.2 Semiconductor clusters

Semiconductor clusters are formed by the elements of solid-state semiconductors such as silicon, germanium, carbon etc. The bond formed is strong, directional and covalent in nature in these type of clusters. Compound semiconductor clusters e.g. $\mathrm{Ga}_x\mathrm{As}_y$ are also under this category that are bound by polar covalent bonds.

1.2.1.3 Ionic clusters

Ionic clusters are formed due to the increase in electronegative difference of two elements of a compound semiconductor clusters. The charged states of an ionic cluster may be positive, negative or neutral. Examples of ionic clusters are $[\mathrm{Na}_x\mathrm{Cl}_y]^{(x-y)+}$, $[\mathrm{Mg}_x\mathrm{O}_y]^{2(x-y)+}$ etc.

1.2.1.4 Rare gas clusters

The rare gas clusters are formed between inert gas elements at low temperature where the cluster elements are found to be bounded by weak van dar Waals force. The inter-atomic attraction between the elements increases from helium (He) to radon (Rn) cluster.

1.2.1.5 Molecular clusters

The supersonic expansion of molecular vapor causes the formation of molecular clusters. The bonding of this class of clusters includes van der Waals, dipole-dipole interaction, multipolar interaction, hydrogen bonding etc. In molecular clusters, the molecules are either of same type e.g. water cluster $[(H_2O)_N]$ or of different types e.g. $(CH_3OH)_N.(H_2O)_M$.

1.2.2 The spherical cluster approximation

In spherical cluster approximation model, clusters are assumed to be spherical. This approximation is very useful to solve some of the complex equations related to cluster growth. For instance, r_c, S_c, V_c are respectively labeled as radius, surface area and volume of a cluster containing n number of atoms. If we consider that all the atoms are identical and r_a, S_a, V_a are radius, surface area and volume of the atoms, respectively then volume of the cluster may be written as,

$$V_c = n \times V_a \tag{1.1}$$

or

$$\frac{4}{3}\pi r_c^3 = n \times \frac{4}{3}\pi r_a^3$$

$$r_c = n^{\frac{1}{3}} r_a \tag{1.2}$$

The surface area of the cluster also can be defined as,

$$S_c = 4\pi r_c^2 = 4\pi \left(n^{\frac{1}{3}} r_a\right)^2 \tag{1.3}$$

hence,

$$S_c = n^{\frac{2}{3}} S_a \tag{1.4}$$

The number of surface atoms (n_s) in a larger cluster can be defined as the ratio of surface of the cluster to the cross sectional area of an atom (A_a) and may be expressed as,

$$n_s = \frac{S_c^2}{A_a^2} \tag{1.5}$$

Putting the values of S_c from equation 1.4, the equation 1.5 reduces to,

$$n_s = 4n^{\frac{2}{3}} \tag{1.6}$$

Moreover, the fraction of surface atom on cluster can be defined as,

$$F_s = \frac{n_s}{n} = 4n^{-\frac{1}{3}} \tag{1.7}$$

1.2.3 Cluster size regime

Based on the number of constituents, clusters may be divided into three possible regimes, small cluster ($<$ 100 atoms), medium sized cluster ($\sim$ 100 - 10000 atoms) and large cluster ($>$ 10000 atoms) [4]. Table 1.1 depicts different cluster parameters for all the cluster sizes.

According to spherical cluster approximation, the diameter of a cluster with n constituent atoms can be written as,

$$d_c = 2 \times r_c = 2r_w n^{\frac{1}{3}} \tag{1.8}$$

where r_w is the Wigner-Seitz radius.

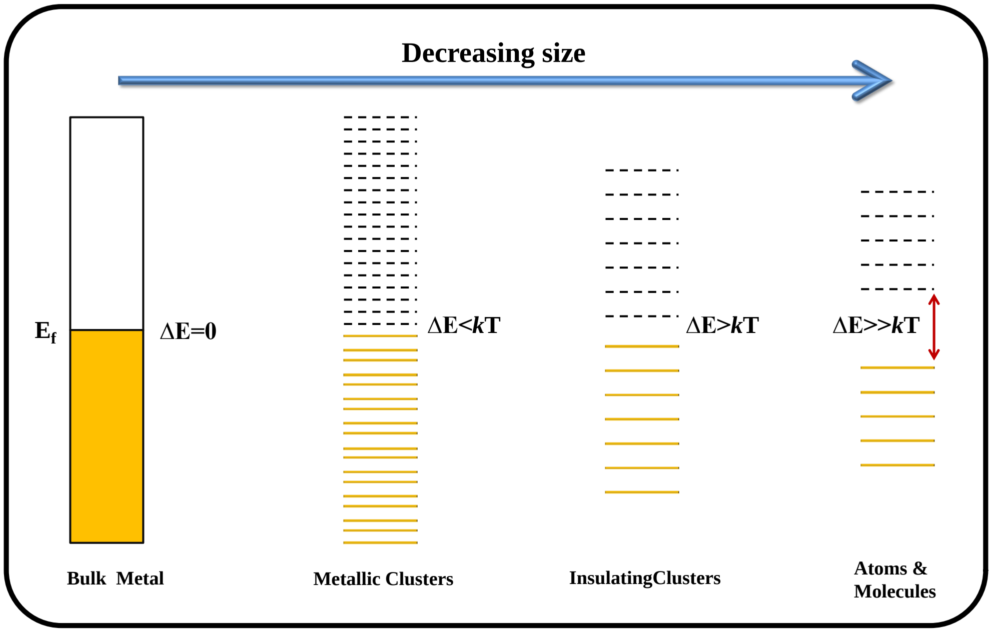

Figure. 1.2: *Influence of particle size on the electronic band structures of metal. Here* ΔE *denotes the energy band gap.*

The properties of small clusters are varied with the size and shape of the clusters. For small clusters, it is very difficult to find out a simple and smooth relation of the dependence of cluster constituent atoms on the cluster properties. For a medium-sized cluster, the cluster properties smoothly vary with the cluster constituents but still reflect the implications of smaller size of the cluster. For large clusters, the properties reflect the corresponding bulk properties.

Table 1.1: Variation of number density of atoms constituting the cluster (n), cluster diameter (d_c), fraction of surface atoms (F_s) in a cluster.

Parameters	Small	Medium	Large
n	$\leq 10^2$	$10^2 - 10^4$	$> 10^4$
d_c (nm)	≤ 1.9	1.9-8.6	>8.6
F_s	≥ 0.86	0.86-0.19	≤ 0.19

Small and medium-sized clusters significantly differ from bulk material in two important properties. In clusters, a large number of their constituent atoms are situated at the surface and their quantum states are quite different from those of the bulk material. In a small cluster, the spacing between two energy levels cannot be neglected and depends on the size of the clusters. Materials show interesting properties, quite different from its bulk-phase when one or more dimensions of a material are reduced to the nanometer scale ($<$ 100 nm). One of such noticeable effects is Quantum confinement effect where the mobility of electron is confined. Due to such effect nanoparticles can also be considered as quantum dot structures. Depending upon the number of degrees of freedom of the electron's movement, the quantum structures are divided into quantum well (2D), quantum wire (1D) and quantum dot (0D). In a quantum dot, electrons are completely confined in specific energy states and their movements are restricted. Due to this phenomenon, the energy difference between the energy states and the band gap energy increases. When the diameter of a quantum structure is less than its "Bohr radius", the thermally excited electrons in the conduction band form a weak bond with its hole by forming an "exciton". The exciton is a bound state in which an electron and hole are attracted to one another by electrical Coulomb attraction force. The distance between the electron and hole in an exciton is measured by the Bohr radius and is termed as exciton Bohr radius. The "band" of energies in QDs becomes distinct energy levels due to this unique confinement characteristics. This exciton Bohr radius can be used as the critical size below which the quantum confinement effect does not take place in a material. According to quantum mechanics, this critical size can be resembled with the De Broglie wavelength of free electron. During thermal excitation of an electron, a threshold is reached where the Kubo gap (ΔE) is equal to the thermal energy. It is found that at low temperature, insulator becomes semiconductor and at high temperature it becomes metal when electrons cross this Kubo gap due to thermal excitation. Moreover, the magnetic properties of small cluster are also found to fluctuate substantially. The transition from metallic to non-metallic behaviour can be realized as a function of decreased particle size as shown in figure 1.2. From UV-Vis spectroscopy study, it is possible to measure the band gap energy of metallic clusters.

1.2.4 Size-dependent melting of clusters

In 1909, Pawlow [5] developed a thermodynamic model where it was predicted for the first time that melting temperature of nanoparticle decreases linearly with the inverse of particle radius. In 1910, he also made an attempt to verify this phenomena [6]. An unambiguous verification of this phenomenon was first observed by Baffat *et al.* [7] in 1976 where the melting point depression of small Au-cluster using a scanning electron-diffraction technique was found. The melting temperature of smallest Au-cluster was found at $\sim$ 300 K much lower than the melting temperature of bulk gold ($\sim$ 1336 K). In a theoretical model Berry *et al.* [8, 9] proposed that the cluster exhibited two phases namely liquid-like and solid-like phases closer to the melting temperature. In 1990, Castro *et al.* [10] measured the melting temperature of Au and Ag clusters using the field emission current from the individual cluster and found the dependence of melting temperature with the clusters size. A decrease in melting temperature with their reduced size has been observed in almost all the free nanoparticles although anomalies in melting behaviour of nanoparticles are also reported. The melting temperatures of Ga and Sn clusters are found to be higher as compared to their bulk counterparts [11, 12].

1.2.5 Applications of nanocluster

Nanoparticles are considered as the functional building blocks of various applications in the area of nanotechnology from fundamental to industrial research and their applications. The reduced sizes of nanoparticles offer various novel properties and interesting behaviour as compared to their bulk counterpart. In order to grow/produce nanoparticles of controlled size, shape and composition, it is necessary to use a standard method of preparation comprising of a well controlled, scalable and clean process and to apply them for various applications. Gas phase synthesis of nanoparticles or nanoclusters is used in variety of applications out of which we discuss here some of the key applications that are found to be very promising in the field of nanoscience and nanotechnology.

1.2.5.1 Catalytic application

The chemical properties of nanoparticles are affected due to the variation of their electronic structures when the size of the nanoparticle decreases. For example, gold in nanometer scale shows active catalytic support in many chemical reactions that is not observed in case of bulk gold [13]. In catalytic research, the preparation of various catalysts by deposition of mass selected cluster ions are studied by many researchers wherein it is found that size-selected gold nanoclusters with a very few number of constituent atom shows significant catalytic behaviour [14,15]. Size selected Pd nanoclusters deposited on alumina film is now considered as a model catalyst [16]. A small variation in particle size in atomic scale leads to a dramatic change in catalytic efficiency of small clusters [17]. Besides the contributions of cluster size and shape, the supporting substrates also play an important role in the catalytic activity e.g. inactive Au and Pd nanoparticles show active catalytic behaviour when deposited on oxide surface [18, 19]. In general, oxidation of Cu nanoparticles decreases with their reduced size but when deposited on amorphous alumina film, the oxidation behaviour of smaller Cu nanoclusters (Cu_4) increases significantly as compared to the larger ones (Cu_{12} and Cu_{20}) [20].

1.2.5.2 Application to energy generation

Nanoparticles are widely used in different energy applications [21, 22] such as photovolatics, battery materials, energy storage, photocatalysis etc. Nanoclusters prepared by gas phase synthesis methods are utilized for various photocatalytic applications namely, CO_2 photo reduction [23], organic pollutant oxidation [24] etc. Gas aggregation synthesis of Si nanoparticles are widely used for photovoltaic applications [25]. Moreover, in order to improve the performance of lithium ion batteries, gas phase nanoparticle synthesis also can be used. Control over the particle size, time efficiency of nanoparticles and their compositions lead to improved electrochemical performances of the lithium ion batteries [26,27]. Furthermore, in one of the solar cell applications it is found that use of size selected Ag and Si nanoclusters in the cell enhances its efficiency up to $\sim 23\%$ [28].

1.2.5.3 Application in sensors

Gas phase synthesis of size-selected metal nanoclusters are used for different sensor applications where special attention is given to control their size, composition and structure by achieving an optimum condition. It is observed that size-selected tin oxide nanoclusters of 3-10 nm diameter have been used for ammonia and hydrogen gas detection at lower temperature range [29]. Further, size-selected Pd nanoclusters are used for the detection of hydrogen molecules [30]. Moreover, Ag nanoparticles below 10 nm diameter are intensively used for the detection of smaller molecules [31]. Cr nanoparticles are found to be a good strain sensor when deposited on polyethylene terephthalate film [32]. In a recent work, the uses of size-selected Cu and Ag nanoclusters show an enhanced sensitivity for glucose sensing [33].

1.2.5.4 Plasmonic application

Metal nanoparticles produced by gas aggregation method are considered as potential candidates for the tuning their plasmonic properties. Cu nanoparticles produce intense and narrow plasmonic spectra in 500 and 800 nm wavelengths. Size-selected Ag embedded nanoclusters in a quartz substrate show enhanced plasmonic properties [34, 35]. Deposition of Al nanoparticles in a CH matrix shows well-pronounced plasmonic bands where size tuning of the nanoparticles influences the bands in the wavelength range of 255-307 nm [36]. Among various metal nanoparticles, Au nanoparticles show strong plasmonic properties and higher chemical stability leading to their use in various plasmonic applications [37]. Moreover, the preparation of hybrid nanoparticles by modifying the composition of two or more nanoparticles has also received considerable attention for various plasmonic applications [38].

1.3 Elementary processes of cluster formation

A non-equilibrium thermodynamic condition is required for the production of clusters provided by various types of cluster sources. Depending on its nature different methods have so far been employed for cluster synthesis. High melting point clusters are produced by laser vaporization method whereas low melting point clusters can be easily produced by thermal vaporization method. There are various methods/techniques available for the production of metal clusters namely, laser vaporization, supersonic expansion, arc discharge, magnetron sputtering, gas-aggregation, electrosprays etc. Magnetron-based gas-aggregation cluster source is widely used for the production of nanoclusters. It is an efficient and easy technique to produce metal nanoclusters. In this method, the vapor atoms/molecules of the sputtered materials repeatedly collide with the inert gas atoms (or molecules) within

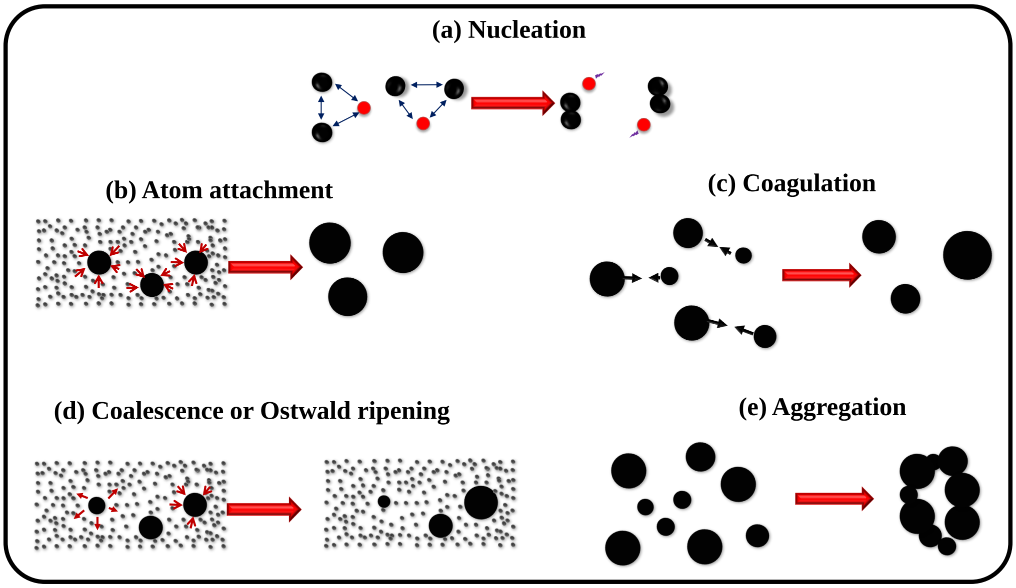

Figure. 1.3: *Elementary processes of cluster formation inside a gas-aggregation cluster source.*

an aggregation chamber to reach supersaturation state and thereby form clusters. The cluster formation process can be divided mainly into two categories namely, nucleation and growth. A detailed description of these two processes is given below.

1.3.1 Nucleation Process

The nucleation process is a three body collision process that occurred between two metal atoms and a buffer gas atom. In case of silver target sputtered by ionized argon gas, the nucleation process may be written as,

$$Ag + Ag + Ar \rightarrow Ag_2 + Ar \tag{1.9}$$

The nucleation process is stabilized by forming a dimer. The dimer either will grow larger or will be destroyed depending on its size. In this process, the buffer gas atom (Ar) is to simultaneously satisfy the energy and momentum conservation and also stabilizes the dimer by removing excess energy released during the bond formation between two colliding metal atoms. Once a dimer is formed, it acts as condensation nuclei for further cluster growth. The existence of the dimers is dependent on the size of the critical cluster radius (r_{cr}) that can be expressed as [2],

$$r_{cr} = \frac{2\sigma m}{K_B T \rho} \frac{1}{ln\phi_k} \tag{1.10}$$

where,

$\sigma \rightarrow$ surface tension of the clusters which is considered as a liquid droplet,

$\rho \rightarrow$ density of the cluster material,

$m \rightarrow$ mass of the cluster,

$\phi_k \rightarrow$ supersaturation condition during formation of dimer,

$K_B \rightarrow$ Boltzmann constant.

Clusters with radius smaller than r_{cr} will evaporate whereas large-sized clusters ($> r_{cr}$) will grow. Theoretical approaches suggest the dimer as a stable nucleus for cluster growth. The rate of generation of dimer during nucleation process depends on the number density of constituent cluster atoms (N) and number density of buffer gas atoms (N_a). Therefore,

$$\frac{dN_d}{dt} = KN^2 N_a \tag{1.11}$$

where K, the rate constant of three body collision process is found to vary between 10^{-33}-10^{-32} cm^6 s^{-1} [39, 40] and for silver its value is $K_{Ag} = 5.5 \times 10^{-33}$ cm^{6}s^{-1} [41].

From equation 1.11 the maximum dimer density can be estimated as,

$$N_d = KN^2 N_a \frac{L}{2\bar{v}} \tag{1.12}$$

where L is the aggregation length and $\bar{v}$ is the average drift velocity of clusters inside the gaseous medium. A schematic of nucleation process of clusters is shown in figure 1.3(a).

1.3.2 Growth processes of clusters

Once a stable dimer is formed, further cluster growth is governed by various independent processes namely, atom attachment process, coagulation process (in kinetic and diffusion regimes), coalescence or Ostwald ripening process and Aggregation process.

1.3.2.1 Atom attachment process

The first mechanism of cluster growth is to convert the sputtered or evaporated metal atoms into metallic clusters. In atom attachment process, the subsequent growth of nucleated dimer occurs via attachment of free atoms to the surface of the dimer. For example, the atom attachment process for a single silver atom/ion (Ag) on a silver dimer/cluster (Ag_n)($n \geq 2$) can be written as,

$$Ag_n + Ag \rightarrow Ag_{n+1} \tag{1.13}$$

The atom attachment process normally takes place inside the aggregation zone right after formation of a dimer. A schematic of atom attachment process is shown in figure 1.3(b). Sometimes the growth process of clusters via atom attachment process is less stable as compared to the dimer formation via nucleation process because the additional energy is transferred to the buffer gas during atom-cluster collision [42]. The rate constant of equation 1.13 depends on the size of the clusters. If the cluster contains 'n' number of atoms, the rate constant can be written as [39, 43, 44],

$$K_{attach} = k_o n^{2/3} \tag{1.14}$$

where k_o, the specific rate constant may be expressed as,

$$k_o = r_w^2 \sqrt{\frac{8T\pi}{m}} \tag{1.15}$$

where T is the cluster formation temperature and r_w is the Wigner-Seitz radius of the cluster material. The values of r_w and k_o for silver are found to be 1.66 Å and 2.2×10^{-11} cm^{3}s^{-1}, respectively.

The characteristics of atom attachment process can be determined by a dimensionless parameter 'G' where,

$$G = \frac{k_o}{K N_a} \tag{1.16}$$

with N_a is the number density of buffer gas atom. $G \gg 1$ indicates the formation of a more stable dimer during nucleation process as compared to the formation of clusters via atom attachment process.

The size-distribution function f_n may be determined if the individual cluster having size $n(t)$ satisfies the following condition,

$$\frac{dn}{dt} = k_o n^{2/3} N \tag{1.17}$$

where t signifies the dimer formation time that later acts as the condensation nucleus for a particular cluster. The size of the cluster after time t will be,

$$n = \left(\frac{Nk_o t}{3}\right)^3 \tag{1.18}$$

On the basis of above equation the cluster size distribution function can be written as,

$$f_n = \frac{C}{n^{2/3}} \tag{1.19}$$

with C as the normalization constant.

Furthermore, the other parameters describing the kinetics of cluster growth may also be determined using the above equation. Hence, the density of clusters (N_{cl}) and average cluster size ($\bar{n}$) are found to be,

$$\bar{n} = 0.31 \times G^{3/4} \tag{1.20}$$

and

$$N_{cl} = 3.2 \times NG^{-3/4} \tag{1.21}$$

1.3.2.2 Coagulation process

Coagulation process of cluster growth is defined as the formation of a larger cluster resulting from the contact of two individual clusters of smaller sizes. The schematic of cluster coagulation process is shown in figure 1.3(c). Considering two small silver clusters containing 'n' and 'm' number of constituent atoms, the coagulation process can be expressed as,

$$Ag_m + Ag_n \rightarrow Ag_{m+n} \tag{1.22}$$

where Ag_{m+n} indicates larger silver cluster containing $(n + m)$ number of atoms.

Under the framework of liquid drop model, the coagulation process is divided into two regimes namely, kinetic regime and diffusion regime. The interaction process between atoms and clusters within the aggregation zone for both the regimes are directly dependent on the Brownian motion of the gas atoms. In kinetic regime of cluster coagulation, it is consider that only one particle at a time strongly interacts with the clusters whereas in diffusion regime it is assumed that many particles simultaneously interact with the cluster.

The criteria of two cluster approach in the diffusion regime of cluster coagulation process may be written as [45],

$$N_{cl}\Lambda^3 \ll 1 \tag{1.23}$$

where Λ is the mean free path of the small clusters in the buffer gas.

The relation between number densities of clusters (N_{cl}) and bound atoms inside the cluster (N_b) is found to be,

$$N_{cl} = \frac{N_b}{\bar{n}} \tag{1.24}$$

The concentration of bound atoms in a cluster is the ratio between the N_b and N_a and it is denoted as c_b. Therefore,

$$c_b = \frac{N_b}{N_a} \tag{1.25}$$

So, combining the equations 1.24 and 1.25, the equation 1.23 is expressed as,

$$\frac{\bar{n}}{c_b^{2/3}} \gg \frac{1}{N_a^{4/3}\sigma_{cl}^2} \tag{1.26}$$

with σ_{cl} as the collision cross-section between cluster and a buffer gas atom and may be expressed as,

$$\sigma_{cl} = \frac{4}{3}\sqrt{\frac{m}{m_a}} r_w^2 \tag{1.27}$$

where m and m_a are the masses of buffer gas atom and metal atom, respectively. If we consider the example of liquid copper cluster coagulation process in the argon gas environment with $\sigma_{cl} = 2.3 \times 10^{-16}$ cm^2 and $c_b = 1\%$, the equation 1.26 is simplified to,

$$N_a \bar{n}^{3/4} \gg 3 \times 10^{23} \sqrt{c_b} \tag{1.28}$$

Considering a typical experimental condition inside a nanocluster source, N_a and $\bar{n}$ are $N_a \approx 4 \times 10^{15}$ cm^3 and $\bar{n} \sim 10^{14}$ atoms. Therefore, in order to fulfill the criteria of equation 1.28, c_b must be very low ($\sim 10^{-10}$). The maximum value of c_b estimated theoretically is found to be ~ 0.5 [46]. Hence, it can be concluded that the growth of nanoclusters occurred mostly by coagulation in the kinetic regime.

Furthermore, solving Smolukhovski equation for the kinetic regime of cluster coagulation [44], the average cluster size ($\bar{n}$) and its distribution function (f_n) may be expressed as,

$$\bar{n} = 6.3 \times (N_b k_o t)^{1.2} \tag{1.29}$$

and

$$f_n = \frac{N_b}{\bar{n}^2} \times e^{-\frac{n}{\bar{n}}} \tag{1.30}$$

1.3.2.3 Coalescence or Ostwald ripening process

A schematic representation of coalescence process of cluster growth is shown in figure 1.3(d). Formation of large clusters by the interaction of clusters with the parent vapor atom takes place in this process. Generally, clusters are found in equilibrium with the surrounding atomic vapor in this process and hence, total rate of atom attachment to the cluster surface is equal to the rate of evaporation of atoms from the cluster surface. Although this phenomena is found to vary with the size of the clusters, the rate of atom evaporation is lower than the rate of atom attachment for a large-size cluster whereas for smaller sized cluster opposite relation is found to be fulfilled. As a result, the larger clusters grow more whereas smaller clusters will evaporate.

In general, for the cluster growth in the diffusion regime of Ostwald ripening process, the following criteria should be fulfilled [45],

$$N_m \lambda_m^3 \ll 1 \tag{1.31}$$

where λ_m is the mean free path of metal atoms in a buffer gas, and may be defined as,

$$\lambda_m = \frac{1}{N_a \sigma_m} \tag{1.32}$$

with σ_m is termed as the gas kinetic cross-subsection of metal atoms in a buffer gas.

The concentration of free metal atom in a buffer gas is the number density ratio of metal atom and buffer gas atom and may be expressed as [47],

$$c_m = \frac{N_m}{N_a} \tag{1.33}$$

Combining the above equations, the criteria of cluster growth in diffusion regime of Ostwald ripening process can be re-written as,

$$c_m \ll N_a^2 \sigma_m^3 \tag{1.34}$$

The important parameters of coalescence process are critical cluster size (n_{cr}) and

and critical cluster radius (r_{cr}) and the relation between the two may be written as,

$$r_{cr} = r_w \times (n_{cr})^{1/3} \tag{1.35}$$

Depending on the size of critical cluster (n_{cr}), two groups of clusters are found. The first group is for small clusters $n < n_{cr}$ where evaporation rate is high as compared to atom attachment rate while the second group represents the larger clusters $n > n_{cr}$ where the evaporation rate is low [45,48–50]. Therefore, the difference in rate of atom evaporation to atom attachment is found to be [45],

$$\Delta J = 4\pi N_m D_m r_w \times \int_0^{n_{cr}} f_n n^{1/3} dn \times \left[exp\frac{2A}{3T} \times (n^{-1/3} - n_{cr}^{-1/3}) - 1 \right] \tag{1.36}$$

With $D_m \rightarrow$ the diffusion coefficient of metal atoms in a buffer gas with A as the specific cluster energy.

Therefore, the average cluster size ($\bar{n}$) and cluster size-distribution function (f_n) for the diffusion regime of cluster coalescence are [45],

$$f_n = \frac{n_{cr}}{3\bar{n}} \times \frac{N_b}{\mu^2} \times P_{diff}(\mu) \tag{1.37}$$

and

$$\bar{n} = \frac{\int_0^\infty f_n n dn}{\int_0^\infty f_n dn} = 1.135 \times n_{cr} \tag{1.38}$$

where μ is the reduced cluster size and may be expressed as [45],

$$\mu = \frac{r_o}{r_{cr}} = \left(\frac{n}{n_{cr}} \right)^{1/3} \tag{1.39}$$

where r_o, the radius of the cluster is expressed as,

$$r_o = r_w \times n^{1/3} \tag{1.40}$$

The probability of distribution function $P_{diff}(\mu)$ in the diffusion regime of coalescence process can be expressed as [45, 48, 51, 52],

$$P_{diff}(\mu) \begin{cases} = 69.4 \times \frac{\mu^2 \times exp[-1/(1-2\mu/3)]}{(\mu+3)^{7/3} \times \left(\frac{3}{2}-\mu\right)^{11/3}}, & for \quad \mu < 3/2 \\ = 0, & for \quad \mu > 3/2 \end{cases} \tag{1.41}$$

After a growth time t, the average cluster size is found as [48, 51],

$$\bar{n} = 1.4 \times N D_m t r_w \frac{A}{T} \tag{1.42}$$

Therefore, the average cluster size ($\bar{n}$) and the distribution function ($P_{kin}(\mu)$) in the kinetic regime of coalescence process can be expressed as [45, 48, 51, 52],

$$\bar{n} = 1.1 \times n_{cr} \tag{1.43}$$

and

$$P_{kin}(\mu) \begin{cases} = 232 \times exp(-1.18\mu) \times \frac{\mu^3 \times exp[-1/(1-2\mu/3)]}{(\mu+3)^{7/3} \times \left(\frac{3}{2}-\mu\right)^{11/3}}, & for \ \ \mu < 3/2 \\ = 0, & for \ \ \mu > 3/2 \end{cases} \tag{1.44}$$

1.3.2.4 Aggregation process

In this process, the clusters are grown by joining two or more metal particles in contact with one another. By association of solid particles a structure is formed. It is further observed that the incident colliding particles mostly preserve their initial shape. This process is called aggregation as the particles are found to aggregate in buffer gas. The cluster aggregation process can be understood from the schematic of figure 1.3(e). The aggregation of smaller clusters or particles leads to the formation of fractal aggregates in various medium [47,53]. The fractal properties of the aggregates can be understood by determining their fractal dimension values. The probability of occurrence of fractal aggregates of metal clusters inside a nanocluster source is very negligible.

1.4 Charging process of metallic nanoclusters

In a magnetron-based nanocluster source, metal nanoclusters are produced by nucleation and growth processes. Along with the growth process, charging of the clusters takes place simultaneously. During charging process both positively and negatively charged clusters are formed along with a small fraction of neutral clusters. Haberland *et al.* [54] showed that the plasma formed by magnetron sputtering process contained 40% negatively charged, 40% positively charged and rest 20% neutral nanoparticles. Recently, Popok *et al.* [55] showed that silver nanoclusters prepared by magnetron-based gas aggregation source may carry up to four negative or four positive charges depending on the sputter conditions. Furthermore, Marmon *et al.* [56] observed a planetary system of bound nanoparticles where larger cluster aggregates are found to be surrounded by a number of small nanoparticles in an orbit. It was then concluded that the planetary system was a result of the electrical and centrifugal force between the central cluster aggregate and the small particles. Momin *et al.* [57] also described the ionization process of metallic clusters. The formation of positively charged clusters occurs through the following processes,

$$M_n^o + Ar^+ \rightarrow M_n^+ + Ar^o \tag{1.45}$$

$$M_n^o + M^+ \rightarrow M_n^+ + M^o \tag{1.46}$$

$$M_n^o + M_m^+ \rightarrow M_n^+ + M_m^o \tag{1.47}$$

For the production of negatively charged cluster ions, electron attachment process is dominant and can be written as,

$$M_n^o + e^- \rightarrow M_n^- \tag{1.48}$$

$$M_n^o + e^- \rightarrow M_{n-1}^- + M^o \tag{1.49}$$

$$M_n^o + e^- + He \rightarrow M_n^- + He \tag{1.50}$$

Based on the above equations, the theoretical approach of cluster charging process provides a relation between positive to negative charged cluster ions [41, 46, 58–61] and may be written as,

$$\frac{N_+}{N_-} = \frac{m_e}{m_i} \times \left(\frac{N_i}{N_e}\right)^2 \times \frac{kT_i + V_c}{kT_e + V_c} \tag{1.51}$$

where,

$$V_c = \frac{e^2}{4\pi\epsilon_o} \times \frac{1}{r_c} \tag{1.52}$$

with m_e, N_e and T_e are electron mass, density and temperature, respectively whereas m_i, N_i and T_i are the ion mass, density and temperature, respectively. ϵ_o indicates the vacuum permittivity and r_c denotes the cluster radius. The above equations suggest that the charge ratio of clusters in a plasma is entirely dependent on the plasma processing parameters and the size of the produced clusters as well. Hence, it can be concluded that the experimental conditions significantly influence the formation of charged clusters. Reports further indicate [59, 62] that the tendency of generation of positively charged cluster ions is very high in a high pressure nanocluster source. Moreover, according to a report by Ganeva *et at.* [60], it was found that the formation of positively charged cluster ion occurs when the gas flow rate is low ($\leq$ 15 sccm), which turned into negatively charged cluster ions at higher flow rate.

1.5 Fundamental of cluster-surface collisions

The morphology of a thin-film produced by cluster beam deposition method is dependent on different factors namely, substrate material, cluster material, substrate temperature and cluster impact energy. Further, the kinetic energy (E_{kin}) of an incoming cluster is considered to be one of the important parameters that determines the cluster surface interaction regime. In general, the cluster-surface interaction process can be divided into three energy regimes, namely low energy regime ($E_{at} \sim$ 0.1 eV/atoms), medium energy regime ($E_{at} \sim$ 1-10 eV/atoms) and high energy regime ($E_{at} >$ 10 eV/atoms) [63,64]. The low-energy cluster surface interaction occurs when the kinetic energy per atom (E_{at}) is lower than the binding energy of the cluster constituent (E_b). This type of interaction is often termed as "soft-landing". In low energy interaction process, clusters just stick on the impact point but retain their compositions with a possibility of distorted shape [65,66]. The thin-film produced in this method can easily be removed from the deposited surface. In medium energy interaction process the value of E_{at} is found to be nearly equal to that of E_b and the deposited clusters strongly adhere to the substrate in this process [67–69]. As a result, the deposited clusters are found to undergo a plastic deformation thereby changing the morphology of the film. There may be a possibility of defect formation on the surface by the energetic cluster impact. This regime of cluster collision on surfaces is a topic of interest because of the influence of cluster energy on the surface morphology and their growth over the surface without being destroyed. The condition for high energy cluster surface interaction is $E_{at} > E_b$. In this energy regime, the clusters completely change their identity upon decomposition and fragmentation processes once they interact with the surface. The energetic cluster also may damage the surface upto several layers depending on the incident kinetic energy of the cluster. Deposition of clusters at a such high energy regime offers several advantages because high energy cluster deposition method is used for good coating over a surface [70, 71]; for the filling of micron sized holes in dielectric coating; for polishing an insulator surface using high energy gas clusters [54, 72, 73] etc. It may be inferred from the above that cluster impact energy is one of the key parameters in the cluster-surface collision that lies between $\sim 10^{-2}$ to 10^{8} eV/atoms. From the above three kinetic energy regimes, the low energy regime or soft-landing cluster deposition process in which the deposited cluster does not fragment and preserve their composition is mainly responsible for further cluster growth on a substrate. In addition to the cluster-surface interaction energy, the sizes of deposited clusters also play a crucial role [74]. The low energy cluster-surface interaction growth may be understood by three of the main growth modes namely Volmer-Weber, Frank-van-der-Merwe and Stranski-Krastanov growth processes. In Volmer-Weber growth mode, the adsorbed atoms interact strongly among themselves than with the substrate surface resulting in the formation of three-dimensional islands over the substrate. As long as the growth proceeds, these islands enlarge and simultaneous growth of atomic layer takes place with a rough surface feature whose height significantly surpasses the thickness of a monolayer. This type of growth mode is observed when small metal clusters are deposited on a weakly interacting substrate via soft landing process. After deposition, these metal clusters are found to be highly mobile over the substrate at room temperature until they become trapped at a step edge or a surface defect or collide with another neighboring cluster and agglomerate into bigger islands. The agglomeration process is directly dependent on the melting point of small clusters i.e., clusters of lower melting points (such as Ag, Au, Sb etc.) merge into large islands upon contact of two clusters [75]. In such case, the clusters are often considered as liquid droplets. Here the cluster-cluster interaction energy dominates over the cluster-surface interaction energy. In Frank-van-der-Merwes mode, the adsorbed atoms exhibit a strong interaction force with the substrate, resulting in the formation of complete monolayer right before the start of another layer. However, in Stranski-Krastanov mode, layer by layer growth can be observed for the adsorbed atoms. The metal clusters of higher melting points (such as Mo, W etc.) deposited on a substrate via soft-landing method do not coalesce with the neighboring clusters and remain stick to the impact site [76]. Moreover, medium-sized clusters with large number of constituent atoms are also found to be less mobile over the surface. In such case, for low coverage the film growth is governed by the Frank-van-der-Merwe growth mode. But as long as the coverage of the film increases beyond one monolayer, the growth mode follows the Stranski-Krastanov growth. In this type of growth, rough surface with bigger cluster aggregates or islands can be observed. The fundamentals of cluster surface collision processes are depicted in figure 1.4(a)-(f) and each of these physical processes are briefly discussed below.

1.5.1 Soft-landing

The clusters are intact at the interaction point without damaging the surface. Although in this process the clusters suffer a small distortion upon impact on the surface but retain its identity.

1.5.2 Ballistic deposition

At medium energy cluster surface interaction, the frontline atoms of the cluster stream collide with the surface atom and are suddenly stopped. But the distant cluster atoms that are still in motion collide with the frontline atoms. This process will lead to transformation of kinetic energy of the cluster atoms into potential energy via plastic deformation of the cluster.

1.5.3 Fragmentation

When the kinetic energy per atom (E_{at}) is sufficiently higher than the cluster binding energy (E_b), the impact of the cluster on the surface leads to the cluster decomposition and fragmentation. This indicates that the coordination bonds between cluster constituents are broken.

1.5.4 Implantation

When a fraction of the cluster fragment penetrates into the substrate, the phenomenon is termed as implantation. In implantation process, the cluster transformation energy of the substrate must exceed the penetration threshold energy of the substrate surface. As a result, an intermixing of cluster and substrate take place at/near the substrate surface. The depth of the collision-induced damage strongly depends on cluster impact energy (E_{kin}) and the value of R signifies the ratio of cohesive energy of cluster to the surface.

1.5.5 Reflection

In the process of cluster deposition with various energies, some of the cluster fragments are backscattered from the surface impact sites. These backscattered cluster fragments can be used to obtain the information of charge and energy transformations of the clusters.

1.5.6 Sputtering

In case of a relatively high-energy cluster surface collision, both the substrate and cluster atoms are found to be ejected from the interaction site. The phenomenon is termed as sputtering. Another possible surface erosion phenomenon at such a high-

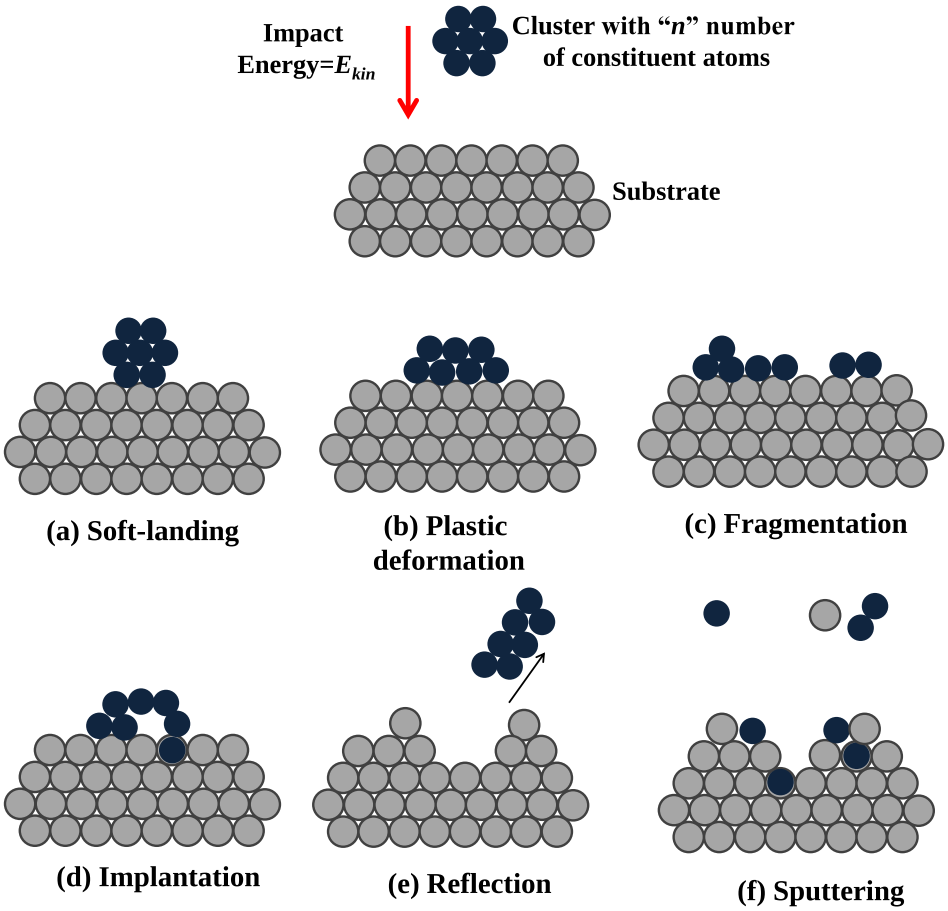

Figure. 1.4: *Schematic representations of fundamental processes in cluster-surface interactions.*

energy impact is crater formation that takes place due to the impact of larger-sized ($\leq$ 100 atoms) clusters.

1.6 Post deposition phenomena of clusters on a substrate surface

As discussed in the previous section, the cluster deposition phenomena on a substrate surface are primarily dependent on the cluster state and its energy. The films produced by deposition of clusters are influenced by many factors such as target

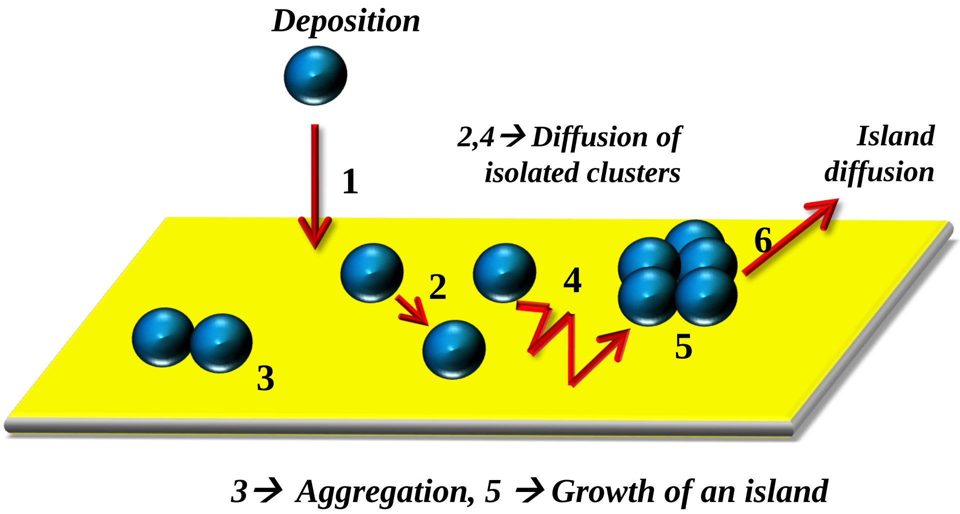

Figure. 1.5: *Elementary processes involved during a low energy cluster deposition.*

material, substrate material, deposition rate etc. In order to fabricate nanoparticle-based devices and study them, it is important to deposit size-selected clusters onto a suitable substrate. The elementary processes involved during deposition of clusters on a substrate are schematically shown in figure 1.5. The interface morphology of the films depends on the method of deposition and surface diffusion process as well.

1.6.1 Method of deposition

In the deposition process, cluster beam arrives at random positions on the substrate surface and subsequently forms chemical bonds with the surface atoms and sticks on the substrate. The deposition process is quantified by a term called 'flux', defined as the number of clusters deposited on a surface per unit area per unit time. In most of the cases, the flux is uniform but in some cases it may be pulsed (changing with time). Introduction to perturbation in depositing flux may affect the film growth significantly. The energy gained during the formation of cluster-surface bonds is dissipated into the substrate lattice leaving the bonds in thermal equilibrium.

1.6.2 Cluster diffusion

In the epitaxial growth of the films, the diffusion process plays an active role. The clusters deposited at lower temperature on a surface with a sufficiently low impact energy (< 1 eV) lead to diffusion and aggregation of clusters over the surface and form larger cluster-aggregates or islands. The assumption of diffusion of small clusters with fewer atoms is taken from the atom diffusion model of thin-film growth. According to this model, the deposited atoms are randomly jumped among adjacent lattice sites in search of the favorable energy positions. Earlier it was assumed that large-sized clusters were unable to diffuse into the substrate but later on the assumption has been proved to be wrong. The diffusion length of clusters can be large and depends on the substrate temperature and binding energy. The diffusion process can be quantified by the diffusion co-efficient (D) and the diffusion time (τ). The relation between the two can be expressed as [77],

$$D = \frac{d^2}{4\tau} \tag{1.53}$$

where d is the diameter of the cluster.

The energy must be larger than the lattice potential energy for an atom to diffuse from one lattice point to another. If E_o is the cluster activation energy required for diffusion, the average number of jump rate can be determined from the Arrheniuss law as,

$$\nu = \nu_o exp\left(\frac{-E_o}{K_\beta T}\right) \tag{1.54}$$

where ν_o is the frequency of small atomic oscillation and the frequency range lies between 10^{12}-10^{13} Hz (Debye frequency).

One of the fundamental diffusion processes is terrace migration of the clusters.

The terrace diffusion initiates the nucleation process for island growth on the terrace of the substrates. When the clusters interact with one or more clusters on the surface, a stable cluster island is formed by ending up with the terrace diffusion. A cluster on the surface continuously diffuses until it collides with another cluster, an island edge or a step. The mobility of the clusters along with the steps around the kinks and corners determines the 2D cluster shape. In an earlier cluster diffusion study by field ion microscope (FIM), Kellogg [78] observed that large-sized clusters had higher diffusivity as compared to small-sized clusters. This type of diffusion mechanism is known as Periphery Diffusion (PD) where the peripheral cluster atoms diffuse due to the change in the centre of mass of the cluster. Another type of cluster diffusion mechanism is known as Evaporation-Condensation (EC) wherein repeated evaporation and condensation of cluster atoms cause the cluster diffusion. In a study by Wang *et al.* [79], it was found that diffusion rate for larger silver clusters were very high and followed the EC diffusion mechanism. For large 3D clusters, the diffusion rate can be predicted by both the PD and EC diffusion mechanisms where the cluster diffusion is caused by the collective motion of the cluster constituent atoms. In a molecular dynamic simulation, the cluster diffusion process is considered as the Brownian motion of clusters over the substrate due to lattice vibrations of both the cluster and surface atoms. The lattice mismatch between the cluster and surface atoms can influence the diffusivity of a cluster. A good lattice match causes low diffusivity observed by Goldby *et al.* [80] for small silver clusters. Although the lattice match between the cluster and substrate is not so good for large clusters due to the longer bond formations of cluster atoms and therefore, the diffusivity is high.

1.6.3 Cluster aggregation

At low temperatures, the cluster aggregation on a surface is irreversible and clusters formed coalesce. The coalescence process is dependent on the size, shape and material composition of the cluster. For the coalescence process to occur the constituent cluster atoms or molecules must overcome the energy barrier for their movement around the parent cluster and establish contact with the other clusters. It is found theoretically that there is no energy barrier or a very low barrier experienced by small metal clusters for coalescence. So, they can rapidly coalesce on the surface. Large-sized metal clusters can also coalesce over the surface with a slow coalescence rate. Goldby *et al.* [80] shows that silver clusters with $\sim$ 50 to 250 constituent atoms per cluster rapidly coalesce over graphite surface and form $\sim$ 14 nm small cluster aggregates or islands.

1.7 Thesis organization

The main theme of this thesis is to study the growth morphology of nanostructures formed on solid surfaces and analyse various properties of the nanostructured films. The thesis is organized into six chapters. In this chapter, nanoclusters formation and their deposition process on a solid surface are briefly discussed. Other five chapters are organized as the following:

In *chapter 2*, a detailed descriptions of various experimental setup and nanocluster production mechanism are discussed. The variation of mass distribution spectra with various system parameters are also included in the chapter. Furthermore, the operating principle of various characterizing facilities namely, atomic force Microscope (AFM), Scanning electron microscope (SEM), X-ray photoelectron spectroscopy (XPS), UV-Vis spectroscopy, Rapid thermal annealing system (RTP) are discussed.

In *chapter 3*, the growth dynamic behaviour of size-selected Cu and Ag cluster deposited films are studied under the framework of dynamic scaling theory. In the study, two types of growth variations are observed for both Cu as well as Ag films.

The influence of shadowing effect on the second growth step of the films are also discussed in this chapter.

In *chapter 4*, the influence of surface morphology of cluster-deposited films on cluster size and cluster beam current is studied. The depositing cluster diameter is varied and it is found that there is an evolution of morphology of the films with increasing cluster diameter. With the evolved morphology, various morphological statistical parameters are also varied. Further, with the change in cluster beam current initially nanodots are formed which later turned into mound-like structures. A transition in wettability behaviour from hydrophilic to hydrophobic also is observed for the cluster deposited films.

In *chapter 5*, the effects of substrate temperature on the morphology of cluster-deposited films are investigated. This study shows that increasing substrate temperature has a profound impact on the size of the cluster aggregates. Further, a novel method for synthesis of bimetallic Ag-Au nanoparticles is proposed. The effect of substrate temperature on the bimetallic nanoparticles is also studied. The compositional changes during the formation of bimetallic nanoparticles are investigated by in-situ XPS techniques.

Finally in *chapter 6*, all the important findings of this thesis works have been summarized.

Chapter 2

Experimental methods and characterization techniques

Synthesis of metal nanoclusters and their deposition procedures in a nanocluster deposition facility have been discussed in this chapter. Besides this, detailed explanations of various sections of the instrument and dependence of mass distribution spectra of produced clusters on different system parameters also are discussed. Finally, the working principles of various characterizing facilities are discussed.

2.1 Introduction

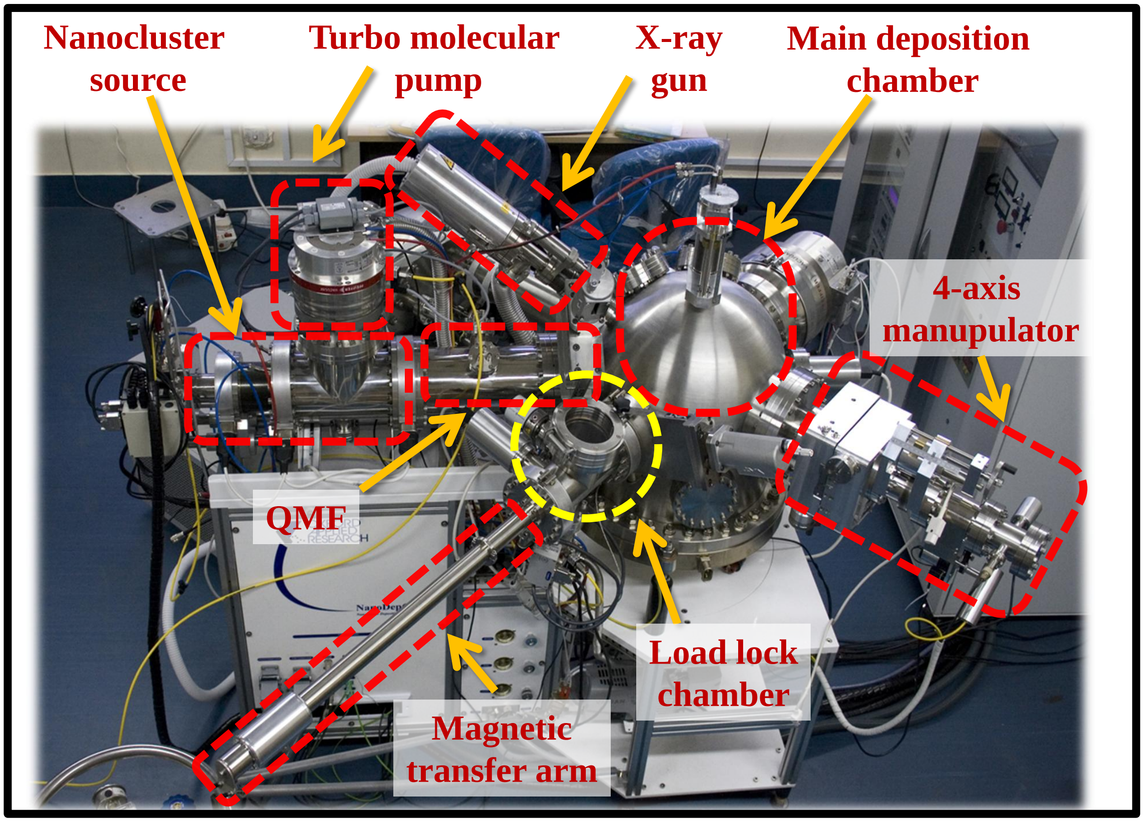

Figure. 2.1: *Nanodep60 instrument facility installed at SINP, Kolkata.*

The research works presented in this thesis are based on the synthesis of size-selected metal nanoclusters and their deposition on solid surfaces. This work mainly focuses on the study of growth process of size-selected metal nanoclusters and investigation of their morphological and compositional modifications. The wetting property of nanocluster deposited films is also investigated. Deposition of size-selected metal nanoclusters has been carried out in a low-energy cluster beam production system (Model: Nanodep60, Oxford Applied Research, UK), shown in figure 2.1. Cluster-deposited films have been characterized using various characterization techniques, mainly microscopic and spectroscopic properties of the deposited films. Atomic force microscopy (AFM) and scanning electron microscopy (SEM) techniques are used for microscopic characterization of the samples. The compositional characterization of the films has been carried out by an in-situ x-ray photoelectron spectroscopy (XPS) technique. The optical and wettability properties of the deposited films have been traced using UV-vis spectroscopy and contact angle measurements, respectively. Moreover, post deposition heat treatment of the films has been carried out using a Rapid thermal annealing system. In this chapter, a detailed description of various sections of the nanocluster deposition system are given. Moreover, a brief description and operational principle of different characterizing tools used for analyzing the cluster deposited films are given.

2.2 Materials

Table 2.1: Various parameters of metal Cu and Ag.

Parameters	**Cu**	**Ag**	**Au**	**Ref.**
Atomic number	29	47	79	
Atomic weight (amu)	63.546	107.868	196.966	[81]
Density (g/cm^3)	8.96	10.49	19.3	[81]
Melting point (^{o}C)	1084.62	961.78	1064	[44]
Ionization energy (eV)	7.726	7.5762	9.2257	[82]
Wigner-Seitz radius (nm)	0.147	0.166	0.165	[46]
Electron affinity (eV)	1.226	1.303	2.309	[83]

In this thesis, copper (Cu) and silver (Ag) are used for the synthesis of size-selected nanoclusters to get them in the form of thin-films. Standard Cu and Ag targets each of 50.8 mm diameter with 99.99 % purity have been used as sources for Cu and Ag nanoclusters, respectively. Some of the important parameters of these metals are summarized in Table 2.1. The sputtering yields of Cu, Ag and Au are found to be 1.59, 2.20 and 1.65, respectively considering Ar$^+$ ion impinging onto the target normally with an energy of 300 eV [84].

2.3 Production and deposition of size-selected metal nanoclusters

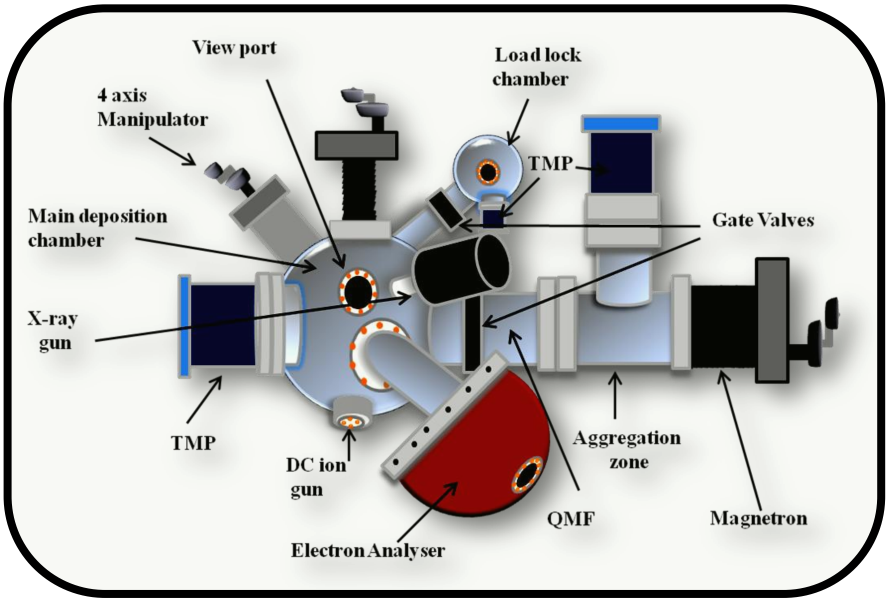

Figure. 2.2: *A schematic diagram of Nanocluster deposition facility.*

The nanocluster deposition system, NanoDep60 as shown in figure 2.1 of Oxford Applied Research, UK was installed at Nanocluster Laboratory at SINP in early 2010. To produce metal nanoclusters of any material, this is India's first kind of size-selected metal nanocluster deposition system facilitating production, deposition and in-situ analysis of the nanoclusters. A schematic diagram of the different sections of the facility is shown in figure 2.2. The production of clusters takes place inside a specially designed nanocluster source (Model: NC200U) based on the concept given by Haberland and groups [54, 70, 85]. The source can be used in both DC and RF sputtering modes for the synthesis of metallic and non-metallic clusters, respectively. In this thesis work, only dc mode of sputtering has been used for the synthesis of metal nanoclusters. The metallic clusters are generated by a dc magnetron sputtering arrangement at $< 10^{-1}$ mbar pressure. The size selection of the clusters has been performed by a Quadrupole Mass Filter (QMF). The QMF is capable of filtering clusters of diameter within the range of 1 to 10 nm. The unique features of this experimental setup offer to produce nanoclusters of equal mass by filtering them from an assembly of clusters with different masses. Hence, it can be considered as a good choice to utilize the facility to produce desired-sized clusters for different applications in the field of nanotechnology. After passing through the QMF, the cluster beam moved towards the main chamber is deposited on the substrate/sample placed on a sample holder at an angle of 45^o with respect to the incident cluster beam. The nanocluster deposition system consists of three main sections namely, nanocluster source for the production of metallic/non-metallic nanoclusters with varying sizes, Quadrupole mass filter for monitoring the cluster mass distribution and selection of a particular mass and main chamber wherein cluster deposition takes place. A detailed report describing the various sections of this instrument and the optimization process by changing different parameters was already published by Mondal and Bhattacharyya [86]. Different sections of NanoDep60 instrument and their working principles are described briefly in the following sections.

2.3.1 Nanocluster Source (NC200U)

The nanocluster source is considered here as the heart of the instrument where nanocluster formation takes place. A schematic diagram of the nanocluster source (NC200U) used in NanoDep60 instrument is shown in figure 2.3. The nanocluster source is equipped with various components namely, a dc magnetron sputtering assembly, an aggregation chamber and a nozzle to transport the generated clusters into the next chamber, two numbers of gas inlets, a linear motion drive to move the magnetron backward and forward direction for changing the aggregation length, water cooling arrangements and evacuation arrangements. The dc magnetron sputtering unit, a component of the nanocluster source is used for the production of clusters of desired material using a suitable target material. A detailed operational principle of the magnetron sputtering process is described in the later part of this section.

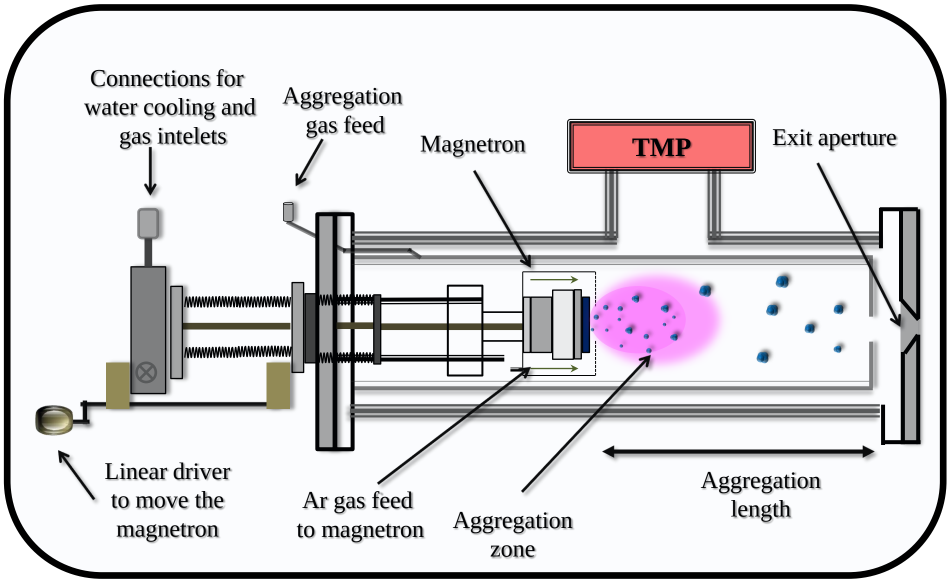

Figure. 2.3: *A schematic diagram of Nanocluster source showing the formation of nanoclusters inside the aggregation zone.*

The atoms/molecules ejected by sputtering process repeatedly collide with the inert gas atoms and nucleate inside the aggregation chamber to form clusters. A detailed description of nucleation and growth processes of clusters inside an aggregation zone is already discussed in section 1.3. The generated clusters are then transported to the next chamber using a carrier gas (Ar or He). The mass spectrum of the produced clusters can be varied by changing the length of the aggregation region. The distance between the magnetron target and the end of the aggregation zone is known as aggregation length. The other parameters namely, gas flow rate, magnetron power, type of working gas being used, thermodynamic conditions of the aggregation region also influence the mass distribution of the clusters. An efficient water cooling arrangement is there to maintain the temperature of the magnetron and the aggregation zone as well. The advantage of magnetron-based gas aggregation-type nanocluster source is to contain clusters having their diameters varied from fraction of a nanometer to 20 nm. Another important feature of this type of source is to produce ionized clusters of desired materials, well adherent to any kind of substrates and form a uniform coating over the substrates.

2.3.2 Magnetron sputtering process

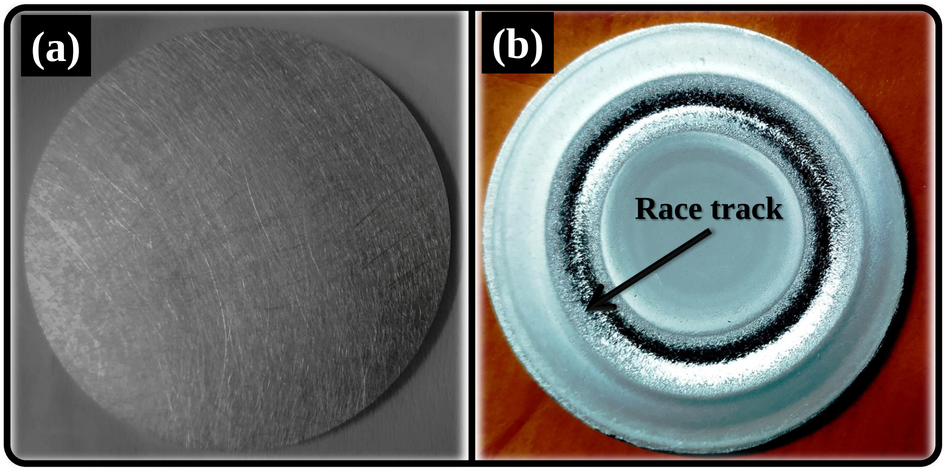

Figure. 2.4: *(a) Unused silver target, (b) Used silver target with circular race track.*

The magnetron sputtering process is one of the well known techniques used for the deposition of thin-films in vacuum. Sputtering is the process of ejecting the target atoms/molecules by bombarding it with energetic ions. The target acts as cathode and the electrically isolated target holder acts as anode which is grounded along with the chassis of the instrument. To ignite the plasma, an inert gas argon is introduced in between the cathode and anode after applying an electric voltage in the range of $\sim$ 100 - 500 V between two electrodes. Due to high voltage, the argon gas becomes ionized and the Ar^+-ions starts sputtering the negatively biased cathode target. As a result of this sputtering, several processes takes place on/around the vicinity of the target surface namely, emission of secondary ions, secondary electrons, reflection of particles, chemical reaction, radiation emission, sputtered cathode atoms etc. In magnetron sputtering process, a ring magnet arrangement is placed underneath the target in such a way that its magnetic fields are in perpendicular to the electric field. Due to this additional magnetic arrangement along with electric field, a Lorentz force is generated which forces the secondary electrons to act on the target in a circular race track [87]. Using this process a high sputter rate of the target can be achieved and more sputtering occurs around a particular region over the target. Hence, more materials will be eroded from the target surface that will produce a circular well on its surface. Figure 2.4(a)-(b) show two silver targets, one is unused and second one used for sputtering where the circular race track can be seen.

2.3.3 Quadrupole Mass Filter (QMF)

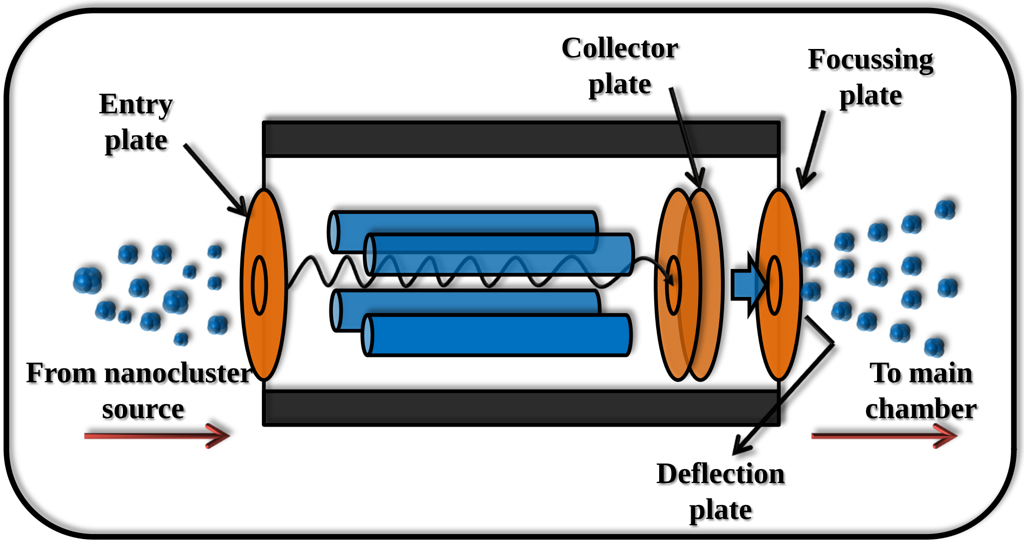

Figure. 2.5: *A schematic diagram of working principle of Quadrupole Mass Filter.*

The quadrupole mass filter (QMF, Model: QMF200, Version 2.0) is placed in between the nanocluster source and the deposition chamber. The main use of QMF is to analyze the incoming clusters from the nanocluster source, electro-statically modify their path and finally filter the charged clusters and transport them to their way of main deposition chamber. The QMF can filter the clusters with a mass ranging from 50 to 3×10^6 amu with an ultimate resolution upto $\sim 2\%$. A schematic diagram of a QMF with its working principle is illustrated in figure 2.5. In general, the QMF consists of four cylindrical rods placed parallel to each other to utilize them to measure the mass distribution of nanoclusters and filter a particular cluster mass. Each pair of rods is connected electrically and positive and negative alternating potentials of equal magnitudes are applied. Incoming clusters from the aggregation chamber enter into the QMF through an aperture of the entry plate. The cluster beam is then allowed to pass through the axes of the quadrupole rods. Due to the presence of alternating potentials across the rods, the cluster beam starts oscillating in a trajectory and clusters ions are selected on the basis of their charge-to-mass (e/m) ratio. Only selected cluster ions contain specific charge-to-mass ratio will successfully pass through the QMF while rest cluster ions follow different trajectories and are trapped within the QMF. Selected cluster ions after leaving the quadrupole rods via the exit aperture fall on the collector plate where their intensity or beam current has been monitored. We can also apply a bias voltage in the range of +12 to -12 V to the plate to extract more charged clusters from the size-selected cluster beam during analysis of cluster mass. The cluster beam current denotes the number of mass selected clusters passing per second through the plate. For instance, if $U+V cos(2\pi f t)$ is the magnitude of ac current applied across the QMF rods, then the mass of clusters selected by the QMF can be expressed as (mentioned in the manual of QMF200 Version 2.0),

$$M = 7 \times 10^7 \frac{kV}{f^2 d^2} \tag{2.1}$$

where V is the ac voltage amplitude, f is the frequency of ac voltage, d is the distance between the main axis and edge of the quadrupole rods and k known as correction factor whose value is nearly equal to unity. The transport of a particular-sized clusters through QMF is possible by adjusting the parameters namely, amplitude of ac voltage (V), component of dc voltage (U) and frequency of ac voltage (f). The ratio of dc to ac voltage component i.e., (U/V) is known as resolution of the QMF responsible for determining the mass band or sized band of selected clusters that pass through the QMF. In this system, the maximum resolution achieved for a U/V ratio is ~ 0.16 at which the narrowest window of selected mass is found. At the end of the QMF and right after the collector plate a X-Y deflector plate is placed which is an important addition to the system. It is well aware that the presence of neutral clusters with the charged clusters cannot be detected by the QMF that can affect the overall mass resolution of the QMF. These neutral clusters in a cluster beam can be separated by using the deflection plate. In order to do so, a suitable voltage is applied to the plate that deflects charged cluster beam towards the substrates and traps the neutral clusters on the plate.

Table 2.2: Important parametrs of QMF200.

Paramaters	**Values**
Operating AC voltage range	1 - 250 kV
AC frequency range	3 - 100 kHz
Mass filtering range	50 - 3×10^6 amu
Usable cluster size resolution	~ 2 %
Diameter of the QMF rods	2.54 cm
Length of the rods	25 cm
Operatioal pressure of QMF200	$< 1 \times 10^{-3}$ mbar

The QMF is interfaced through a computer controlled software QUVI2. Using this software we can record the mass distributions of clusters that pass through the QMF and by changing different parameters we can tune the cluster mass spectrum. A snapshot of the QUVI2 software is shown in figure 2.6. The different parameters related to QMF can be controlled and monitored using the software. The set value

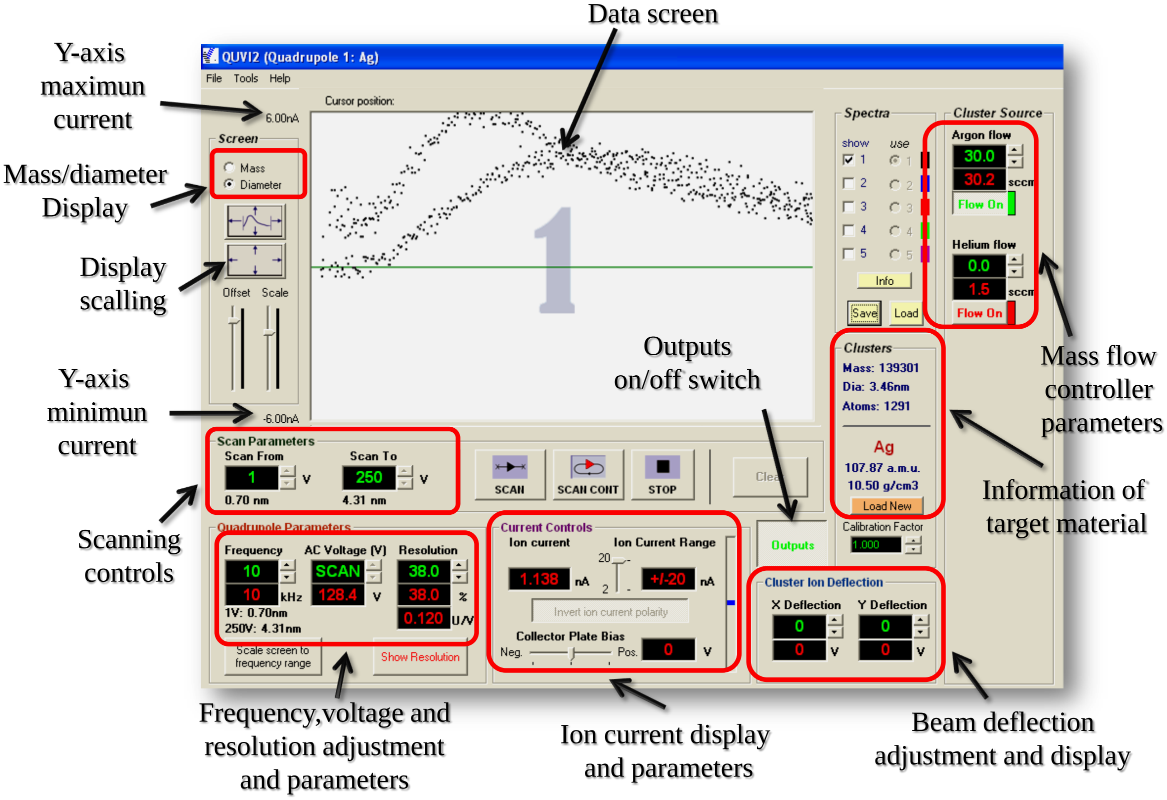

6.00nA

-6.00nA

○ Mass
● Diameter

Scan Parameters: Scan From 1 V (0.70 nm); Scan To 250 V (4.31 nm)

Quadrupole Parameters: Frequency 10 / 10 kHz; AC Voltage (V) SCAN / 128.4 V; Resolution 38.0 / 38.0 %; 0.120 U/V
1V: 0.70nm
250V: 4.31nm

Current Controls: Ion current 1.138 nA; Ion Current Range +/-20 nA
Collector Plate Bias: Neg. Pos. 0 V

Cluster Ion Deflection: X Deflection 0 / 0 V; Y Deflection 0 / 0 V

Argon flow 30.0 / 30.2 sccm, Flow On
Helium flow 0.0 / 1.5 sccm, Flow On

Clusters
Mass: 139301
Dia: 3.46nm
Atoms: 1291

Ag
107.87 a.m.u.
10.50 g/cm3

Calibration Factor 1.000

Figure. 2.6: *A screenshot of QUVI2 software window captured during the QMF operation.*

of a parameter is indicated by green display whereas the actual value is found in a red display. The quadrupole parameters like ac frequency (f), ac voltage (V) and resolution can be controlled using the software. The ac frequency can be set within a range of 3-100 kHZ, the ac voltage can be set from 1-250 V for mass filtering of the clusters. Each voltage represents a particular-sized cluster. The resolution of mass selection can be set from ~ 2 % to ~ 100 % and its equivalent U/V value can be monitored in an added red display. Apart from the quadrupole parameters, the cluster source parameters namely, Ar and He gas flow can also be controlled by this software. The range of gas flow can be set between 0-100 sccm for both the gases. The gas flow in the nanocluster source is controlled by mass flow controllers (MKS instrument) attached to the nanocluster source. Some of the important parameters of QMF200 are summarized in Table 2.2.

2.3.4 Main deposition Chamber

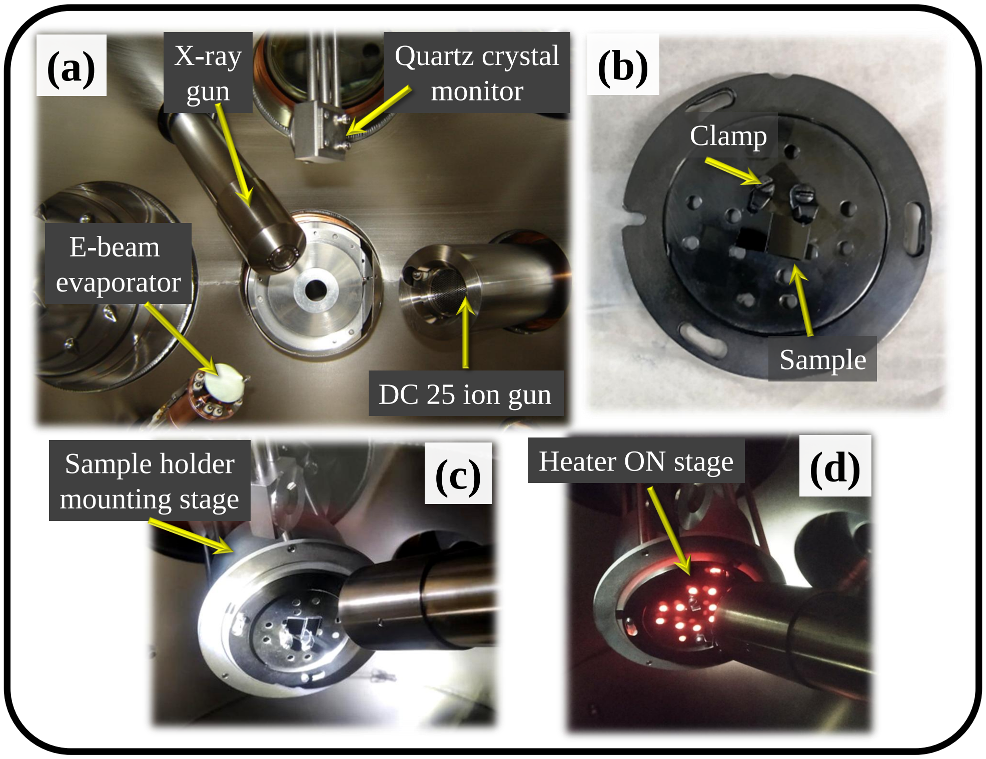

Figure. 2.7: *(a) Inside view of main deposition chamber, (b) Molybdenum sample holder, (c) Sample holder mounted inside the chamber, (d) During the annealing of the sample.*

The main deposition chamber is designed in such a way that all the port axes pass through the center of the chamber. An inner view of the main deposition chamber is shown in figure 2.7(a). The main deposition chamber is equipped with many components used to modify or analyse the substrate before or after deposition. These components are quartz crystal thickness monitor, E-beam evaporator, DC ion gun, x-ray gun and hemispherical electron analyzer. After passing through the QMF, the size-selected cluster beam is directed towards the substrate placed in the main deposition chamber. The sample is placed on a molybdenum substrate holder for deposition. The image of molybdenum substrate holder is shown in figure 2.7(b). The sample holder is placed in such a way that the substrates make an angle of

45^o with the incoming cluster beam. The image of substrate holder mounted to metal stage supported by three rods is shown in figure 2.7(c). The substrate holder stage is connected to a 4-axis manipulator operated manually from outside and is used to move the substrate holder in forward-backward and up-down directions. The substrate holder can be rotated upto a speed of 30 rpm and equipped with an in-situ heating facility upto a temperature of 600 ^{o}C using a SiC-based heating element. The substrate holder may be biased to a voltage ranging from -5 to +5 kV using external dc power supply so as to facilitate soft landing of charged clusters onto the substrate. An image of the substrate holder during the heating of the sample is shown in figure 2.7(d). There is an additional chamber known as Load lock chamber attached directly to the main deposition chamber. The substrate is put in this chamber first before loading into the main chamber. The purpose of this chamber is to maintain the ultra-high vacuum level of main chamber during the transportation of samples. A magnetically transfer arm is used for the movement of the sample between the main chamber and load lock chamber. A brief description of some of the attachments to the main deposition chamber is given below.

2.3.4.1 DC Ion Source

The DC ion source is primarily used for surface modification for various applications such as parallel beam etching, substrate cleaning, substrate sputtering and ion beam assisted deposition etc. The ion source can be used for various gases such as Ar, N_2, O_2, H_2 etc. To minimize the charging effect on the substrate surface a plasma beam neutralizer along with filament-based electron injection source is equipped in a DC ion source. The DC ion source, DC25 has been equipped here to produce an ion beam with energy ranges from 100 eV to 1 keV with a maximum beam current of 40 mA. The diameter of the ion-beam produced by DC25 ion source is around 25 mm. Moreover, the source is equipped with various grids to apply them for a particular application. For example convex grid can be employed to irradiate large area of a sample by maintaining high uniformity, concave grid can be used to focus the ion beam to a specified area etc.

2.3.4.2 X-ray Photoelectron Spectroscopy Unit

The XPS unit attached to the main deposition chamber contains a x-ray gun and a standard 150 mm hemispherical electron analyzer (VSW Ltd). The x-ray gun used here consists of a twin (Al/Mg) anode source of UHV compatibility. It is attached to the main chamber using a standard CF34 flange. The x-ray produced by the gun directly interacts with the surface at an oblique incident angle. The gun is mounted on a linear motion drive so as to move the gun in order to adjust the intensity of the emitted x-ray. The anode of the x-ray gun can be chosen manually and the maximum operating voltage and current are 12 kV and 2 A, respectively. The generated x-ray passes through a thin aluminium foil to restrict the entry of various ions and secondary electrons into the main chamber.

In Nanodep60, a hemispherical electron analyzer is attached to the main chamber. The photoelectrons emitted from the sample surface upon interaction with the x-ray pass through the analyzer. A constant electric potential is applied between two concentric hemispheres. At the exit slit of the hemisphere, an array of five channeltron electron detectors are placed to enhance the electron collection efficiency. A detailed explanation of production of x-ray, its detection by hemispherical electron analyzer and its measurement methods are given in the later section of this chapter.

2.3.5 Vacuum system

The complete vacuum system of the instrument can be divided into three parts namely, main deposition chamber, nanocluster and QMF chamber and the load lock chamber. The main deposition chamber along with the hemispherical electron analyzer are evacuated using a turbo molecular pump backed by a rotary pump to attain a vacuum $\sim 5 \times 10^{-10}$ mbar. The capacity of the turbo molecular pump is 1250 l/s. The load lock chamber is evacuated by a small-sized turbo molecular pump also backed by a rotary pump to reach an ultimate vacuum $\sim 3 \times 10^{-8}$ mbar within a few hours. The capacity of the turbo pump is ~ 67 l/s. The third pumping arrangements is located in between the nanocluster source and the QMF chamber. The complete section is evacuated by a turbo molecular pump after attaining a rough vacuum using a rotary pump. The capacity of this turbo pump is ~ 685 l/s and a vacuum $\sim 10^{-6}$ mbar is achieved using the pump. The x-ray gun attached to the main deposition chamber is separately pumped down using an ion pump during XPS operation. All the three regions of the system are isolated from each other with the help of gate valves. The first gate valve is located between the main deposition chamber and QMF chamber. The second gate valve is present between the main deposition chamber and the load lock chamber.

2.3.6 Optimization of mass distribution of produced nanoclusters

The sizes of the deposited nanoclusters on a substrate are directly related to the mass distribution or size distribution spectrum of the produced nanoclusters. By tuning the mass spectrum of produced clusters the morphology of the deposited film and their inherent property can be changed. The formation of a mass distribution spectrum is primarily dependent on various parameters of the system. The QMF is used to monitor the mass distribution of the produced clusters. A mass distribution spectrum is plotted as beam intensity versus the corresponding mass of the clusters. The beam intensity is measured by a collector plate of the QMF indicating the number of clusters per unit time. The optimization of the mass spectra is necessary to perform the deposition of clusters of desired size on a substrate. The various system parameters play significant role for tuning the mass distribution of clusters produced that are discussed in the following sections.

2.3.6.1 Ar flow rate

Figure 2.8 shows the mass distribution spectra of produced Ag-nanoclusters at different Ar flow rates. It is seen from the figure 2.8(a) that cluster formation does not take place up to an Ar flow rate of 10 sccm. The formation of proper mass distribution spectra is observed at an Ar flow rate of 15 sccm and above. The beam intensity of mass distribution spectra keeps on increasing at Ar flow rates of 15 to 30 sccm although the peak position or mean cluster diameter is almost constant for every spectra. From 30 to 45 sccm, the intensity as well as the peak position of the spectra are found to remain the same. Above 45 sccm, the peak intensity and its positions are found to be decreased with the increase in Ar flow rate. The above phenomenon of change of mass spectra may be explained on the basis of principles of sputtering. At relatively low Ar flow ($<$ 15 sccm), sputtering of the target does not occur properly due to inadequate Ar^+ ions and as a result, beam current is not significant. The sputtering starts at a particular value of Ar flow and the sputtering rate increases with the increase in its flow rate so that more number of particles condenses to form clusters and consequently the beam current increases. At higher Ar flow rates ($>$ 45 sccm), access amount of Ar molecules does not contribute much towards the sputtering process and they will quickly leave the aggregation zone along with the formed clusters. This process does not allow to form bigger clusters and, therefore, the beam current will be lower as reflected in the mass spectra. Hence, the above observations confirm that the optimum Ar flow rate for any experiment should lie between 20 to 45 sccm.

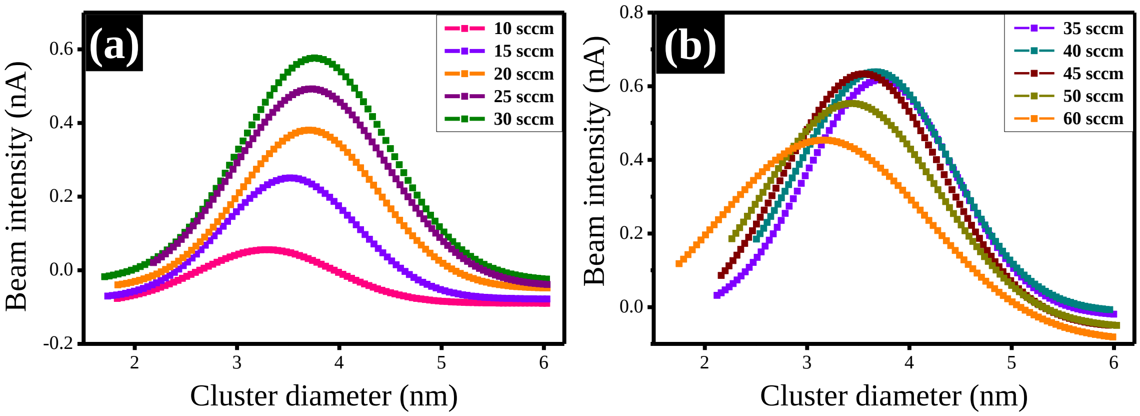

Figure. 2.8: *Mass distribution of Ag-nanoclusters at different Ar flow rates (a) 10 - 30 sccm and (b) 35 - 60 sccm.*

2.3.6.2 He flow rate

The system offers an option to introduce helium gas to the nanocluster source but the purpose of He gas is entirely different from that of argon gas. He gas is used here to change the cluster mass distribution spectra. Figure 2.9 (a)-(c), shows various mass distribution spectra at different He flow rates. It is observed from the figure that when the He flow rate increases from 0 to 20 sccm, the peak position of the spectra rapidly decreases from mean cluster diameter 3.3 to 2.7 nm and at a flow rate above 20 sccm, the peak position or mean cluster diameter decreases very slowly. In cluster formation process, the role of He gas is to condense the clusters inside the aggregation zone via three body collision process termed as cluster seed. He gas is also used to control the cluster size distribution. With increasing He flow rate the distribution curve becomes narrower and the mean cluster diameter shifts towards the lower side because increasing He gas pressure prevents further growth of the cluster seeds into larger clusters. The increase in He flow rate also contributes to cluster nucleation process for production of more cluster seed. This is the main reason for the change of shape of the distribution curve with increasing He gas flow

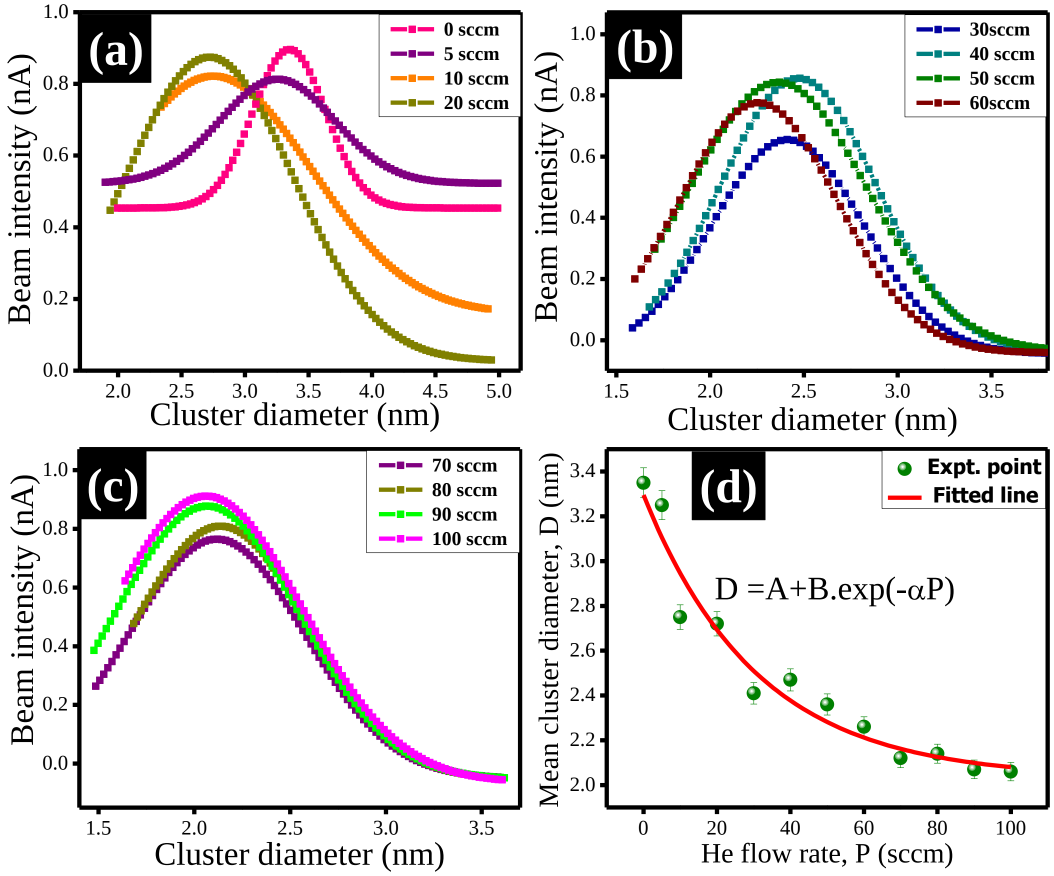

Figure. 2.9: *Mass distribution of Ag-nanocluster at different He flow rates (a) 0 - 20 sccm, (b) 30 - 60 sccm and (c) 70 - 100 sccm; (d) Variation of mean cluster diameter at various He flow rates. The variation can be best fitted with a exponential decay function,* $D = A + B.exp(-\alpha P)$, *where the value of the constants A,B and* α *are found to be 2.03, 1.27 and 0.03, respectively.*

rate as depicted in figure 2.9(a).

The beam intensities of the mass spectra at different He flow rates are found to be constant. The variation of cluster diameter with He flow rates is also observed by Ayesh *et al.* [28, 88]. They explained this phenomena on the basis of mean free path of the nucleated clusters inside the aggregation zone. An increase in He flow rate in the nanocluster source decreases the mean free path of cluster inside the chamber and the already nucleated clusters or seeds do not get adequate time to grow properly and leave the aggregation zone. Hence, small-sized clusters at higher He flow rates

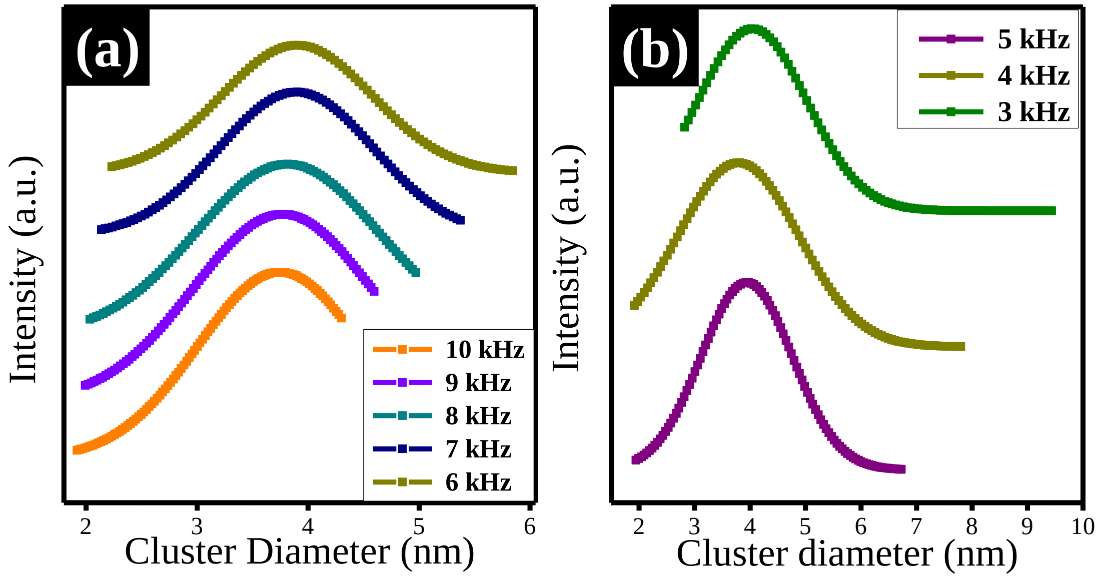

Figure. 2.10: *Variation of mass spectra of Ag-nanoclusters at (a) 10 - 6 kHz and (b) 5 - 3 kHz frequency ranges.*

are observed. The variation of mean cluster diameter with He flow rates can be fitted with an exponential decay function and the fitted curve is indicated by the red solid line in figure 2.9(d). The rate of decrease of the mean cluster diameter (D) with increasing He flow is found to follow the equation given below,

$$\frac{dD}{dP} = -const \times D + const \tag{2.2}$$

From the solution of the above equation the mean cluster diameter (D) is found as,

$$D = A + B \times exp(-\alpha P) \tag{2.3}$$

Here, A,B and α are constant and their values are found to be 2.03, 1.27 and 0.03, respectively.

2.3.6.3 Frequency variation

The mass spectra appeared at different frequencies are shown in figure 2.10. From equation 2.1, the mass of the cluster passed through the QMF is inversely proportional to the frequency of the ac voltage applied to the QMF rods. It can be seen from figures 2.10(a) and (b) that as the frequency decreases, the scanned regions of the mass spectra increases. Large-sized nanoclusters may be allowed to pass through the QMF at lower frequencies. In all the spectra, beam intensities are found to be almost equal and for better representations, the spectra has been plotted in its present form. Further, it is noticed from the mass distribution spectra that the peak positions or average cluster diameter is constant ($\sim$ 4 nm) over the full range of frequency. It may be concluded that since the spectra at 4, 5 and 6 kHz frequencies show proper Gaussian distribution, these frequencies may be used further for experimental purposes. In figure 2.10, it is found that the range of maximum selectable mass or size of a nanocluster increases with the decrease in AC frequency (f). Hence, we can say that the mass distribution spectra appeared in figure 2.10 follow the above equation. But in this figure, the mean cluster diameter is found to be constant for all the frequencies. This is because the mean cluster diameter varies only with the change of Ar or He gas flow rates, already shown in the figure 2.8 and figure 2.9. So, the movement in the average cluster diameter does not follow equation 2.1.

2.3.6.4 Variation of resolution

The mass distribution spectra of Ag-nanoclusters for various QMF resolutions is shown in figure 2.11. Each spectrum contains a variation in diameter of nanoclusters ranging from 2 to 6 nm. The beam intensity of the produced mass spectrum is decreased with the decrement of QMF resolution and finally the beam current is $\sim$ 0

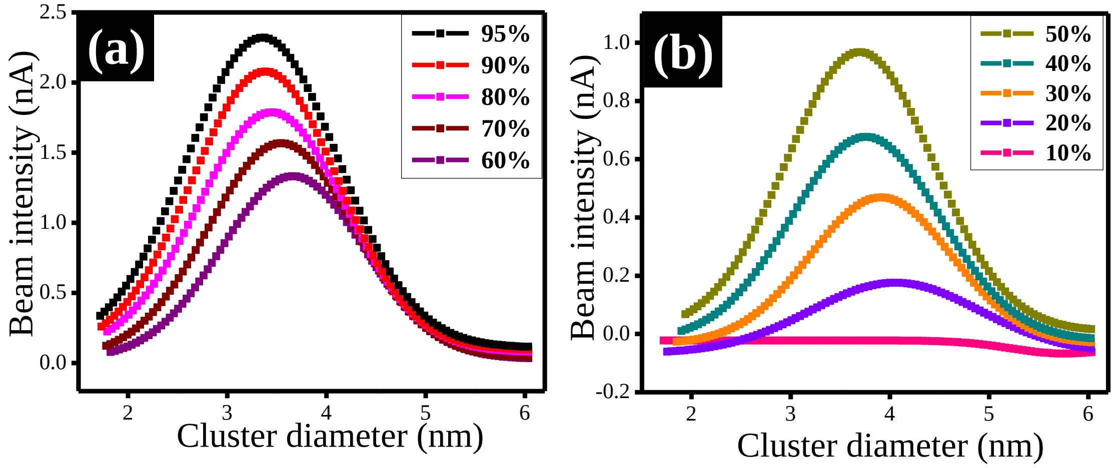

Figure. 2.11: *Variation of mass spectra of Ag-nanoclusters with the QMF resolution (a) 95% - 60%, (b) 50% - 10%.*

nA for a resolution of ∼ 10%. The average cluster diameter of the mass spectra are found to be shifted towards higher value as the resolution is decreased.

2.4 Characterization Techniques

2.4.1 Atomic force microscope

In early 1980's, the scanning probe microscope (SPM) technique was invented whose contribution in the field of material science now-a-days is essential. Unlike other spectroscopic techniques, SPM has been operated in real space and providing local information of a surface. Using SPM, it has possible to obtain important fundamental properties viz. chemical and physical properties of a surface. In an SPM, the scanning of a surface is made by a sharp tip (or probe) that approaches very close to the surface. Atomic force microscopy (AFM) technique is one of the members of SPM family that was first demonstrated by Binny and Quate in 1986 [89]. As compared to other SPM facilities, AFM is a widely used technique because of its ability to operate in different environments.

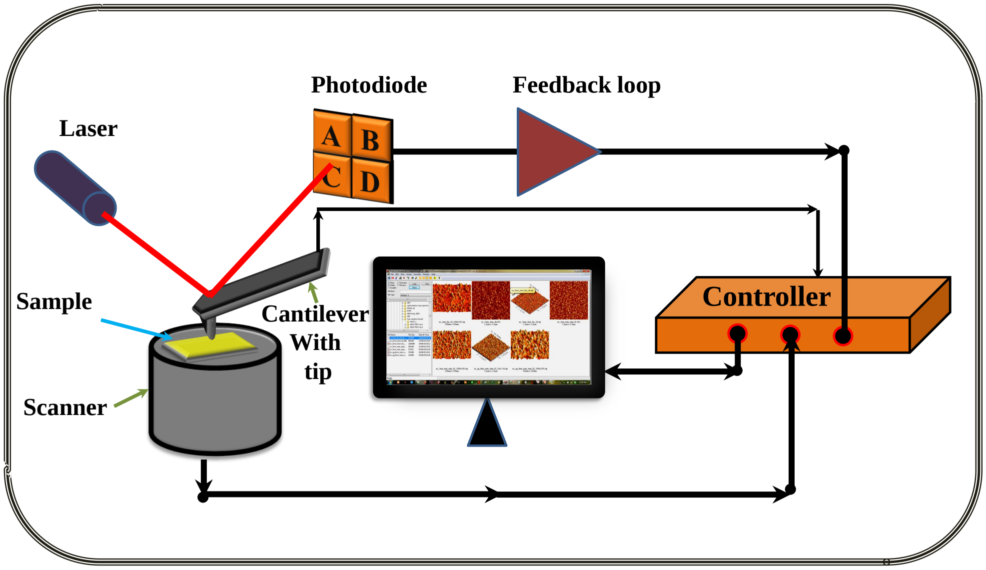

Figure. 2.12: *A schematic diagram of principle of operation of AFM.*

AFM can generate a high resolution 3D image of an object by simply scanning it with the sharp tip. The basic operation of an AFM depends on the force of interaction between the tip and the scanned surface. The operational principle of an AFM can be understood from the schematic diagram presented in figure 2.12. The major components of an AFM instrument are as follow: (1) a cantilever with a sharp probe to detect the interaction force during the measurement; (2) a position sensitive photodiode; (3) a scanner with movement control facility; (4) a controller attached to a computer equipped with interface software.

The AFM along with its various components used for measurements is shown in figure 2.13. The sensing part of an AFM consists of a micrometer-sized cantilever whose one end is integrated with a probing tip. The tip along with the cantilever is usually made of Si, SiO_2 or Si_3N_4. In order to imaging a surface, the tip along with the cantilever moves backward and forward over the sample surface. The force of interaction experienced by the tip during a scan depends on the spring constant of the cantilever. It follows the Hooke's law where the interaction force on the cantilever can be written as $F = -kx$, with k as the spring constant and x denotes the amount of deflection of the cantilever. The tip of the cantilever usually is deflected by a very small force that depends on the stiffness of the cantilever. The piezoelectric scanner and the feedback loop act simultaneously to control the movement of the tip during a scan. The deflection of the cantilever can be measured by the beam bounce method where a laser light is reflected from the top of the cantilever and fallen on a position sensitive photodiode detector. The magnitude of deflection measured by the photodiode detector is used to produce a three-dimensional map of the scanned surface. Since the separation between the tip and the sample surface is very small, the van der Waals force dominants over the other forces during tip sample interaction. Depending upon the tip to sample separation, an AFM can be operated in three modes, namely (1) contact mode, (2) non-contact mode and (3) tapping mode. To understand the different operation modes, the variation of interaction force, $F(r)$ along with the tip to sample distance (r) is shown in figure 2.14. It is evident from the figure that when the AFM operates in the contact mode i.e. when the tip is nearly in contact with the surface it experiences a repulsive van der Waals force. As the tip to sample separation increases the repulsive force decreases and beyond a critical separation, the attractive van der Waals force dominants in non-contact AFM mode. A detailed explanation for each modes of AFM is described below.

2.4.1.1 Contact Mode

In contact mode operation, the tip of the cantilever brought closer to the sample surface (< 0.5 nm) also is considered as soft physical contact between the tip and the surface. A repulsive force will be generated between the tip and the sample surface because of the closer proximity of the surface. To perform imaging, the force is maintained at a fixed value keeping the distance between the tip and the surface fixed with the help of a feedback electronic arrangement. As the tip maintains a constant

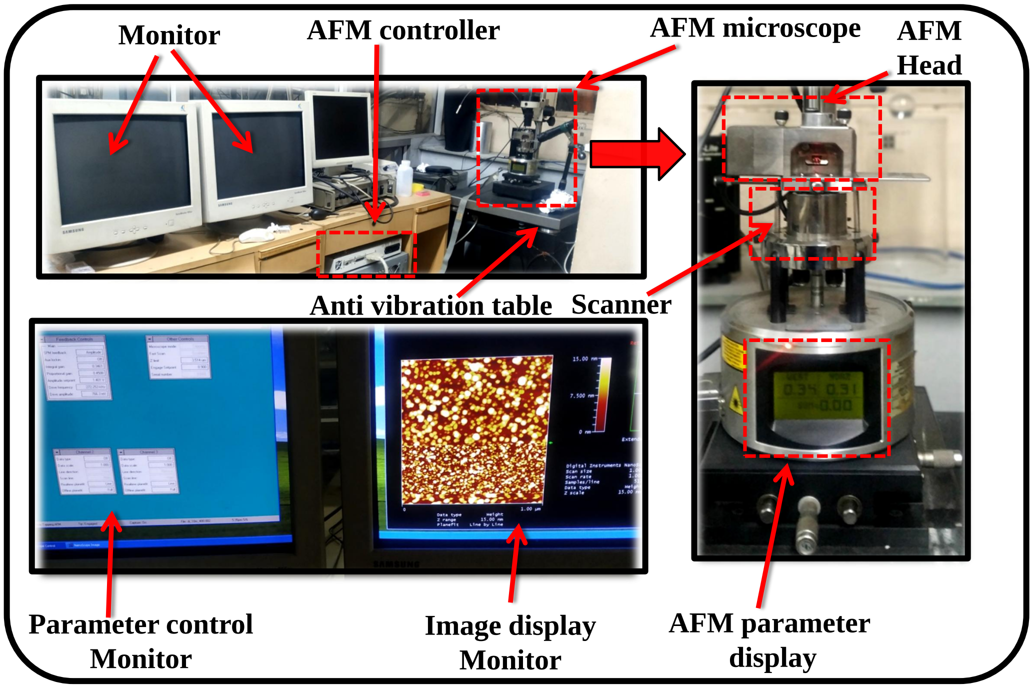

Figure. 2.13: *Atomic force microscopy setup.*

height during scanning, it will experience different forces at different position of the surface and consequently deflection of the cantilever takes place which is detected by the photodiode. This process will lead to the topographical mapping of surface with a resolution in nanometer scale. In particular, the contact mode of operation is used for solid surfaces but this technique is not applicable for soft samples. The main disadvantage of contact mode operation is surface damage and the tip damage as well. In tapping mode of AFM, the shortcomings arisen at contact mode are overcome.

2.4.1.2 Tapping Mode

In this mode of operation, keeping at a constant frequency, the tip interacts with the sample and the corresponding phases are recorded as a function of distance between tip and sample. During the operation, the overall change in amplitude is kept constant leading to the construction of topographical mapping of the surface at nanometer spatial resolution. In this mode, relatively large amplitudes are chosen so that the tip can oscillate between the repulsive and attractive forces. As a result, the tip periodically taps the surface throughout the operation. Hence, the possibility of damaging the tip or the surface during the operation using tapping mode is very low as compared to contact mode. Tapping mode in AFM are used for characterization of soft samples *viz.* delicate biological samples etc.

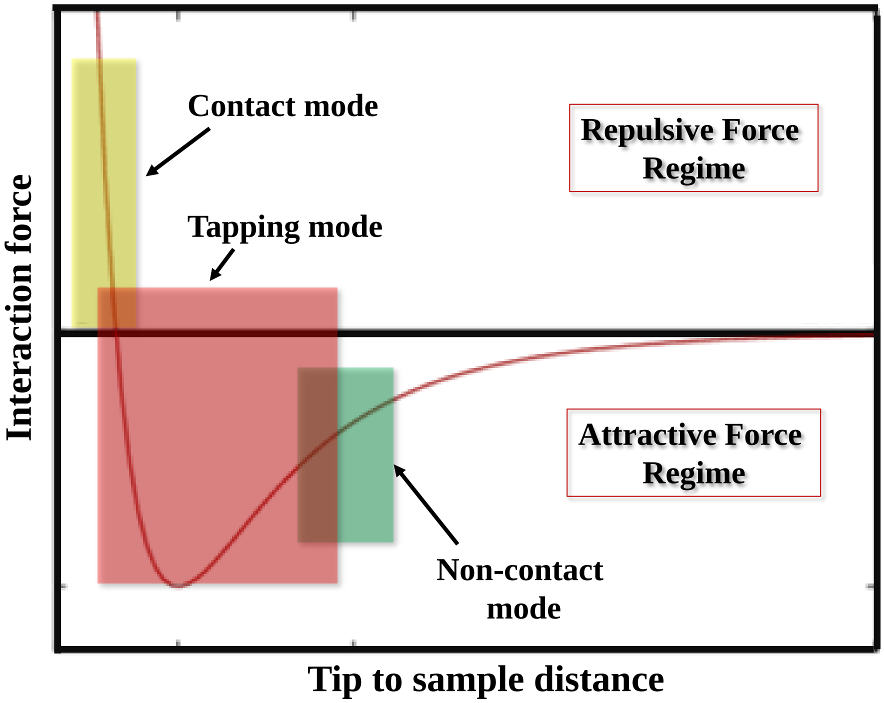

Figure. 2.14: *Force versus distance curve for different AFM operation modes.*

2.4.1.3 Non-contact Mode

In contact mode and tapping mode AFM, the sharpness of the tip becomes blunt during repeated operations due to direct contact between the specimen and apex of the tip. In non-contact mode of operation, the amplitude of oscillating tip is kept constant while approaching towards the surface so that it can fluctuate only under attractive force. This mode restricts the interaction between the tip and the surface and thereby the tip damage may be prevented. In this mode, initially the frequency

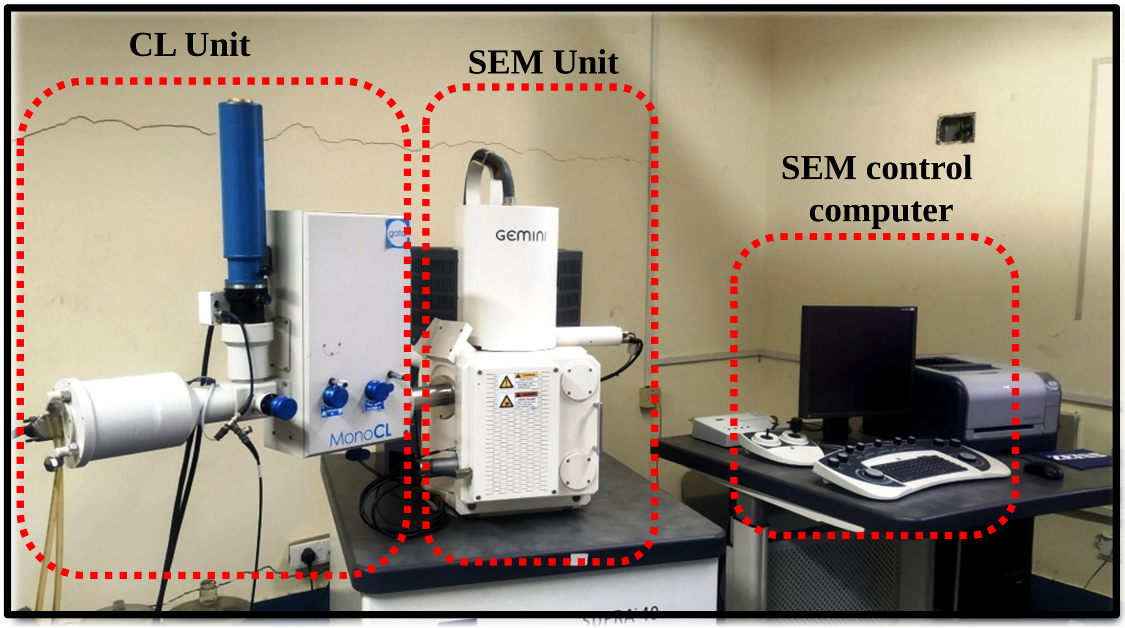

Figure. 2.15: *Scanning electron microscope setup.*

of the tip is kept at its resonant frequency and during the operation the change in resonant frequency of the tip is kept constant leading to topographical mapping of the surface with atomic-scale resolution. Generally, the non-contact AFM mode is used to characterize soft samples like liquid sample, polymer sample etc.

In this work, the AFM images of all the films are obtained using a Multimode SPM Nanoscope IV (Veeco, USA) in tapping mode.

2.4.2 Scanning Electron Microscope

In 1920s, scientists observed that electron beam in a vacuum behaved similar to the light wave and based on this concept the first ever electron microscope was built in 1931. The electron microscope is the improved version of optical microscope where resolutions up to nanometer scale may be achieved. Hence, the structures or objects not visible by traditional optical microscope can be viewed and analyzed using an electron microscope. In electron microscopy technique interactions occur between energetic electrons and the atoms of the sample and as a result, a topographical mapping of the surface is possible. A voltage is applied to accelerate the electrons emitted from the electron source and the accelerated electron beam is focused with the help of a set of magnetic lens arrangements. As the name suggests Scanning electron microscope (SEM) is one type of electron microscope where high energy focused electron beam is utilized to scan the sample surface to get a raster. After irradiation, backscattered electrons as well as secondary electrons emitted from the sample surface are collected by a detector. All collected electrons from different positions of the sample are used to construct a topographical image of the scanned surface. The magnification of SEM image can be increased or decreased by reducing or enlarging the scan area of the sample. The signals received from the backscattered and secondary electrons are measured and mapped into brighter and darker pixels using an in-built image processing setup. During imaging, the speed of scanning can be tuned manually. For observation of the surface a fast scanning mode is used while slow scanning mode is chosen for detailed imaging and recording purpose.

A schematic diagram describing the basic operational principle of a SEM is shown in figure 2.16. The optics of a SEM is made of various components viz., electron gun, two types of magnetic lens namely, condenser and objective lenses, a scanning coil, an electron detector etc. Details of various components as well as surface interactions with electron probe are discussed below.

2.4.2.1 Electron Gun

The electron gun is used for the electron beam generation. In a thermionic emission-type electron gun, thin tungsten filament is used as a cathode due to its higher melting point and may heated upto $\sim$ 2800 K. The thermionic emission of electrons takes place at $\sim$ 2200 °C. A positive voltage $\sim$ 1 to 30 kV is applied to

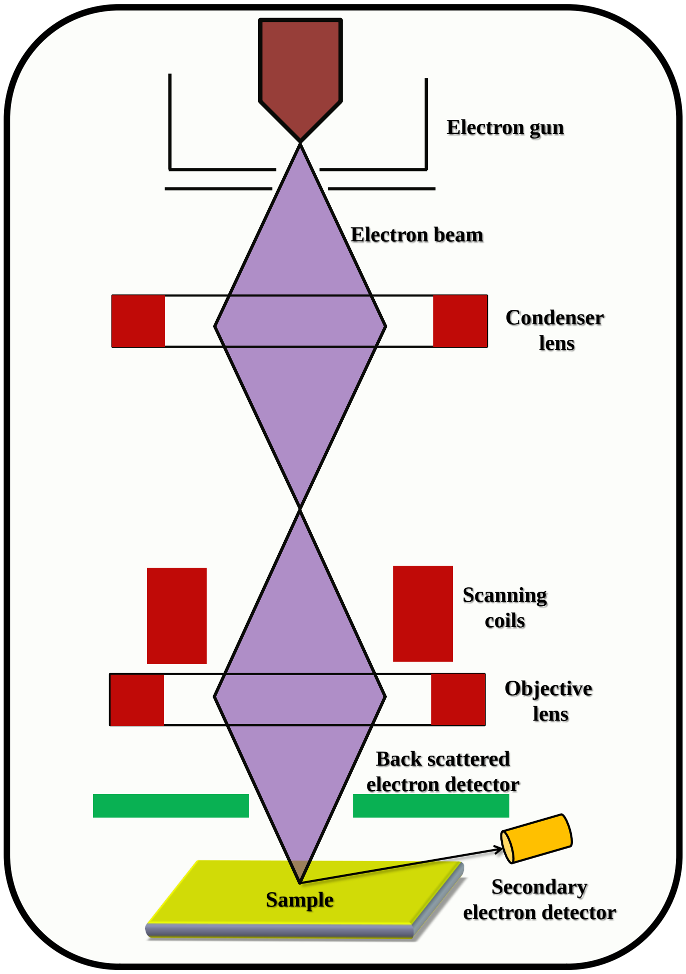

Figure. 2.16: *A schematic diagram of basic operational principle of SEM.*

accelerate these electrons towards the anode. An electron extraction arrangement is made at the anode and these electrons are focused by an additional electrode placed in between cathode and anode, known as Wehnelt electrode operated at a negative voltage. A focused and pencil electron beam of diameter $\sim$ 15 to 20 μm is then produced and used for sample scanning. In many thermionic emission-based electron gun, instead of tungsten filament lanthanum hexaboride (LaB_6) single crystal also is used as cathode.

2.4.2.2 Magnetic lens arrangements

As the electron beam comes out of the electron gun, two sets of electromagnetic lenses namely, condenser lens and objective lens placed below the electron gun are used to control the electron beam diameter. The purpose of the electromagnetic lenses is to produce an fine electron probe on the sample surface. Just below the condenser lens, an aperture is placed to prevent the extraneous electrons to reach the objective lens from the condenser lens. By adjusting the condenser lens, the intensity of the electron probe can be changed. Lastly, the role of objective lens comes into play. This lens is useful for the production of final narrow beam for surface scanning. The image quality of the SEM will depend on the performance of these objective lenses.

2.4.2.3 Specimen stage

A stable and movable stage is used to mount the sample for scanning. The movement of the stage should be smooth enough in all direction to achieve a high quality image. The stage may be moved in different directions to change the image resolution, depth of focus, the field of view of scanned area etc. The stage is also equipped with tilting and rotating facilities.

2.4.2.4 Electron detectors

After a successful interaction between the sample atoms and electron probe, secondary and backscattered electrons are emitted along with other electrons. These secondary electron signals are collected by a secondary electron detector (Everhart-Thornley) and backscattered electrons are collected by a backscattered electron detector, a solid-state detector. These detectors convert the collected electrons signal into a digital image that is displayed on a computer screen.

2.4.2.5 Surface interaction with electron probe

When an electron beam interacts with a sample surface the primary electrons enter into the sample surface and are repeatedly scattered inside and then gradually lose its kinetic energy and finally absorbed within the specimen. The range of scattering within the specimen by the electrons varies from < 100 nm to 10 μm depending on various parameters such as energy of the incoming electron beam, atomic number of the sample elements, atomic density of the specimen etc. For instance, if the energy of the incoming electron beam is low then the scattering range will be smaller. On the contrary, if the elements of the specimen are of lower atomic density and smaller atomic number, the scattering by the primary electron will be large. During irradiation, energy exchange takes place between the primary electrons and specimen atoms and as a result, various types of electrons and electromagnetic waves are emitted from the irradiated region. Apart from the high energy backscattered and low energy secondary electrons various electromagnetic waves such as x-rays, cathodoluminescence are also emitted after irradiation. Different types of detectors are used to collect each of the signals. Apart from imaging, the SEM utilizes these signals for different purposes namely, energy dispersive x-ray spectroscopy (EDS) for elemental analysis, optical analysis etc. A schematic diagram illustrating the emission of various signals from the irradiated specimen is shown in figure 2.17.

In SEM operation, usually two types of electrons are detected for imaging namely secondary electron (SE) and backscattered electron (BSE). Secondary electrons are generated due to inelastic collision of primary electron beam with the electrons present inside the atom of the sample. These secondary electrons are emitted usually from the near surface region of the sample and their energy range is very low that ranges between 0 - 50 eV. These electrons are detected and used to get

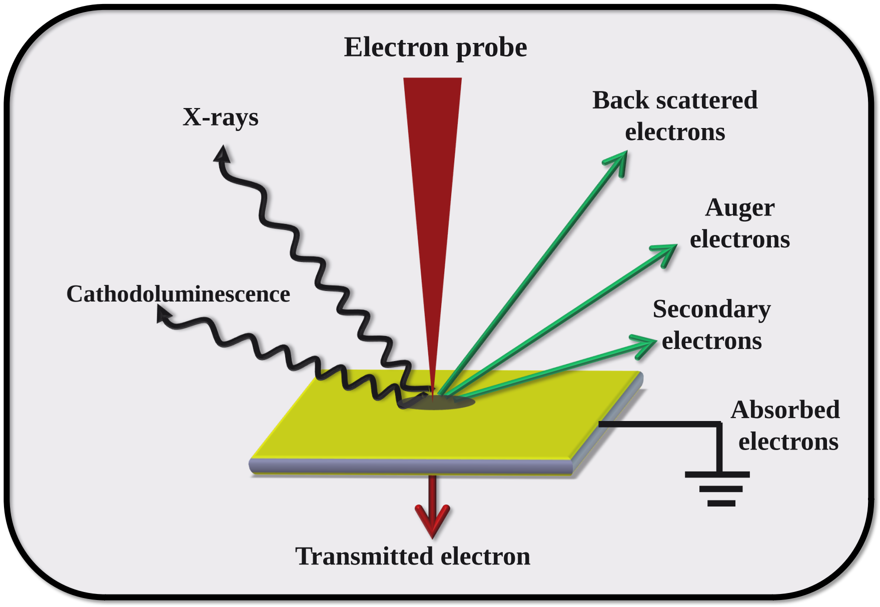

Figure. 2.17: *A schematic diagram of emission of various electrons after irradiation of sample surface with high energy electron probe.*

topographical information of a surface. On the other hand, BSEs are generated due to the occurrence of elastic collision between the electron beam and the nuclei of the sample atoms. The amount of BSEs is dependent on the atomic number (Z) of the sample. Hence, scattering from a sample with bigger Z value provides more BSEs as compared to sample with smaller Z value. These BSEs are capable of providing information of sample topography, different phases, magnetic field and crystallography. The energy spectrum of SEs and BSEs are shown in figure 2.18. This spectrum is plotted as N(E) vs E where the number of emitted SEs and BSEs are indicated by N(E) and their energy is represented by E.

In this thesis work, the SEM images of all the films are grabbed using a FESEM from Zeiss, SUPRA 40 instrument shown in figure 2.15. The basic difference between the conventional SEM and FESEM is the electron generating process. In SEM, electron beam is generated by heating a tungsten filament, which may contaminate the sample surface. In FESEM, no thermal energy is required as it uses a field

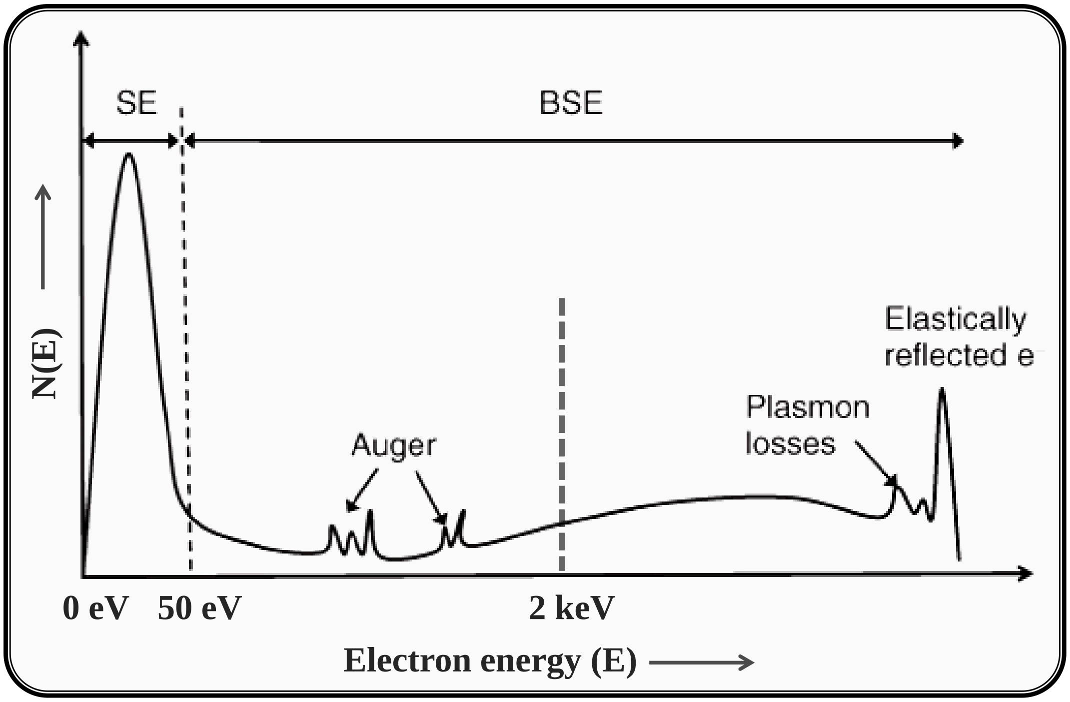

Figure. 2.18: *The energy spectrum of emitted seconday electron (SE) and backscattered electron (BSE).*

effect electron gun which concentrates low energy as well as high energy electrons at electrical potential range of 0.02 - 5 kV. A conventional SEM provide spatial resolution within the range of 3 - 7 nm, however a FESEM can provide a resolution of ∼ 1.5 nm or better, which is another advantage of FESEM over SEM.

2.4.3 X-ray Photoelectron Spectroscopy

The concept of X-ray photoelectron spectroscopy (XPS) technique was initially developed by Kai Siegbahn and his co-workers in 1967 for which he was awarded Nobel prize in Physics in 1981. XPS is used for identifying and quantifying elemental compositions present at/near the surface. In early days, it was also known as electron spectroscopy for chemical analysis (ESCA). The physics behind the concept of XPS is photo-electric effect, known for excitation of bounded electrons in an atom by x-ray photons. If the energy of the x-ray photon is sufficiently high, it will knock out the

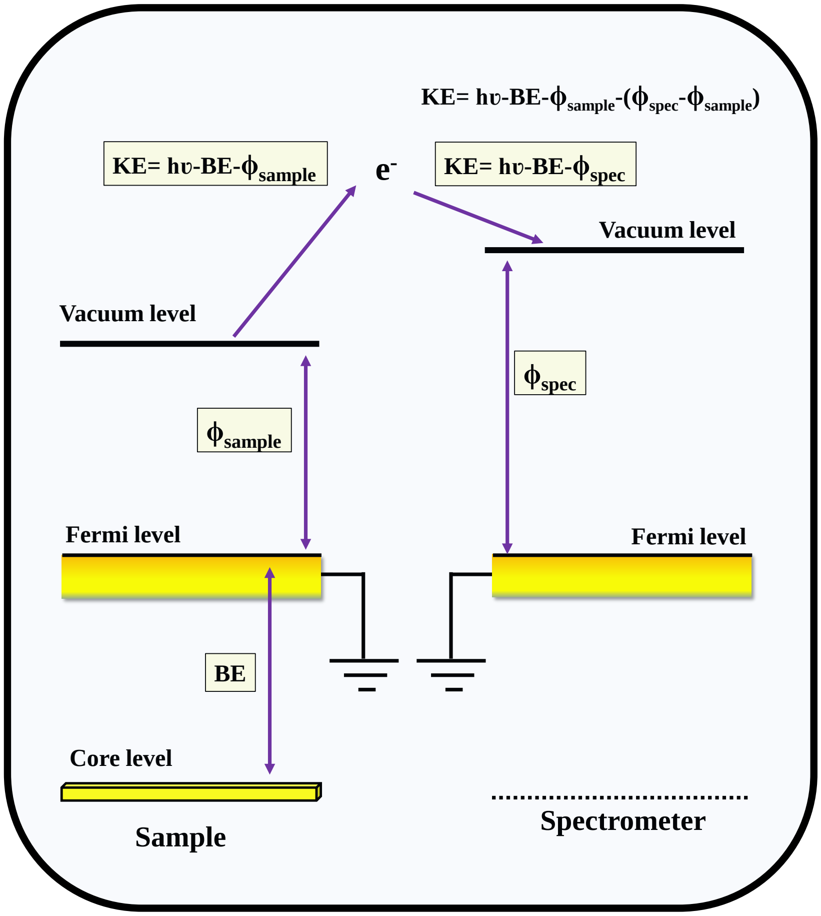

Figure. 2.19: *A schematic diagram of different energy levels when the sample is in contact with the spectrometer.*

electrons from the sample with a certain kinetic energy. If the photon energy is very high, it can also penetrate deep into the sample but the penetration depth depends on the atomic number of the element. The electrons ejected in this process are known as photoelectrons. A typical XPS spectrum shows the number of electrons detected at a specific binding energy. Every element produces its characteristic XPS peaks corresponding to the configuration of the electrons within the atoms, e.g., 1s, 2s, etc. The detected electrons in each peak are related directly to the quantity of element within the sample volume. Relative sensitivity factor (RSF) is used to estimate atomic percentage values by dividing each raw XPS signal intensity with the corresponding RSF.

In a XPS spectrum, derived binding energy (E_b) is used instead of kinetic energy (E_K). The relation between the kinetic energy E_K, binding energy E_b and photon energy $h\nu$ can be written as,

$$E_K = h\nu - E_b - \phi \tag{2.4}$$

where ϕ is the work function of the spectrometer. The binding energy may be considered as the energy difference between initial and final states of photoelectrons after they left the atom. During data accumulation, the reference point of energy scale is considered using the Fermi energy level, E_F as the sample is electrically connected to the spectrometer. Figure 2.19 illustrates a schematic diagram of energy levels using which kinetic energies are estimated and recorded by the spectrometer. In general, XPS spectrum is considered as the finger print of elements. Apart from identifying and quantifying the surface elements, it is also used to understand the chemical states of the elements from the shift in peak position.

2.4.3.1 XPS specrometer

The XPS instrument is maintained at ultra-high vacuum (UHV) having a chamber pressure $\sim$ 10^{-9} to 10^{-10} mbar to allow longest mean free path for the ejected photoelectrons and to avoid any form of sample contamination. The sample is transferred to the XPS chamber (main chamber) using a load lock chamber so as to ensure its minimum effect on the chamber vacuum. The sample is initially irradiated with x-ray photons generated using a standard x-ray gun equipped with Al-K$_\alpha$ (1486.6 eV) or Mg-K$_\alpha$ (1253.7 eV) anode. The x-ray gun is mounted on the instrument in such a way so as to ensure an oblique incidence onto the sample. Therefore, more x-ray interaction with the sample surface takes place. The anode of the x-ray gun is chosen manually and the maximum voltage applied and current are configured for

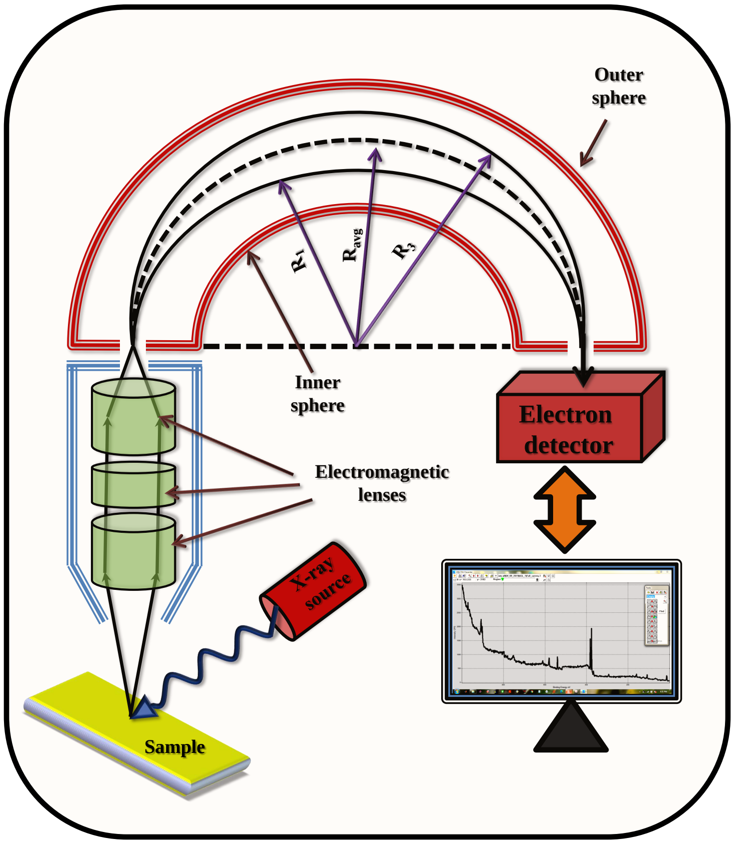

Figure. 2.20: *A schematic diagram of hemispherical electron analyzer of a XPS system.*

this system as 12 kV and 2 A, respectively. The produced x-ray then passes through a thin (~ 1.5 μm) aluminum foil covered window to prevent the entry of other ions and secondary electrons originated during x-ray production to the chamber.

The overall surface analysis by the XPS technique is accomplished by collecting the electrons, ejected during irradiation of surface and analyzing their kinetic energies. There are different types of electron analyzers available out of which this system is equipped with hemispherical electron analyzer. The emitted photoelectron are guided to the detector after passing through the hemispherical analyzer. The analyzer mainly consists of two concentric hemispheres one is inside of the other. If the radius of inner and outer hemispheres are R_{in} and R_{out}, respectively, their average radius will be, $R_{avg}= (R_{in} + R_{out})/2$. A specific potential difference is applied between two hemispheres for a constant analyzer energy mode. The emitted photoelectrons are decelerated and focused to the entrance slit of the analyzer with the help of electrostatic lenses. Hence, electrons with kinetic energy E_o entered through the analyzer slit are confined to follow a circular path of radius R_{avg}. This particular kinetic energy (E_o) of the electrons is known as pass energy or transmission energy. The potential difference applied across the two hemispheres depends on the electron pass energy and the analyzer dimension. This process of analysis keeping the electrons' kinetic energy constant is known as fixed analyzer transmission. Finally, at the exit slit of the analyzer, the electrons collide with the detector where energies of the electrons are measured. By adjusting the lens retarding potentials, the XPS spectrum can be obtained and plotted as photoemission intensity versus their kinetic energies. A schematic diagram describing the overall process is shown in figure 2.20. The specific potentials applied between two hemispheres may be written as,

$$V_{in} = E_o \left[3 - 2 \left(\frac{R_{avg}}{R_{in}} \right) \right] \tag{2.5}$$

$$V_{out} = E_o \left[3 - 2 \left(\frac{R_{avg}}{R_{out}} \right) \right] \tag{2.6}$$

2.4.3.2 Energy Resolution of the XPS system

The energy resolution of the XPS system depends mainly on the three parameters namely, (i) linewidth of the x-ray source (ΔE_p), (ii) full width at half maxima (FWHM) of the photoelectron emission (ΔE_n) and, (iii) energy resolution of the analyzer (ΔE_a). If all the parameters follow a Gaussian line shape, the energy resolution of the XPS can be written as,

$$(\Delta E) = \sqrt{(\Delta E_p)^2 + (\Delta E_n)^2 + (\Delta E_a)^2} \tag{2.7}$$

where ΔE_p depends on the type of x-ray photon source. For standard x-ray sources i.e., Mg-K_α and Al-K_α the values of ΔE_p are found to be 0.85 and 0.7 eV, respectively [90] that are equal to their respective intrinsic linewidth. The values of ΔE_n are directly related to the sample that vary from < 0.1 to > 1.0 eV depending on several other factors namely, the type of analyzers used and their operating conditions.

2.4.3.3 Interpretation of XPS spectrum

In XPS technique, solid sample surface has been irradiated with energetic x-ray photon and ejected electrons are collected and counted by the detector to produce XPS spectrum. There are two types of XPS spectra namely, survey spectrum and high-resolution spectrum. The survey spectrum is obtained at the energies ranging from 0 to 1000 eV with low energy resolution. Survey spectrum provides information of all the elements present in the sample surface from their respective characteristic peaks at their corresponding binding energy values. The high resolution XPS spectrum is captured for a small binding energy range and used to analyze the electronic states or chemical bonds of individual elements. In a XPS spectrum, the intensity of the peaks indicates the amount of element(s) present in the sample surface while the position of a peak gives the details of a particular element(s) or its (their) chemical composition(s). The quantitative analysis of atomic concentration of an element present on the surface is performed by calculating the area under the curve of the elemental peak. The atomic concentration of any element depends on the peak intensity and sensitivity factor of that element. For instance, if n_x is number of x-th element with peak intensity I_x and sensitivity factor is S_x, its atomic concentration, C_x can be estimated as [91],

$$C_x = \frac{n_x}{\sum n_i} = \frac{I_x/S_x}{\sum I_i/S_i} \tag{2.8}$$

where n_i represents the total number of atoms present on the surface, I_i and S_i are the peak intensity and sensitivity factor of i-th element, respectively.

All the XPS data presented in this thesis are recorded using Mg-K$_\alpha$ source (photon energy=1253.7 eV) and operated using 162 W power and a Class150 Bolt on hemispherical electron analyzer from VSW Scientific Instruments Spectrometer. All are attached to the main deposition chamber of nanocluster growth/deposition system to facilitate the in-situ XPS measurements after growth/deposition.

2.4.4 UV-vis spectroscopy

The UV-vis spectroscopy is an optical technique used to characterize a sample using the absorbed or reflected spectrum in ultraviolet and visible regions contributed by its chemical compositions. When a light is absorbed by the molecules it gets excited to a higher energy state producing a broad energy band transitions at different energies and finally loses its energy via non-radiative transition. This concept is used in UV-vis spectroscopy technique. The technique works either in absorption or reflectance mode. In absorption mode, the UV-Vis spectrometer measures the incident light and the transmitted light passed through the sample and compare them for the absorbance estimation. If the intensity of incident light is I_o and intensity of transmitted light is I, then transmittance, T of the sample is given by,

$$T = \frac{I}{I_o} \tag{2.9}$$

and the absorbance can be written in terms of transmittance as,

$$A = -log\,(T) = -log\left(\frac{I}{I_o}\right) \tag{2.10}$$

Again, according to Lambert Beers law, [92], absorbance may be written as,

$$A = \varepsilon c d \tag{2.11}$$

where ε is the molar absorptivity of the material, c is concentration and d is the optical path length. Hence, the expression for transmission may be written as,

$$T = e^{-\varepsilon c d} \tag{2.12}$$

The spectrometer can also be used in reflectance mode. In this case, if we consider I_o as the intensity of incident light and I is the intensity of reflected light from a solid surface, the intensity ratio can be considered as reflectance, R and may be expressed as,

$$R = \frac{I}{I_o} \tag{2.13}$$

The experimental arrangements of reflection and transmission mode for two different samples are shown in figure 2.21. Generally, the measurements in absorbance mode is performed on a transparent sample for the quantitative analysis of the chemical compositions of a film. However, for an opaque sample reflection mode is used to measure the properties of the surface. The above mentioned equation for reflectance (eq. 2.13) is valid for both specular and diffuse reflectance. To get the information of a rough surface, diffuse reflectance spectroscopy technique is extremely useful as compared to specular reflectance spectroscopy. In specular reflectance mode, the value of reflectance is zero at all angles except the reflected angle. However, in diffuse reflectance mode the value of reflectance is non-zero at all the angles as the reflected light is found to be scattered in every directions. So, more information of the rough surface can be acquired in diffuse reflectance mode. In

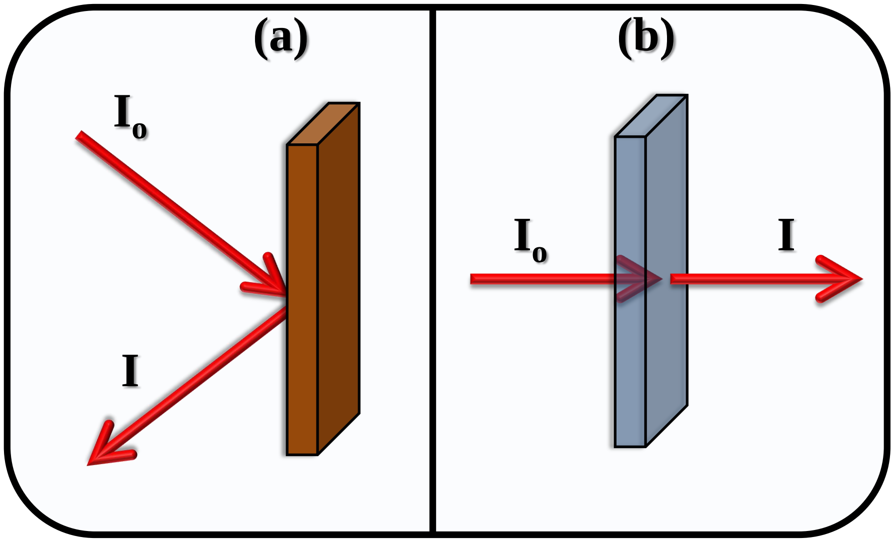

Figure. 2.21: *(a) Reflection mode of measurements, (b) Transmission mode of measurements.*

the present case, we performed UV-Vis spectroscopy measurements in reflection mode using a UV-Vis Lambda 750 spectrometer (Perkin-Elmer). The spectrometer consists of various components namely, a light source, a sample holder, a monochromator or a prism to extract different wavelengths using a beam of light and a photodetector. In this technique, a beam of light emitted from the light source entered into a monochromator where monochromatic light of a particular wavelength gets extracted. Each monochromatic light is then divided into two beams by a beam splitter. One of the beams is used for interaction with the sample for analysis while another beam is used as the reference beam. Finally, the intensities of both the beams are measured and compared by a photodetector to produce the final data. The photodetector can simultaneously measures the intensities by bifurcating the optical path of the beams. In reflection mode, the scanning is performed in 200-800 nm range where 200-400 nm range is for ultraviolet region and 400-800 nm range is for visible region. In diffuse reflectance spectroscopy instrument, the sample is placed near the incident light window during measurement where a beam of light is reflected from the sample and headed towards the detector with the help of a sphere. In this method, the specular light is left out and cannot reach to the detector. As a result, the instrument is only capable of measuring the diffused reflected light.

2.4.5 Contact angle measurements

The wetting property of a surface can be studied by the measurements of water contact angle on the surface. For a small contact angle value ($< 90^o$), the surface is hydrophilic i.e. higher wettability whereas the surface can be considered to be hydrophobic i.e. low wettability for higher value of contact angle ($> 90^o$). The contact angle can be measured when a liquid-gas interface meets a solid surface. There are numerous techniques available for measuring contact angle out of which we will discuss here about the "telescope-goniometer" technique. The first ever telescope-goniometer technique was used by Bigelow and co- workers [93] and later on, in 1960s the first commercial telescope-goniometer-based instrument was designed by W.A. Zisman. Using this technique the contact angle is measured by simply extrapolating a tangent over the sessile drop profile from the liquid-solid-gas interface point to estimate the protractor reading. The experimental setup consists of a horizontal sample holder stage, a camera, an illumination source, a telescope, a micrometer pipette to generate a liquid droplet and an image analysis software. A schematic diagram of the contact angle measurement setup is shown in figure 2.22. Initially a water droplet of volume $\sim$ 5 μl is prepared by a micro-pipette and then drop-casted it on the surface of a sample. The sample is placed on the sufficiently flat horizontal stage. Once a droplet is placed over the surface it is illuminated by a background light and the reflection is recorded by the telescope and captured by a camera. Later on, the captured image is used for estimation of the contact angle. The analysis is carried out using ImageJ software with drop-analysis plugin. To analyze the image, a baseline is drawn parallel to the solid surface of the image. The horizontal nature of the line indicates the surface of the solid sample where the droplet was deposited. Afterwards, the edge of the baseline

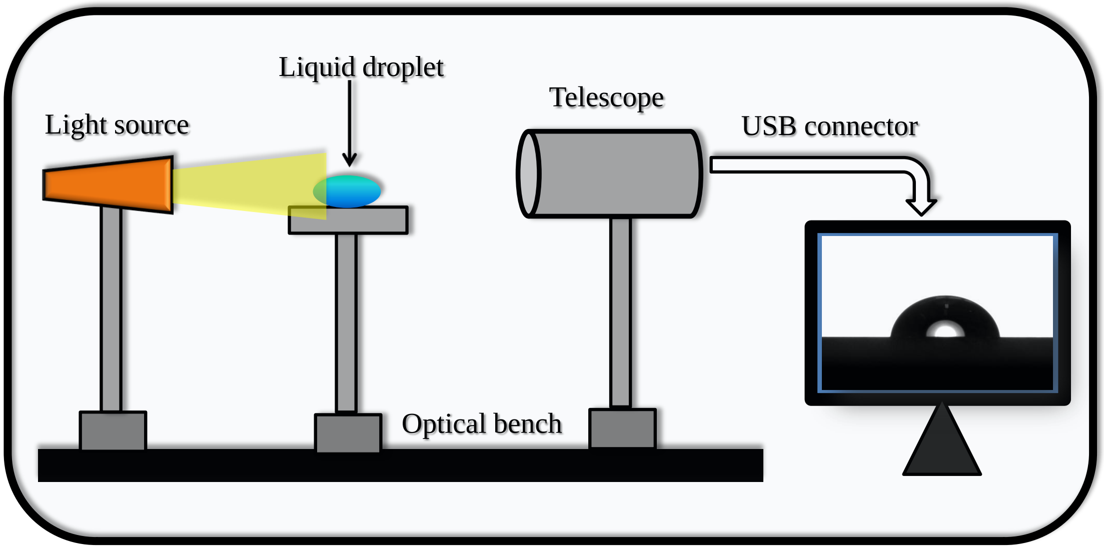

Figure. 2.22: *A schematic diagram of water contact angle measurement facility.*

is drawn manually over the sessile drop profile. Finally, a tangent is drawn at a point where the edge of the droplet meets the baseline. The angle formed between the tangent and the base of the droplet is considered as the contact angle of the droplet. To minimize the errors in measurements, the contact angles were measured on both side of the sessile drop profile and their average is considered as the final result.

2.4.6 Rapid thermal Annealing: A surface modification technique

Rapid thermal annealing (RTA) is a popular and effective process for thermal treatment of a sample as compared to a conventional furnace. In this process, annealing of a film is performed at a temperature with a very fast ramp up rate of 50 °C/sec for a very short time. The ramp down rate is also ∼ 50 °C/sec up to a certain temperature. The process time is also very short typically 1-3 min as compared to conventional furnace. The benefits of annealing a film with RTA process are enhancement of diffusion coefficient of the film, decrease in stress and microscopic defects in a film, reduction of adsorbed oxygen on the sample surface etc. The fast heating can be achieved by a group of ten halogen lamps placed above the substrate stage. The heating chamber is equipped with gas inlet and exhaust valves so as to introduce various gases like argon, nitrogen, oxygen etc. into the chamber during annealing. The system is also equipped with an evacuating facility comprising of a turbo molecular pump backed by a rotary pump to achieve a vacuum level of $\sim 10^{-6}$ mbar. Temperature of the chamber is measured by a thermocouple and a pyrometer. The temperature can be controlled by a feedback electronics. Compressed air is used to maintain a constant temperature in the chamber throughout the annealing process. Parameters *viz.* namely, temperature ramp rate, annealing time, gas flow rate, gas(es) used etc. may be varied using a computer controlled software to achieve a desired oxidation/annealing condition.

Chapter 3

Dynamic scaling study of size-selected metal nanocluster films

---

This chapter describes the growth behaviour of size-selected Cu- and Ag-nanocluster-deposited films under the framework of dynamic scaling theory. The influence of shadowing effect on the growth mechanism of Ag-nanocluster-deposited films with deposition time is also discussed here.

.

Related publications

1. *"Surface scaling behaviour of size-selected Ag-nanocluster film growing under subsequent shadowing process"*, **Pintu Barman**, Anindita Deka, Shyamal Mondal, Debasree Chowdhury, and Satyaranjan Bhattacharyya *J. Phys. D:*

Appl. Phys. **53** (2020) 325302.

2. *"Growth dynamics of copper thin film deposited by soft-landing of size selected nanoclusters ,"*, Shyamal Mondal, Debasree Chowdhury, **Pintu Barman** and Satyaranjan Bhattacharyya *Eur. Phys. J. D* **71** (2017) 327.

3.1 Introduction

In last few decades, the studies on growth kinetics on a surface during the thin-film deposition process has been a very interesting research direction [94–97]. The deposition of thin-films with precise thickness, size and density by controlling the deposition conditions is an interesting topic in the field of material science for basic research and technological applications as well. The kinetic energy of the incoming cluster beam must be very low in order to retain the size and shape of the deposited clusters for soft-landing deposition or low energy interaction process between the clusters and a substrate [54,98]. The surface morphology obtained by the soft landing method is primarily affected by three parameters namely deposition, desorption and surface diffusion. The kinetic energy of the cluster beam and the sticking coefficient of the depositing clusters are responsible for the desorption phenomena, while the surface diffusion term is mainly dependent on the cluster surface interaction energy, size and structures of the deposited clusters [99, 100]. In soft landing deposition process the deposited particles start to move or diffuse over the substrates even at a very low temperature due to the weak interaction between the deposited clusters and substrate [101, 102]. In diffusion process, movement of clusters leads to collisions as well as agglomerations between the neighboring clusters the ultimately ends up by producing large cluster islands on the substrates. The self-affine scaling behaviour of a growing surface is dependent on certain morphological parameters [103]. The study of dynamics of a growing surface is only possible by characterizing and analyzing different scaling exponents under the framework of dynamic scaling theory [104]. There are mainly three scaling exponents in dynamic scaling theory to characterize various kinds of surface morphology namely, roughness exponent (α), growth exponent (β) and dynamic exponent (z). The roughness exponent signifies the degree of surface irregularity in a local length scale; the growth exponent indicates the rate of change in interface width of a surface in logarithmic scale; and the dynamic exponent of a growing surface signifies the change in lateral correlation lengths of the surface with time in logarithmic scale. In scaling theory, for a certain values of these exponents some of the universality classes are there to determine the type of the surface growth. In such a way most of the experimental systems are included in these pre-existed models [105–107] although some of the experimental systems do not fall under any of these models. To understand these type of surface growth, one has to take help of some non-local growth effects. The studies on initial stage growth mechanism of cluster-assembled films are very interesting from fundamental aspects. The growth dynamic study for size-selected cluster-deposited films are not much explored by researchers, although few studies are there where growth dynamics of cluster assembled films without size-selection are reported [108–110]. The growth dynamic study is important from application point of view because an appropriate choice of deposition conditions leads to precise control over the nucleation and growth of cluster film on an appropriate substrate useful in tailoring the properties of the films. By investigating the scaling behaviour of a film, it is possible to get an insight information of the films. Normally, the beam current of size-selected cluster beam is within nano Amp range [86] and thereby it is possible to produce and investigate initial stage growth of a film where coverage of the film always is found to be below 100%.

In this chapter, we have studied the dynamic scaling behaviour of growing films prepared by size-selected Cu- and Ag-nanoclusters. The films are deposited on a ultrasonically cleaned Si (100) substrates containing native oxide layer on the surface. Silver nanoparticle has immense interest in various fields such as catalytic [111], biomedical [112], electronic devices [113], solar cell [114], photocatalytic [115] etc. Size-selected clusters are important in many applications e.g., the size of the Ag-nanocluster significantly influences the activity of the chemical reaction where it is used as catalyst [116, 117]. It is also found to be used to increase the sensitivity while using as a glucose sensor [33] and in memory device applications [118]. Cu-nanoparticles are also considered as material of interest because of its easy availability and its importance in various technological applications such as catalytic, antimicrobial coating etc. [119–121].

3.2 Dynamic scaling theory

The dynamic scaling theory is a powerful tool to understand the physical mechanism involved behind the growth behaviour of a surface and also provides useful information on the surface and interface. According to the scaling theory, the interface width or root mean square (RMS) roughness, $w(r,t)$ of a surface denotes the fluctuations in overall surface height $h(\vec{r},t)$ around an average surface height $< h >$. By measuring the interface width, the roughness of a film can be characterized statistically. The interface width may be expressed mathematically as,

$$w(r,t) = \left\langle [h(\vec{r},t) - < h >]^2 \right\rangle_{\vec{r}}^{1/2} \tag{3.1}$$

Here t represents the growth time and $\langle ... \rangle_{\vec{r}}$ denotes the average value of all the $\vec{r}$ in a system with size L $(r \leq L)$. This equation is useful to measure both the local width where $r \ll L$ and the global width as well with $r = L$.

According to dynamic scaling theory, the interface width of a surface always follows Family-Vicsek relation [122] that can be written as,

$$w(r,t) = t^{\alpha/z} f\left(r/t^{1/z}\right) \tag{3.2}$$

where α is the roughness exponent and z is the dynamic exponent. The scaling function $f(u)$ behaves as,

$$f(u) \propto \begin{cases} u^{\alpha}, & if \quad u \ll 1 \\ const, & if \quad u \gg 1 \end{cases} \tag{3.3}$$

Depending on the value of the argument $u \equiv (r/t^{1/z})$, the scaling function $f(u)$ constitutes two kind of scaling steps. For $u \ll 1$, the interface width $w(r,t)$ varies as r^{α} whereas for $u \gg 1$, the interface width follows a power law and varies with growth time t i.e., $w(r,t) \propto t^{\beta}$. Here β is the growth exponent and for a self-affine surface it satisfies the following condition,

$$\beta = \frac{\alpha}{z} \tag{3.4}$$

The growth exponent β basically describes the time dependent dynamics of surface roughening process [104]. Two steps of scaling function $f(u)$ are separated at a length of $r = \xi$, where ξ is termed as lateral correlation length. It is directly dependent on the growth time of a surface as $\xi \propto t^{\frac{1}{z}}$. Hence, within the range of lateral correlation length, two heights of the surface at two random points can be considered as correlated. Apart from the interface width, there is another statistical scaling function known as height-height correlation function (HHCF) used to measure the lateral autocorrelation of the surface height of a thin-film. For a homogeneous random surface the HHCF can be expressed as,

$$G(r,t) = \left\langle [h(\vec{r_2},t) - h(\vec{r_1},t)]^2 \right\rangle \;, \quad r = |\vec{r_2} - \vec{r_1}| \tag{3.5}$$

where $h(\vec{r_1},t)$ and $h(\vec{r_2},t)$ indicate the surface heights at position $\vec{r_1}$ and $\vec{r_2}$, respectively [123]. Again, the condition of self-affine surface will be fulfilled if the

HHCF function satisfies the relation,

$$G(r,t) = 2 \times [w(t)]^2 f\left(\frac{r}{\xi}\right) \tag{3.6}$$

Thus, following the above equation HHCF shows an asymptotic behaviour [104] and can be written as,

$$G(r,t) \propto \begin{cases} r^{2\alpha} & if \quad r \ll \xi \\ 2w^2 & if \quad r \gg \xi \end{cases} \tag{3.7}$$

The lateral correlation length of a surface can be measured using the relation,

$$\xi = \left(\frac{2w(r,t)^2}{\rho^2}\right)^{\frac{1}{2\alpha}} \tag{3.8}$$

where ρ denotes the RMS local surface slope. There is an another function known as Power spectral density (PSD) function that manifests the scaling behaviour of a random isotropic surface. The PSD function is the Fourier transform of the height of a surface measured in reciprocal space. The time-dependent PSD function can be expressed as,

$$PSD(k,t) = \langle H(k,t)H(-k,t)\rangle \tag{3.9}$$

where $H(k,t)$ is the Fourier transform height of the surface and k represents the spatial frequency in reciprocal space. According to dynamic scaling theory, the PSD function also satisfies the Family-Vicsek relation and may be written as,

$$PSD(k,t) = k^{-(2\alpha+1)} s(kt^{1/z}) \tag{3.10}$$

where the scaling function can be written in a generalized form as [124, 125],

$$s(kt^{1/z}) \propto \begin{cases} (kt^{1/z})^{2\alpha+1} & ; (kt^{1/z}) \ll 1 \\ Const & ; (kt^{1/z}) \gg 1 \end{cases} \tag{3.11}$$

3.3 Growth dynamics of size-selected Cu-nanocluster-deposited films

3.3.1 Experimental details

Size-selected Cu nanocluster of diameter ∼ 3 nm (number of atoms per cluster ∼ 1100) were chosen for deposition on Si(100) substrates containing native oxide layer on their surface. The mass spectra recorded by the QMF are adjusted by tuning various parameters to get the highest ion current (∼ 3 nA) of the selected beam. Ar and He flow rates were maintained at 25 and 10 sccm, respectively during the deposition. The base pressure of the main chamber and magnetron chamber was recorded as 2.0×10^{-9} and $< 5.0\times 10^{-4}$ mbar, respectively. The pressure of the main chamber and magnetron chamber was increased upto 4.8×10^{-4} and 2.5×10^{-1} mbar, respectively during the operation. A set of samples were prepared for a deposition time of 10, 20, 60 and 80 min. Since soft landing deposition is the objective, no bias was applied to the substrate. Also, we did not use substrate rotation for the deposition of nanoclusters. The magnetron power was kept at 50 W during the deposition and the optimum resolution of the QMF was maintained at ∼ 38%. The morphologies of the thin-films were investigated by Atomic force microscopy in tapping mode. The compositional analysis of the films were done by an in-situ x-ray photoelectron spectroscopy set up using a Mg-K_α source (energy = 1253.7 eV).

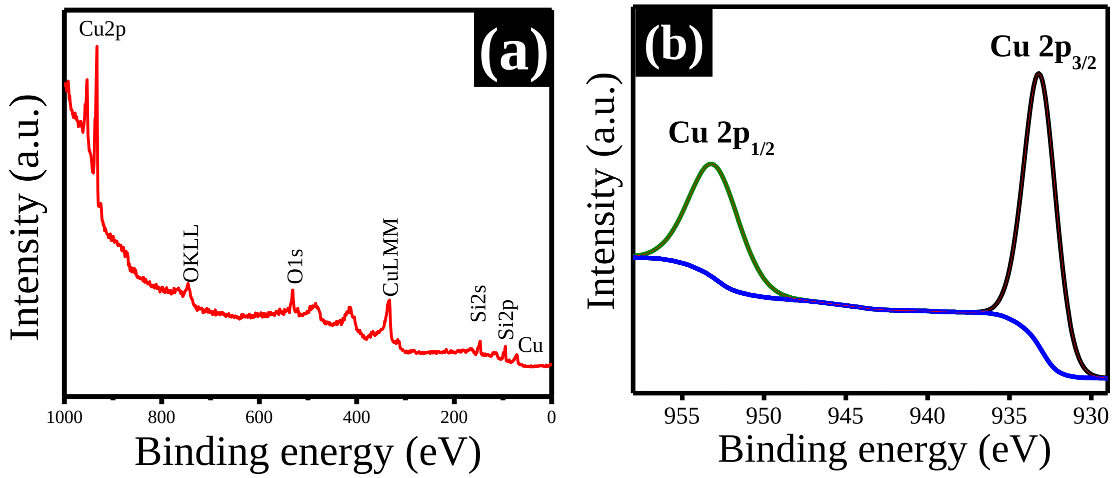

Figure. 3.1: *(a) XPS survey spectrum for Cu film deposited for 20 min, (b) High-resolution XPS spectrum of Cu 2p state for the same sample.*

3.3.2 Results and discussions

Figure 3.1(a) shows the survey spectrum of Cu-nanocluster-deposited film on Si(100) substrates for a deposition time of 20 min. The Cu 2p peak appeared at 933 eV binding energy in the survey spectrum confirms the presence of Cu clusters on the substrate. Moreover, the HR-XPS spectrum of Cu 2p shown in figure 3.1(b) confirms the absence of oxidation of Cu clusters. The O 1s peaks appeared in the survey spectrum are due to presence of native oxide layer on the Si substrates. Besides the above, no other peaks were found in the spectra indicating the surface evolution with time solely attributed to either cluster-cluster or cluster-surface interactions.

Figure 3.2 depicts a series of three dimensional AFM images representing the surface morphologies of Cu-nanocluster-deposited films for varied deposition time. The grain sizes are found to increase in both the lateral and vertical directions with deposition time. In order to see the vertical growth the line profiles from the corresponding AFM images are extracted and shown in figure 3.3. The increment of surface height of the cluster deposited films with the increase in deposition time

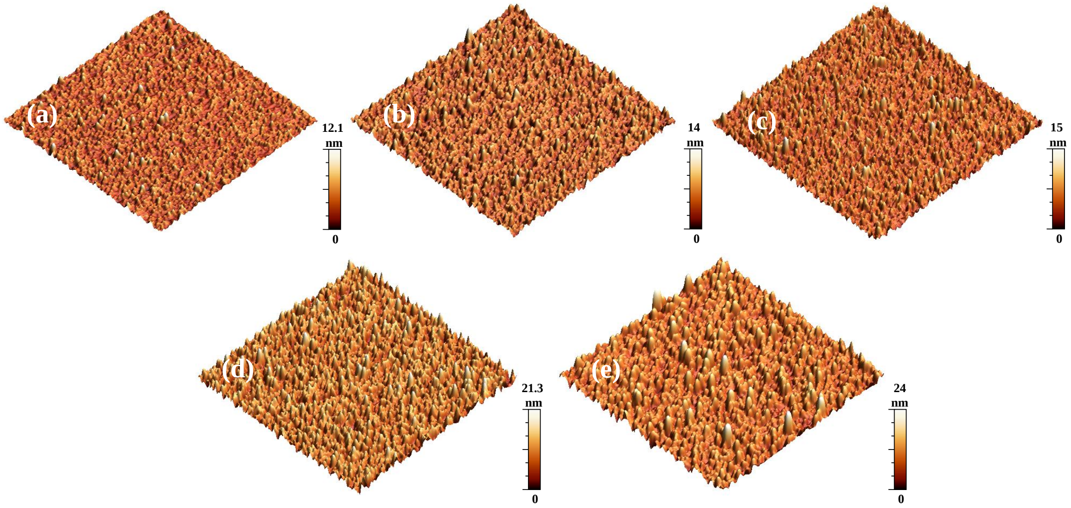

Figure. 3.2: *Typical two dimensional AFM images with scan area of (1 $\mu m \times 1$ μm) of size-selected Cu-nanocluster-deposited films on Si(100) substrate for deposition times of (a) 10 min, (b) 20 min, (c) 40 min, (d) 60 min and (e) 80 min.*

indicates the higher roughening of surface over time.

The roughening behaviour of the surfaces can be verified by studying the change in interface width with deposition time. In order to do this, at first the HHCF is extracted from the corresponding AFM images. Figure 3.4(a) shows the bi-logarithmic variation of $G(r,t)$ with scan length r for all the samples. For all the films, the HHCF curve initially increases linearly with the increase in r for small values of r and all the curves saturate at higher values of r. The upward shifts of the HHCF for all r values indicate vertical growth of the films. The roughness exponent (α) of the films are estimated from the linear fitting of the first step of HHCF curve using the relation found in equation 3.7.

The variation of roughness exponent versus deposition time illustrated in figure 3.4(b) shows α initially increases from 0.68 to 0.83 for the samples deposited at 10 to 20 min and thereafter, it saturates. The interface width of the films is measured from the saturation region of the HHCF curve using the relation $\sqrt{G(r,t)/2}$. The

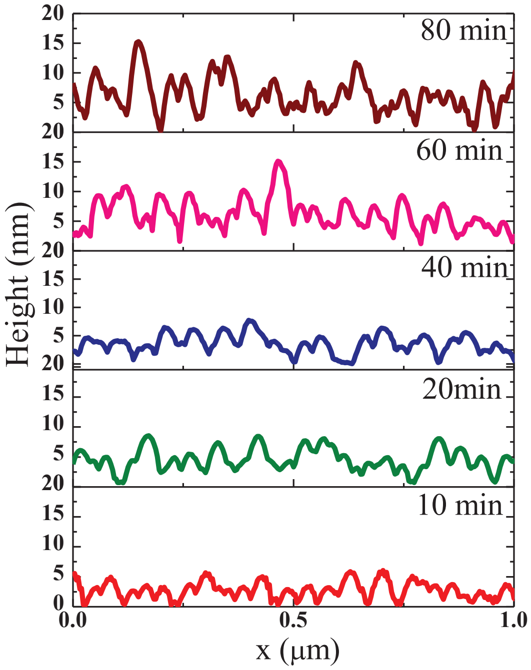

Figure. 3.3: *Height profiles extracted from the corresponding AFM images of the Cu-nanocluster-deposited films.*

logarithmic variation of interface width of the films at different deposition times is shown in figure 3.4(c). The interface width variation shows two growth steps having two growth exponent values $\beta_1 = 0.14 \pm 0.02$ and $\beta_2 = 0.83 \pm 0.45$. Here the lower β value suggests initial stage growth of the Cu-nanocluster-deposited films whereas the higher β value suggests a rapid growth of the films for longer deposition time. From the plot of height distribution function, $P(h)$ of the films as shown in figure 3.4(d), it is found that the peaks are broadened with the increase in deposition time and deviate from a pure Gaussian function. The deviation of the peaks can be quantified by the measurements of surface skewness, S that provides information on variation of symmetry distribution from a reference point. For a zero value of skewness, the surface represents a pure Gaussian type distribution. In the present case, the skewness of all the films are found to be greater than zero signifying symmetric distributions break. Moreover, figure 3.4(d) shows a bimodal height distributions of the films upto a deposition time of 40 min and above this the distributions are found to be mono-

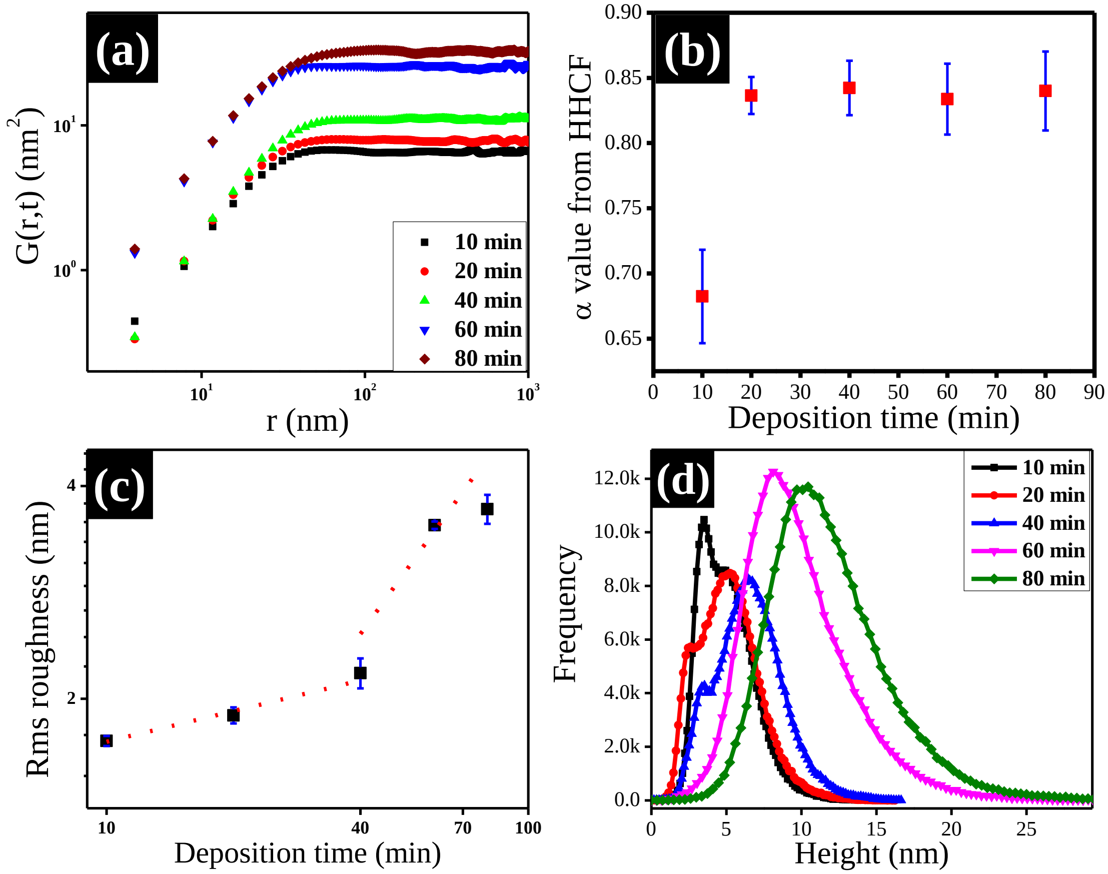

Figure. 3.4: *(a) Log-log plot of G(r) vs lateral distance r, (b) Variation of roughness exponent with deposition time, (c) Log-log variation of RMS roughness with deposition time, (d) Height distribution for Cu-cluster films deposited at different times.*

modal. The reason behind this peculiar behaviour of height distributions may be explained on the basis of clusters and their agglomeration. During the initial stage of deposition, the surface coverage of cluster-deposited films is very low and in AFM measurement, the tip will measure both the surface and the objects present on the surface and consequently, it provides two types of height information, one is for the substrate and another one is for the deposited clusters. For longer deposition time (> 40 min), the clusters will start to agglomerate with the pre-existed clusters due to an increased cluster flux resulting in the formation of bigger islands. So, the coverage of the film increases. In this case, during the substrate scan the tip cannot measure the

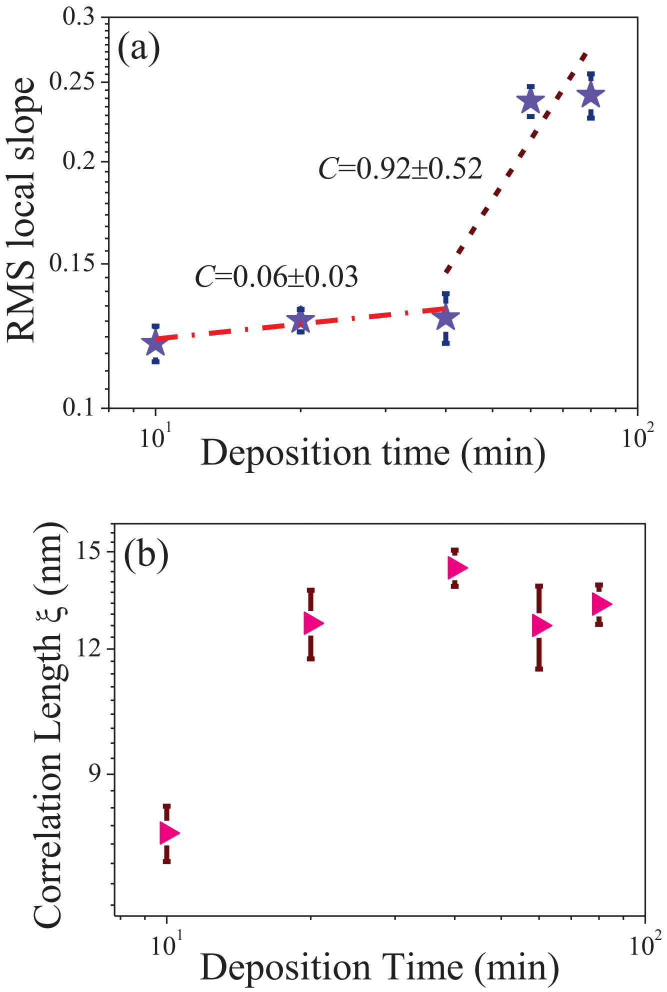

Figure. 3.5: *Log-log variation of (a) RMS local slope, (b) Correlation length with deposition time.*

heights of the substrate separately and the overall height information is dominated by the clusters islands. So, the bimodal behaviour in height distribution spectra vanishes for longer deposition time.

Figure 3.5(a) shows the bi-logarithmic variation of slope of rms local roughness (ρ) with the deposition time. Similar to rms roughness (w) the variation of ρ also exhibits two scaling steps with a crossover deposition time at 40 min. Initially the variation of ρ is almost constant for lower deposition time ($t < 40$ min) with a slope $C_1 = 0.06 \pm 0.03$ whereas the variation is rapid for a longer deposition time ($t > 40$

min) with a slope of $C_2 = 0.92 \pm 0.52$. The correlation length of each of the films estimated using the equation 3.8, and plotted against deposition time, t is depicted in figure 3.5(b). It is found from the figure that the values of correlation length, ξ saturate for longer cluster deposition time.

In summary, the growth dynamics of the deposited films for size-selected Cu nanoclusters exhibit two types of growth steps with two β values i.e., $\beta_1 = 0.14 \pm 0.02$ and $\beta_2 = 0.83 \pm 0.45$ with a crossover deposition time at 40 min. The roughness exponent (α) values for longer deposition time ($t > 20$ min) is found to be $\sim 0.84 \pm 0.01$. These scaling exponents of the films do not match well with the previously reported values [98, 108–110]. Moseler *et al.* [98] prepared thin-films by energetic Cu cluster beam and found the growth mechanism as Edward-Willkinson type. Buzio *et al.* [110] observed the values of growth exponent $\beta = 0.42 - 0.50$ and roughness exponent $\alpha = 0.64 - 0.68$ for the low energy carbon cluster-deposited films on Si and Cu substrates using a supersonic microplasma method. Palasantzas *et al.* [108, 109] observed the values of $\beta = 0.62 \pm 0.07$ and $\alpha = 0.45 \pm 0.05$ for low energy Cu nanocluster-deposited films on Si substrates using gas aggregation methods. In the present case, the observed higher value of roughness exponent of the films for longer deposition time indicates the probability of surface diffusion of deposited nanoclusters occurred even at room temperature and the same is reported earlier [101, 102]. For longer deposition time, the probability of agglomeration of clusters increases as the spatial distance between the neighboring cluster decreases due to the increase in surface coverage of cluster-deposited films. As a result, the surface height increases and the rms roughness of the films also increases with the increase in cluster deposition time. On the other hand, the physical mechanism behind the rapid increase in rms roughness at the second growth step with higher β value may be attributed to some non-local effects like shadowing effect [126]. In this process the peaks of the surface receive more particles as compared to valleys during the surface growth . Hence, the peaks grow faster and the overall roughness of the films rapidly increases. A detailed explanation of the non-local shadowing effect and its role in surface growth is discussed in the next section of this chapter.

3.3.3 Conclusion

In conclusion, the growth dynamic behaviour of Cu-nanoclusters deposited on Si substrates by soft landing deposition process is studied. At an early stage of deposition, random distribution of clusters takes place where the probability of aggregation and diffusion are found to be negligible. The AFM images show the void spaces in the films upto a deposition time of 40 min. Hence, it can be concluded that an increased film roughness is due to an increase in number density of the clusters. The overall variation of interface width with deposition time shows the cluster-cluster aggregation as the dominant mechanism of surface growth.

3.4 Surface scaling behaviour under shadowing process

3.4.1 Experimental details

In this work, size-selected Ag-nanocluster of diameter $\sim$ 4 nm (number of atoms per cluster = 1750) on 10×10 cm^2 Si(100) substrates was deposited. The substrates were ultrasonically cleaned in acetone followed by ethanol for 15 min each to remove the organic contamination from the surface at the time of loading into the main deposition chamber. At that time, the base pressure in the main deposition chamber and the aggregation chamber were maintained at 2.0×10^{-9} and $< 5.0\times10^{-4}$ mbar, respectively. During the deposition, the pressure of main deposition chamber and aggregation chamber is increased to $\sim 4.8\times10^{-4}$ and 2.5×10^{-1} mbar, respectively. To study the growth dynamics of Ag-nanocluster film, a series of samples were prepared for various deposition times viz. 5, 7, 10, 12, 15, 20, 23, 25, 28 and 30 min. The ion current was maintained at $\sim$ 0.5 nA during cluster deposition and all other system parameters were kept at a constant value. The samples were prepared using soft-landing deposition method where no bias was applied to the substrate during the deposition. The morphologies of the deposited films were studied by atomic force microscopy in tapping mode and by a field emission scanning electron microscopy. The compositional analyses of the films were performed by x-ray photoelectron spectroscopy facility using a Mg-K_α source. The optical properties of the films were studied using the UV-Vis reflectance technique.

3.4.2 Results and discussions

Figure 3.6 shows the two dimensional AFM morphology of the size-selected Ag-nanocluster-deposited films for all the samples. The AFM images of the films reflect the evolution of the Ag-nanocluster-deposited surface with the increase in deposition time. Three dimensional AFM image with a scan area (1 μm ×1 μm) of the same sample is shown in figure 3.7 to get a clear view of their surface morphology. It is evident from the 3D surface morphology of the films that the height of the cluster-deposited films increases very slowly upto a deposition time of 20 min whereas density of films is found to increase rapidly. The height of the deposited clusters are also found to be increased suddenly and gets saturated for a deposition time of 30 min.

Figure 3.8(a) shows the bi-logarithmic plot of power spectral density function versus spatial frequency for all the deposited films. The PSDF curve shows power law behaviour with a negative slope for smaller values of spatial frequency k that confirms the presence of kinetic roughening within that range. The PSDF curve for all the samples shows similar behaviour for higher k values where it saturates signifying

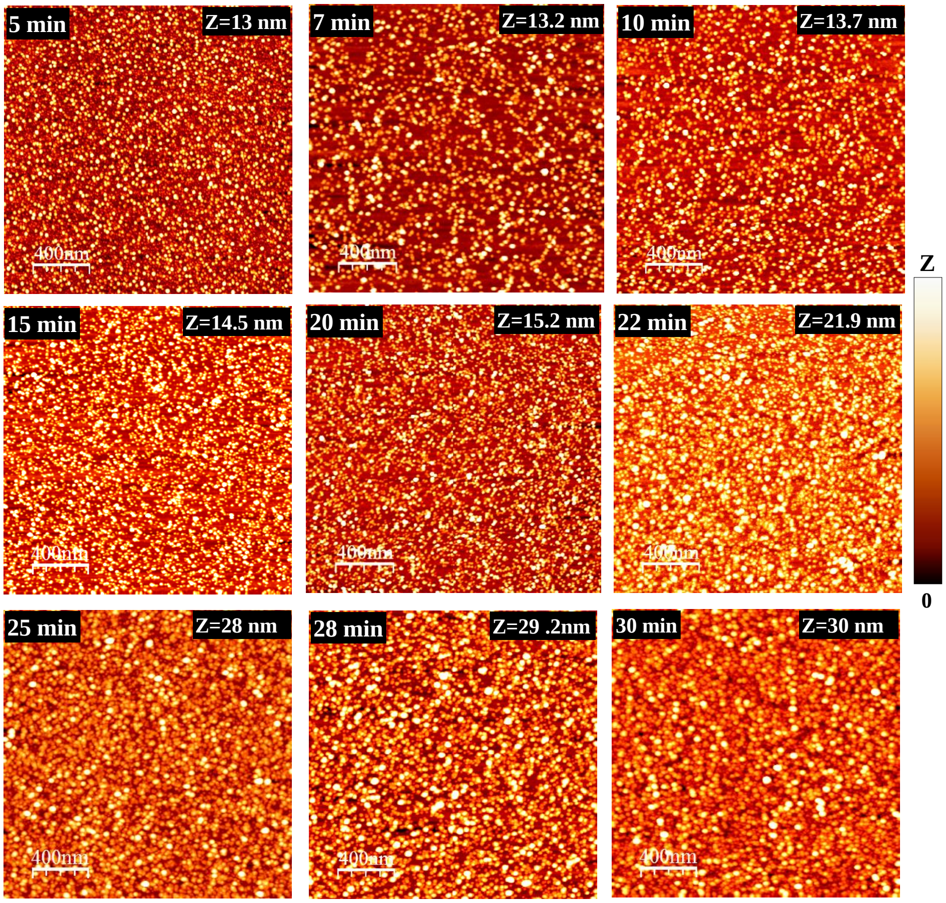

Figure. 3.6: *Typical two dimensional AFM images with scan area of (2 μm ×2 μm) of size-selected Ag-nanocluster-deposited films on Si(100) substrate at varying deposition time.*

absence of any type of lateral correlation on the surface height within this particular range. Moreover, for the complete range of k, we did not found any kind of peak in any of the PSDF curve indicating non-existence of any surface periodicity in the cluster-deposited films. Further, it is seen from the saturation region of the PSDF curves that all the curves up to a deposition time of 20 min overlap and beyond that an upward shift in the curves is seen. Therefore, there is a transition in growth occurs above 20 min of deposition. Figure 3.8(b) shows the logarithmic variation of height-height correlation function, $G(r,t)$ versus scanning length r for all the samples. It is observed that the $G(r,t)$ shows two types of variation with increasing r. Initially for small values of r, the variation of $G(r,t)$ increases linearly beyond which the HHCF

Figure. 3.7: *Typical three dimensional AFM images with scan area of (1 $\mu m \times 1$ μm) of size-selected Ag-nanocluster-deposited films on Si(100) substrate for various deposition times.*

values do not change at all and gets saturated. It is also found that the HHCF curves shift towards the positive y-axis with the increase in deposition time signifying an increase in rms roughness of the films with deposition time. Non-existant oscillatory behaviour in the HHCF curve for the entire r range suggests that the deposited films are self-affine in nature. The value of roughness exponent, α for each of the film can be found by estimating the slope obtained by the linear fit of the first step of the HHCF curve using the equation 3.7. The obtained roughness exponent values for all the films are found to be almost constant and the average roughness of the films is found to be $\alpha = 0.76 \pm 0.02$. The rms roughness or interface width, w of the films

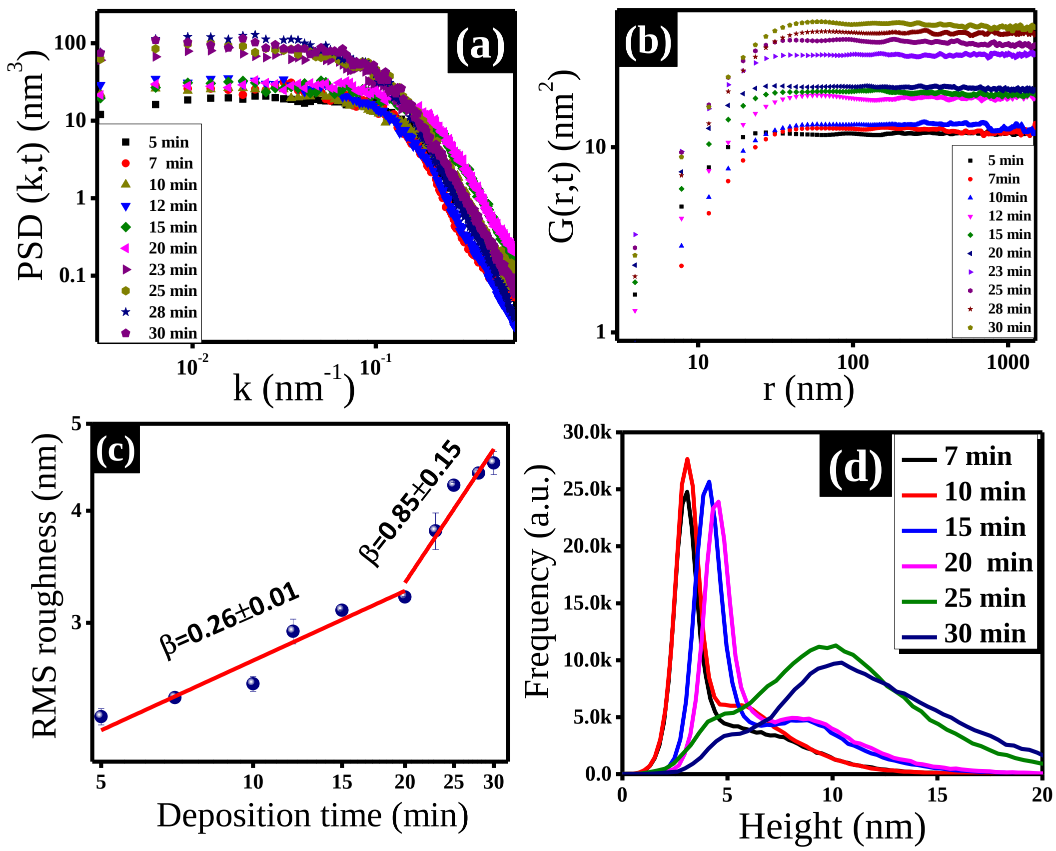

Figure. 3.8: *(a) Bi-logarithmic plot of power spectral density (PSD) function versus spatial frequency (k); (b) log-log plot of height-height correlation function versus scanning length, r; (c) log-log plot of rms roughness, $w(r,t)$ versus deposition time, t; (d) height distibutions of the films.*

can be calculated from the saturation region of the HHCF curve using the relation, $w = \sqrt{G(r,t)/2}$. The logarithmic variation of rms roughness of the films with the deposition time is shown in figure 3.8(c). The overall variation can be best fitted with two linear fittings and two growth exponents (β) are found. The estimated growth exponent in the first step is $\beta_1 = 0.26 \pm 0.01$ for deposition time upto 20 min whereas the same for the second step is $\beta_2 = 0.85 \pm 0.15$ for deposition time above 20 min. Figure 3.8(d) shows the variation of height distribution function for all the samples and it is found that in all the cases the distribution is bimodal in nature. The higher intensity of the distribution during initial deposition stage is found to reduce as the deposition progresses. At the early stage of deposition, the number density of Ag-clusters on the surface are very low and hence, during scanning the AFM tip can measure the height of both the surface and the largely distributed clusters on the surface. The number density of the deposited clusters increases with deposition time and beyond a certain deposition time the number density remains constant due to agglomeration of newly deposited clusters with the already existed clusters leading to formation of larger cluster islands on the substrate. During AFM scan, the tip cannot measure the height contributed by the surface and records only the presence of smaller and larger clusters.

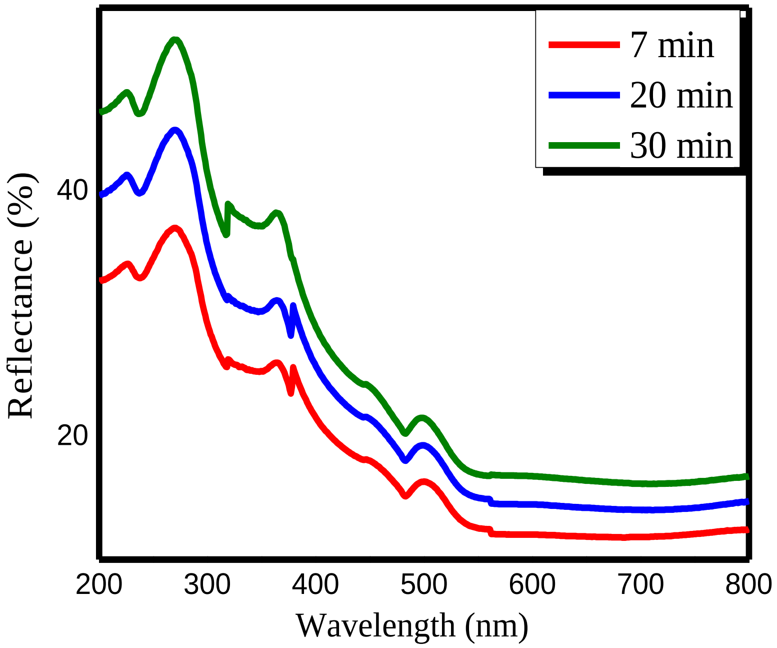

Figure. 3.9: *UV-Vis reflectance spectra of Ag-nanocluster-deposited on Si(100) for 7, 20 and 30 min.*

Figure 3.9 shows the UV-Vis reflectance spectra for size-selected Ag-nanocluster films for the samples with deposition times of 7, 20 and 30 min. It is observed that the reflectance of the films increases with an increase in deposition time. The average reflectance of the spectra are estimated as 19, 22 and 26% for samples deposited for

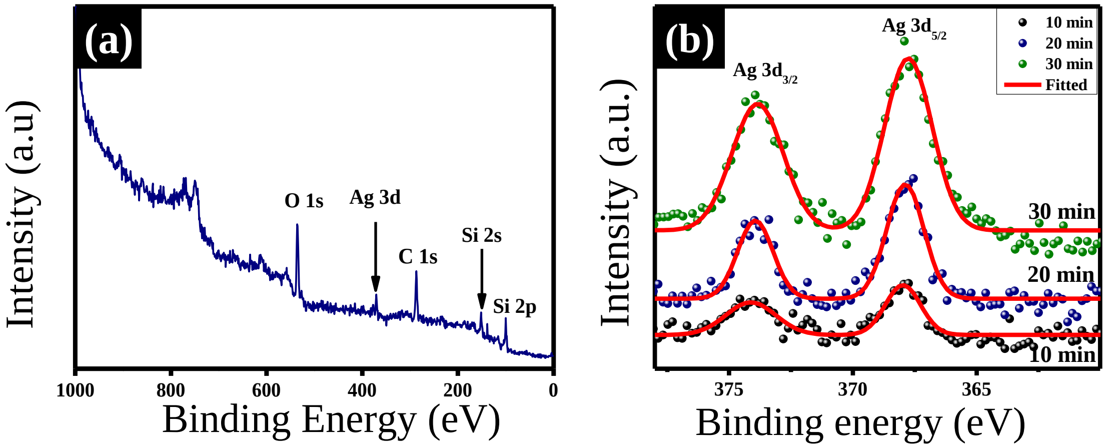

Figure. 3.10: *(a) XPS survey spectrum of Ag-nanocluster-deposited film for a deposition time of 20 min, (b) High-resolution XPS spectra of Ag 3d states for cluster-deposited film with deposition times of 10, 20 and 30 min.*

7, 20 and 30 min, respectively. Therefore, the amount of deposited Ag-nanoclusters on the substrate increases with deposition time that in turn increases the coverage of Ag films. This increased coverage of Ag is able to reflect more light and the average reflectance increases.

The elemental compositions of the films are investigated by XPS technique. Figure 3.10(a) illustrates the XPS survey spectrum of 20-min-deposited film wherefrom the presence of Ag is evident from the Ag 3d peaks at $\sim$ 368 eV. The contribution of substrate also is observed in the form of Si 2s and Si 2p peaks. The O 1s peak appears in the survey spectra due to native oxide film present on the silicon surface. The high resolution core level Ag 3d spectra for three of the samples are shown in figure 3.10(b). The binding energies for Ag 3d are 368, 367.9 and 367.75 eV for the samples deposited at 10, 20 and 30 min, respectively. The binding energy shift towards negative values. The negative shifting indicates the shifting of Ag 3d peak towards lower BE value. One of the possible reasons for such a shift in BE is that the surface contains bigger cluster aggregates as compared to the films deposited for smaller time. Due to longer deposition time, the amount of Ag cluster on the surface increases and they agglomerate to form bigger sized cluster-aggregates or islands. The same is corroborated by the morphology of AFM and SEM images. Another possibility for the shift may be due to the chemical effect in which nanoparticles react with the elements/compounds (such as oxygen, carbon) present in the surrounding environment or the substrate material via adsorption. It was earlier found that the binding energy shift of core level spectra took place due to surface charging effect [127], size effect of the deposited nanoparticles [128] and chemical effect [129]. In one of the studies Shin *et al.* [130] observed the size effect of deposited Ag nanoparticles and their chemical effect as well and finally concluded that the negative binding energy shift of the peaks occurred only due to the presence of large-sized particles. In the present case the charging effect may completely be ruled out because the substrate was kept at grounded condition. However, the chemical effect cannot be discarded in our case. Therefore, the binding energy shift occurs either due to the effect of particle size or due to the influence of the chemical effect occurred in the sample surface. In figure 3.10(b), the relative intensity of Ag 3d doublet is found to increase with the deposition time. This is due to the presence of higher amount of Ag atoms on the Si surface as compared to the films deposited for smaller times. The increased amount of Ag cluster for longer deposition time can be verified from the size-distribution histograms extracted from the corresponding SEM images shown in figure 3.11. In the histograms, the fitted curve is narrower for smaller deposition time which keeps on broadening with the increase in deposition time. The narrower curve indicates lower amount of Ag on the surface as compared to the broader one and the same can be extracted from the area under the respective curves.

The morphology of Ag-nanocluster-deposited films is also investigated by SEM technique. The SEM image of the films and their corresponding histograms are illustrated in figure 3.11. It is seen from the SEM images that as the deposition time

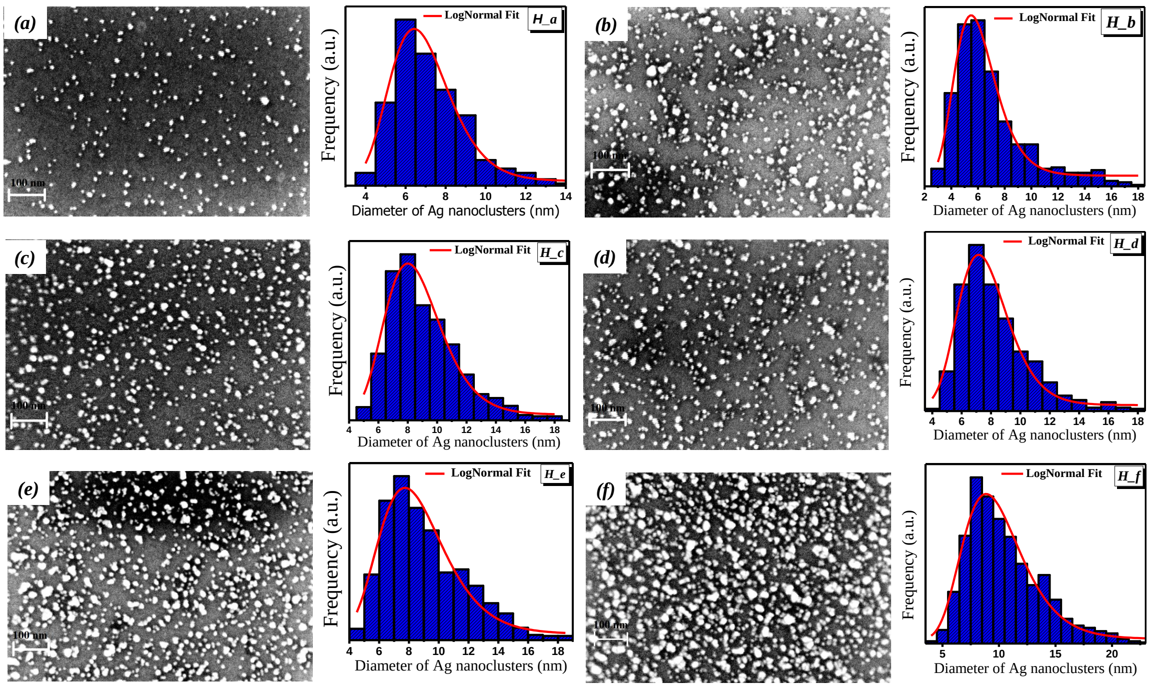

Figure. 3.11: *SEM images obtained for Ag-nanocluster-deposited films on Si(100) substrates for a deposition time of (a) 7 min (b) 10 min (c) 15 min (d) 20 min (e) 25 min and (f) 30 min; the size-distribution histograms extracted from the corresponding SEM images of deposition time (H_a) 7 min (H_b) 10 min (H_c) 15 min (H_d) 20 min (H_e) 25 min and (H_f) 30 min.*

increases, the number of particles and the surface converges of Ag increases. Large-sized particles or cluster islands are appeared on the surface for longer deposition time. The SEM images are in well agreement with the AFM images. For better understanding, the lateral size of each of the particles are measured using ImageJ software and the derived size-distribution spectrum are put on the right side of the corresponding SEM image as evident in figure 3.11. It is noticed from the figure that the distribution range increases with the deposition time due to the formation of large-sized particles. The size distributions of the films can be well fitted with lognormal distribution function and the mean cluster size of every spectra may be estimated.

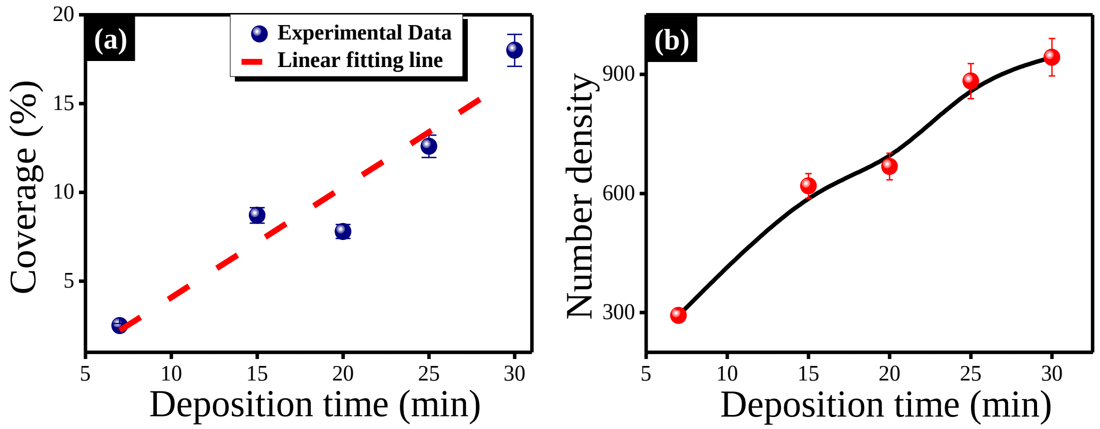

Figure. 3.12: *Variation of (a) percentage coverage and (b) number density of Ag-nanocluster-deposited films with various deposition times.*

The mean cluster size of each distribution is found to be almost constant. The large-sized cluster islands are visible for longer deposition time. The surface coverage of Ag films and their corresponding number densities may be estimated by analyzing the images. Figure 3.12(a) shows the variation of coverage of Ag films with deposition time. It is found that the surface coverage increases linearly with deposition time. The variation of number density with deposition time is shown in figure 3.12(b). It is found that the number density and the surface coverage vary for shorter deposition time. But the variation is slow and afterwards saturates for longer deposition time.

In summary, there are two growth steps for the Ag-nanocluster-deposited films. The growth exponent (β) for the two steps is found to be 0.26 ± 0.01 for deposition time upto 20 min and 0.85 ± 0.15 for deposition time above 20 min. The roughness exponent (α) is found to be constant for all the deposition time with an average value of $\alpha = 0.76 \pm 0.02$. The first growth step where the interface growth of the nanoclusters is similar to the KPZ growth model. The KPZ growth model is a non-linear growth model, where it is expected that the growth occurs in a direction along the normal of the local surface. In KPZ model, they argued that the random surface growth via ballistic deposition can be modeled by a stochastic continuum equation for the interface height. This model is found to be very helpful in order to study the interfaces of a rough surface. In this model, desorption or the creation of pores over the surface are considered as the major relaxation processes. With the help of simulation, this model predicts the values of scaling exponents for 2+1 dimensional surface and the predicted values of growth exponent, β is found to be ~ 0.24 and roughness exponent, $\alpha \sim 0.38$. The second growth step appeared for longer deposition time ($t > 20$ min), the estimated growth exponent suggests the formation of a rough surface. Yang *et al.* [131] observed the growth process of polycrystalline Cu film at a substrate temperature of 700 K and found the growth exponent $\beta = 0.88$. They proposed bulk diffusion process as one of the reasons for surface growth. In the present case, the bulk diffusion process may be ignored as the experiments were performed at room temperature. Since none of the pre-existed theoretical models match well with the obtained experimental value of growth exponent β in the second growth step, other non-local effect such as shadowing, re-emission etc. may be responsible for cluster growth in the second step. The shadowing effect mainly depends on the surface height factor during the growth of a surface. This effect originates when deposition takes place either by random angular distribution process or keeping substrate in tilted position [132–134]. As a result, the growing/depositing surface features block the incoming beam from reaching the valleys and the growth of valleys does not occur and only the taller surface features grow. Hence, the overall surface is very rough. A schematic diagram explaining the effect of shadowing and re-emission process during surface growth is shown in figure 3.13 where an obliquely incident nanocluster beam falls on the substrate at an angle of 45^o. After a certain time of deposition, the surface covers with both clusters and clusters-aggregated islands. These cluster islands create a self shadowed region in the valleys on the other side of the direction of the cluster beam. So, incoming clusters can not reach the self shadowed region directly. In this

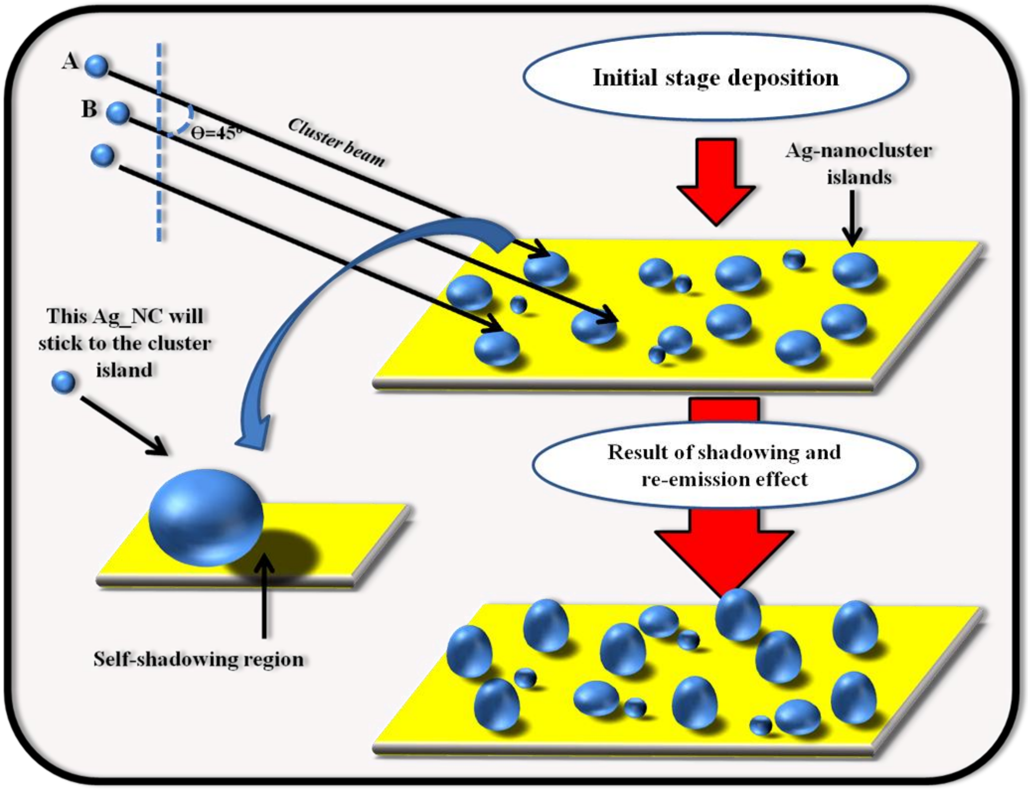

Figure. 3.13: *A schematic illustration of dynamic surface growth by shadowing and re-emission effect.*

figure, “A” and “B” are marked as two incoming size-selected Ag nanoclusters. At the time of deposition, “A” will be captured by the taller surface of the cluster islands due to its large sticking co-efficient and the cluster “A” merges with the islands. This process is called shadowing effect where the growth of taller surface takes place and the overall surface roughness increases. Additionally, some of the incoming nanoclusters e.g. B cannot be captured by the taller surface due to either of its higher kinetic energy or its low sticking coefficient. These incoming particles will either bounce back from its impact point and deposited on other point or repeatedly bounce and finally reach the valleys where they get deposited. The re-emission process often occurs when the kinetic energy of the incoming particle is very high. But in the present case we are dealing with soft-landing deposition process where the kinetic energy of the incoming cluster beam is very low. Hence, the possibility of occurrence of re-emission during surface growth can be ruled out.

It is found from the simulation that for a pure shadowing growth of a surface without any re-emission effect the growth exponent will be equal to 1 [135,136]. In the current experiment, the interface growth of Ag-cluster-deposited films for longer time are found to be dominated by the shadowing process and estimated growth exponent is $\beta = 0.85 \pm 0.15$ i.e. very close to 1. Further, besides the shadowing effect, another effect known as steering effect is able to influence the trajectory of incoming cluster and inclines them towards the taller surface. This effect is mainly originated due the attractive force between the taller surface and the incoming clusters.

3.4.3 Conclusion

The growth dynamics of size-selected Ag-nanocluster films deposited by soft landing process on Si(100) substrates are studied by AFM, SEM and XPS techniques. The scaling behaviour of the films shows two types of growth steps and surfaces are found to be self-affine in nature. The two growth steps are separated by a crossover deposition time of 20 min where the first step of growth follows the KPZ growth model while the second growth step is found to be dominated by the non-local shadowing effect. The roughness exponent values of all the films are found to be constant. SEM morphology of the films also is in well agreement with the AFM morphology. From the lateral height distributions extracted from SEM images it is found that bigger cluster islands are formed for longer deposition time. The large-sized islands formed on the surface are found to be affected. The XPS spectra show a negative shift in binding energy. The optical property of the films are measured and found that average reflectance of the film increases with the increase in deposition time.

Chapter 4

Scaling aspects and wettability transition on fractal surface developed by size-selected Ag-nanoclusters

---

In this chapter, the Ag-cluster aggregate growth behaviour is analysed using time independent scaling theory. Various morphological parameters are determined statistically under the framework scaling theory. Further, the wettability property of the cluster films is studied. Finally, a correlation between the surface statistical parameters and the wettability of the films are interpreted.

Related publications

1. *"Wettability transition on fractal surface developed by size-selected Ag-nanoclusters"*,

Pintu Barman, Anindita Deka, Supratic Chakraborty and Satyaranjan Bhattacharyya (Submitted)

2. *"Scaling aspects of the surface morphology for size-selected Ag-nanocluster films"*, **Pintu Barman**, Anindita Deka, Supratic Chakraborty and Satyaranjan Bhattacharyya (Submitted)

3. *"Evolution from mono-dispersed to mound like structures of size-selected Ag-nanocluster films"*, **Pintu Barman**, Anindita Deka and Satyaranjan Bhattacharyya *AIP Conf. Proc.* **2265** (2020) 030249.

4.1 Introduction

The thin-film deposition of metal nanoclusters with controlled shape and size on a wafer/substrate using gas aggregation process is one of the active research direction for years because of their importance in various applications [33, 65, 77, 137–139]. In the field of material science, silver nanoparticles are used in various applications e.g. plasmonic [34], catalytic [111], electronic [113], biomedical [140], solar cell [114] etc. Size-selected Ag-nanoclusters having cluster size ranging from 1 to 10 nm are useful in various biomedical applications [140]. The optical properties of silver nanoparticles with a specific size and shape are found to be very efficient in light trapping applications [141, 142]. Besides the technological applications, information on fundamentals of metal cluster deposition also is very pertinent to produce nanoparticles of desired size and shape. The morphology of a film surface determines various properties of the film and by tuning the morphology it is possible to change the surface properties. The understanding of growth of a thin-film on a particular surface is very important in order to tune its properties for a specific application. To understand a film surface the concept of scaling theory is very useful. Statistical characterization of some of the parameters related to scaling theory is carried out to have an insight of the film surface. Some of these statistical parameters are interface width or rms roughness of a surface, roughness exponent, lateral correlation length, skewness and kurtosis of a surface, fractal dimension etc. These parameters are estimated under the framework of time independent scaling theory to verify whether a surface is mounded [143] or self-affine [144, 145]. The morphology of thin-films deposited by physical methods such as magnetron sputtering is often found to be self-affine in nature and conventionally follows fractal characteristics. The topographical complexities and randomness of a thin-film surface can be understood by analyzing one of the fractal parameters known as fractal dimensions (FDs) [104].

There are several methods to calculate the fractal characteristics of a surface and these are height-height correlation method, power spectral density method, box counting method, triangulation method etc. For last a few years, many researchers have studied the thin-film surface using fractal analysis method. Le *et al.* [146] estimated the surface energy of Co-based thin-film morphology as a function of fractal dimension using variation correlation function model. Raoufi [147] used box-counting method in order to analyze the fractal dimensions of as-deposited and thermally annealed indium tin oxide thin-films and he noticed that the fractal dimension of as-deposited films was significantly higher as compared to the annealed films. Dallaeva *et al.* [148] employed morphological envelop method to calculate the fractal dimensions of magnetron sputter-deposited aluminium nitride epilayers where they observed the enhancements of fractal dimension with the increase in substrate temperature. Arman *et al.* [149] analyzed the fractal dimensions of multilayer Cu thin-films using power spectral density and morphological envelop methods and found an enhancement of fractal dimension with the increase in film layers. Mwema *et al.* [150] also adapted the power spectral density method for the measurements of fractal dimensions of Al thin-film and found the variation of fractal dimensions with different substrates. Yadav *et al.* [151] analyzed the fractal dimension of rippled silicon surface using height-height correlation function and autocorrelation function methods. The ripples patterned on the Si surfaces are generated by bombarding with ion beams where the fractal dimension is found to be decreased with ion doses. By analyzing the fractal parameters of a surface many underlying surface properties can be understood as well as modified [152]; One of such properties is wettability property of a surface. Two of the surface parameters namely, topography and surface elements primarily influence the wettability property of any surface. By tuning these two parameters the wettability property of a surface can be modified. The wettability property of a surface can be measured in terms of contact angle measurements. Depending on the interaction between the water droplet and a surface, the surface can be categorized as hydrophilic or hydrophobic or super-hydrophobic surface. Different kinds of wettable surfaces have their own advantages and disadvantages from application perspective. Hydrophilic surfaces are used in biomedical, anti-fogging applications etc. Hydrophobic and super-hydrophobic surfaces can be used in different cleaning applications such as self-cleaning, anti-icing, anti-adhesion etc. [153–155].

4.2 Methodology

4.2.1 Time independent scaling theory

The growth phenomena of a thin-film surface can be completely understood by measuring some of the statistical parameters. An introductory explanations of such parameters are given below.

4.2.1.1 Root mean square roughness

The root mean square (rms) roughness or interface width is the fluctuation of surface height with reference to a mean surface height [123, 156] and related to the vertical properties of a film. The rms roughness may be expressed as,

$$< w >= \sqrt{\frac{1}{N_x N_y}} \sqrt{\sum_{i=1}^{N_x} \sum_{j=1}^{N_y} [h(x_i, y_j) - < h(x_i, y_j) >]^2} \tag{4.1}$$

where $h(x_i, y_j)$ indicates the height of the surface at the digitized coordinates (x_i, y_j) obtained from a two dimensional digitized surface i.e. from an AFM image. Here $N_x \times N_y$ represents the total number of pixels present on the digitized surface.

Also, $< h(x_i, y_j) >$, the average height of the surfaces may be written as,

$$< h(x_i, y_j) >= \sqrt{\frac{1}{N_x N_y} \sum_{i=1}^{N_x} \sum_{j=1}^{N_y} h(x_i . y_j)} \tag{4.2}$$

4.2.1.2 Autocorrelation Function

The interface width of a surface is only used for the information of global height of a surface and interface but it fails to provide information about the correlation of surface height. In that case another important statistical function known as autocorrelation function, $R(r)$ has been introduced. It is used to measure the correlation of two random heights on a surface [123, 156]. If the vector distance between two random points is $\vec{r}$ and the scanning is performed along the x direction of the surface, then it can be defined as,

$$R(r) = R(ml) = \frac{1}{N_y (N_x - m) < w >^2} \sum_{j=1}^{N_y} \sum_{i=1}^{N_x - m} h(x_i + m, y_j) h(x_i, y_j) \tag{4.3}$$

where l is the lateral distance between two adjacent discrete points and m is the total number of digitized points that are being used for the calculations.

If the lateral distance is zero i.e. $l = 0$, then using equations 4.1 and 4.3 we get $R(r) = R(0) = 1$. For a surface with self-affine nature, the autocorrelation function exponentially decreases with the increasing distance r. Although it shows oscillatory behaviour with increased r for a mounded surface [151], the lateral correlation length (ξ) of any surface can be calculated using this autocorrelation function. The equivalent value of r at which the autocorrelation function $R(r)$ decreased to $\frac{1}{e}$ times of its original value is called lateral correlation length [156] and may be expressed as,

$$R(\xi) = \frac{1}{e} \tag{4.4}$$

The surface height between two random points cannot be correlated beyond the lateral correlation length.

4.2.1.3 Height-height correlation function

The height-height correlation function, $G(r)$ can be determined along the fast scan axis, x using the following relation [157],

$$G(r) = G(ml) = \frac{1}{N_y(N_x - m)} \sum_{j=1}^{N_y} \sum_{i=1}^{N_x - m} [h(x_i + m, y_j) - h(x_i, y_j)]^2 \tag{4.5}$$

Similar to autocorrelation function, HHCF is another function that can be used to determine the surface anisotropic nature i.e. self-affine or mounded surface. For self-affine surface $G(r)$ behaves as,

$$G(r) \propto \begin{cases} r^{2\alpha} & if \quad r \ll \xi \\ 2w^2 & if \quad r \gg \xi \end{cases} \tag{4.6}$$

4.2.1.4 Power Spectral Density function

The power spectral density (PSD) function of a surface signifies the Fourier transform of autocorrelation function in reciprocal space. It can be written as,

$$P(k) = \frac{< w >^2}{2\pi} \int_0^\infty R(r) e^{ikr} \, dr \tag{4.7}$$

where k denotes the spatial frequency that varies between $1/L < k < N/2L$ for an $L \times L$ system.

According to the scaling theory, the relation between power spectral density and spatial frequency k is found as,

$$P(k) \propto k^{-\sigma} \tag{4.8}$$

where σ is called power law exponent. The relation between the Hurst exponent and power law exponent of a surface can be written as [156],

$$\sigma = d + 2\alpha \tag{4.9}$$

Here d is known as Euclidean dimension and for a 2D surface its value is found to be 2. So, using equation 4.9, we can derive the Hurst exponent of a surface as,

$$\alpha = \sigma/2 - 1 \tag{4.10}$$

4.2.1.5 Fractal Dimension

The concept of fractal dimension of a surface signifies the volume that have been occupied by the fractal object in a three dimensional surface topography. In case of a self-affine surface, the fractal dimension of the surface is directly related to the Hurst exponent value of that surface and the value of fractal dimension for most of the surfaces has been lying between 2 and 3. For a minimum value of fractal dimension the surface can be considered as locally smooth whereas its maximum value suggest a locally jagged surface where the fractal object is presumed to be occupied all the available volume in that surface. In case of self-affine surface, the fractal dimension,

D_f is calculated either from the Hurst exponent or the power law exponent [156,158]. Mathematically the relation can be written as,

$$D_f = d + 1 - \alpha \tag{4.11}$$

Hence, the fractal dimension for a surface with an unit Hurst exponent value will be equal to Euclidean dimension of that surface. Again the relation between the fractal dimension and power law exponent can be derived as,

$$D_f = 4 - \sigma/2 \tag{4.12}$$

From equation 4.11 & 4.12, it is clear that the values of α and σ must be decreased for the enhancement of fractal dimension.

4.2.1.6 Skewness and Kurtosis

The 3^{rd} and 4^{th} order of moment can be written in terms of skewness and kurtosis [123]. The skewness and kurtosis can be determined using the following equations,

$$< S >= \frac{1}{< w >^3}\sqrt{\frac{1}{N_x N_y}\sum_{i=1}^{N_x}\sum_{j=1}^{N_y}[h(x_i, y_j)- < h(x_i, y_j) >]^3} \tag{4.13}$$

and

$$< K >= \frac{1}{< w >^4}\sqrt{\frac{1}{N_x N_y}\sum_{i=1}^{N_x}\sum_{j=1}^{N_y}[h(x_i, y_j)- < h(x_i, y_j) >]^4} \tag{4.14}$$

The skewness is defined as the measure of the distribution symmetry with reference to a mean surface height and a dimensionless quantity. The skewness lies between positive to negative value. A positive value of skewness indicates an

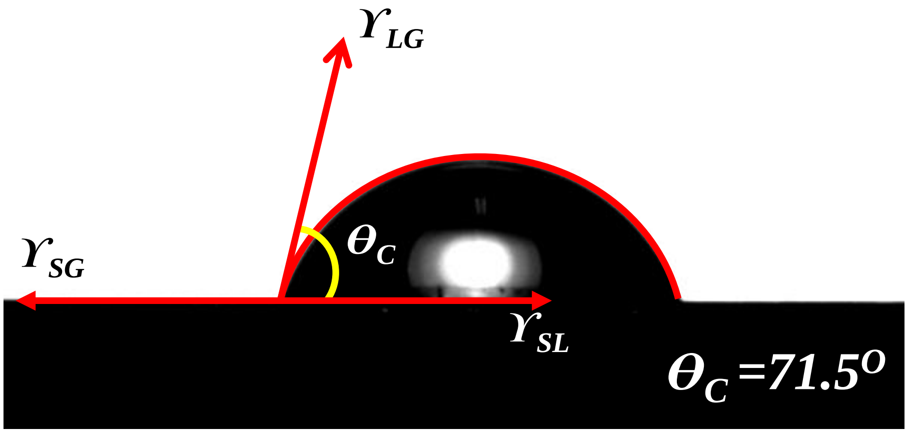

Figure. 4.1: *A snapshot of a water droplet deposited on pristine silicon surface showing schematically the various energies acted on the droplet.*

asymmetric distribution where its asymmetric tail expands towards more positive height as compared to its mean height. A negative value of skewness suggests a distribution where the tail is expanding towards more negative height as compared to its mean height. For a pure Gaussian like symmetric distribution, the skewness value is zero.

The kurtosis is defined as the sharpness of the height distribution function. The kurtosis value represents the randomness of the surface profile with reference to a perfectly random surface. The kurtosis value is 3 for a perfectly random surface with Gaussian height distribution. For $K < 3$, the distribution is exaggerated with the appearance of a mild peak and the distribution is called platykurtic. For $K > 3$, the distribution shrinks with the appearance of a sharp peak and is known as leptokurtic.

With these fundamental mathematical parameters, the experimental results are explained to unfold the mechanism of surface growth.

4.2.2 Contact angle theory

The wettability property of a solid surface can be known by measuring the angle formed between a liquid droplet and the surface. It is called contact angle and represented by θ_C. Depending on the value of contact angle, a surface is considered as hydrophilic surface when $\theta_C < 90^o$ and hydrophobic surface when $\theta_C > 90^o$. The contact angle value depends on many factors on the surface such as, surface composition, surface roughness, the size and shape of the particles present on the surface etc. In 1805, Thomas Young developed a model [159] according to which the contact angle formed by a liquid directly depends on different energies like solid-liquid interface energy ($\gamma_{_{SL}}$), solid-gas interface energy ($\gamma_{_{SG}}$) and surface tension of the liquid ($\gamma_{_{LG}}$). A snapshot of a liquid droplet deposited on a pristine silicon surface showing the various energies acting on the droplet is depicted in figure 4.1. If θ_Y is Young's contact angle, at the equilibrium condition,

$$\gamma_{_{SG}} = \gamma_{_{SL}} + \gamma_{_{LG}} cos\theta_Y \tag{4.15}$$

Therefore,

$$cos\theta_Y = \frac{\gamma_{_{SG}} - \gamma_{_{SL}}}{\gamma_{_{LG}}} \tag{4.16}$$

Young's model can be used only for an ideal surface in which the surface should be non-reacting, homogeneous and atomically flat. Failed to qualify the above criteria the wettability property of a surface cannot be explained by Young's model. In case of a rough surface the obtained contact angle (CA) values would be different from a flat surface of the same material. In 1936, Wenzel suggested a model [160] for a rough surface where the liquid droplet was considered to be larger than the surface roughness and all the grooves, cavities or scratches of the surface would be filled with liquids. He modified Young's equation by introducing a roughness co-efficient term R_f. If θ_W is the Wenzel's contact angle for a rough surface, the Wenzel equation can be written as,

$$cos\theta_W = R_f \times \frac{\gamma_{SG} - \gamma_{SL}}{\gamma_{LG}} \tag{4.17}$$

or

$$cos\theta_W = R_f \times cos\theta_Y \tag{4.18}$$

The roughness co-efficient (R_f) denotes the ratio of total geometrical area to the overall projected area of the rough surface. From the Wenzel's modified equation, we can draw the following conclusions: (i) initially if the surface is hydrophilic in nature i.e., $\theta_Y < 90^o$, θ_W will decrease with the increase in R_f; (ii) if the surface is initially hydrophobic in nature i.e., $\theta_Y > 90^o$, then the value of Wenzel's contact angle will increase with the increase in R_f values.

If the rough surface does not follow the condition set by Wenzel's model and the grooves and cavities of the rough surface are partially or completely filled with air instead of liquid droplet, this type of rough surface cannot be explained by the Wenzel's theory. Hence, a new model came into play known as Cassie-Baxter's model [161]. We consider f_s is the fraction of solid surface area and f_g is the area filled with air and in contact with the liquid droplet. The equation 4.15 can be written for a Cassie Baxter surface as,

$$f_s\gamma_{SL} + f_g\gamma_{LG} + \gamma_{LG}cos\theta_{CB} = f_s\gamma_{SG}$$

$$f_s\gamma_{_{SL}} + f_g\gamma_{LG} + \gamma_{_{LG}}cos\theta_{CB} = f_s(\gamma_{_{SL}} + \gamma_{_{LG}}cos\theta_Y)$$

$$f_g\gamma_{LG} + \gamma_{_{LG}}cos\theta_{CB} = f_s\gamma_{_{LG}}cos\theta_Y$$

$$cos\theta_{CB} = f_scos\theta_Y - f_g \tag{4.19}$$

Again, $f_s + f_g = 1$, therefore equation 4.19 will be,

$$cos\theta_{CB} = f_scos\theta_Y - (1 - f_s)$$

Finally,

$$cos\theta_{CB} = -1 + f_s(1 + cos\theta_Y) \tag{4.20}$$

where θ_{CB} is contact angle formed for a Cassi-Baxter surface.

4.3 Scaling aspects of Ag-nanocluster films

4.3.1 Experimental details

Ag cluster beam were produced inside the gas aggregation-type magnetron sputter nanocluster source. The produced beam was then passed through a quadrupole mass filter in order to produced a size-selected cluster beam. In the present experiment, three kinds of size-selected cluster beams with cluster diameters $\sim$ 4, 5 and 6 nm, respectively were prepared and deposited on Si(100) substrates. Generally, a cluster mass can be calculated in terms of its diameter using the equation, $m = \pi\rho d^3/6$ [4], where $d = 2r$ is the diameter of the cluster and ρ is the density of the material. The number of atoms constituting the cluster with radius r can be written as $n = (r/r_w)^3$, where r_w is the Wigner-Seitz radius and for silver, its value is $r_w = 0.166$ nm [44]. Considering the equation, the number of atoms present on clusters of diameters 4, 5 and 6 nm are found to be $\sim$ 1750, 3416 and 5903, respectively. The size-selected beams were deposited on ultrasonically cleaned silicon substrates for 7 min. Before the deposition, the pressure in the main deposition chamber and magnetron chamber were recorded as 2.0×10^{-9} and $> \ 5.0 \times 10^{-4}$ mbar. During the deposition, the pressure of these two chamber was $\sim 4.1 \times 10^{-4}$ and 2.1×10^{-1} mbar, respectively. The topography of the deposited films were investigated by atomic force microscopy in tapping mode probed by a Si tip with a nominal radius of curvature of $\sim$ 8 nm and the measured data points per line is 512. The XPS analysis were performed using a hemispherical electron analyzer using an Mg-K$_\alpha$ source of photon energy of 1253.7 eV .

4.3.2 Results and discussions

Figure 4.2(a)-(c) show the size-distribution spectra of Ag-nanoclusters produced inside the aggregation chamber are recorded by the quadrupole mass filter (QMF). Utilizing these size distribution spectra, three size-selected beam of cluster diameter $\sim$ 4, 5 and 6 nm were selected by the QMF. The two dimensional AFM images of these films produced by the size-selected cluster beams are shown in figure 4.2(d)-(f). Preliminary observation of 2D AFM images says the areal density as well as coverage of the film increases as the cluster diameter increases from 4 to 6 nm. Moreover, formation of larger particles or cluster islands on the surface can be seen for large cluster diameter films.

To observe the vertical view of the deposited particles, the 3D AFM morphology of the same films are shown in figure 4.2(g)-(i). From the 3D surface morphology,

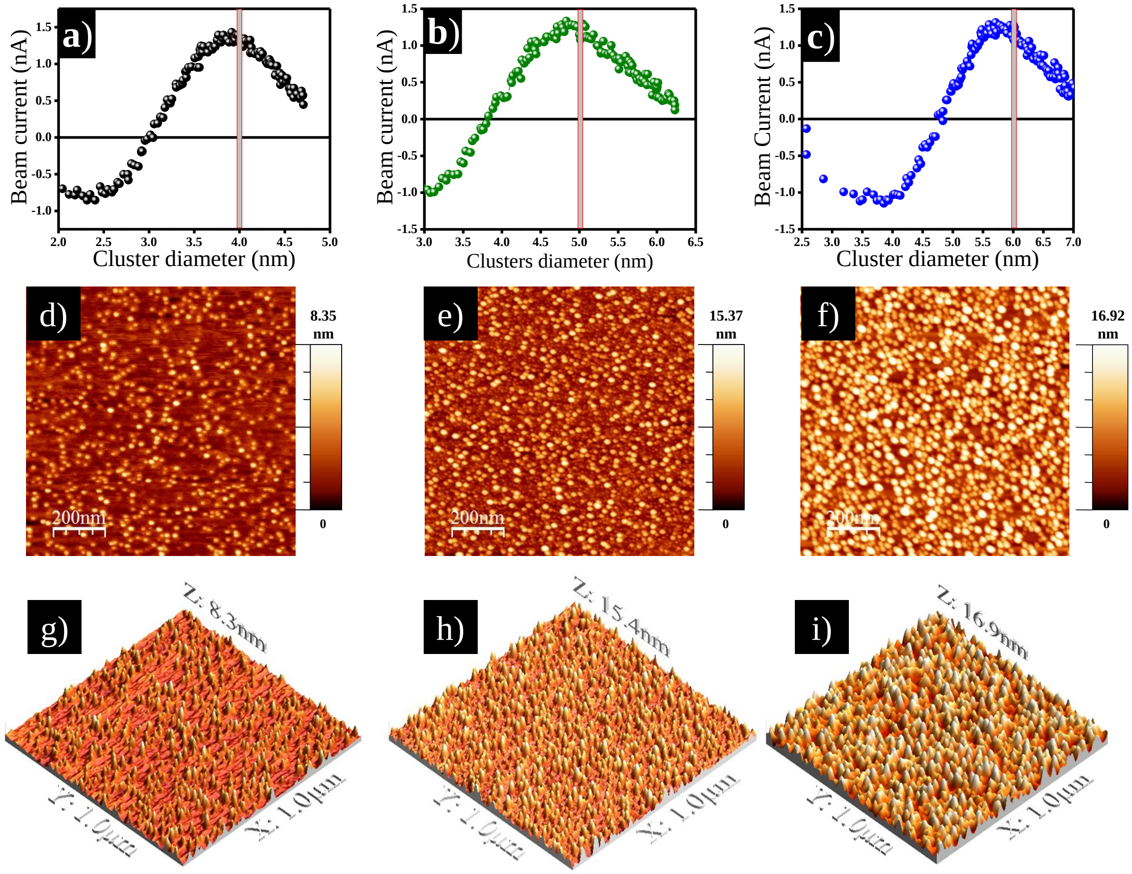

Figure. 4.2: *Size distribution spectra produced inside the cluster source to utilize these spectra to select a cluster beam with diameter (a) 4 nm (b) 5 nm and (c) 6 nm; The 2D AFM images with scan size* ($1\ \mu m \times 1\ \mu m$) *produced for cluster-deposited films of diameters (d) 4 nm (e) 5 nm and (f) 6 nm; 3D AFM micrographs of the films with cluster diameters (g) 4 nm (h) 5 nm and (i) 6 nm.*

formation of isolated small cluster aggregates on the surface of the films is observed for small cluster-sized (∼ 4 nm) film. The films produced by the clusters with 5 nm diameter shows formation of two types particle variations over the substrate with slightly increased coverage as compared to the previous film. Finally, for the film of cluster diameter of ∼ 6 nm, the surface mostly covers with large-sized cluster aggregates with a higher coverage as compared to previous two morphologies.

The lateral size of the cluster aggregates formed on the surface having dimensions well below the nominal tip diameter cannot give the precise size due to the

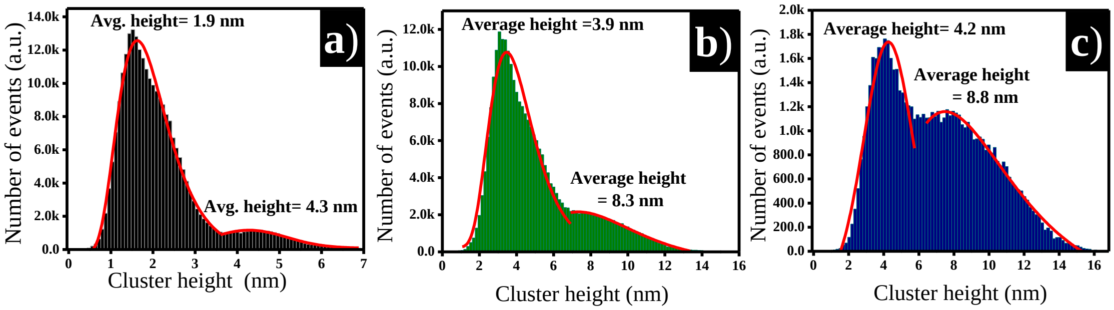

Figure. 4.3: *Height distribution spectra of cluster films with a cluster diameter of (a) 4 nm, (b) 5 nm and (c) 6 nm. All the distributions are fitted with log-normal function where the red solid line indicates the fitted curves.*

AFM tip convolution effect whereas no such problem occurred during the estimation of height of the cluster aggregates by the AFM. Measured height distribution spectra of all the films are illustrated in figure 4.3(a)-(c). In all cases the height distributions show two types of variations where the first maxima appears at a smaller value as compared to the selected cluster diameter while the second maxima appeared at a higher value than the selected diameter. The smaller maxima represents the height of the fragmented clusters on the substrate. In dealing with the formation of metal nanoclusters and their deposition, the cluster is often compared with the liquid droplets [162]. A stable structure formed on the substrate depends on the process of aggregation [156] or fragmentation [64] of deposited clusters over the substrate. The process of aggregation and fragmentation of clusters are dependent on the type of interactions occurred among the droplets and/or between the substrate and droplet. Hence, the higher maxima appeared in the height distribution spectra in figure 4.3 is due to aggregation of several clusters. The deposited clusters are mobile over the surface due to the interactions among the clusters and substrate. Considering the height distribution spectra, the height asymmetry of the surfaces can be found out by measuring the surface skewness (S) and kurtosis (K). The characteristics of the expansion height distribution and the sharpness of distribution of any surface are

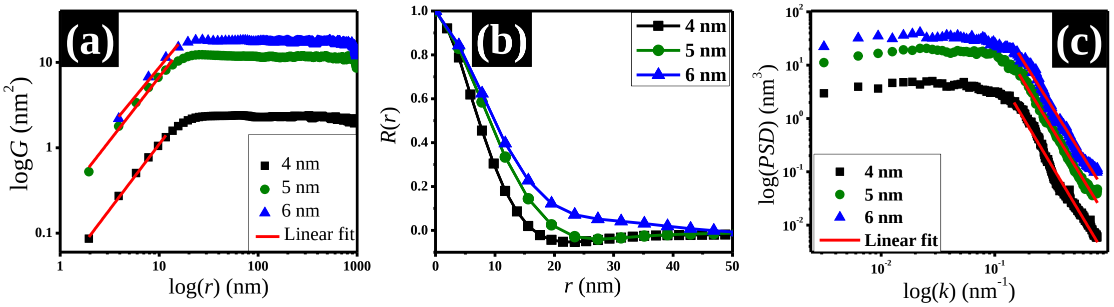

Figure. 4.4: *(a) Bi-logarithmic plot of HHCF vs scanning length, r. The red solid line indicates the linear fitting for the measurements of α; (b) Variation of normalized autocorrelation function, $R(r)$ with scanning length r; (c) log-log plot of PSD function versus spatial frequency, k. The higher region of the curve is best fitted with linear function for the estimation of δ as indicated by the red solid line.*

measured in terms of the surface kurtosis. The measured values of surface skewness and kurtosis for all the films are presented in Table 4.1. The skewness values of the surfaces are found to be decreased as the depositing diameter of the clusters increases. The kurtosis value changes from positive to negative as the size of deposited clusters increases. Therefore, it can be concluded from the combined values of surface skewness and kurtosis that the height distributions approach towards symmetrical distribution with small domination of valleys as the depositing cluster size changes from smaller to its larger value.

Figure 4.4(a) shows the logarithmic variation of height-height correlation function, $G(r)$ with the scanning length, r for all the films. All the curves show two kinds of variation with r. For smaller values of r, the HHCF curve increases linearly that gives the value of local roughness exponent (α). For higher values of r, the HHCF curves saturate. The local roughness exponent developed for the films by clusters of diameters of 4, 5 and 6 nm are 0.77, 0.74 and 0.71, respectively. The interface width of the films is measured from the saturation region of HHCF curve and is summarized in Table 4.1. The estimated roughness of the films is found to be increased with the increase in diameter of deposited cluster due to the vertical growth of the films. The same can also be observed from the 3D AFM morphology of the films presented in figure 4.2(g)-(i). Moreover, an upward shifts in HHCF curves are observed with the increase in diameter of the depositing clusters.

Figure 4.4(b) shows a variation of normalized autocorrelation function with the scanning length r for all the films. An exponential decrease in all the ACF curves with an increase in r confirms the self-affinity nature of the deposited films. The value of r at which the ACF decreased to $\frac{1}{e}$ times of its initial value is termed as lateral correlation length (ξ). The estimated values of lateral correlation length of the films containing depositing cluster size of 4, 5 and 6 nm are found to be 9.2, 11.2 and 12.4 nm, respectively. An increase in lateral correlation length suggests an increased correlation between two random heights of the films. In order to measure the surface complexity, the fractal dimension of each of the films is calculated using power spectral density method. Figure 4.4(c) shows the logarithmic plot of power spectral density function with spatial frequency. All the curves show two kinds of variation by creating two regions. In the first region, the PSD function curves gets saturated with k whereas in the second region the PSD function curve linearly decreases with the increased value of k. This power law behaviour in PSD curve for higher k value reveals the presence of fractal nature on the surface. The slope of linear portion of the PSD function curve gives the power law exponent (δ) using which the fractal dimension (D_f) of the films can be estimated. The estimated values of fractal dimension of the films are shown in Table 4.1. The D_F of the films is found to increase as the size of the depositing cluster increases. Generally, a higher value of fractal dimension indicates a complex surface as compared to the lower one. In the present case, the computed fractal dimension values are close to the previously measured values for cluster assembled films [162]. The Hurst exponent values of the films can also be measured using the equation 4.10 by utilizing the value of power law exponent. If

Table 4.1: Morphological parameters of cluster-deposited films.

Selected cluster diameter	**Interface width** $< w >$ **(nm)**	**Correlation length** ξ **(nm)**	**Hurst exponent** α	**Fractal dimension** D_f	**Skew.** S	**Kurt.** K
4nm	1.08	8.9	0.78	2.22	1.72	3.3
5nm	2.41	11.2	0.75	2.25	1.21	0.874
6nm	3.04	12.40	0.70	2.30	0.471	-0.583

we compare the Hurst exponent values obtained by the PSD and HHCF methods, a similar value can be observed. The obtained Hurst exponent values are found to decrease with the increase in depositing cluster size and the values are listed in Table 4.1. A decreased value of Hurst exponent indicates the formation of locally jagged surface found to be porous structures made by the larger cluster aggregates in the present case.

Summarizing the above results, it is found that isolated small cluster aggregates are formed for clusters of 4 nm diameter whereas smaller and larger cluster aggregates are formed over the surface for 5 nm-sized clusters. For clusters of 6 nm diameter, mostly larger cluster aggregates are formed with an average height of 8.8 nm. Hence, it can be inferred that the size of the depositing clusters certainly influence the topography of the films and their various morphological parameters. Because with the increased cluster size their corresponding masses also increase and as a result, evolution of the morphology occurs for the large-sized clusters than that of small-sized clusters. Further, this depends on the soft landing deposition technique where it is considered that the size and shape of a depositing cluster will remain same even after the landing on a surface [64]. This kind of evolved film morphology enhances the fluctuation of corresponding surface height and as a consequence, an increase in interface width and correlation length of the films are observed.

Figure 4.5(a) shows the XPS survey spectra for all the deposited films. In the survey spectra different peaks and their intensities are appeared as a function of

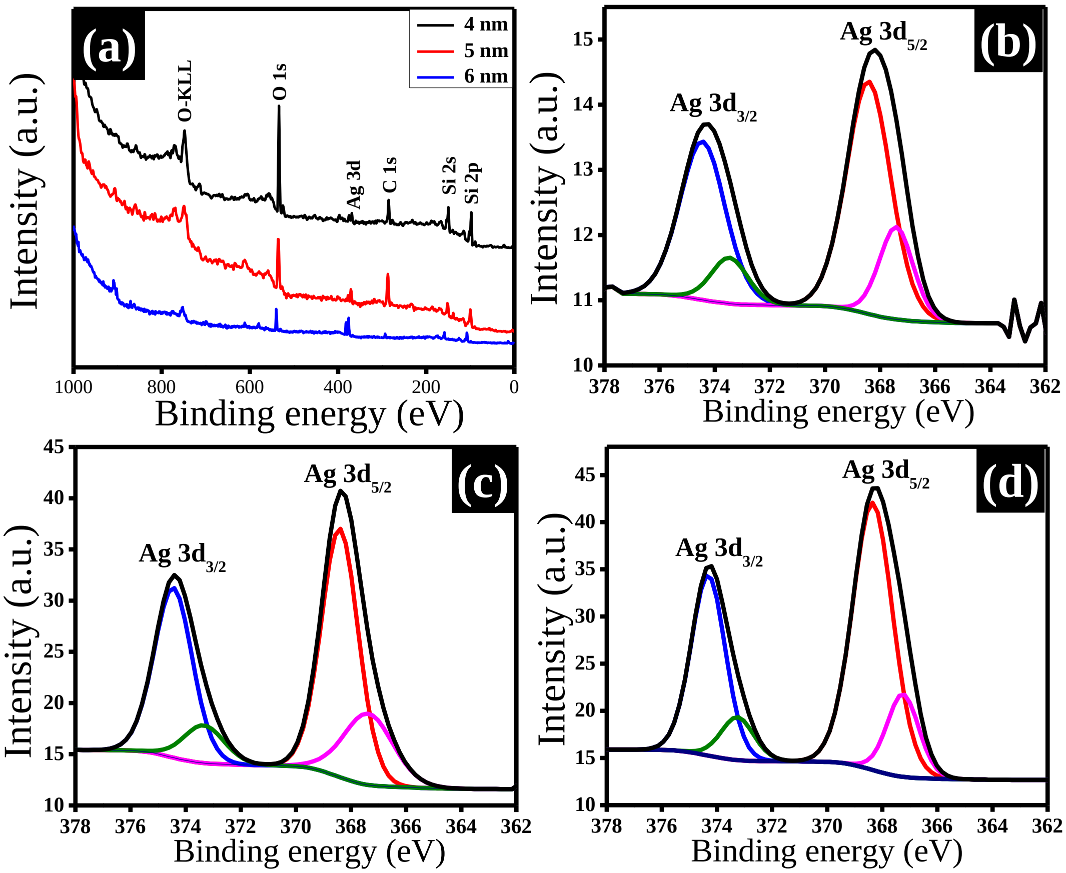

Figure. 4.5: *(a) XPS survey spectra of all the films. HR-XPS spectra of core level Ag 3d for the films having cluster diameters of (b) 4 nm (c) 5 nm and (d) 6 nm.*

binding energies. The peaks are Si $2P_{3/2}$ (BE = 99.1 eV), Si 2s (BE = 150.5 eV), C 1s (BE = 284.3 eV), Ag 3d (BE = 368.1 & 374.1 eV), O 1s (BE = 531.2 eV), Ag $3p_{3/2}$ (BE = 573 eV) and Ag $3p_{1/2}$ (BE = 604.1 eV). Auger peak of O-KLL is also found to be appeared in the survey spectra.

For analyzing different chemical states, high-resolution XPS (HR-XPS) scan have been performed for Ag 3d core-level spectra. Figure 4.5(b)-(d) shows the deconvoluted Ag 3d core level spectra of the films having cluster diameters of 4, 5 and 6 nm, respectively. All the Ag 3d peaks are deconvoluted into four peaks out of which two are metallic silver and other two peaks indicate oxidized silver. The peak positions of metallic silver are found at 368.1 and 374.1 eV attributing to Ag $3d_{5/2}$ and

Ag $3d_{3/2}$, respectively. The deconvoluted peaks appeared at binding energies of 367.2 and 373.2 eV signifies silver ions of Ag_2O. The silver oxide peaks are appeared due to the exposure of the samples to ambient prior to the XPS measurements. Another possible reason is pre-absorbed oxygen layer in the form of native oxides present on the Si surface. In case of metal, usually positive binding energy shift is observed in its core-level spectra when it gets oxidized and the positive BE shift increases with the increase of metallic oxidation states. The electronegativity differences between the metal atom and the cation are generally used to explain the positive BE shifts between metal oxides and metal. Since the cation's valence region has a lower electron density than the metal atoms, the core-hole screening of core level electrons from the nucleus is reduced. As a consequence, the unscreened core electrons of the oxides have higher BEs than that of the metal. But in case of silver oxide, the BE shift is found to be opposite as compared to conventional metal oxides (e.g. TiO_2). It is because, the BE shift of silver oxide is affected by various other factors like extra-atomic relaxation energy, work function changes and lattice potential apart from the electronegative differences between the Ag metal and its corresponding oxide [163]. Furthermore, with the evolved surface morphology, the intensity of the peak increases.

4.3.3 Conclusion

In the conclusion, the cluster films prepared by depositing size-selected Ag-nanoclusters are studied by the AFM technique. The size of the depositing clusters has made a significant impact on the surface morphology of the deposited films and their surface parameters. Various surface parameters associated with the films are determined upon analysing different scaling functions. Finally, chemical analysis of the films by XPS technique reveals that all the films contain metallic silver with a trace amount of silver oxide.

4.4 Wettability transition on fractal surface

4.4.1 Experimental details

Size-selected Ag-nanoclusters of diameter $\sim$ 4 nm (number of atoms per cluster = 1750) were deposited on ultrasonically cleaned Si(100) substrates by soft-landing method. A series of samples were prepared by varying the intensity of the size-selected cluster beam. In order to achieve different beam intensity or beam current, a number of system parameters were tuned. Depositions were carried out at ion currents ranges between 0.5 ± 0.1 to 1.5 ± 0.1 nA and the deposition time was kept constant at 15 min. Prior to the experiment, the base pressures of main deposition chamber and magnetron chamber were $\sim 2.0 \times 10^{-9}$ and $< 5.0 \times 10^{-4}$ mbar. For convenience, the films prepared at ion currents of 0.5, 0.7, 0.9, 1.1, 1.3 and 1.5 nA are labeled as $\#A1$, $\#A2$, $\#A3$, $\#A4$, $\#A5$ and $\#A6$, respectively. The surface morphology of the deposited films was characterized by FESEM and AFM in tapping mode with a silicon tip of nominal radius of curvature $\sim$ 8 nm. Further, the chemical composition of the films are investigated by the XPS with Mg K_α source of photon energy 1253.7 eV. The XPS spectra were obtained at a operating voltage of 9 kV and current of 18 mA using a pass energy of 20 eV. For the measurements of contact angle, sessile drop method is employed using a standard contact angle goniometer. In the measurement process, a 4 μl volume deionized water is placed on different positions of the surface and average of all the contact angle values are measured to minimize the error.

4.4.2 Results and discussions

4.4.2.1 Size-distribution spectra

Figure 4.6 shows the size distribution spectra of nanoclusters produced in the nanocluster source. All the spectra were recorded by the QMF for various system parameters and size-selected beam of $\sim$ 4 nm diameter were extracted for deposition. The selected diameter is indicated by a gray rectangle in the figure and the higher beam current in the selected region is observed gradually from figures 4.6(a) to 4.6(f). The measured ion currents from figures 4.6(a) to 4.6(f) are found to be 0.5 ± 0.1, 0.7 ± 0.1, 0.9 ± 0.1, 1.1 ± 0.1, 1.3 ± 0.1 and 1.5 ± 0.1 nA. The parameters set to get spectra for clusters of a specific size were utilized to get 4 nm-diameter clusters for the deposition purpose. It is found that the ion current for the selected diameter does not fluctuate much from its original value throughout the experiment. Furthermore, the size-distribution spectra are found to vary from negative to positive ion current. These spectra represent the sum of both negative and positive ion currents provided by various-sized clusters. In the present case, the positive ion current is contributed by mostly negatively charged clusters.

4.4.2.2 Surface morphology of cluster deposited films

Figure 4.7 shows the films prepared by size-selected Ag-nanoclusters by varying the average beam currents. The SEM images are shown in the inset of the corresponding images. All the films shown here were deposited by low energy cluster impact process as no external biased was applied to the substrates. The lateral sizes of deposited cluster aggregates were measured for each of the films from the corresponding SEM images and plotted in the form of histogram as shown in figure 4.8. The average size of the deposited cluster aggregates can be determined using the

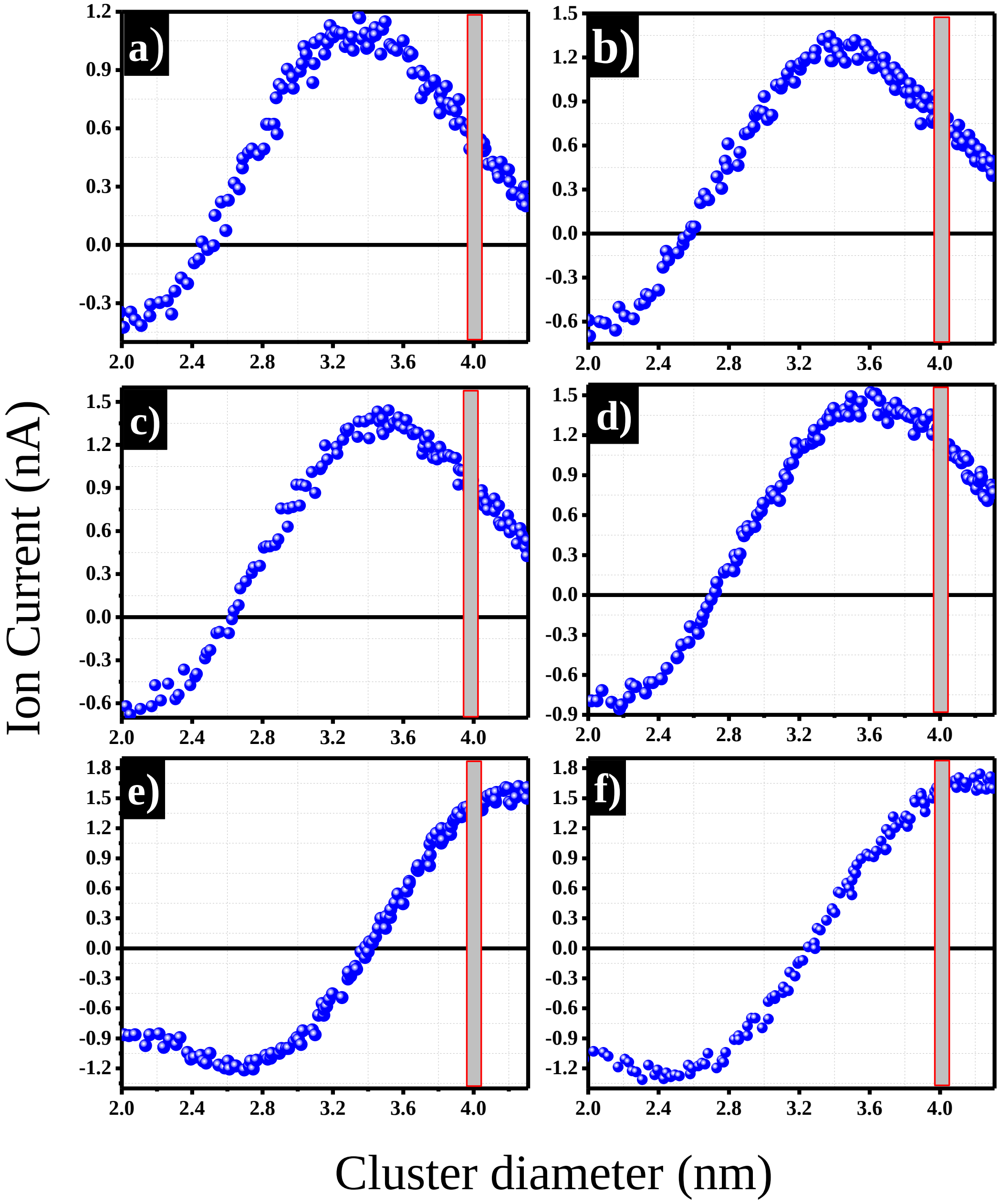

Figure. 4.6: *Size-distribution spectra recorded during the formation of nanoclusters of Ag in the nanocluster source and the corresponding ion current intensity obtained for a selected diameter of* ~ 4 *nm are (a)* 0.5 ± 0.1 *nA, (b)* 0.7 ± 0.1 *nA, (c)* 0.9 ± 0.1 *nA, (d)* 1.1 ± 0.1 *nA, (e)* 1.3 ± 0.1 *nA and (f)* 1.5 ± 0.1 *nA.*

histograms by fitting the distribution with log-normal function. Fragmentation of deposited nanocluster aggregates has occurred along with the larger clusters as evident from the SEM image in figure 4.7(a)-(d). From the size distribution histogram, bi-modal nature in sizes for the deposited clusters are found as evident from figure 4.8(a)-(d). In particular, for an ion current value of ∼ 0.5 nA, the average lateral size of the deposited cluster aggregates are found to be ∼ 6 and ∼ 15 nm as shown in figure 4.8(a). This kind of bi-modal behaviour in the size distribution histograms are consistently appeared for an average ion current upto 1.1 nA. Further, on perusal of the SEM images of the films deposited with ion currents of 0.5 and 0.7 nA, it is found that the shape of the smaller and larger cluster aggregates are circular with a homogeneous distribution over the substrate. With the increase in average ion current, the lateral size of the cluster aggregates increases and takes shape from circular to elliptical as observed in figure 4.7(c)-(d). When the deposition occurs for an average ion-current value higher than 1.1 nA, some irregular-shaped clusters aggregated and worm like structures are formed on the surface as shown in figure 4.7(e)-(f). These elongated worm-like shapes are formed due to the coalescence of two or more cluster aggregates. The lateral size of these cluster aggregates are measured considering an average size of the aggregates. The size distribution histograms are depicted in figure 4.8(e)-(f) where the distribution is mono-modal. The measured values of average cluster aggregates for an average ion current of 1.3 and 1.5 nA are found to be 34.5 and 41.6 nm, respectively. This kind of evolved morphology for cluster-deposited films were previously observed when the films underwent rapid thermal annealing process [164–166]. Moreover, the dewetting of thin-films due to subsequent thermal annealing causes similar morphology evolution [167].

From the above SEM images and their analyses, it can be inferred that the morphological evolution of the cluster-deposited films occurs as a function of average ion current. Initially, when the size-selected cluster beam is weak or the average ion current is low, the incoming nanoclusters moved towards the bare Si surface are randomly deposited over the substrate. These deposited clusters then move over the

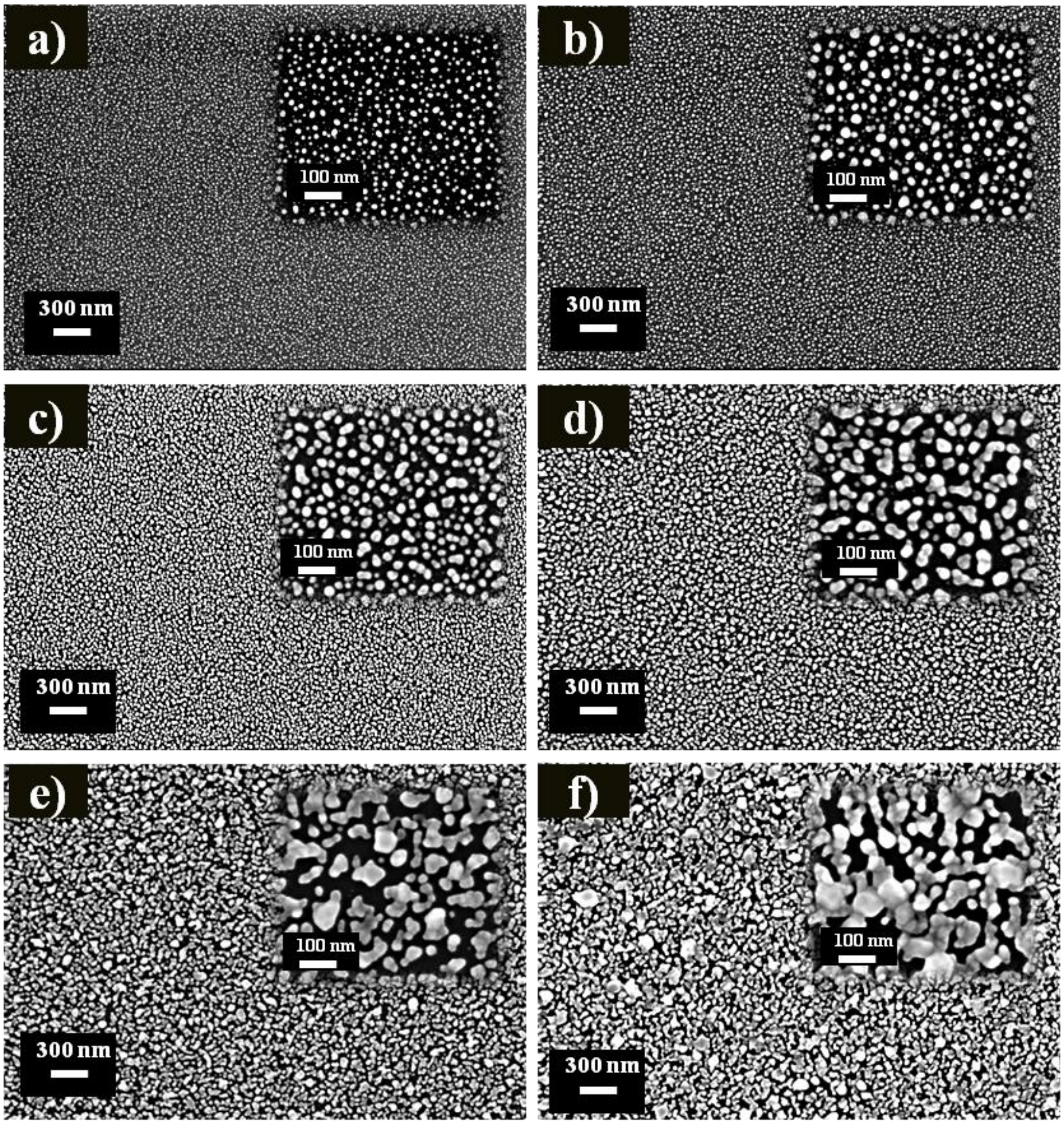

Figure. 4.7: *SEM micrograph of silver nanocluster aggregates for the samples (a) #A1, (b) #A2, (c) #A3, (d) #A4, (e) #A5, and (f) #A6. Magnified image of the same film is shown in the inset.*

substrate surface and get stabilized either by forming bonds with the neighboring clusters or with the substrate surface. Hence, these stabilized clusters act as nucleation sites for the upcoming clusters. The process involved in cluster deposition is often considered very similar to the liquid drop model where the produced and deposited clusters act as liquid droplets where a small droplet joins with the other

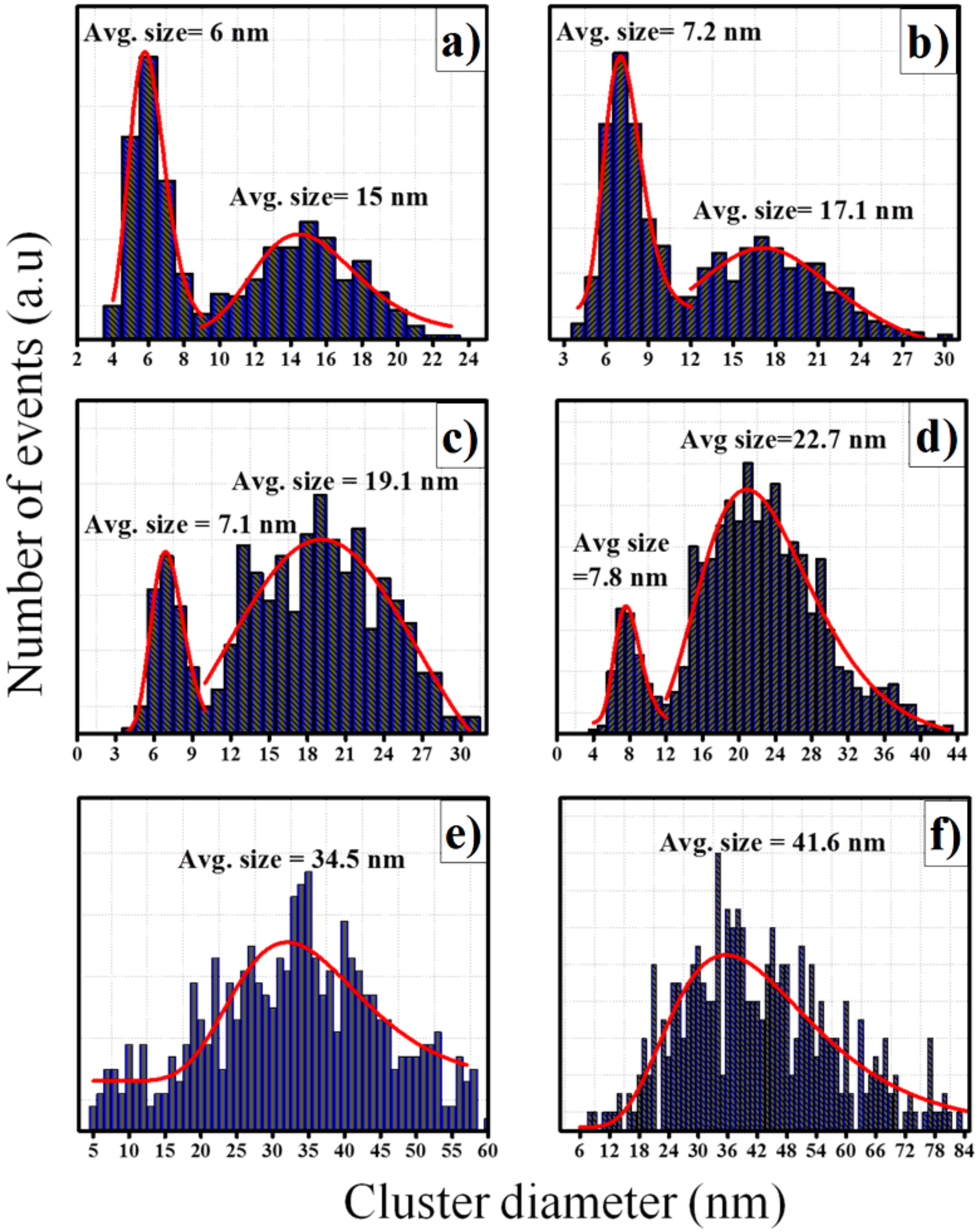

Figure. 4.8: *Size distribution histograms of silver nanocluster aggregate for the samples (a) #A1, (b) #A2, (c) #A3, (d) #A4, (e) #A5, (f) #A6.*

droplets and formed a larger droplet. In the present case, the evolution of the films occurs due to the joining of smaller clusters on the substrate. As a result, at lower ion current values two type of cluster size distributions can be seen. The lower average size is solely contributed by the as-deposited nanoclusters while the upper

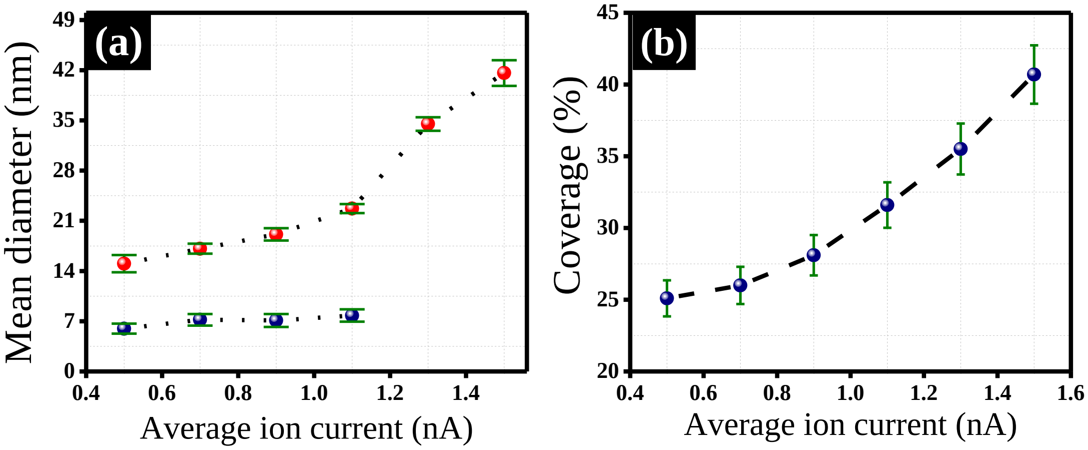

Figure. 4.9: *Variation of (a) average size of the cluster aggregates; (b) coverage of silver nanocluster-deposited films with average ion currents.*

mean size is contributed by the aggregates of smaller-sized clusters. When the beam current increases further the size of the aggregates on the surface increases as more smaller clusters join the already existed cluster aggregates. When the average ion current exceeds 1.1 nA, the contributions of the small-sized clusters on the films are negligible and mostly the larger cluster aggregates are formed with a mono-modal size distribution. In this case, the contributions by larger aggregates are more that consequently enhance the shape and size of the aggregates. In the process of morphological evolution of the films, the deposited cluster aggregates lose their regular shape and form irregular worm-like elongated shape. The variation of average cluster aggregate sizes as a function of average ion current is shown in figure 4.9 (a). Since the size distribution histogram shows two kinds of sizes upto an ion current of ∼ 1.1 nA, we observe two types of size variations. The first variation represents the smaller size contributed by the deposited small nanoclusters found to be almost constant with the increase in average ion current. The second variation is contributed by larger size of deposited cluster aggregates found to increase exponentially. The variation of percentage of coverage of the cluster-deposited films as function of average ion current is shown in figure 4.9(b). The coverage of the films increases exponentially with the increase in average ion current.

Figure 4.10 shows a typical three dimensional AFM micrographs of silver cluster-deposited films for different average ion currents. The evolution of the nanostructures can be seen with the increase in average ion current. Initially small cluster aggregates are formed that are evolved into mound-like structures for higher ion currents. The later features of the AFM morphology of the films are close to the morphology obtained in SEM images. Furthermore, from height distribution spectra it is found that the average heights of the deposited nanostructures increase from 8.2 to 40.2 nm with the increase in average ion current from 0.5 to 1.5 nA. Utilizing the AFM data, some of the important statistical surface parameters are determined under the frame work of time-independent scaling theory. The measured surface parameters are interface width, Hurst exponent, correlation length, fractal dimensions etc using which the surface characteristics of the deposited films are explained.

The rms roughness or interface width of the deposited films are calculated using the equation 4.1. Figure 4.11(a) shows a logarithmic variation of rms roughness of the films with the average ion currents. The obtained experimental data are fitted linearly and the slope is found to be 1.03 ± 0.13. The estimated slope provides a rough idea about the quick formation and growth of nanostructures with increasing average ion current. The correlation between surface height cannot be measured by the interface width where autocorrelation function plays an important role. The variation of normalized autocorrelation function, $R(r)$ with the scanning length r in log-log scale for all the films is shown in figure 4.11(b). Each of the variation decreases exponentially with the increase in r. The exponential behaviour in the variation of autocorrelation function suggests the self-affine nature of the films. Using equation 4.4, the lateral correlation length (ξ) of each of the films is determined and listed in

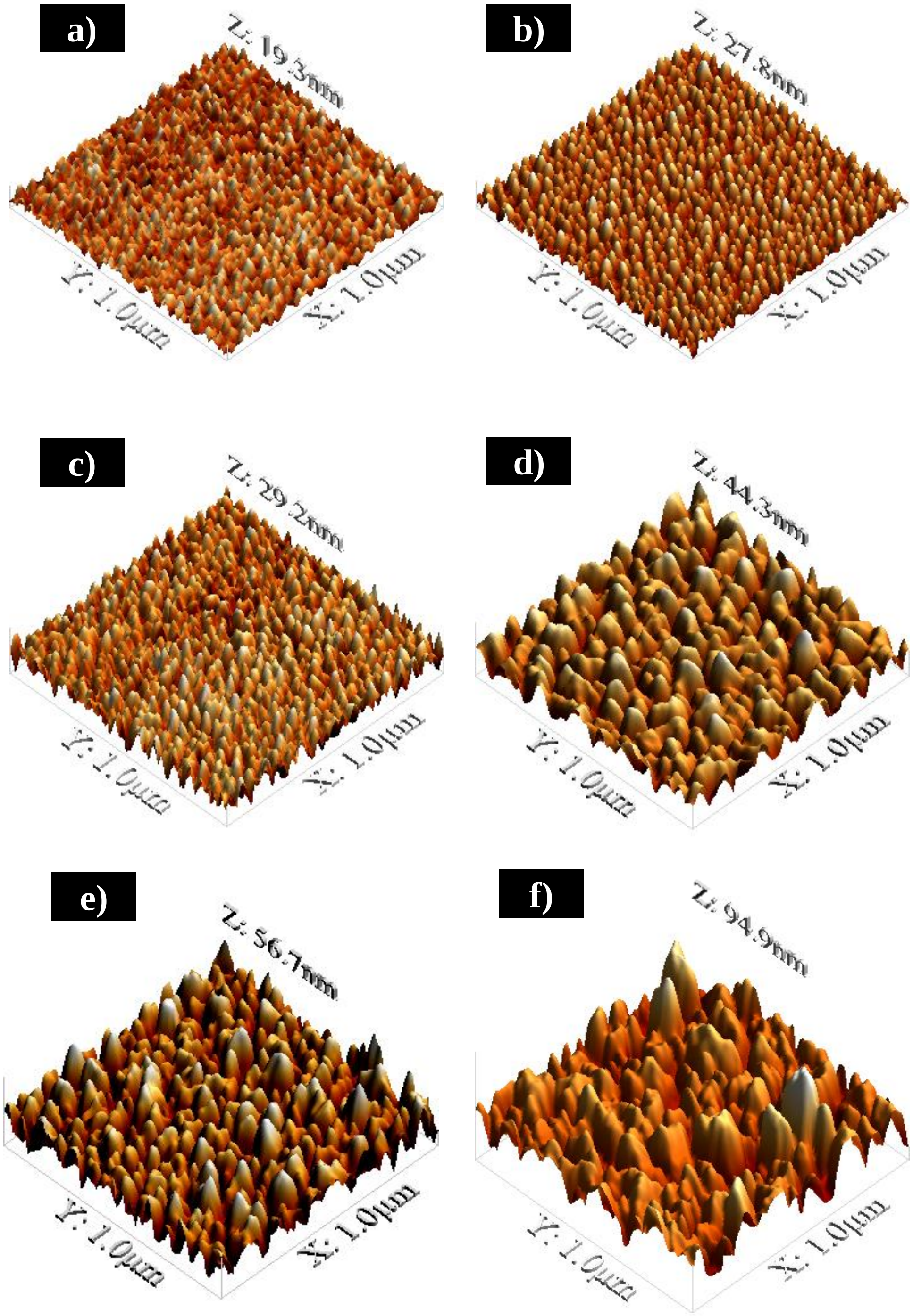

Figure. 4.10: *The 3D AFM morphology of silver nanocluster aggregates for the sample (a) #A1, (b) #A2, (c) #A3, (d) #A4, (e) #A5 and (f) #A6.*

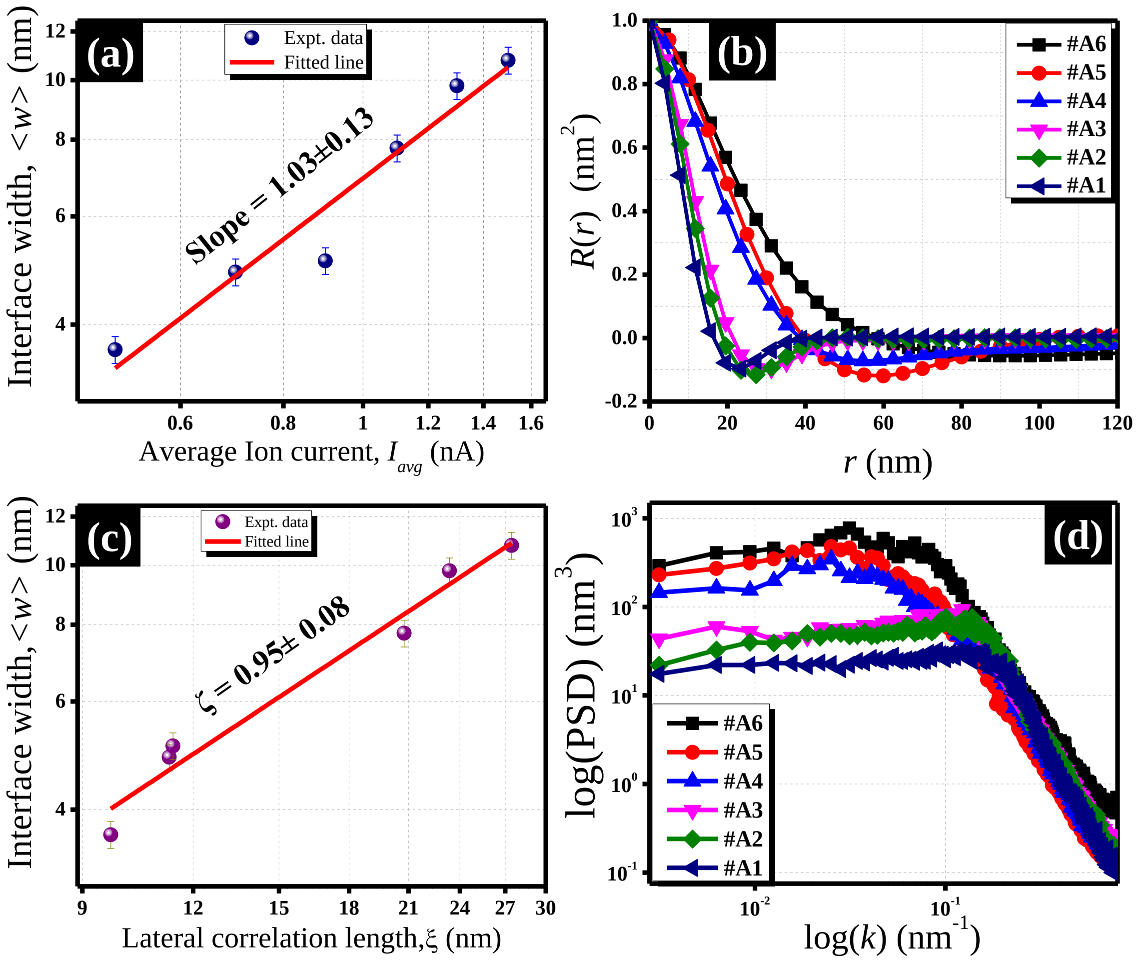

Figure. 4.11: *(a) Logarithmic variation of interface width of the films as a function of average ion current; (b) Variation of normalized autocorrelation function with scanning length; (c) log-log variation of interface width vs lateral correlation length; (d) Power spectral density function variation of the films.*

Table 4.2. It is evident from the table that as the average ion current increases the value of ξ obtained for the films increases gradually from 9.76 to 27.61 nm. It indicates that the correlation in surface height of the deposited nanostructures increases with ion current.

Further investigation of the films is carried out by measuring the global roughness exponent (ζ). The global roughness exponent is ascertained by plotting the interface width of each film surface against their obtained lateral correlation length.

Figure 4.11(c) shows the logarithmic plot where the obtained experimental values are fitted linearly and the corresponding slope is defined as the global roughness exponent. In particular, the global roughness exponent indicates the vertical growth with respect to lateral growth of the films and can be estimated using the equation $w \sim \xi^{\zeta}$ [143]. In the present case, the obtained value of global roughness exponent is $\zeta = 0.96 \pm 0.08$, nearly equal to unity. Such a high value of ζ indicates vertical growth with average ion current in contrast to lateral growth of the cluster deposited films. Figure 4.11(d) shows the log-log plot of PSD function versus spatial frequency k. Initially for small k values, the PSD function is saturated for all the films but for its higher values the curve decreases linearly indicating a negative linear slope, defined as δ, that provides an in-depth information of the transport and growth mechanism of the film surface. The Hurst exponent and fractal dimension of each of the films may be estimated putting the corresponding values of δ using equations 4.10 and 4.12, respectively. The obtained values of Hurst exponent of the films are found as 0.93, 0.88, 0.69, 0.67, 0.625 and 0.54 for an average ion current of 0.5, 0.7, 0.9, 1.1, 1.3 and 1.5 nA, respectively. The Hurst exponent of any surface lies between 0 to 1, where 0 signify the formation of local rough surface whereas the unit value of Hurst exponent indicates a locally smooth surface. Hence, the obtained results of Hurst exponent suggest that there is a transition in roughness of the films from a locally smoother to the locally coarse surface as we go from lower to higher average ion current. This transition behaviour of the films also is supported by the graph illustrated as figure 4.11(a). In the PSD function curve, the power law behaviour for higher k values signifies the fractal nature of the films. The acquired fractal dimension of the films is found to be 2.07, 2.12, 2.31, 2.33, 2.375 and 2.46 for an average ion current of 0.5, 0.7, 0.9, 1.1, 1.3 and 1.5 nA, respectively. The measured fractal dimension of the films is found close to the previously reported fractal dimensional of cluster assemble films where the measurements are performed using deposition-diffusion- aggregation (DDA)

Table 4.2: Topographical parameters of the films extracted from corresponding AFM images and measured water contact angle values.

Sample name	**Ion current** I_{avg} **(nA)**	**Interface width** $< w >$ **(nm)**	**Correlation length** ξ **(nm)**	**Hurst exponent** α	**Fractal dimension** D_f	**Contact angle** θ_C
#A1	0.5	3.64	9.7	0.93	2.07	80.7^o
#A2	0.7	4.87	11.28	0.88	2.12	86.3^o
#A3	0.9	5.08	11.40	0.69	2.31	87.1^o
#A4	1.1	7.75	20.8	0.67	2.33	89.7^o
#A5	1.3	9.79	23.4	0.62	2.38	92.6^o
#A6	1.5	10.77	27.5	0.54	2.46	98.2^o

model [162, 164]. The obtained values of various surface parameters are summarized in Table 4.2.

4.4.2.3 XPS analyses

The elemental compositions of the films of size-selected Ag clusters are analysed by the XPS measurements. Figure 4.12(a) shows the XPS survey spectra of Ag-cluster-deposited films for average ion currents of 0.5, 0.9 and 1.5 nA. Each of the spectra shows the peaks of various elements present in the film. The peaks of various elements and their binding energies are: Si $2p_{3/2}$ at BE = 99.1 eV, Si 2s at BE = 150.5 eV, C 1s at BE = 284.3 eV, Ag 3d at BE = 368.1 eV & 374.1 eV, O 1s at BE = 531.2 eV, Ag $3p_{3/2}$ at BE = 573 eV and Ag $3p_{1/2}$ at BE = 604.1 eV. Besides the Ag 3d peaks, additional peaks of Ag $3p_{1/2}$ and Ag $3p_{3/2}$ indicate presence of metal silver in the deposited films. From the survey spectra, it can be seen that the intensities of Ag 3d and Ag 3p peaks increase whereas the intensities of Si and O peaks are found to be decreased with the increase in average ion currents. The film surface produced by depositing nanoclusters via gas aggregation method exhibits porous structure as clusters are initially randomly deposited over the surface and coverage of the nanostructures increases only with the increase in either deposition time or beam flux. In this case the beam flux is varied from 0.5 to 1.5 nA and

Table 4.3: Atomic concentration of different elements present on the film surfaces.

Sample	**Ag (at. %)**	**O (at. %)**	**Si (at. %)**	**C (at. %)**
#A1	25	15.8	50.4	8.8
#A2	32.7	15.1	43.7	8.5
#A3	48.5	13.6	30.1	7.8
#A4	49.9	13.1	29.4	7.6
#A5	56.9	11.9	23.9	7.3
#A6	70	7.2	17	5.8

we observe a morphological evolution of the Ag nanostructured films. From the calculation of SEM image of the film with an ion current of ∼ 1.5 nA, it is found that the coverage of Ag nanostructure over the Si surface is ∼ 40 % indicating a large portion of the substrate surface still empty. Also from the close observation of SEM image, we can clearly see the underlying Si surface. As a result we found both the Si 2p and O 1s peaks in the survey XPS spectrum for the sample with ion current of ∼ 1.5 nA. The atomic concentrations of the elements present on the surface for each of the films are calculated from their corresponding high resolution scans for each peak and the obtained values are summarized in Table 4.3. The total atomic concentration variation of Ag with average ion current is shown as a histogram in figure 4.12(b).

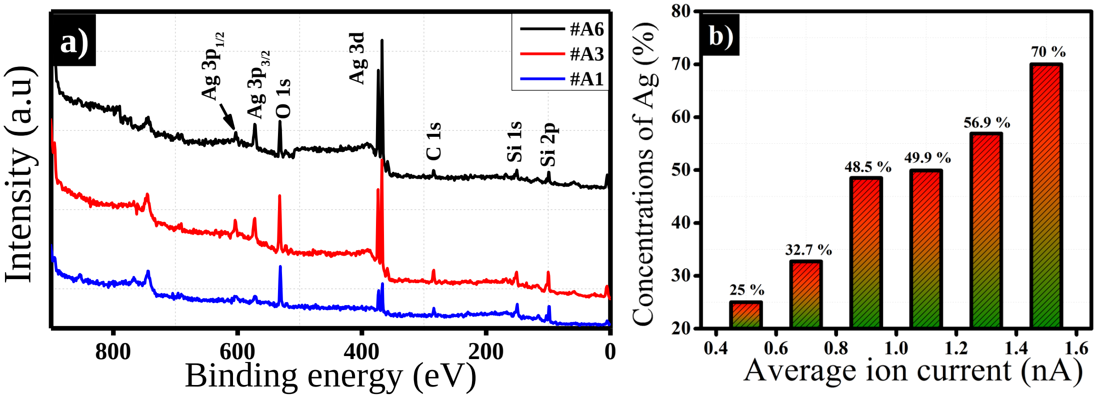

Figure. 4.12: *(a) XPS survey spectra taken for the samples #A1, #A2 and #A3; (b) Variation of total atomic concentrations of silver with average ion currents.*

From the figure 4.12(b), it is found that for small average ion current of 0.5 nA, the total concentration of silver is $\sim 25\%$ that gradually increases to $\sim 70\%$ with an increase in ion current to 1.5 nA. Moreover, the total atomic concentrations of both oxygen and silicon are found to be decreased simultaneously with the average ion current. The increased size of the deposited cluster aggregates on the substrate absorb or adsorb lesser surface oxygen as compared to smaller cluster aggregates and hence, the total atomic concentration of oxygen decreases with the increased ion current. Moreover, the total surface coverage occupied by the larger cluster aggregates are more as compared to smaller aggregates due to which the total atomic concentration of silicon is found to be decreased with the increase in average ion current.

The core-level Ag 3d spectra obtained for all the films are shown in figure 4.13. In all the cases, the doublet peaks of Ag 3d are found at the binding energies of 368.1 and 374.1 eV for Ag $3d_{5/2}$ and Ag $3d_{3/2}$, respectively. The obtained binding energies of Ag 3d for the Ag cluster aggregates are in agreement with the previously reported values for metallic Ag 3d nanoparticles [168, 169]. In one of our recent paper [145], we reported a shift in binding energy for core level Ag 3d due to the size effect of the deposited cluster aggregates. But in the present case we did not notice any peak shifts for Ag 3d. It is reported that this kind of peak shifting occurs when the deposited particle size is smaller than 10 nm [170]. Because of their smaller size, the changed position of their valance bands influences the obtained XPS peaks by shifting them towards higher BE value. In the current scenario, the minimum average size of cluster aggregates is found to be ~ 15 nm for an ion current of 0.5 nA. Hence, the shift in BE of Ag 3d peaks due to deposited cluster aggregates does not take place. Moreover, there are no trace of oxidation of the metallic silver. Therefore, it can be concluded that the deposited films contain only pure metallic silver.

Furthermore, it is found that with the increase in average ion current, the area

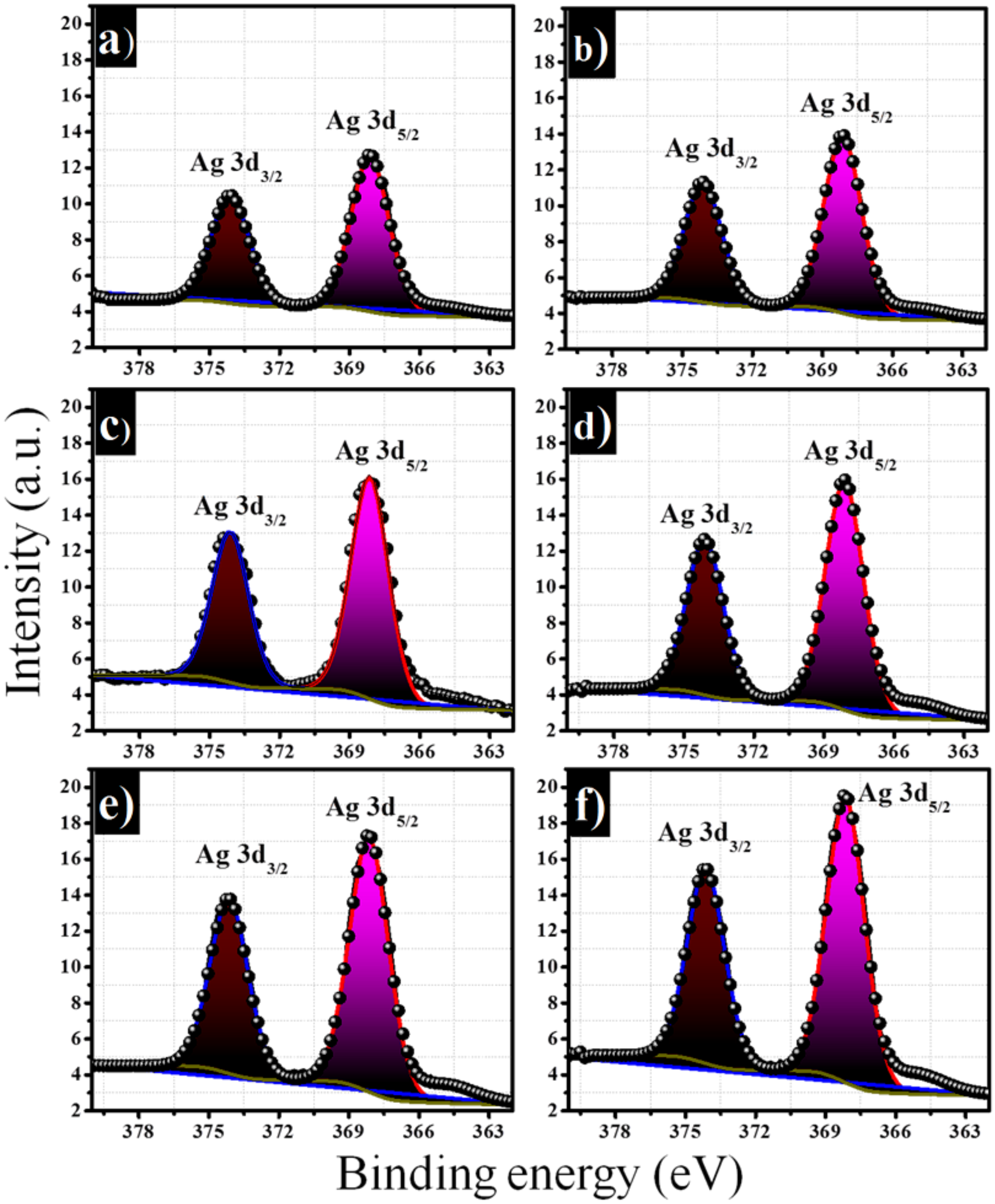

Figure. 4.13: *HR-XPS spectra of core-level Ag 3d peaks for the samples: (a) #A1, (b) #A2, (c) #A3, (d) #A4, (e) #A5 and (f) #A6.*

under curve of the peaks associated with core level Ag 3d increases. This signifies the increased amount of total atomic concentration of Ag on the films due to the increase in average ion current and the same is presented in figure 4.12(b). The peak positions and area under curve of Ag 3d peaks for each of the films are estimated and

Table 4.4: Binding energy and peak area of Ag 3d estimated from HR-XPS spectra.

Sample	**Ag 3d$_{5/2}$ BE(eV)**	**Ag 3d$_{5/2}$ Area(a.u)**	**Ag3d$_{3/2}$ BE(eV)**	**Ag3d$_{3/2}$ Area (a.u)**
#A1	368.10	962.8	374.11	647.0
#A2	368.10	1133.1	374.11	737.1
#A3	368.10	2727.1	374.11	1751.5
#A4	368.11	2895.2	374.11	1838.6
#A5	368.11	3135.7	374.14	2025.8
#A6	368.12	3416.1	374.13	2221.6

summarized in Table 4.4.

4.4.2.4 Contact angle analyses

The snapshots of measured water contact angle on as-deposited Ag cluster films are shown in figure 4.14. The contact angle (CA) of the film prepared with lowest average ion current is found to be $\theta_c = 80.7^o$ that increases upto hydrophilic limit of $\theta_c = 89.7^o$ for an average ion current of 1.1 nA. But the film deposited at highest average ion current of 1.5 nA gives a CA of $\theta_c = 98.2^o$. Hence, the contact angle varies from hydrophilic to hydrophobic region with the increase in average ion current. The enhanced CA values of the films can be corroborated with their morphologies extracted from their respective SEM images and the corresponding histograms. It is found that the obtained CA values are within the hydrophilic limit as long as the lateral size distributions are bi-modal in nature for smaller cluster aggregates and CA values are found in hydrophobic region for the films with mono-modal size distribution for larger cluster aggregates.

In Wenzel's model, it is found that when the water droplet fills the grooves and cavities of a rough surface, the wettability property of the surface is directly dependent on the roughness factor R_f and the roughness factor for each of the films are measured from their corresponding AFM images. The roughness factor of the

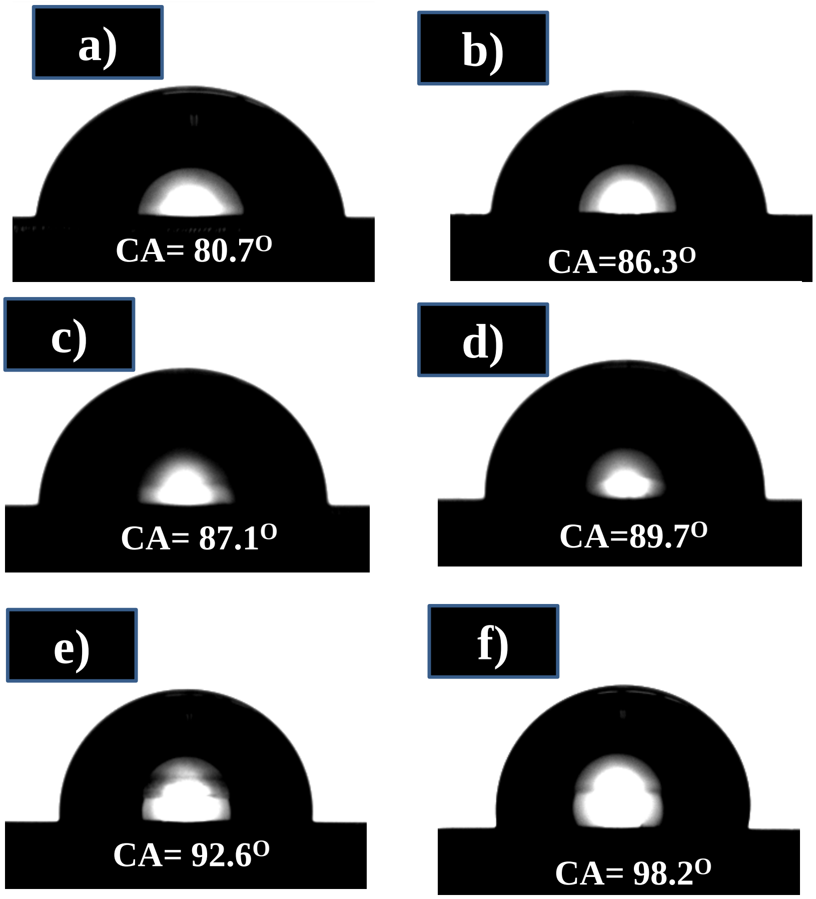

Figure. 4.14: *Snapshots of the water contact angle on Ag-cluster aggregate samples: (a) #A1, (b) #A2, (c) #A3, (d) #A4, (e) #A5 and (f) #A6.*

films are found as 1.19, 1.25, 1.278, 1.318, 1.368 and 1.625 for an average ion currents of 0.5, 0.7, 0.9, 1.1, 1.3 and 1.5 nA, respectively. It also was reported [158, 171] that the water contact angle on a smooth Ag surface was found as $\sim 95^o$. Using the CA along with the roughness factor, the theoretical Wenzel's contact angle for each of the deposited film may be found out using the equation 4.18. The obtained Wenzel's CA values are plotted and compared with our experimental CA values and the graph is shown in figure 4.15(a). At lower average ion current, a large difference between the experimental and theoretically obtained CA values are observed. The difference keeps on decreasing as ion current increases. Finally, for an average ion current of

1.5 nA both the theoretical and experimentally obtained contact angles are found to be almost equal. Hence, it can be said that the surface developed for an average ion current of 1.5 nA follows the Wenzel's model. This can be explained considering the CA value of pristine Si surface to be $\theta_C = 71.5^o$ and shown in figure 4.1. The obtained CA value for Si surface lies within hydrophilic region [172]. When the deposition is performed at lower average ion currents, the bare silicon surface is covered with smaller Ag cluster aggregates and the coverage is found to be very low. As a result, the water droplet will be in contact with both the surfaces during the measurement of contact angle. On this surface, the Ag cluster aggregates will influence the water droplet and, therefore, the obtained CA value is larger than that of bare Si surface. As the average ion currents increase the coverage of silver cluster aggregates on silicon surface increases and consequently the droplet will be more influenced by the more number of Ag cluster-aggregates and an increase in CA value of the surface is observed. Thus with the increase of Ag coverage, the hydrophilic behaviour of Si surface decreases and its hydrophobicity increases. Finally, the coverage of deposited Ag cluster-aggregates at an average ion current of 1.5 nA dominates over the silicon surface and the experimental CA value approaches close to its theoretical value.

The experimental CA values are also compared with the theoretical Cassie-Baxter model. In order to implement the Cassie-Baxter model, it is assumed that the water droplet can't fill the nano-grooves of the rough surfaces. In such a condition, the grooves will either partially or completely filled with air. Hence, the fraction, f_s for each of the samples is estimated to measure the Cassie-Baxter theoretical CA value using equation 4.20. The obtained theoretical values are plotted and compared with the experimental CA values and shown in figure 4.15(b). The obtained theoretical values are much larger than that of the experimental CA values. Thus, it can be inferred that the wettability property of the deposited films does not satisfy the

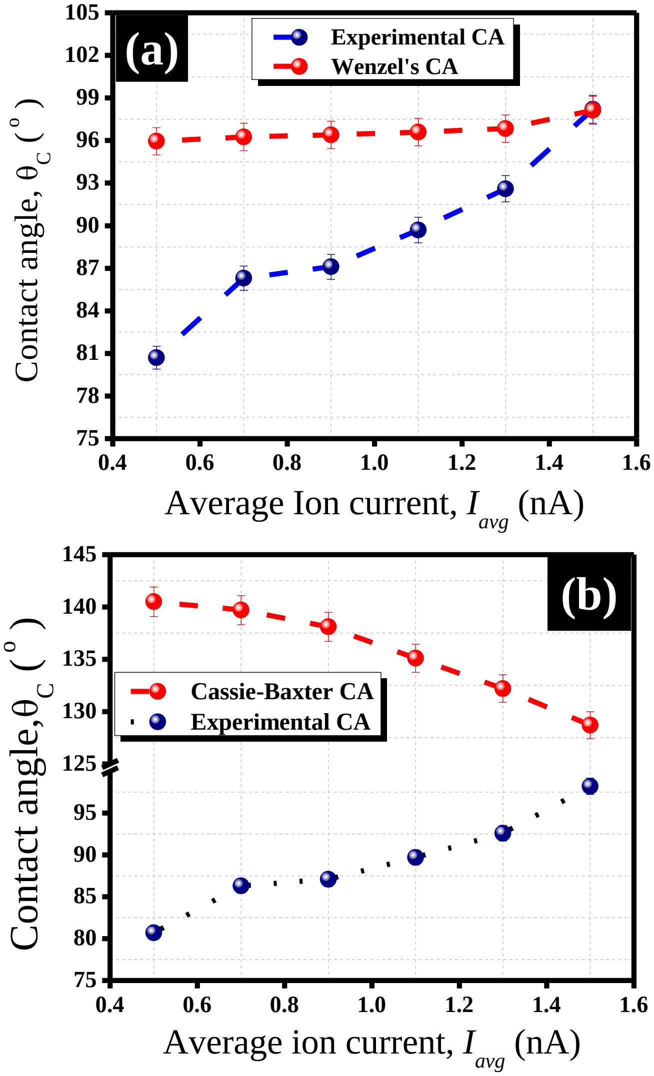

Figure. 4.15: *Variation of experimental and theoretical contact angle values as a function of average ion currents using (a) Wenzel's model, (b) Cassie-Baxter's model.*

criteria of Cassie-Baxter model.

The change in contact angles may be explained using one of the morphological parameters of the films called fractal dimension. It is already observed from AFM analyses that the fractal dimension of the films increases with morphological evolution. The enhanced fractal dimension of the films can influence the wettability property of the surfaces. The correlation between the fractal dimension of the films and their water contact angles can be drawn by plotting the CA values of the films as a function

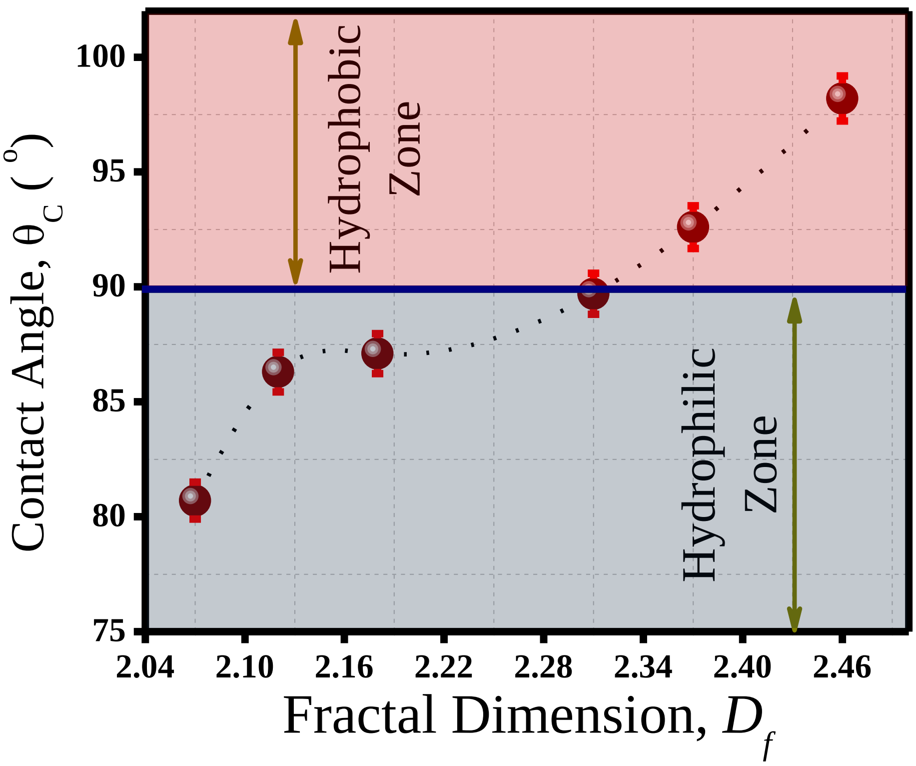

Figure. 4.16: *Variation of water contact angle as a function of fractal dimension of the films.*

of their fractal dimension. Figure 4.16 shows the monotonic variation of CA values with average ion currents. It is found that initially the obtained contact angle value is small for smaller fractal dimension values and it lies in the hydrophilic region. As long as the surface fractality increases the wettability property of the films shows more hydrophobic behaviour with a higher CA value. Finally, for the highest fractal dimension, the corresponding film reflects a complete hydrophobic nature and the obtained CA value is within the hydrophobic zone. Hence, it can be inferred that the fractal dimension of the films influences their wettability property. Onda *et al.* [152] already theoretically as well as experimentally showed that higher fractal surface has more water repellent capacity as compared to smaller fractal surface. In consonance with our observations, Yadav *et al.* [151] also found that an increase in fractality of ion beam bombarded rippled surface is observed with the hydrophobicity but wettability transition of the films was not observed.

4.4.3 Conclusion

Cluster-aggregated Ag films using a size-selected Ag-nanocluster beam were deposited by varying the average ion current. From the AFM and SEM analyses, morphological evolution of the films are observed. A bi-modal behaviour is found from size-distribution histograms at lower average ion currents whereas the distribution is mono-modal in nature for higher average ion currents. Smaller clusters are observed for lower average ion current whereas aggregates are formed on the substrates evolving mound-like structures at higher average ion currents that are evident from the 3D AFM morphology. From the statistical analyses of the AFM data, it is further found that the obtained film surfaces are self-affine in nature and the films contain fractal characteristics. Various morphological parameters of the films such as fractal dimension, interface width, correlation length are found to be increased with the increase in average ion currents. Chemical compositions of the deposited films are investigated by XPS where the presence of metallic silver is verified. The wettability property of the films is measured using the water contact angle measurements. A transition in surface wettability is found from hydrophilic to hydrophobic nature along with the morphological evolution of the films. Finally, the experimental CA values are compared with theoretical CA values and found that surface developed with higher average ion currents satisfies the criteria of Wentzel's model.

Chapter 5

Morphological and compositional studies of thermally treated cluster deposited films

---

In this chapter, the morphological and chemical analyses of thermally treated Ag-cluster films are made. Morphologies of cluster deposited films are studied on Si and modified Si surfaces at various substrate temperatures. In the later part of this chapter, studies on bimetallic Ag-Au nanoparticles are included where size-selected Ag-nanoclusters were deposited on as-deposited Au-film. The morphological and composition studies of the Ag-Au nanoparticles also are carried out at an elevated substrate temperature.

Related publications

1. *"Interaction of size-selected Ag-clusters on Au-thin films: A composition study with in-situ XPS analysis at an elevated temperature"*, **Pintu Barman**,

Anindita Deka, and Satyaranjan Bhattacharyya *J. Phys. D: Appl. Phys.* **54** (2021) 275301.

2. *"Thermal diffusion driven island formation and fragmentation of size-selected Ag-nanocluster films"*, **Pintu Barman**, Anindita Deka, Shyamal Mondal, Debasree Chowdhury, and Satyaranjan Bhattacharyya *AIP Conf. Proc.* **2115** (2019) 030306.

5.1 Introduction

In the field of material sciences, metal nanoparticles draw the attention of researchers due to their novel properties that led them to use in different applications such as catalysis [111], biomedical [173], optical [174], electrical [175], magnetic [176] etc. Ag-nanoparticles are considered as material of interest because of its various novel properties which may be utilized in many applications such as optical, antibacterial, catalytic etc [177–179]. Gold nanoparticles are also used in various applications, specially for catalytic and plasmonic applications [180, 181]. In order to use the nanoparticles in certain applications, their growth behaviour study [144, 145] is very important to control the morphology as well as size and shape of the nanoparticles. Now-a-days, researchers are exploring the nanoparticles containing alloys, composite metals, mixtures containing more than one type of nanoparticle etc. to improve the properties and functionalities as well of the devices. The synthesis of bimetallic nanoparticles has been a new research trend among the researchers for about two decades as alloyed nanoparticles offer different properties as compared to its monometallic counterpart. Bimetallic alloy nanoparticles are used in various applications namely, bimetallic Ni-Au nanoparticles as catalyst in Au/NiO [182], NiCr alloy nanoparticles as a resistor [183], Ag-TiO_2 nanocomposites in plasmonics [184], Au-TiO nanocomposites in photo-catalysis [185] etc. Moreover, bimetallic Ag-Au nanoparticles are also used in various applications such as solar cell [186], optical [187–190], sensing [191] etc. Tuning of properties of bimetallic nanoparticles is possible by changing the composition of individual elements constituting the alloy nanoparticles. Various synthesis and growth methods of Ag-Au nanoparticles have been discussed by the researchers. Kumar and co-workers [192] used one of the simple methods known as spray pyrolysis method for the production of Ag-Au nanoparticles. Ristig *et al.* [193] used wet chemical co-reduction process for the synthesis of Ag-Au nanoparticles. Oh *et al.* [194] used laser-induced dewetting method for the production of Ag-Au nanoparticles on a glass substrate. In order to study the catalytic property, Wang *et al.* [195] used a novel one-pot synthesis method for the production of Ag-Au nanoparticles. Verma *et al.* [196] used pulsed laser deposition method for the production of Ag-Au nanoparticles. Production of nanoparticles using a gas-aggregation cluster source also is a popular method in fundamental and industrial researches. In order to produce nanoparticles of two or more metals in a single step process, a modification of the cluster source is necessary. Llamosa *et al.* [197] used a modified cluster source known as multiple ion cluster source (MICS) for the production of core-shell Ag-Au and Cu-Au spherical nanoparticles. Martinez *et al.* [198] used a modified cluster source consisting of individual magnetron setup to fabricate bimetallic AgAu and trimetallic AgAuPd nanoparticles in a one step method. In a gas aggregation cluster beam deposition process, clusters of desired materials have formed inside the aggregation chamber prior to its deposition on a substrate. Although this process has the advantage of controlling the size and composition of the produced nanoparticles, it does not allow us to monitor the real time growth of nanoparticles. Hence, a two-step fabrication method is used here for the production of bimetallic Ag-Au nanoparticles using gas-aggregation cluster source. In this method, we have produced bimetallic nanostructure consisting of Ag and Au in a novel method where size-selected Ag nanoclusters were deposited on a magnetron sputtered Au thin-film whose thickness is comparable to Ag nanocluster size. After the deposition, the films were annealed under ultrahigh vacuum condition at an elevated temperature to get bimetallic nanoparticles. This method permits us to monitor the real time chemical changes occurred on the surface in the process of production of bimetallic nanoparticles by in-situ XPS measurements. In previous cluster related studies [164–166, 199], it was found that fragmentation of cluster deposited films take place when they went through the rapid thermal annealing

(RTP) process. This kind of thermal fragmentation is useful to get films contains monodispersed nanostructures [200, 201]. In the present experiment, the annealed temperature is well below the eutectic temperature of Ag silicide and Au silicide for the production of bimetallic nanoparticles where the produced particles retain their spherical shape and uniformity on overall size distribution. This also can be considered as a novel method for the production of bimetallic nanoparticles with tunable composition and narrow size distribution. The morphologies of the obtained films are analysed by AFM and SEM techniques. The chemical composition of the films are investigated by x-ray photoelectron spectroscopy.

5.2 Thermal diffusion driven island formation and fragmentation

5.2.1 Experimental details

In this experiment, a beam of size-selected clusters with diameter ~ 4 nm are deposited on temperature treated Si(100) and untreated Si(100) substrates keeping the deposition time constant. Prior to the experiment, Si substrates were ultrasonically cleaned in acetone followed by propanol for 15 min each. Si(100) substrates were then annealed at 500 ^{o}C in N_2 environment for 15 sec with a temperature ramp rate of 25 ^{o}C/sec using a rapid thermal annealing system (Model: JETFIRST100 jipelec), these substrates were termed as RTA treated Si(100). The size-selected clusters are produced inside a aggregation chamber using the magnetron sputtering process. During the experiment the magnetron power was kept at 52 watt (290 V and 181 mA). The deposition pressure in the main deposition chamber and the magnetron chamber was found as $\sim 4.8 \times 10^{-4}$ and $\sim 2.5 \times 10^{-1}$ mbar, respectively. The quadrupole parameters were adjusted to obtain a beam current of ~ 0.5 nA

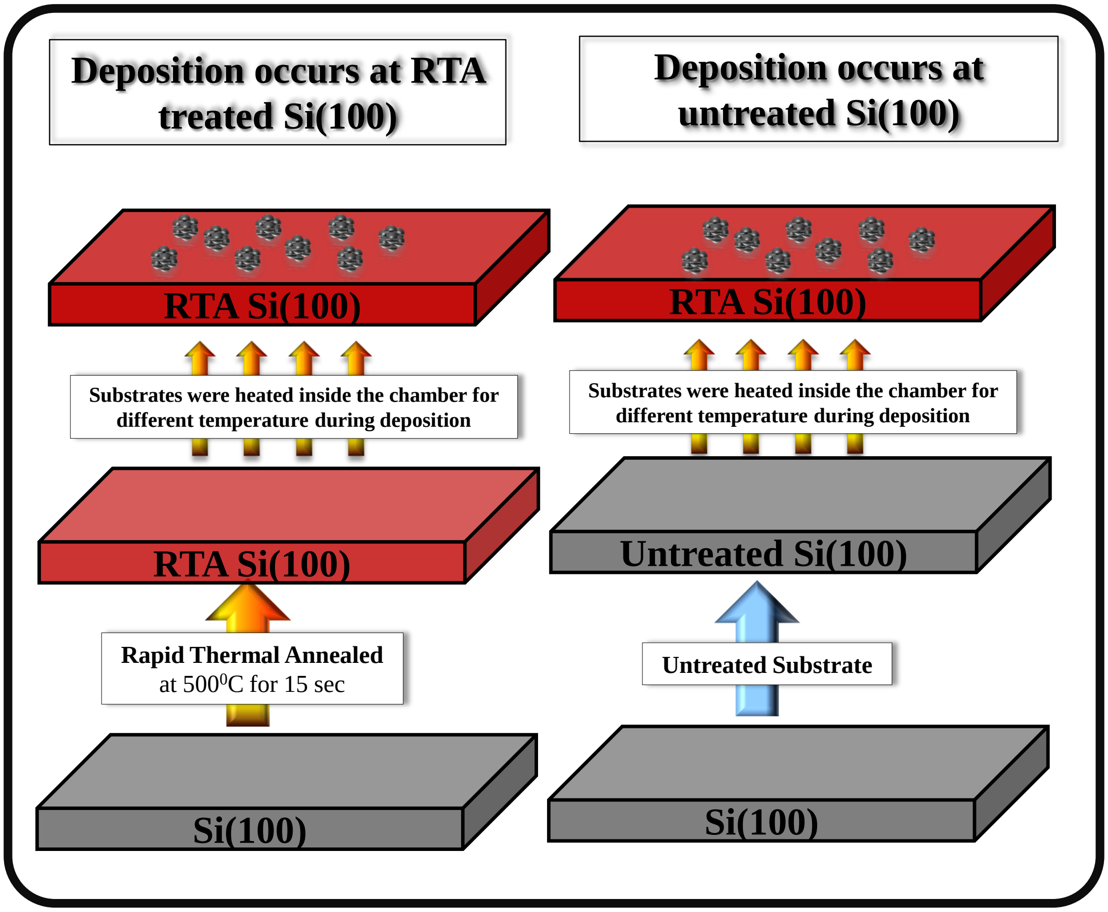

Figure. 5.1: *A schematic representation of size-selected Ag-nanocluster deposition on RTA treated and untreated Si(100) substrates.*

for performing the experiment. Figure 5.1 shows a schematic diagram describing the film deposition process on untreated and RTA treated Si(100) substrates. The morphologies of the deposited films are analysed by AFM and SEM techniques. The AFM images are captured in tapping mode using a Si tip with a nominal radius of curvature $\sim$ 8 nm. The lateral size of the deposited films are measured using a field emission scanning electron microscope (FESEM) system with a gun voltage of 5 kV.

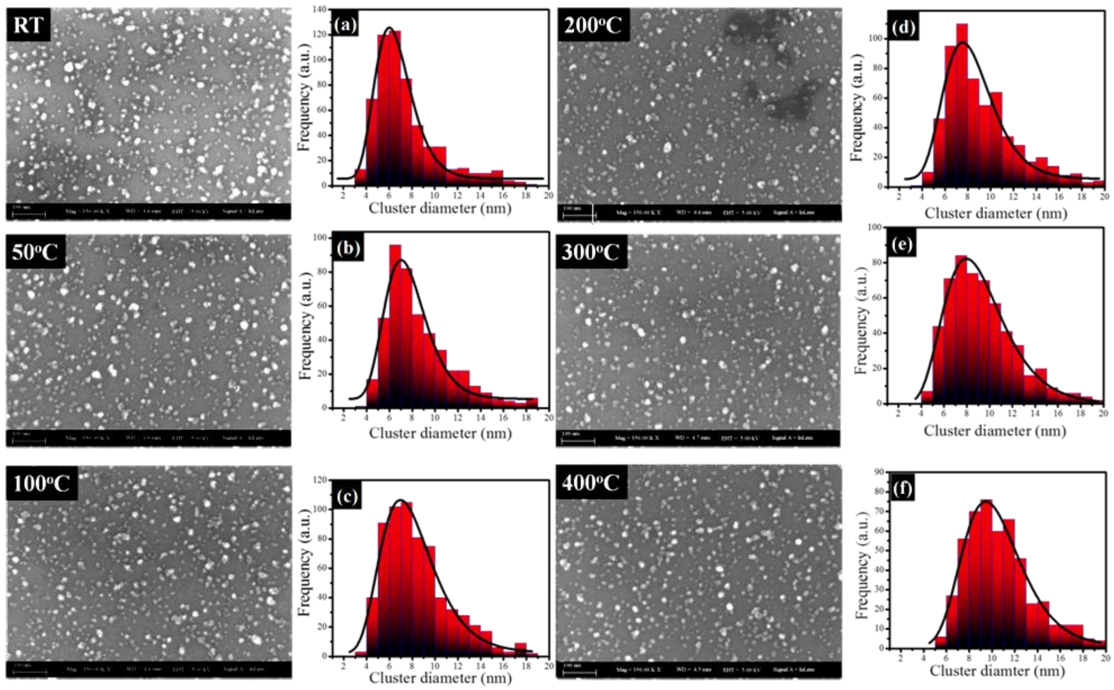

Figure. 5.2: *SEM images of the films deposited on untreated Si (100) substrates at various substrate temperatures. The size-distribution histograms of the particles deposited at (a) 25 ^{o}C (b) 50 ^{o}C (c) 100 ^{o}C (d) 200 ^{o}C (e) 300 ^{o}C and (f) 400 ^{o}C.*

5.2.2 Results and discussions

Figure 5.2 shows the SEM images of morphologies of Ag-cluster-deposited films on untreated Si(100) substrates at various substrate temperatures along with their respective size distribution histograms where the substrate temperature during Ag-cluster deposition is varied from room temperature (25 ^{o}C) to 400 ^{o}C. The deposited Ag-clusters and their smaller aggregates are also seen on the surfaces of untreated Si. To get an idea about the size of the deposited particles, each of the clusters and its aggregates were individually measured from their corresponding SEM images using ImageJ software. The measured lateral sizes of the particles are then plotted as a histogram which is shown at the right side of respective SEM images. The distribution of the histogram for the film deposited at room temperature is found to be narrower. The distribution keeps on broadened as the cluster deposition temperature increases.

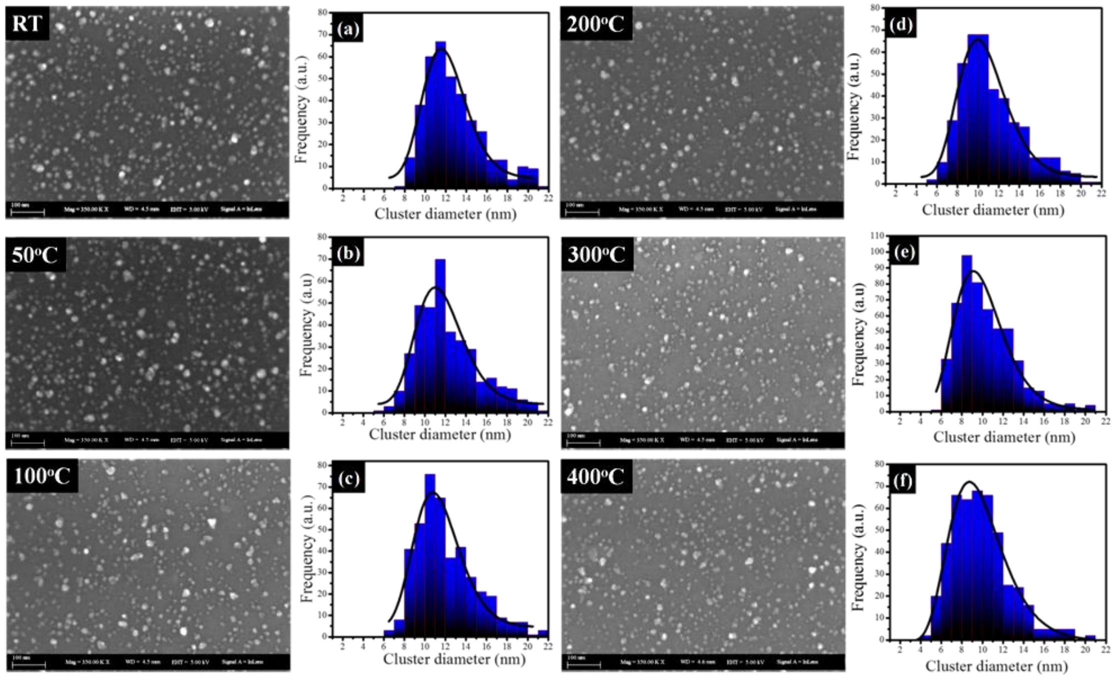

Figure. 5.3: *SEM images of the films, deposited on RTA treated Si (100) substrates, at various substrate temperatures. The size-distribution histograms of the particles deposited at (a) 25 °C (b) 50 °C (c) 100 °C (d) 200 °C (e) 300 °C and (f) 400 °C.*

In the histogram, the distribution of lateral sizes of the particles are found to be varied from ∼ 2 to ∼ 20 nm. The size-distribution histograms are best fitted with lognormal function and the fitted curves are indicated by the black solid line in the figure. The average cluster diameter is estimated using the fitting for each histogram. The calculated average cluster diameter for the film deposited at room temperature is found to be ∼ 6.4 ± 0.1 nm. The average cluster diameter is found to keep increasing with the increase in substrate temperature. Finally, for the clusters deposited at 400 ^{o}C the estimated average cluster diameter is found as ∼ 10.1 ± 0.2 nm. The value of average cluster diameter for all the films are listed in Table 5.1.

Figure 5.3 shows the morphology as well as the size-distribution histograms of Ag-cluster deposited films on RTA treated Si(100) substrates. The deposited clusters and their aggregates can be clearly seen on the RTA treated Si substrates.

The size-selected Ag-nanoclusters were deposited on RTA treated Si substrates at various substrate temperatures ranging from room temperature ($\sim 25\ ^{o}$C) to 400 ^{o}C. The lateral size of the deposited particles is estimated using the SEM images and plotted as a histograms as shown at the right side of respective images. The SEM images are analysed using ImageJ software. From the size-distribution histograms, it is found that the distributions are almost same in all the cases and the range of distributions varies from $\sim$ 5 to $\sim$ 22 nm. All the distributions are best fitted with the lognormal function indicated by the black solid lines over every histograms. The average cluster diameter are measured using this fitting. The measured value of average cluster diameter for the film deposited at room temperature is found to be $\sim$ 11.9 ± 0.14 nm. The average cluster diameter of the films are found to be decreased with the increase in deposition temperature. Finally, the obtained average cluster diameter of the film is found to be $\sim$ 9.5 ± 0.13 nm at a deposition temperature of 400 ^{o}C. The values of all the average cluster diameters of the films are tabulated in Table 5.1. It can be inferred from the above that the morphology of cluster-deposited films are affected by the substrate modification through substrate annealing at 500 ^{o}C using RTA. In Table 5.1, it can be seen that the modified substrates largely affect the average size of the deposited clusters. It is found for the films deposited on the untreated Si substrate that the average diameter of the deposited clusters increases with increasing deposition temperature. Many defects also are found on its surface. After the deposition of nanoclusters, the clusters start moving over the surface and get trapped within these surface defects causing lesser cluster diffusion. But as the deposition temperature increases, the diffusion of clusters over the surface increases and as a result, more clusters will merge and appear as larger island. Hence, an increase in average size of the cluster aggregates is observed with the deposition time. From the Table 5.1, it is found that the average size of the deposited cluster aggregates is decreasing very slowly with the increase in deposition

Table 5.1: *Average cluster diameters obtained from the histograms for cluster-deposited films.*

Substrate temperature (^{o}C)	**Average cluster diameter on untreated Si (nm)**	**Average cluster diameter on RTA treated Si (nm)**
25 (RT)	6.4 ± 0.1	11.9 ± 0.14
50	7.5 ± 0.14	11.5 ± 0.21
100	7.7 ± 0.13	11.21 ± 0.21
200	8.1 ± 0.2	10.5 ± 0.14
300	8.8 ± 0.13	9.7 ± 0.17
400	10.1 ± 0.16	9.5 ± 0.13

temperature. For the RTA-treated Si substrates, negligible defects are expected to be present on the surface and, therefore, the deposited nanoclusters can freely roam around the surface without being trapped into any defects. So, the probability of diffusion will be higher and the clusters deposited even at room temperature show high average cluster aggregates. When the deposition was made at higher temperature, a decrease in average cluster size is found. Though negligible defects are present on the temperature-treated substrates, such a decrease may be due to fragmentation of deposited cluster aggregates for the excessive diffusion of cluster aggregates over the surface. This excessive diffusion might cause collisions between cluster aggregates leading to a decrease in average cluster aggregates size.

Figure 5.4 shows the AFM morphologies of the films deposited on untreated Si substrates. In all the images, the Ag-cluster aggregates with nearly spherical in shape are found to occupy the Si substrates. From the AFM analysis, we have measured the root mean square (rms) roughness of each of the films. The obtained rms roughness values for the films deposited at substrate temperature of 25, 50, 100, 200, 300, 400 and 500 ^{o}C are found as 3.9, 4, 4.6, 4.65, 4.4, 4.1 and 3.9 nm, respectively. The rms roughness of the films initially increases up to a temperature of 200 ^{o}C and beyond that the roughness keeps on decreasing. Hence, it can be said that the cluster deposited films start flattened at a temperature above 200 ^{o}C. The

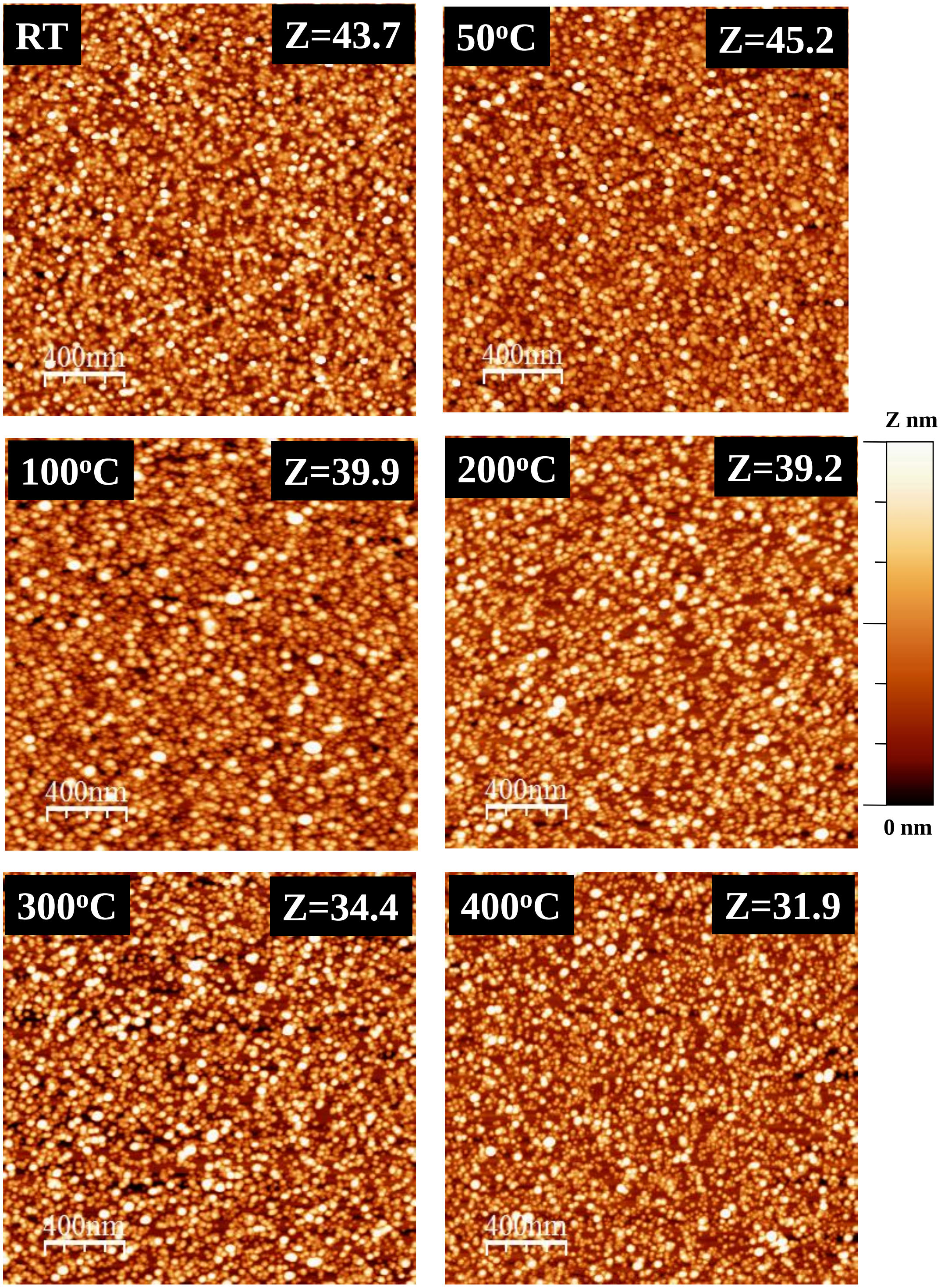

Figure. 5.4: *Typical (2 μm × 2 μm) scan-sized AFM micrographs of the films deposited on untreated Si(100) substrates at various substrate temperatures.*

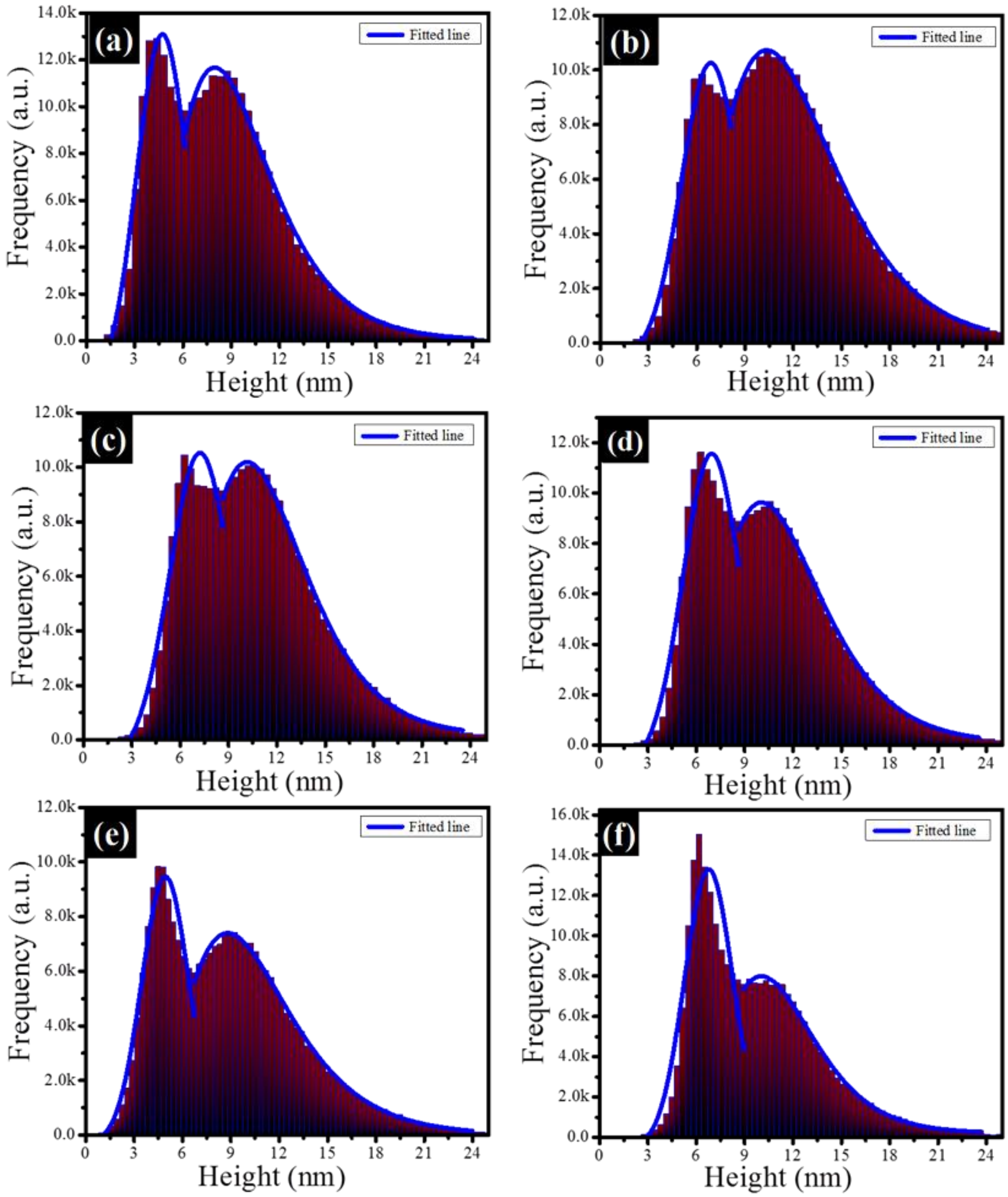

Figure. 5.5: *Height distribution histograms of the films deposited on untreated Si (100) substrates at substrate temperatures of (a) 25 ^oC (b) 50 ^oC (c) 100 ^oC (d) 200 ^oC (e) 300 ^oC and (f) 400 ^oC.*

AFM images for the cluster films deposited above 300 ^{o}C, aggregates are found to rearrange their shapes into almost spherical as compared to the previous films. The

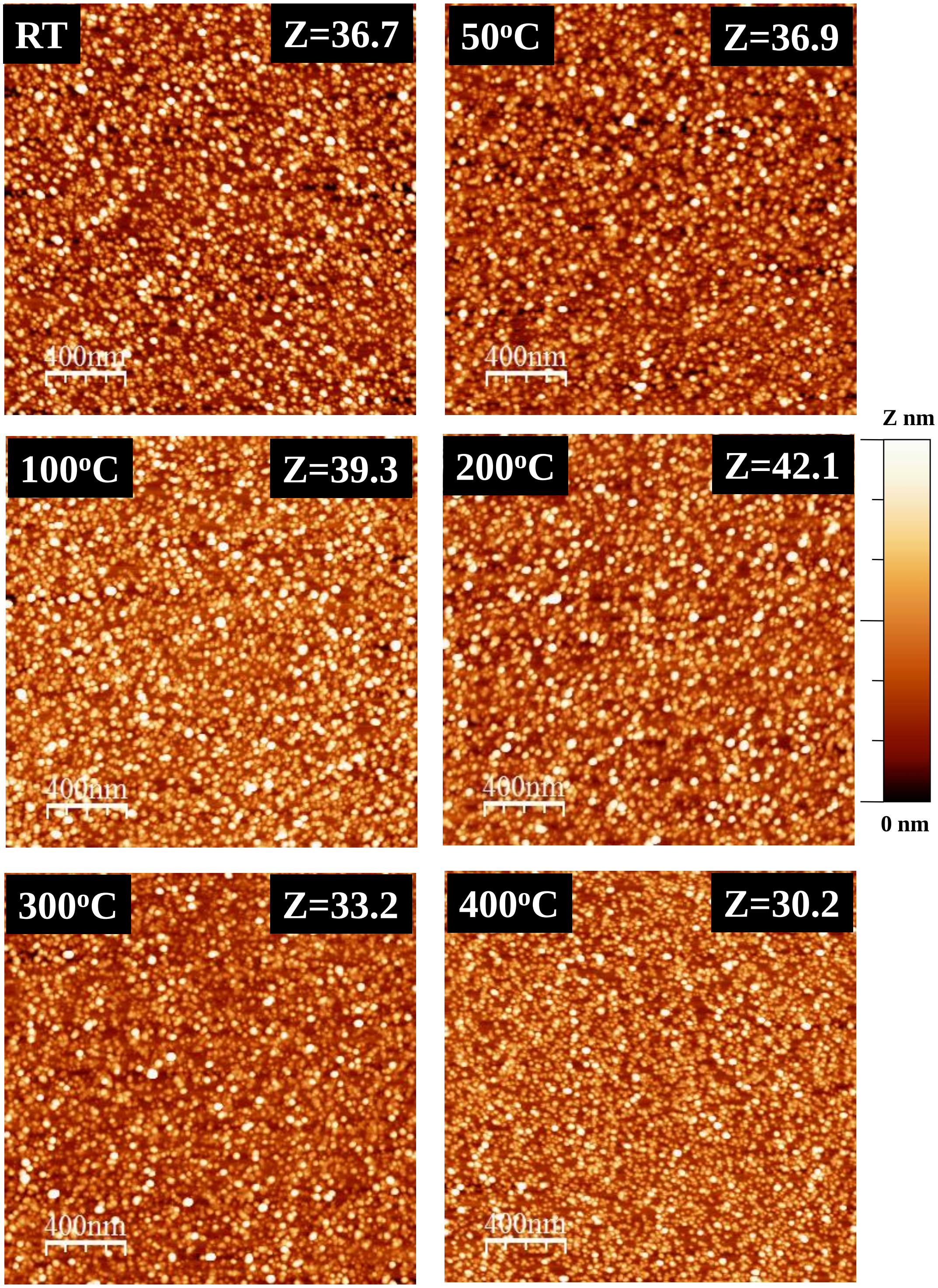

Figure. 5.6: *Typical (2 μm × 2 μm) scan-sized AFM micrographs of the films deposited at various temperatures on temperature-treated Si(100) substrates.*

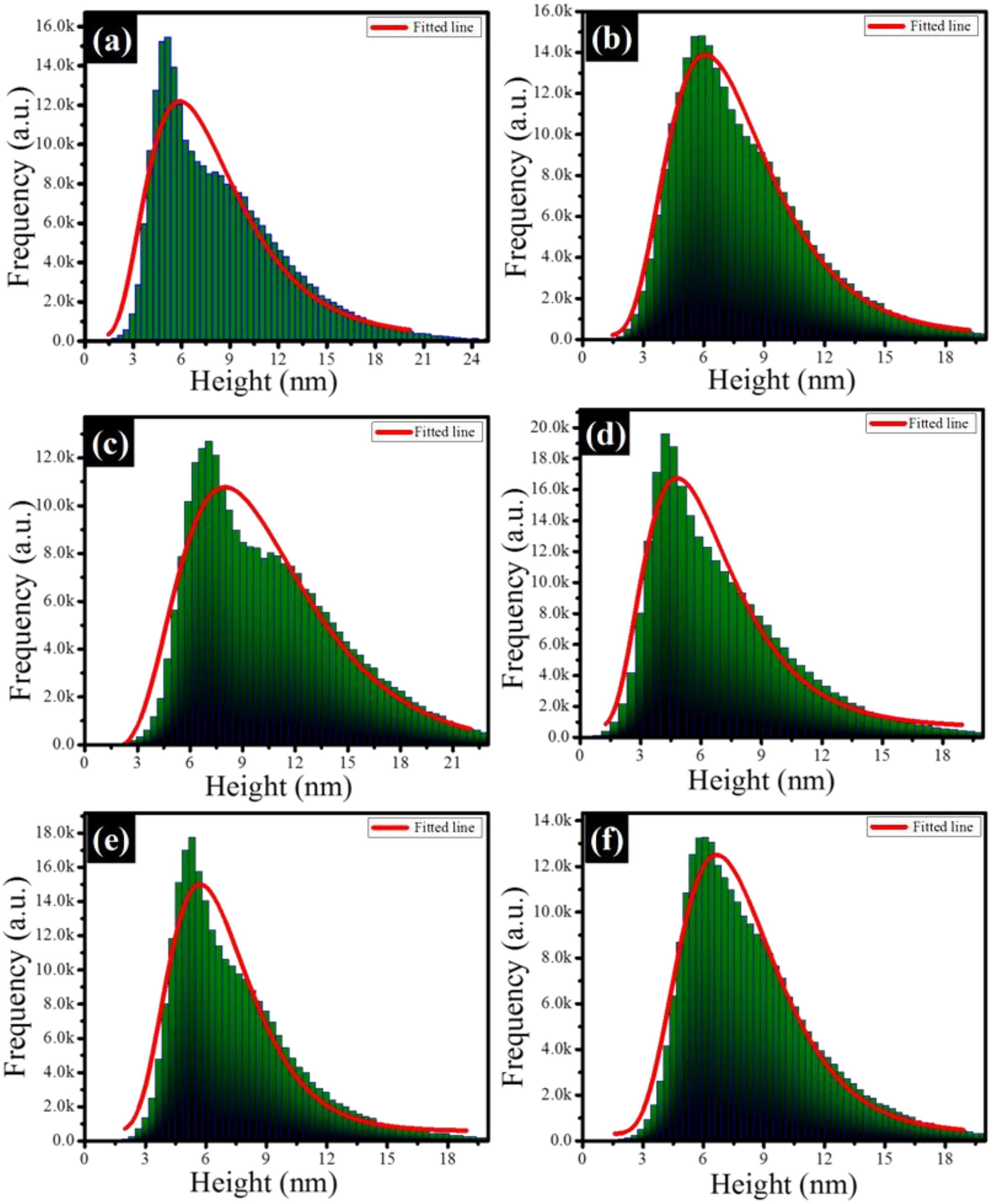

Figure. 5.7: *Height distribution histograms of the films deposited on temperature treated Si (100) substrates at substrate temperature of (a) 25 ^oC (b) 50 ^oC (c) 100 ^oC (d) 200 ^oC (e) 300 ^oC and (f) 400 ^oC.*

height distributions of the deposited cluster aggregates on untreated Si substrates for each of the films are shown in figure 5.5(a)-(f). In all the histograms, the height distribution is found to be bi-modal in nature. All the histograms best fitted with lognormal function as indicated by the blue solid lines contain two height maxima. The first average height maxima is appeared between 5 to 7 nm while the second height maxima is appeared between 9 to 11 nm for all the films. The bi-modal height distribution of the films suggests the presence of more fragmented particles as well as larger cluster aggregates on the surface. The SEM images also corroborate the above observations.

Figure 5.6(a)-(f) shows the AFM morphologies of the films deposited at various substrate temperatures on temperature-treated Si substrates. The AFM images show the formation of nearly spherical-shaped cluster aggregates on the surfaces. The obtained values of rms roughness of the films deposited on RTA Si substrates at substrate temperatures of 25, 50, 100, 200, 300, and 400 ^{o}C are found as 3.5, 4, 4.55, 3.7, 3.3 and 3 nm, respectively. The rms roughness of the films is found to be increased upto a temperature of 100 ^{o}C and it decreases with further rise in the deposition temperature. The height distribution histograms of these films are presented in figure 5.7(a)-(f). Unlike the previous histograms for the films deposited on untreated Si substrates, the distribution is found to be mono-modal in nature. All the histograms are best fitted with lognormal function which is shown as the red solid lines over the histograms. The obtained average height values for all the films are within the range of 7.3 to 9.5 nm. This indicates the formation of uniform cluster aggregates on the RTA treated Si substrates.

5.2.3 Conclusion

In this study, size-selected Ag-nanoclusters of diameter $\sim$ 4 nm were deposited on two types of Si substrates namely, normal and RTA treated substrates at 500 ^{o}C. The clusters deposited on normal Si substrate show an increase in lateral size whereas the second kind of films shows a slow decrease in lateral size with the deposition temperature. From the AFM morphology, the first kind of films shows an increase in rms roughness upto 200 ^{o}C and beyond that the rms roughness decreases whereas the second kind of films shows the increase in rms roughness upto 100 ^{o}C and beyond that it decreases. Moreover, the first kind of the films shows a bi-modal height distribution while the second one shows mono-modal nature in height distribution histograms.

5.3 Ag-cluster on Au thin-film at elevated temperature

5.3.1 Experimental details

In this experiment, a thin-film of Au was deposited on an ultrasonically cleaned Si(100) substrates. The deposition was performed in a high vacuum chamber using a conventional dc magnetron sputtering setup. Before the experiment, the base pressure of the main deposition chamber was maintained at $\sim 10^{-8}$ mbar.

The thickness of the Au thin-film was kept at $\sim$ 5 nm by using the already calibrated parameters of the dc magnetron sputtering system. The as-prepared Au thin-film was then loaded into the main deposition chamber of nanocluster deposition system where the deposition of size-selected Ag nanoclusters were taken place on the Au film. The size-selected Ag-nanoclusters of diameter of $\sim$ 5 nm (number of atoms per cluster = 3380, mass = 360000 amu) were deposited on Au-film using soft-landing method. During the deposition of nanoclusters, the pressure of the magnetron chamber was increased from 5×10^{-4} to 2.3×10^{-1} mbar while during the deposition the pressure inside the main deposition chamber was increased to 4.7×10^{-5} mbar from a base pressure of 2.3×10^{-9} mbar. The post deposition annealing of the as-

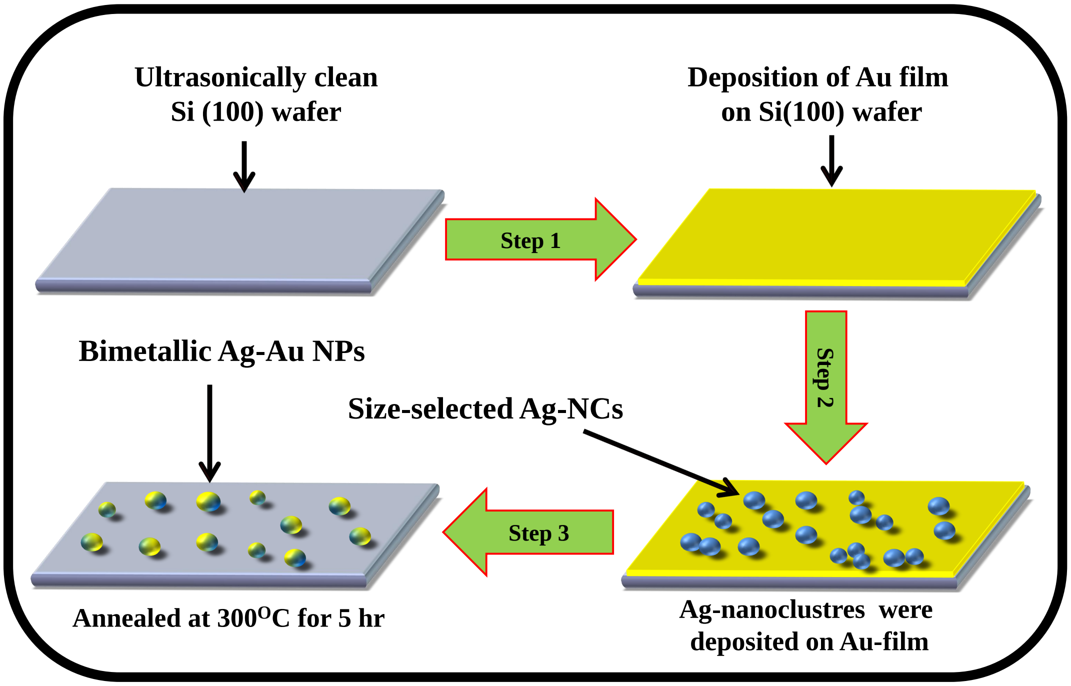

Figure. 5.8: *A schematic representation of formation of Ag-Au bimetallic nanoparticles.*

deposited film was performed at a temperature of ∼ 300 ^{o}C by utilizing an in-situ heating facility under ultra high vacuum condition. A schematic diagram describing the replica of the experimental procedure is shown in figure 5.8. The main goal of this experiment is to study the morphological and chemical intermixing of gold and silver over Si substrate without forming any metal-silicide composition. Hence, the as-deposited Ag-Au film was deliberately annealed at a temperature of 300 ^{o}C well below the eutectic melting temperature of silver-silicon alloy (∼ 840 ^{o}C) [202] and the eutectic temperature of gold-silicide (∼ 370 ^{o}C) [203]. The morphological analyses of the films were performed by the AFM in tapping mode using a Si tip of nominal radius of curvature value ∼ 8 nm and field emission scanning electron microscopy. The real time chemical intermixing of the Ag-Au composition during annealing the sample was studied by the in-situ x-ray photoelectron spectroscopy setup using a Mg-K$_\alpha$ source with photon energy of 1253.7 eV. The obtained XPS spectra were calibrated with

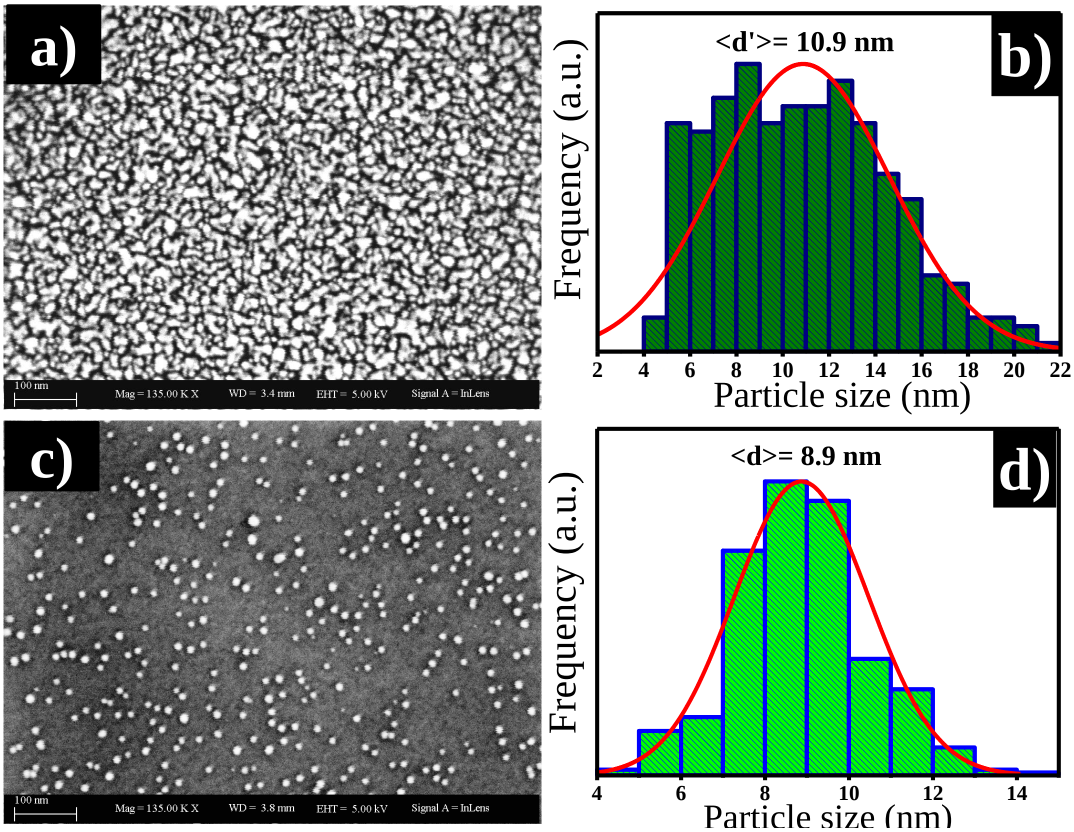

Figure. 5.9: *(a) SEM image and (b) corresponding histogram of the as-deposited Ag-Au film, (c) SEM image and (d)corresponding histogram of the Ag-Au film annealed at 300 ^{o}C for 5 hour.*

reference to Au 4f$_{7/2}$ of a gold foil at 84.0 eV. The sample was annealed at 300 ^{o}C for 5 hr at an interval of 1 hr and for the convenience we indicate the as-deposited Au-film as p-Au, as-deposited Ag-Au film as A0, annealed Ag-Au film from 1 hr to 5 hr as A1 to A5, respectively.

5.3.2 Results and discussions

5.3.2.1 Morphological analyses

Figure 5.9(a), shows the SEM micrograph of as-deposited Ag-nanoclusters on Au thin-film at room temperature. Some irregular shaped Ag-cluster aggregates are found to be formed over the Au-film. Each of the Ag-cluster aggregates represents the sum of many agglomerated neighboring Ag clusters over Au-film. The size-distribution histogram of these cluster aggregates is shown in figure 5.9(b). The histogram is obtained by measuring individual cluster aggregates manually with the help of ImageJ software. During the measurement, each of the cluster aggregates are considered to be circular and the lateral size of the particles are measured by drawing a line that passes through the center of the particle. In the size-distribution histogram, the lateral sizes of the cluster aggregates are found to vary from ~ 4 to ~ 22 nm.

The size-distribution is best fitted with Gaussian function indicated by the red solid line and from the fitting the average size of the cluster aggregates are found as $< d' > = 10.9$ nm. The measured average diameter of the cluster aggregates is much larger than the actual diameter i.e. 5 nm selected for deposition. This is because of the movement of deposited Ag-clusters over Au film where the Ag clusters are moved over the Au surface until it gets stabilized. To stabilized the Ag-clusters, either they have to form a bond with the substrate surface or with the neighboring clusters. In this process cluster aggregates are formed which is found to grow larger with the attachments of more incoming clusters and ultimately irregular shaped cluster islands are formed. The clusters are often assumed to be liquid drops [164,165,201] depending on the size and shape of the clusters and its resultant transformation on a surface. In this process it is assumed that clusters are compact in size and the binding energy between cluster-cluster is large as compared to that of cluster-surface. This is useful in determining the character of cluster evolution process on a particular surface until the surface is more or less free. In an ideal case, it is assumed that solid metal clusters are spherical in shape and after deposition they start moving on the surface due to diffusion process. In this process, interaction of clusters with surface leads to the formation and growth of cluster aggregates. Subsequent clusters join the cluster aggregates and form cluster islands as well as porous films containing small cluster aggregates. Using this concept, the process of film growth for Ag-clusters has been discussed elsewhere [164, 201].

The morphological changes occur when the as-deposited Ag-Au film undergo vacuum annealing for 5 hours at 300 ^oC as evident in figure 5.9(c). Formation of isolated circular nanoparticles on Si surface has been found in the SEM images. In the later part of this chapter, it is shown from the XPS analyses that these nanoparticles contain both the silver and gold in metallic state. Hence, these particles are considered as bimetallic Ag-Au nanoparticles (NPs). The size-distribution histograms of these bimetallic nanoparticles are measured using ImageJ software and presented in figure 5.9(d). In the histograms the lateral sizes of the particles are found to vary from $\sim$ 4 to $\sim$ 14 nm which is much narrower as compared to the distribution of Ag-cluster island formed on Au film. The distribution can be best fitted with Gaussian function shown by the red solid line in figure 5.9(d) and from the fitting the average particle size is found as $< d > = 8.9$ nm.

In particular, when a cluster film undergoes thermal annealing the fragmentation of cluster aggregates and cluster-islands takes place. In the present case when the as-deposited Ag-Au film undergoes annealing for a longer time, the irregular-shaped cluster aggregates with the thin Au film starts melting over the substrate. In the process of melting, the deposited features start re-arranging their size and shape to minimize the surface free energy energy of the films. Due to this we observe a decrease in coverage of the annealed film as compared to as-deposited film and can be verified from the SEM and AFM morphology. In the present experiment, the film annealed at 300 ^oC is lower than the melting point of bulk Au ($\sim$ 1064 ^oC) and bulk Ag ($\sim$ 962 ^oC). Although the melting temperature of bulk metal is very high, it is found that the melting temperature of nano-particle decreases with the decrease in their size [165,200]. Apart from this, many other theoretical and experimental studies reveal that the melting temperature of gold and silver in nano scale decreases with their reduced size [204–206]. The SEM images shown in figure 5.9(a) and (c) indicate similar melting phenomena and a decrease in particle size and shape is observed as compared to irregular cluster islands of as-deposited Ag-Au film. Hence, it is concluded that the as-deposited Ag-Au film experiences the molten state under the influence of annealing temperature at 300 ^{o}C for an annealing time of 5 hours under high vacuum conditions. In figure 5.9 the total number of atoms decreases after annealing the films at 300 ^{o}C for 5 hours and the same is depicted in microscopic images obtained by SEM and AFM. In both the images, we found a decrease in particle size after annealing the films for 5 hours. A rough estimation of total number of atoms present on the surface can be obtained from the size distribution curves shown in figure 5.9(b) and (d). The area under the curve represents the total number of atoms. The measured value of the area for the as-deposited film is found to be $\sim$ 266; while for the annealed film the area under the curve is found as $\sim$ 93. The decreased area of annealed film suggests that the total number of atoms on the surface decreases as compared to as-deposited film.

Figure 5.10(a) and (b) shows the AFM micrographs of as-deposited Ag-Au and annealed Ag-Au films. From the AFM images, it is is found that for the as-deposited film the surface is covered with irregular-shaped cluster aggregates whereas for the annealed film spherical shaped isolated particles are found on the surface. The morphologies obtained in AFM images are found to be in agreement with that of SEM images. The sizes of the particles appeared in the AFM image in figure 5.10(b) are found to be of slightly larger in diameter as compared to the particles that appeared in figure 5.9 (c) due to the convolution effect of the AFM tip. In this effect, the AFM tip will always overestimate the actual size of the particles during scan because of average particle radius smaller than the nominal tip radius. This tip convolution

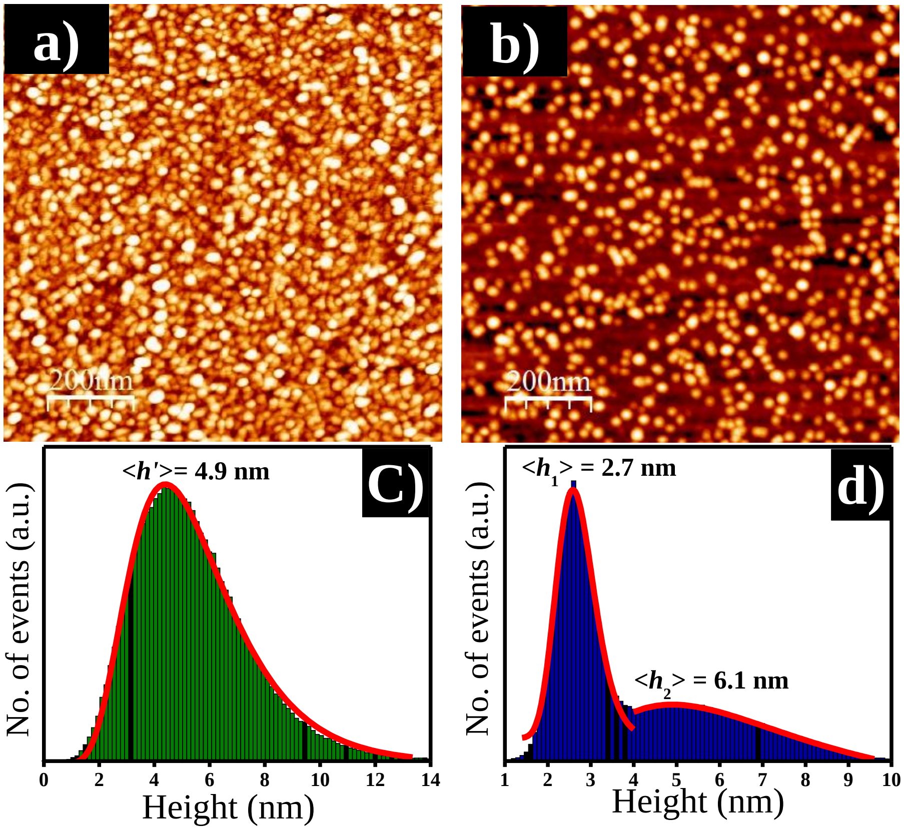

Figure. 5.10: *Typical AFM images with scan size ($1\ \mu m \times 1\ \mu m$) of (a) as-deposited Ag-Au film, (b) annealed Ag-Au film at 300 ^{o}C for 5 hours. The height-distribution histograms of the (c) as-deposited Ag-Au film, (d) annealed Ag-Au film. Solid red lines indicates the lognormal fitted curve.*

effect does not come into play during the measurements of particle height. The height distribution histograms of as-deposited and annealed Ag-Au films are extracted from their corresponding AFM images using the AFM image analysis software known as WsXM. Figure 5.10(c) represents the height distribution histograms of as-deposited Ag-Au films best fitted with the lognormal function as indicated by the red solid line. The average height is found to be $< h' > = 4.9$ nm. Figure 5.10(d) shows the height distribution histogram of annealed Ag-Au film. The overall distribution shows two types of peaks fitted with lognormal function as indicated by the red solid lines. The first peak shows the average height as $< h_1 > = 2.1$ nm whereas the second peak is appeared at the height of $< h_2 > = 6.1$ nm. The first height maxima ($< h_1 >$)

represents the average height of the exposed Si surface and the second height maxima ($< h_2 >$) represents the average height appeared due to the presence of NPs on the Si surface. Therefore, the actual average height of the NPs present on the surface is found to be $< H > \; = \; < h_2 > - < h_1 > \; \sim \; 3.4$ nm. Using the average height $< H >$ along with average lateral diameter $< d >$ of the nanoparticles, the average aspect ratio of the nanoparticles may be estimated. The average aspect ratio of the nanoparticles is found as ~ 1.5 indicating the shape of the nanoparticles formed on the surface almost spherical. From the AFM images, the rms roughnesses of the as-deposited and annealed Ag-Au are also measured. The obtained rms roughnesses of both the films are found as ~ 1.9 and ~ 1.8 nm, respectively. Hence, it can be concluded that the rms roughness of the film is not affected by the annealing process at all.

5.3.2.2 XPS analyses

The XPS survey spectra of as-deposited Au film on Si substrate and as-deposited Ag-NCs on Au-film at room temperature is shown in figure 5.11. From the XPS survey spectra of as-deposited Au film, various strong peaks such as Au 4f, Au 4d, O 1s, C 1s along with the weak peak of Si 2p are observed. In the XPS survey spectra obtained for as-deposited Ag-NCs on Au films, the presence of gold and silver is verified from the dominant peaks of Au 4d, Au 4f, Ag 3d, Ag $3p_{1/2}$, Ag $3p_{3/2}$. Apart from the dominant peaks we also observe weak peaks of O 1s and C 1s. In both the XPS survey spectra, weak signals of Si and O are found. This is because XPS is a surface sensitive technique in which we are able to get elemental information from the outermost 8 - 15 nm of the material (or thin-film) as the incident x-ray can penetrate 8 - 15 nm in the film depending on the atomic number of the metal. In the present case, the Au thin film is a continuous layer above which size-selected clusters are deposited. These Ag nanoclusters agglomerate over the gold thin film

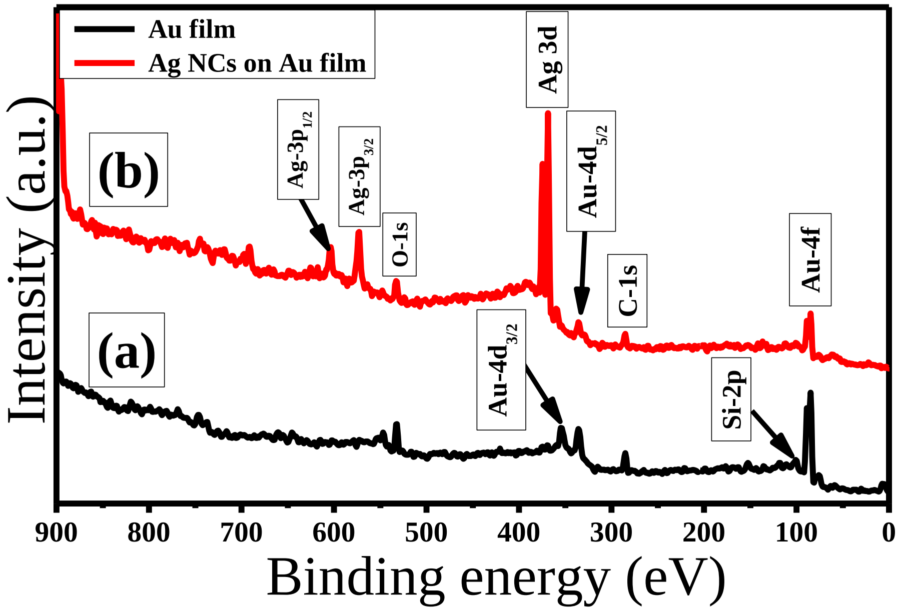

Figure. 5.11: *XPS survey spectra at room temperature for the (a) as-deposited Au film on Si substrate (b) as-deposited Ag-Au film on Si substrate.*

with a coverage of ∼ 80%. Hence, we get very weak signals of O and Si than that of Au. The atomic concentrations of each of the elements present on the surface are also estimated by taking their appropriate relative sensitivity factors (RSF). Using the first spectrum, the total atomic concentration of Au and Si are found as 59% and 19%, respectively whereas, in the second spectrum these concentrations decreases to 11% and 8%, respectively. This is because the surface of the film associated with second spectrum is fully covered with the newly deposited Ag-NCs and the same is corroborated by morphology found in AFM and SEM studies. Due to the presence of Ag-cluster aggregates on the upper surface, the x-ray could not reach the lower surfaces and as a result, concentration of both the Au and Si is found to reduce as compared to their corresponding previous values. The total concentration of Ag dominates over the concentration of other element present, which is ∼ 62%.

High-temperature XPS survey spectra of the films annealed for 1 hour to 5

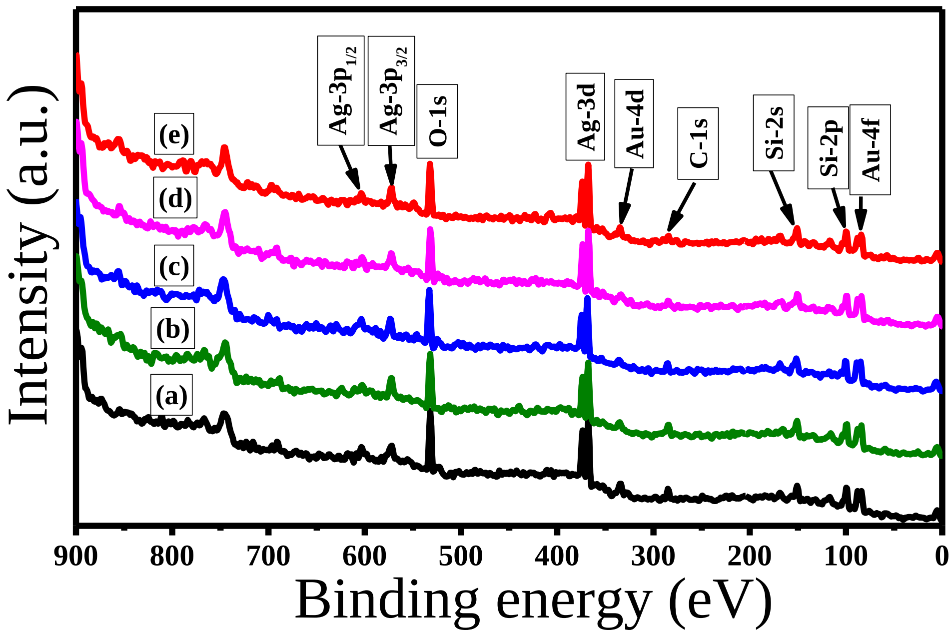

Figure. 5.12: *High-temperature XPS survey spectra of the Ag-Au films annealed at 300 º C for (a) 1 hour,(b) 2 hours, (c) 3 hours, (d) 4 hours, and (e) 5 hours.*

hours at an interval of 1 hour are illustrated in figure 5.12. With the increase in annealing time, significant changes are observed on the spectra. In all the spectra, various peaks of gold, silver, oxygen and carbon are found to be appeared. The strong peak that appeared at the binding energy of 367 eV corresponds to Ag 3d. Moreover, additional two peaks of silver are found at the binding energies of 602 and 571 eV for Ag $3p_{1/2}$ and Ag $3p_{3/2}$, respectively. The peaks found at ∼ 84 and ∼ 334 eV correspond to Au 4f and Au 4d states, respectively. A strong peak of O 1s is observed at ∼ 532 eV for every spectra. Furthermore, it is found that with the increase in annealing time the Si 2p peak appeared more prominently. In particular, as the annealing time increases the nanocomposite film starts melting and diffusion of Ag and Au occurs over the surface. Due to this we found a reduced coverage of the nanocomposites and the Si surface is more exposed to the x-ray which is also observed in the SEM and AFM morphologies. The XPS peaks appeared due to the underlying Si surfaces found at ∼ 149 and 99 eV are assigned to Si 2s and Si 2p, respectively.

Table 5.2: *Elemental composition of Au film, Ag-NCs on Au (A0) and annealed samples using Quantitative surface analysis of XPS data.*

Sample	**Au (at. %)**	**Ag (at. %)**	**Si (at. %)**	**O (at. %)**	**C (at. %)**
p-Au	59	0	19	15	7
A0	11	62	8	12	7
A1	10	28	29	24	8
A2	8	21	37	25	8
A3	7	19	40	26	7
A4	6	19	41	26	7
A5	5	16	46	27	6

The total estimated atomic concentration for all the elements present on each of the spectrum are summarized in Table 5.2. From Table 5.2, it is found that the total atomic concentration of Ag decreases from 62% to 28% after 1 hour of annealing and the total concentration of Au decreases from 11 % to 10%. Moreover, an increase of total concentration of Si from 8% to 29% is found to be due to the diffusion of Ag and Au over the Si surface. As the annealing time is increased from 1 to 5 hours, the total concentration of Si keeps on increasing because of further exposure of the substrate surface to x-ray due to more diffusion of Ag and Au. Hence, the total concentration of Au and Ag are also found to be decreased. Throughout the annealing process, the concentration oxygen is found to be slightly increased from 24% to 27%.

The variation of total atomic concentration of various elements with annealing time is illustrated in figure 5.13. It is found that the total concentration of Ag decreases exponentially whereas the concentration of Au decreases linearly as the annealing time increases. The diffusion of Au and Ag over Si surface at such a high temperature is one of the reasons for the reduced concentrations. However, sublimation of top Ag layer with the increased annealing time may be another possible reason for such an abrupt decrease in total Ag concentration. The sublimation of the films is also supported by the nature of the curve obtained in high-resolution Si 2p spectra where it is found that the intensity of the deconvoluted Si-Si peak increases

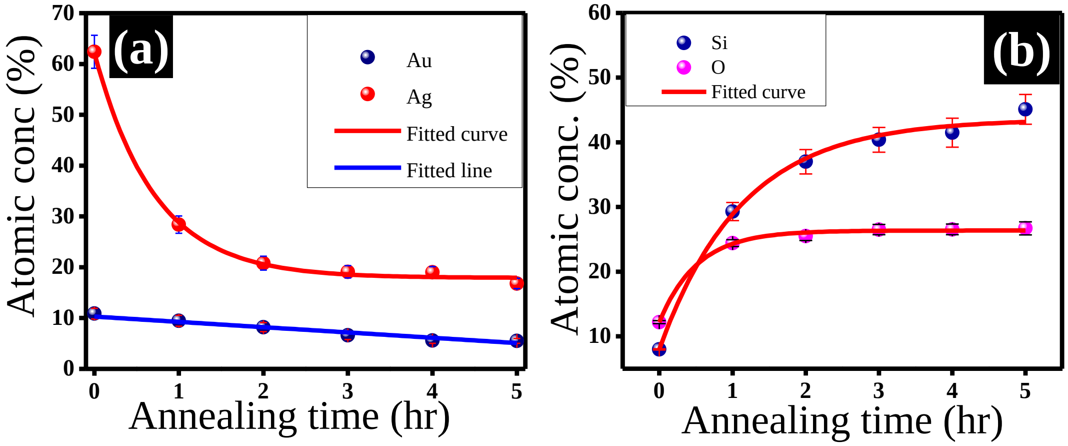

Figure. 5.13: *Variation of total atomic concentration of (a) Ag and Au, (b) Si and O with annealing time.*

with annealing time. Furthermore, the total atomic concentrations of Si and O are found to increase exponentially with the annealing time.

5.3.2.3 High-resolution X-ray photoelectron spectroscopy (HR-XPS)

The analysis of HR-XPS spectra is made for all the samples in order to understand the chemical states of the elements. In this regards, the deconvoluted HR XPS spectra of Ag 3d and Au 4f along with O 1s and Si 2p are discussed below.

(a) Ag 3d core-level spectra: Figure 5.14 shows the high-resolution XPS spectra of core level Ag 3d of as-deposited Ag-NPs on SiO_2 substrate, as-deposited Ag-Au alloy film and vacuum annealed Ag-Au films. In all the spectra, two spin orbit splitted peaks of silver namely Ag $3d_{5/2}$ and Ag $3d_{3/2}$ are found to be separated by $\sim$ 6 eV [207]. For comparison, the deconvoluted peaks of Ag 3d of as-deposited Ag nanoparticles on a bare silicon substrate are shown in figure 5.14(a). Upon deconvolution, four peaks are observed out of which two peaks found at 368.3 and 367.5 eV are associated with Ag $3d_{5/2}$. Other two peaks appeared at 374.3 eV and 373.5 are associated with Ag $3d_{3/2}$. Figure 5.14(b), shows the deconvoluted Ag 3d

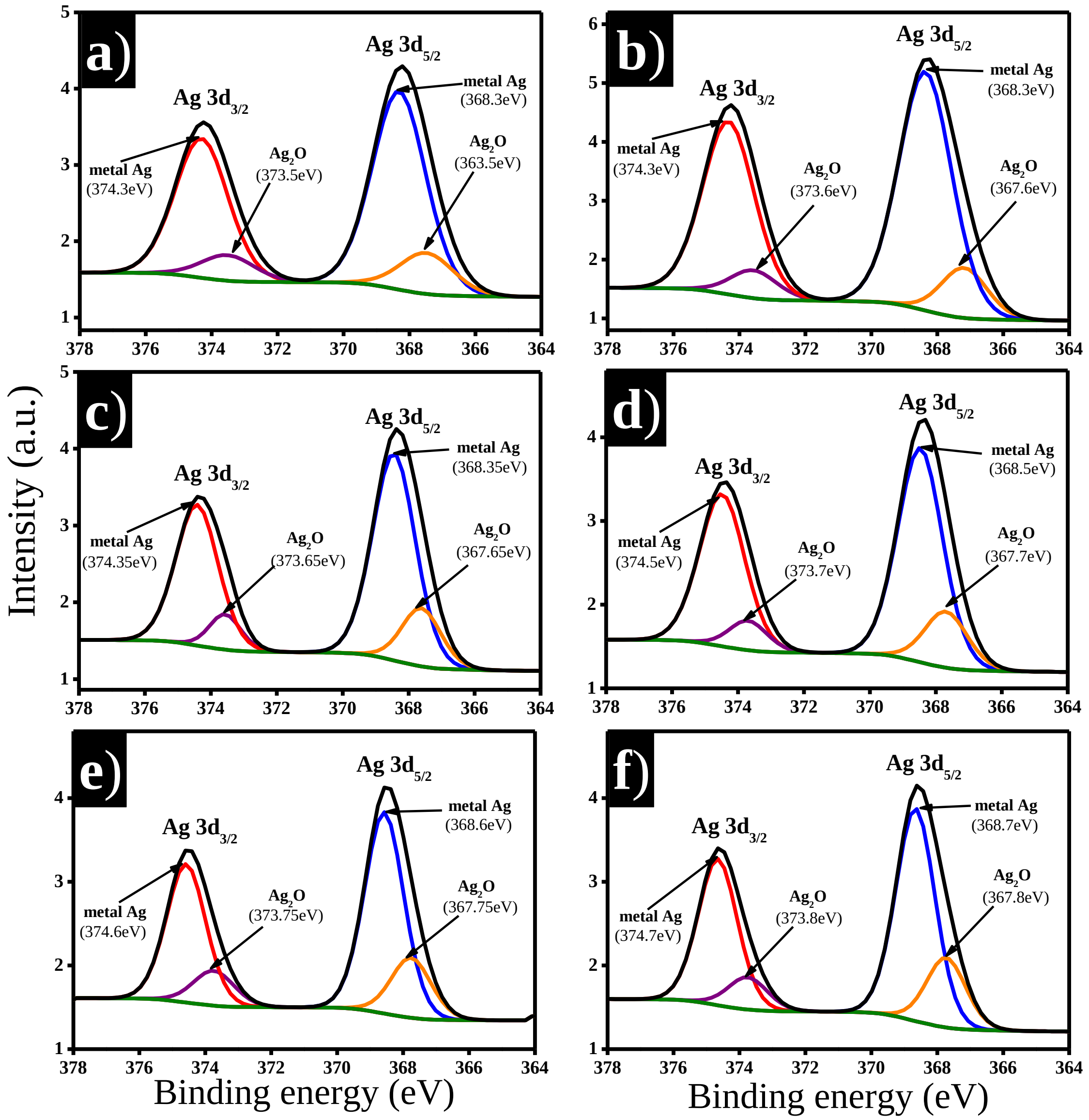

Figure. 5.14: *Deconvoluted high-resolution XPS spectrum of core level Ag 3d for (a) as-deposited Ag-NPs on Si/SiO$_2$, (b) as-deposited Ag-Au film and vacuum annealed at 300 ^{o}C Ag-Au film for annealing time of (c) 1 hour, (d) 2 hours, (e) 3 hours and (f) 4 hours.*

spectra for the as-deposited Ag-Au film. The obtained peak positions of Ag-Au alloy film are found to be exactly similar to the peak positions for the monometallic Ag-NP-deposited film. After deconvolution. it shows four peaks, out of which the components of Ag 3d$_{5/2}$ are found at the binding energy positions of 368.3 eV and 367.6 eV which correspond to metallic silver and silver ions of Ag$_2$O, respectively [208, 209]. In a similar way, the components of Ag $3d_{5/2}$ found at the binding energies of 374.3 and 373.6 eV are associated with metallic silver and Ag ion of Ag_2O, respectively [208,209]. The observed peak position of metallic silver is found to be slightly higher than that of the peak position obtained for bulk Ag 3d [169, 210] and the results are in good agreement with the reported values of Ag-Au alloy nanoparticles [211, 212]. The core-level Ag 3d peak of Ag-Au film annealed at 300 ^{o}C for 1 hour under ultrahigh vacuum condition is shown in figure 5.14(c). After deconvolution, we found four peaks where two of them are associated with metallic Ag whereas other two peaks represent oxidized silver. The observed deconvoluted peaks are found $\sim$ 0.1 eV higher than the deconvoluted peaks of Ag 3d for the as-deposited Ag-NPs films and as-deposited Ag-Au film. In similar manner the deconvoluted metallic and oxide peaks show a shift in peak positions towards higher binding energies as the annealing time increases from 1 to 5 hours as shown in figure 5.14(c)-(f). The final peak positions of metallic silver are found at 368.7 and 374.7 eV and oxide peaks are appeared at 367.8 and 373.8 eV for the 5 hr-annealed film. The observed binding energy shift in Ag 3d is possibly due to the deposited particle size effect also observed in our previous study. A report by Salido *et al.* [170] also shows the influence of size effect that causes the binding energy shifting of Ag 3d peaks towards higher value. In the present experiment, from the morphology obtained in SEM and AFM we find that the particle sizes decrease with the annealing time. Furthermore, Ag is highly electonegative in nature whereas Au shows higher electron affinity. There is a possibility of transfer of electrons from Ag to Au responsible for Ag peak shift. The observed peak positions and their FWHM of all the spectra are summarized in Table 5.3. Moreover, the total relative concentration contributed by metallic silver in the Ag 3d spectra is found between $\sim$ 76 to $\sim$ 78%. Furthermore, in Table 5.3 the obtained FWHM values of the deconvoluted peaks are found constant for the samples annealed for more than 1 hour.

Table 5.3: Elemental analysis of core level Ag 3d spectra of Ag-NPs, as-deposited Ag-Au alloy film (A0), and vacuum annealed (at 300^{o}C) Ag-Au alloy NPs (A1-A5).

Sample	**Ag 3d$_{5/2}$**		**Ag 3d$_{3/2}$**	
	BE(eV)	FWHM	BE(eV)	FWHM
Ag-NPs	368.3	1.9	374.3	1.9
A0	368.3	1.85	374.3	1.85
A1	368.35	1.53	374.35	1.52
A2	368.5	1.5	374.5	1.5
A3	368.6	1.4	374.6	1.4
A4	368.7	1.4	374.7	1.4
A5	368.7	1.4	374.7	1.4

(b) Au 4f core-level spectra: Figure 5.15 shows the high-resolution XPS spectra of core-level Au 4f for the as-deposited Au-film, as-deposited Ag-Au film and vacuum annealed Ag-Au films. Due to spin-orbit splitting effect all the Au 4f spectra show two photoemission peaks namely Au 4f$_{7/2}$ and Au 4f$_{5/2}$ separated by a binding energy $\sim$ 3.7 eV [207]. The intensity ratio of Au 4f$_{7/2}$ and Au 4f$_{5/2}$ for each of the spectra are found to be $\sim$ 1.33. For comparison, we have shown the Au 4f peaks of as-deposited Au-film on Si substrates in figure 5.15(a). The spectrum shows two metallic peaks of Au 4f at the binding energies of 84 and 87.7 eV associated with Au 4f$_{7/2}$ and Au 4f$_{5/2}$, respectively. The obtained values are in agreement with the binding energy of bulk Au 4f. Figure 5.15(b) represents the high-resolution Au 4f spectrum for the as-deposited Ag-Au film. The obtained peak positions show exact match with the peak position for as-deposited Au-film. The intensity and FWHM of these peaks are found to be decreased as compared to the peaks appeared for Au-film. The core-level Au 4f peaks of Ag-Au films annealed at 300 ^{o}C for 1 to 5 hours under ultrahigh vacuum condition is shown in figure 5.15(c)-(f). It is found that as the annealing time increases, the peak positions of Au 4f continuously shift towards higher value. Since Au has higher electron affinity as compared to Ag, there is a probability of exchange of electron from Ag to Au that may be responsible for the Au 4f peak shift towards higher value [213,214]. Apart from the peak shift, the peak area

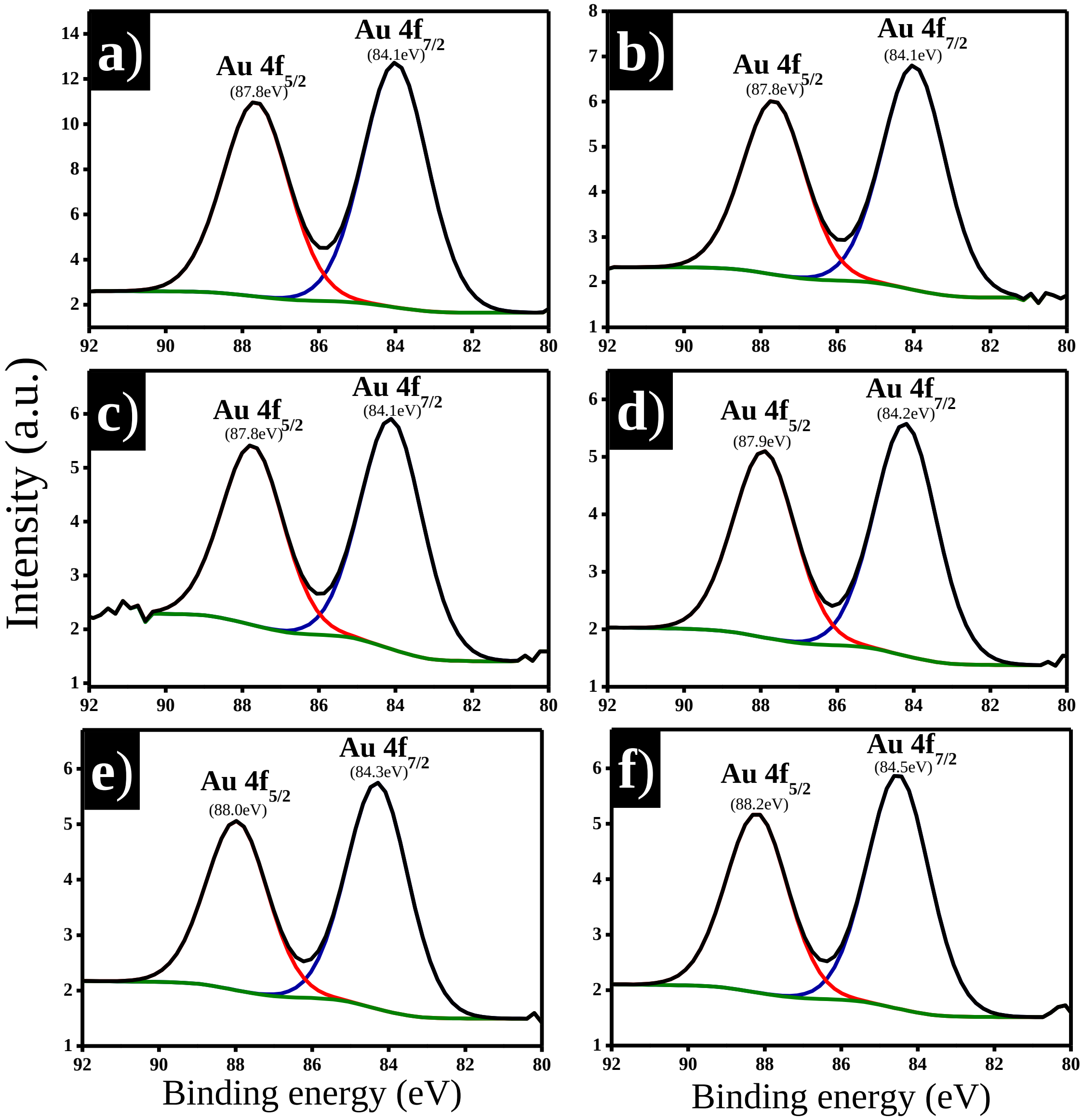

Figure. 5.15: *Deconvoluted high-resolution XPS spectrum of core level Au 4f for (a) as-deposited Au-film on Si/SiO$_2$, (b) as-deposited Ag-Au film, and vacuum annealed (at 300 ^{o}C) Ag-Au film for annealing time of (c) 1 hour, (d) 2 hours, (e) 3 hours and (f) 4 hours.*

is also found to be decreased with the increase in annealing time. Moreover, from the analysis of the Au 4f spectra, it is found that Au is not chemically bonded with oxygen to form gold oxide at any stage and the same is verified from the absence of gold oxide peaks at the binding energies at 89.5 and 85.8 eV for Au 4f$_{5/2}$ and Au 4f$_{7/2}$, respectively [213]. The final peak positions of Au 4f doublet peak for the annealed

Table 5.4: XPS data for the core level Au 4f spectrum of Au-film, as-deposited Ag-Au alloy film (A0), and vacuum annealed (at 300 ^{o}C) Ag-Au alloy NPs (A1-A5).

Sample	**Au 4f$_{7/2}$**		**Au 4f$_{5/2}$**	
	BE(eV)	FWHM	BE(eV)	FWHM
Au-film	84.1	2	87.8	2
A0	84.1	1.94	87.8	1.94
A1	84.1	1.93	87.8	1.93
A2	84.2	1.92	87.9	1.92
A3	84.3	1.90	88.0	1.91
A4	84.5	1.91	88.2	1.91
A5	84.5	1.91	88.2	1.91

film are found at 84.5 eV for Au 4f$_{7/2}$ and 88.2 eV for Au 4f$_{5/2}$ that correspond to metallic Au [211, 215, 216]. The obtained binding energies are found similar to Au 4f of bimetallic Ag-Au alloy particle, reported by Sangpour *et al.* [211, 212]. The peak positions and FWHM of Au 4f doublet peaks for each of the spectra are listed in Table 5.4 where it is found that the FWHM values of the peaks are constant for the films annealed beyond 1 hour.

(c) O 1s core-level spectra: Figure 5.16 shows the deconvoluted XPS spectra for O 1s for all the samples. For the as-deposited Ag-Au film, the obtained O 1s spectrum is shown in figure 5.16(a). The deconvolution of this peak shows three peaks which are appeared at the binding energy positions of 530.3, 531.8 and 533.1 eV. The peak found at the binding energy position of 530.3 eV corresponds to AgO [217] whereas the peak appeared at binding energy of 533.1 eV is associated with SiO_2 [218]. The peak found at the binding energy of 531.8 eV is attributed to carbon-oxygen bond [218] appeared due to the presence of carbon contamination on the sample and it is found to be partially oxidized with the increase in annealing time. Upon perusal of all the O 1s spectra, we have not found any evidence of formation of gold-oxide on the films. Figure 5.16(b) shows the high-resolution O 1s spectrum for the 1 hour-annealed film. After deconvolution, it shows three peaks at binding energies of 531.7, 530.8 and 532.3 eV. The peak appeared at the binding energy of 530.8 eV corresponds

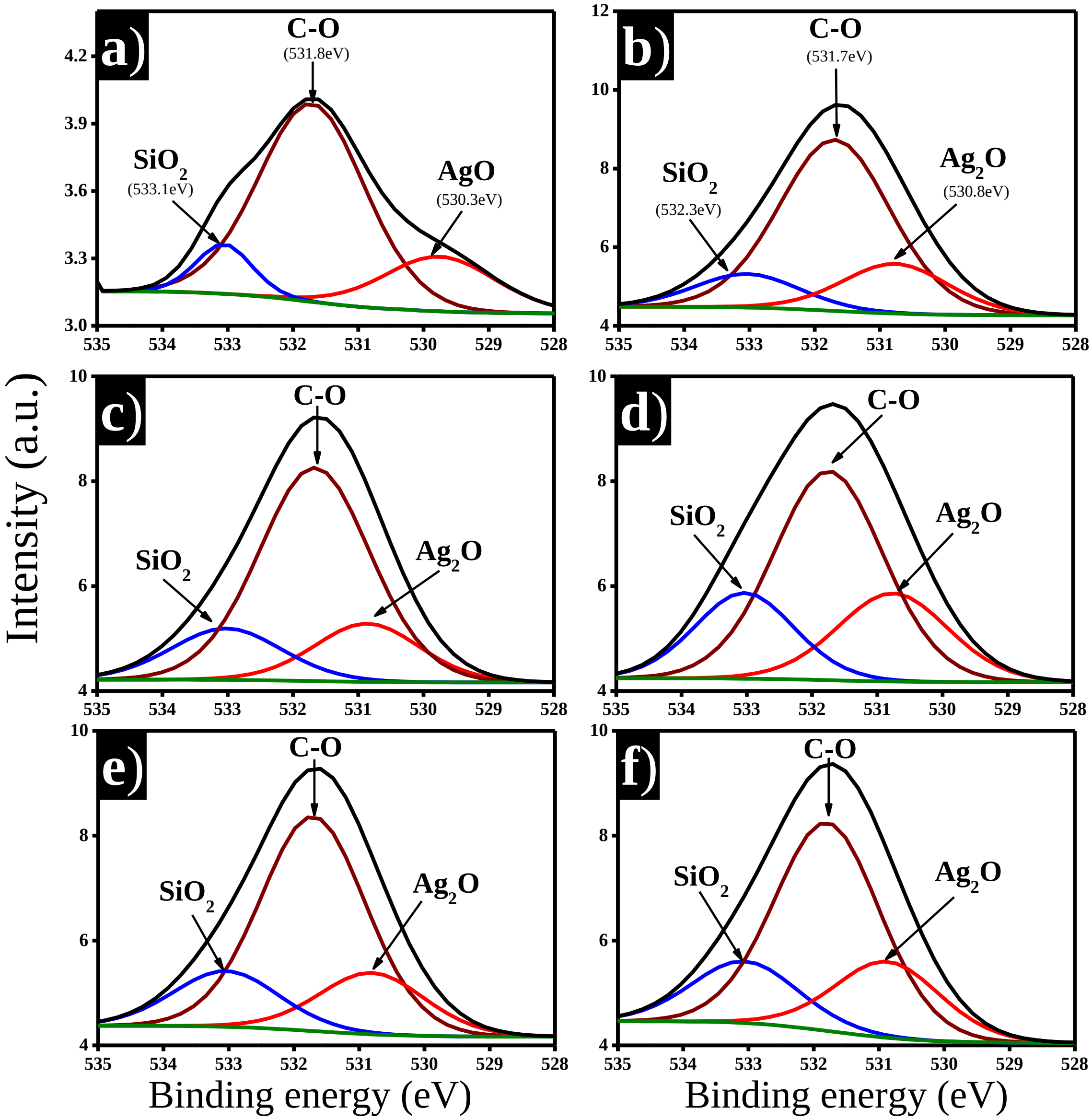

Figure. 5.16: *Deconvoluted high-resolution XPS spectrum of core level O 1s for (a) as-deposited Ag-Au film, and vacuum annealed (at 300 °C) Ag-Au film for annealing time of (b) 1 hour, (c) 2 hours, (d) 3 hours, (e) 4 hours and (f) 5 hours.*

to Ag_2O which might be originated due to a shift in AgO peak of as-deposited film because the AgO structure cannot survive at high temperature [163]. We also observe a shift in peak values for SiO_2 from binding energy of 533.1 to 532.3 eV upon annealing of the as-deposited film for 1 hour. As the annealing time increases, the O 1s peaks consistently show three deconvoluted peaks as shown in figure 5.16(c)-(f).

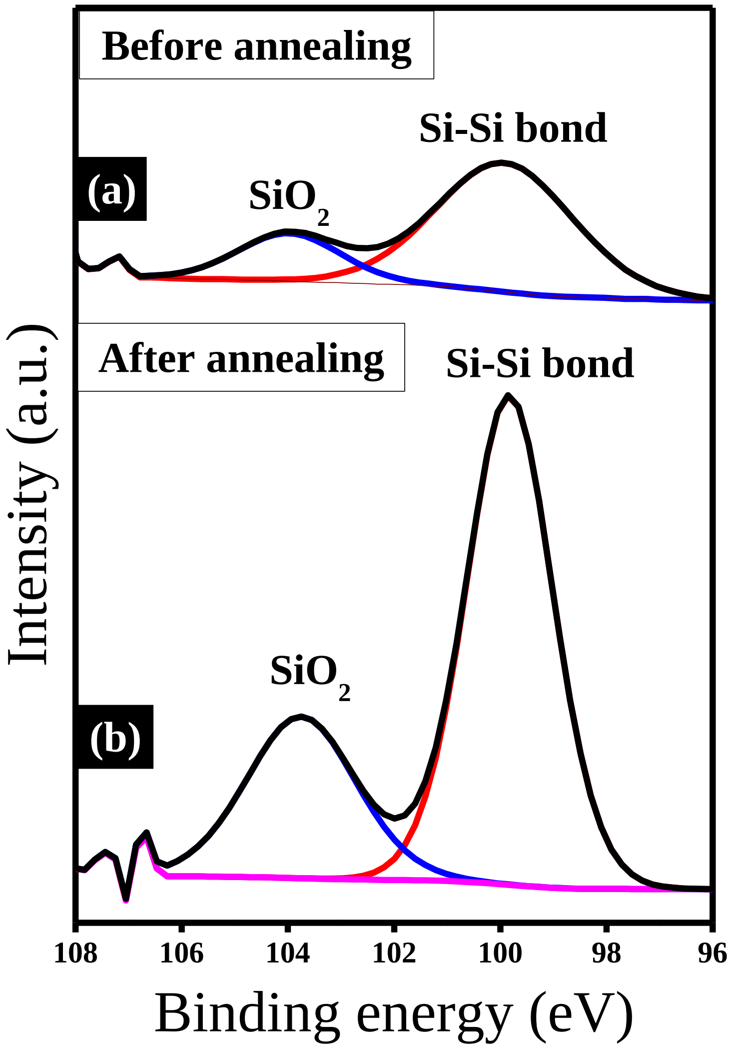

Figure. 5.17: *Deconvoluted high-resolution XPS spectrum of core level Si 2p for (a) as-deposited Ag-Au film and (b) vacuum annealed (at 300 ^oC) Ag-Au film for annealing time of 5 hours.*

(d) Si 2p spectra: Figure 5.17 shows the high-resolution Si 2p spectra of the as-deposited and 5-hour annealed Ag-Au film. The as-deposited Ag-Au film in which the total atomic concentration of Si is found as $\sim$ 8 % show very low intense peaks appeared at the binding energies of 99.8 and 103.7 eV. The peak appeared at 99.8 eV represents the Si-Si bond of bulk Si substrate which is found beneath the silicon-oxide layer [219]. The other peak appeared at 103.7 eV is associated with SiO$_2$ and its presence is further verified from the deconvoluted O 1s peak appeared at 533.1 eV.

These two peaks of Si 2p are appeared in all the annealed films, although the intensity of the peaks are found to be gradually increased. The deconvoluted XPS spectra of Si 2p for the 5 hour-annealed film in figure 5.17(b) also corroborate the observation. Moreover, from the deconvoluted Si 2p spectra, we did not found any metal silicide peak at any stage. The possibility of formation of metal-silicide on the annealed films is ruled out. From the obtained spectra of Si 2p, it is also found that the intensity of the peaks for as-deposited Ag-Au film is very low as compared to the annealed film also corroborate the observations on an increase in atomic concentration of Si from 8% to 46% as evident from Table 5.2. At the early stage of deposition, when the surface is fully occupied by the Ag and Au for the as-deposited Ag-Au film, the emitted photoelectrons from the Si surface is very low as compared to the annealed film where the Si surface is found fully exposed. This occurs due to the escape depth of photoelectrons and we get a low intense Si 2p spectrum for as-deposited film whereas we observe an intense Si 2p spectrum for the annealed film.

5.3.3 Conclusion

In conclusion, a new method is employed to produce bimetallic Ag-Au NPs in an ultra-high vacuum chamber followed by an annealing process. The formation of bimetallic Ag-Au NPs are monitored by in-situ x-ray photoelectron spectroscopy technique. With the increase in annealing time, the total composition of silver and gold in the bimetallic NPs are found to decrease and finally at an annealing time for 5 hour the obtained composition ratio of silver to gold is found to be $\sim$ 3:1. From FESEM analyses, the produced bimetallic NPs are found to be uniformly distributed over the substrate with a narrow size-distribution having an average particle diameter of $\sim$ 8.9 nm. AFM measurements reveal insignificant changes in the roughness of the films before and after annealing. The obtained average aspect ratio suggests that the produced bimetallic NPs are almost spherical in shape. From the HR-XPS analysis we observe binding energy shift of core level silver and gold spectra as a consequence of particle-size effect.

Chapter 6

Summary and future scope

In this chapter, the overall thesis works along with the important findings are summarized.

6.1 Summary

The main goal of this thesis is to understand the growth mechanism of metal nanoclusters on Si substrate under various experimental conditions and the influence of interfacial growth over different film properties such as morphological, optical and wetting properties. In order to study their growth behaviour on the substrate, metal nanoclusters were grown within a gas-aggregation nanocluster source and then deposited their size-selected beam on a Si substrate. Apart from the growth behaviour study, an attempt is also made to prepare bimetallic Ag-Au nanoparticles using two-step synthesis method to study their microscopic and spectroscopic properties. The chapter-wise significant findings are described in the thesis as stated below-

In Chapter 1, a brief introduction of nanoclusters, their types and formation mechanism as well as their importance in various fields of research are discussed. Apart from that a detailed explanation of cluster-surface interaction and their role in various types of growth processes are discussed.

In Chapter 2, production of metal nanoclusters and their optimization inside a magnetron based nanocluster source are discussed. Along with that a detailed explanation of various microscopic and spectroscopic tools used for the characterization of nanoclusters are discussed.

In Chapter 3, the growth dynamics of size-selected Cu and Ag nanoclusters is studied on Si substrates. To study the dynamics of surface growth, experiments were carried out at different deposition times. Various surface statistical parameters of the deposited films were analyzed using the AFM micrographs of the films. From the study, it is found that at initial stage of film formation, deposited metallic clusters are randomly distributed over the substrate where the probability of agglomeration

and diffusion of clusters are very low. After a certain time of deposition, the growth of another layer takes place over the pre-existed first layer. Therefore, a change in rms roughness of the films is observed. Experimentally obtained growth exponent (β) exhibits two steps of evolved surface where the first one is associated with sub-monolayer accumulation of the nanoclusters and second one is associated with the multi-monolayer growth. The first growth step is found to follow the Kardaar-Parisi-Zhang model. The most important achievement of this research is to find a second growth step with a higher growth exponent mostly dominated by the shadowing effect. The shadowing effect comes into play when deposition occurred at non-normal incidence. In this process, the pre-existed cluster aggregates act as taller surface which captured most of the incoming clusters and prevent them from reaching the lower lying surface areas or valleys. Although the shadowing effect is dominant in the second growth step, the probability of occurrence of re-emission also exists and as a consequence we find the value of growth exponent(β) slightly lower than unity.

In Chapter 4, the evolution of surface morphology of cluster deposited films as a function of incident ion current has been observed. The knowledge of evolution of the surface morphology for nanocluster-deposited surface has tremendous importance for the development of nanopaticle-based devices. An important issue of surface roughening by depositing size-selected Ag-nanoclusters on planner Si substrates for different ion beam currents is addressed here. It is found that with the increase in ion beam current the Ag cluster aggregates on the surface are enhanced by increasing their size and shape as well. Initially cluster aggregates form small nano-dot structures that evolve into mound-like structure at higher ion currents. Upon analyzing the size-distribution histograms, it is found that the size distribution is bi-modal in nature up to a certain ion beam current which turns out to be mono-modal for higher ion beam current. The upper average size is found to be increased monotonically with ion beam current. The character of the film growth were analysed by AFM measurements using

which we have estimated some of the important surface statistical parameters such as interface width, autocorrelation function, Hurst exponent and fractal dimension. The interface width of the films increases very rapidly with the evolution of the films. The lateral correlation length (ξ) of the films increases with ion beam current. The fractal dimension value of the films also increases with ion beam current suggesting formation of locally jagged surface at higher ion current. From the compositional analysis of the films it is found that the total concentration of silver on the surface increases monotonically with ion beam current. The presence of metallic silver is observed for all the Ag-cluster aggregate films. The water contact angle (CA) study reveals that there is a transition in wettability from hydrophilic to hydrophobic nature of the film with the increase in ion current. The increased amount of silver on the surface with increased ion current may be one of the possible reasons for the change in wettability of the films. Moreover, one of the surface morphological parameter namely, fractal dimension may be another contributory factor influencing the wetting property of the films. It is also observed that the surface developed for highest ion current only satisfies the Wenzel's model.

In Chapter 5, the behaviour of different cluster properties are investigated by varying the deposition temperature of the films. The study shows that the average Ag-cluster aggregate size over the untreated Si substrate increases with the increase in annealing time. But the average cluster size is found to be decreased when the clusters deposited on thermally treated Si substrate was further annealed for longer time. Considering the above morphological variation with annealing temperature and time an attempt is made to synthesize the bimetallic Ag-Au nanoparticles on Si substrate. The bimetallic Ag-Au nanoparticles were prepared by two-step synthesis methods where size-selected Ag-nanocluster with diameter of 5 nm was deposited on an as-prepared Au-film and annealed at an elevated temperature of $\sim 300\ ^{o}$C upto an annealing time of 5 hours. From the morphological investigation of the films, it

is found that the size of bimetallic nanoparticles over the Si film decreases with the increase in annealing time that may be due to diffusion of Ag and Au over Si surface. It is also found that the obtained bimetallic nanoparticles are uniformly distributed over the surface with a narrow size distribution. The composition of these bimetallic nanoparticles were investigated by in-situ XPS measurements. It reveals that after 5 hours of annealing the compositional ratio of Ag to Au on the bimetallic nanoparticles is found as $\sim$ 3:1. It is also observed that the core level Ag 3d and Au 4f peaks shifted towards higher binding energy with increasing annealing time indicate a decrease in size of the bimetallic Ag-Au nanoparticles with annealing time. The analysis of core level O 1s peaks shows that a small fraction of silver of the bimetallic nanoparticles gets oxidized whereas no trace of oxidation of gold is observed. Moreover, metal silicide peaks in the high resolution XPS spectra are not observed at any stages of annealing.

6.2 Future scope

Controlling the size of the nanoclusters during their synthesis is one of the important factors for the fabrication of various nanoparticle-based devices. Production of size-selected nanoclusters has a wide variety of applications due to their unique behaviour as compared to their bulk counterparts. Considering the research observations and conclusion of this thesis, there are several research directions that may be pursued in future. A few of research activities to be pursued in future are the following:

- Study on the size-effect of silver cluster on its surface plasmonic properties and utilize the properties for enhancing the efficiency of the solar cell.
- Study on the surface enhanced Raman scattering (SERS) of Ag nanoclusters of

a particular size and use the property for the fabrication of sensor-based devices.

- Study on the optical properties of bimetallic Ag-Au nanoparticles by tuning its compositions for various device applications.
- Study on modification of the target material(s) for the production of multi-metallic nanoclusters in a single step with controlled size, shape and composition.

Bibliography

[1] R.P. Feynman, A lecture ("There's Plenty of Room at the Bottom: An Invitation to Enter a New Field of Physics") given by Physicist Richard Feynman at the Annual American Physical Society meeting at Caltech on December 29, 1959; *California Institute of Technology Journal of Engineering and Science* **4** (1960) 23.

[2] H. Haberland, *Clusters of atoms and molecules*, First ed., Springer-Verlag, New York, 1994.

[3] M. Wolf, *RSC Adv.*, **11** (2021) 18187.

[4] R.L. Johnston, *Atomic and molecular cluster*, First ed., Taylor & Francis, New York, 2002.

[5] P. Pawlow, *Z. Phys. Chem.* **65** (1909) 1.

[6] P. Pawlow, *Z. Phys. Chem.* **74** (1910) 562.

[7] P. Baffat, J.P. Borel, *Phys. Rev. A* **13** (1976) 2287.

[8] R.S. Berry, J. Jellinek, G. Natanson, *Phys. Rev. A* **30** (1984) 919.

[9] R.S. Berry, D.J. Wales, *Phys. Rev. Lett.* **63** (1989) 1156.

[10] T. Castro, R. Reifenberger, E. Choi, R.P. Andres, *Phys. Rev. B* **42** (1990) 8548.

[11] A.A. Shvartsburg, M.F. Jarrold, *Phys. Rev. Lett.* **85** (2000) 2530.

[12] G.A. Breaux, R.C. Benirschke, T. Sugai, B.S. Kinnear, M.F. Jarrold, *Phys. Rev. Lett.* **91** (2003) 215508.

[13] M. Arenz, S. Gilb, U. Heiz, *Chem. Phys. Sol Surf.* **12** (2007) 1.

[14] U. Landman, B. Yoon, C. Zhang, U. Heiz, M. Arenz, *Topics in Catalysis.* **44** (2007) 145.

[15] U. Heiz, A. Sanchez, S. Abbet, W.D. Schneider, *Eur. Phys. J. D* **9** (1999) 35.

[16] M.D. Kane, F.S. Roberts, S.L. Anderson, *Int. J. Mass Spectrom.* **370** (2014) 1.

[17] U. Heiz, W.D. Schneider, *J. Phys. D Appl. Phys.* **33** (2000) R85.

[18] H. Poppa, *Catal. Rev.* **35** (1993) 359.

[19] M. Chen, D.W. Goodman, *Chem. Phys. Sol. Surf.* **12** (2007) 201.

[20] N. Mammen, L. Spanu, E.C. Tyo, B. Yang, A. Halder, S. Seifert, M.J. Pellin, S. Vajda, S. Narasimhan, *Eur. J. Inorg. Chem.* **2018** (2017) 16.

[21] H. Zhang, H. Zhou, Y. Wang, S. Li, P. Biswas, *Energy & Fuels* **35** (2021) 63.

[22] C. Schulz, T. Dreier, M. Fikri, H. Wiggers, *Proc. Combust. Inst.* **37** (2019) 83.

[23] L.Y. Lin, S. Kavadiya, X. He, W.N. Wang, B.B. Karakocak, Y.C. Lin, M.Y. Berezin, P. Biswas, *Chem. Eng. J.* **389** (2020) 123450.

[24] S.Y. Dhumal, T.L. Daulton, J. Jiang, B. Khomami, P. Biswas, *Appl. Catal. B.* **86** (2009) 145.

[25] I. Dogan, M.C. van de Sanden, *Plasma Process. Polym.* **13** (2016) 19.

[26] M. Armand, J.M. Tarascon, *Nature.* **451** (2008) 652.

[27] T.J. Patey, R. Bchel, S.H. Ng, F. Krumeich, S.E. Pratsinis, P. Novk, *J. Power Source.* **189** (2009) 149.

[28] M. Haila, A.I. Dosari, A.I. Ayesh, *J. Appl. Phys.* **114** (2013) 054305.

[29] A. Lassesson, M. Schulze, J.V. Lith, S.A. Brown *Nanotechnology* **19** (2008) 015502.

[30] M. Khanuja, S. Kala, B.R. Mehta, F.E. Kruis, *Nanotechnology* **20** (2008) 015502.

[31] V. Prysiazhnyi, F. Dycka, J. Kratochvil, J. Sterba, V. Stranak, *Anal Bioanal. Chem.* **412** (2020) 1037.

[32] M. Zheng, W. Li, M. Xu, N. Xu, P. Chen, M. Han, B. Xie, *Nanoscale.* **6** (2014) 3930.

[33] K. Said, A.I. Ayesh, N.N. Qamhieh, F. Awwad, S.T. Mahmoud, S. Hisaindee, *J. Alloys Compd.* **694** (2017) 1061.

[34] S.M. Novikov, V.N. Popok, A.B. Evlyukhin, M. Hanif, P. Morgen, J. Fiutowski, J. Beermann, H.G. Rubahn, S.I. Bozhevolnyi, *Langmuir.* **33** (2017) 6062.

[35] V.N. Popok, S.M. Novikov, Y.Y. Lebedinskij, A.M. Markeev, A.A. Andreev, I.N. Trunkin, A.V. Arsenin, V.S. Volkov, *Plasmonics* **16** (2021) 333.

[36] O. Polonskyi, O. Kylian, M. Drabik, J. Kousal, P. Solar, A. Artemenko, J. Cechvala, A. Choukourov, D. Slavinska, H. Biederman, *J. Mater. Sci.* **49** (2014) 3352.

[37] J. Langer, S.M. Novikov, L.M. Liz-Marzan, *Nanotechnology* **26** (2015) 322001.

[38] V. Singh, C. Cassidy, P. Grammatikopoulos, F. Djurabekova, K. Nordlund, M. Sowwan, *J. Phys. Chem. C* **118** (2014) 13869.

[39] B.M. Smirnov, *Phys.-Usp.* **37** (1994) 621.

[40] V.N. Kondratiev, Rate Constants of Gas Phase Reactions. NATIONAL STANDARD REFERENCE DATA SYSTEM; 1972 Jan 1.

[41] B.M. Smirnov, I. Shyjumon, R. Hippler, *Phys. Rev. E* **75** (2007) 066402.

[42] B.M. Smirnov, Uspekhi. Fiz. Nauk. **181** (2011) 713.

[43] B.M. Smirnov, *Phys.-Usp.* **40** (1997) 1117.

[44] B.M. Smirnov, *Clusters and small particles in Gases and Vapors*, First ed., Springer-Verlag, New York, 2000.

[45] B.M. Smirnov, *Nanoclusters and Microparticles in Gases and Vapors*, First ed., De Gruyter, Germany, 2012.

[46] P.V. Kashtanov, B.M. Smirnov, R. Hippler, *Phys.-Usp.* **50** (2007) 455.

[47] B.M. Smirnov. *Phys.-Usp.* **54** (2011) 691.

[48] L.D. Landau, E.M. Lifshitz, *Course of theoretical physics :Physical Kinetics*, First ed., Pergamon Press, Oxford, 1981.

[49] I.M. Lifshitz, V.V. Slyozov, *J. Phys. Chem. Solids* **19** (1961) 35.

[50] D. Weaire, S. Mcmurry, *Some fundamentals of grain growth*, Edited by: H. Ehrenreich, F. Spaepen , First ed., *Solid State Physics*, Academic Press, 1996, pp 1-36.

[51] I.M. Lifshitz, V.V. Slezov. *Sov. Phys. JETP* **35** (1958) 331.

[52] V.V. Slezov, V.V. Sagalovich, *Sov. Phys. Usp.* **30** (1987) 23.

[53] T.A. Witten, L.M. Sander, *Phys. Rev. Lett.* **47** (1981) 1400.

[54] H. Haberland, M. Mall, M. Moseler, Y. Qiang, T. Reiners, Y. Thurner, *J. Vac. Sci. Technol. A* **12** (1994) 2925.

[55] V.N. Popok, L. Gurevich, *J. Nanopart. Res.* **21** (2019) 171.

[56] S. Marom, M. Plesser, R. Modi, N. Manini, M. Di Vece, *J. Phys. D: Appl. Phys.* **52** (2019) 095301.

[57] T. Momin, A. Bhowmick, *Rev. Sci. Instrum.* **81** (2010) 075110.

[58] T. Peter, O. Polonskyi, B. Gojdka, A.M. Ahadi, T. Strunskus, V. Zaporojtchenko, H. Biederman, F. Faupel, *J. Appl. Phys.* **112** (2012) 114321.

[59] O. Polonskyi, P. Solar, O. Kylian, M. Drabik, A. Artemenko, J. Kousal, J. Hanus, J. Pesicka, I. Matolinova, E. Kolibalova, D. Slavinska, *Thin Solid Films* **520** (2012) 4155.

[60] M. Ganeva, A.V. Pipa, B.M. Smirnov, P.V. Kashtanov, R. Hippler, *Plasma Sources Sci. Technol.* **22** (2013) 045011.

[61] B.M. Smirnov, *Fundamental of Ionized gases*, First ed., Wiley-VCH Verlag GmbH, Weinheim, 2012.

[62] M. Ganeva, T. Peter, S. Bornholdt, H. Kersten, T. Strunskus, V. Zaporojtchenko, F. Faupel, R. Hippler, *Contrib. Plasma Phys.* **52** (2012) 881.

[63] C. Binns, *Surf. Sci. Rep.* **44** (2001) 1.

[64] V.N. Popok, I. Barke, E.E. Campbell, K.H. Meiwes-Broer, *Surf. Sci. Rep.* **66** (2011) 347.

[65] P. Melinon, V. Paillard, V. Dupuis, A. Perez, P. Jensen, A. Hoareau, J.P. Perez, J. Tuaillon, M. Broyer, J.L. Vialle, M. Pellarin, *Int. J. Mod. Phys. B* **9** (1995) 339.

[66] P. Melinon, B. Prevel, V. Dupuis, A. Perez, B. Champagnon, Y. Guyot, M. Boudeulle, M. Pellarin, P. Dugourd, M. Broyer, *Mat. Sci. Eng. A* **217-218** (1996) 69.

[67] H. Haberland, Z. Insepov, M. Moseler, *Phys. Rev. B* **51** (1995) 11061.

[68] I. Yamada, *Nucl. Instrum. Methods Phys. Res. B* **99** (1995) 240.

[69] Y. Qiang, Y. Thurner, T. Reiners, O. Rattunde, H. Haberland, *Surf. Coat. Technol.* **100** (1998) 27.

[70] H. Haberland, M. Karrais, M. Mall, Y. Thurner, *J. Vac. Sci. Technol. A* **10** (1992) 3266.

[71] H. Haberland, Z. Insepov, M. Kurrais, M. Mall, M. Moseler, Y. Thurner, *Nucl. Instrum. Meth. B* **80** (1993) 1320.

[72] Z. Insepov, I. Yamada, M. Sosnowski, *J. Vac. Sci. Technol. A* **15** (1997) 981.

[73] H. Kitani, N. Toyoda, J. Matsuo, I. Yamada, *Nucl. Instrum. Meth. B* **121** (1997) 489.

[74] A. Dollinger, C.H. Strobel, H. Bleuel, A. Marsteller, G. Gantefr, D.H. Fairbrother, X. Tang, K.H. Bowen, Y.D. Kim, *J. Appl. Phys.* **117** (2015) 195302.

[75] M. Schmidt, R. Kusche, B. von Issendorff, H. Haberland, *Nature.* **393** (1998) 238.

[76] X. Li, K. Wepasnick, X. Tang, D. H. Fairbrother, K. H. Bowen, A. Dollinger, C. H. Strobel, J. Huber, T. Mangler, Y. Luo, S. Proch, G. Gantefoer, *J. Appl. Phys.* **115** (2014) 104304.

[77] P. Jensen, *Rev. Mod. Phys.* **71** (1999) 1695.

[78] G.L. Kellogg, *Surf. Sci. Rep* **21** (1994) 1.

[79] S.C. Wang, G. Ehrlich, *Surf. Sci.* **239** (1990) 301.

[80] I.M. Goldby, L. Kuipers, B.V. Issendorff, R.E. Palmer, *Appl. Phys. Lett.* **69** (1996) 2819.

[81] D.R. Lide, *CRC Handbook of Chemistry and Physics*, 89th ed., CRC Press, New York, 2009.

[82] H. Partridge, C.W. Bauschlicher, S.R. Langhoff, *Chem. Phys. Letts.* **175** (1990) 531.

[83] P. Neogrady, V. Kello, M. Urban, A.J. Sadlej, *Int. J. Quantum Chem.* **63** (1997) 557.

[84] N. Laegreid, G.K. Wehner, *J. Appl. Phys.* **32** (1961) 365.

[85] H. Haberland, B.V. Issedorff, J. Yufeng, T. Kolar, *Phys. Rev. Lett.*, **69** (1992) 3212.

[86] S. Mondal, S.R. Bhattacharyya, *Rev. Sci. Instrum.* **85** (2014) 065109.

[87] R. Hippler, S.R. Bhattacharyya, B.M. Smirnov, *Formation and Deposition of Nanosize Particles on Surface*, Edited by: M. Bonitz *et al.*, First ed., *Introduction to complex plasmas*, Springer-Verlag Berlin Heidelberg, 2010, pp 299-314.

[88] A.I. Ayesh, N. Qamhieh, S.T. Mahmoud, H. Alawadhi, 2012. *J. Mater. Res.* **27** (2012) 2441.

[89] G. Binnig, C.F. Quate, C. Gerber, *Phys. Rev. Lett.* **56** (1986) 930.

[90] J.F. Moulder, W.F. Stickle, P.E. Sobol, K.D. Bomben, *Handbook of X-ray photoelectron spectroscopy*, First ed., Perklin-Elmer corporation, USA, 1992.

[91] J.F. Watts, J. Wolstenholme, *An Introduction to Surface Analysis by XPS and AES*, First ed., Wiley, USA, 2003.

[92] W. Jacob, A. Keudell, T. Schwarz-Selinger, *Braz. J. Phys.* **30** (2000) 510.

[93] W.C. Bigelow, D.L. Pickett, W.A. Zisman, *J. Colloid Sci.* **1** (1946) 513.

[94] P. Meakin, Phys. Rep. **235** (1993) 189 .

[95] T.H. Healy, Y.C. Zhang, *Phys. Rep.* **254** (1995) 215.

[96] J. Krug, *Adv. Phys.* **46** (1997) 139.

[97] J. Krug, *Scale Invariance, Interfaces, and Non-Equilibrium Dynamics*, First ed., Plenum, New York, 1995.

[98] M. Moseler, O. Rattunde, J. Nordiek, H. Haberland, *Phys. Rev. B* **164** (2000) 522.

[99] T. Karabacak, Y.P. Zhao, G.C. Wang, T.M. Lu, *Phys. Rev. B* **66** (2002) 075329.

[100] P. Jensen, A.L. Barabasi, H. Larralde, S. Havlin, H.H. Stanley, *Phys. Rev. B* **50** (1994) 15316.

[101] L. Bardotti, P. Jensen, A. Hoareau, M. Treilleux, B. Cabaud, *Phys. Rev. Lett.* **74** (1995) 4694.

[102] S. Mondal, S.R. Bhattacharyya, *Appl. Phys. A* **116** (2014) 1621.

[103] F. Family, T. Vicsek, *Dynamics of Fractal Surfaces*, First ed., World Scientific, Singapore, 1991.

[104] A.L. Barabasi, H.E. Stanley, *Fractal Concepts in Surface Growth*, First ed., Cambridge University Press, Cambridge, UK, 1995.

[105] S.F. Edwards, D.R. Wikinson, *Proc. R. Soc. Lond. A* **381** (1982) 17.

[106] M. Kardar, G. Parisi, Y.C. Zhang, *Phys. Rev. Lett.* **56** (1986) 889.

[107] S.D. Sarma, C.J. Lanczycki, R. Kotlyar, S.V. Ghaisas, *Phys. Rev. E* **53** (1996) 359.

[108] G. Palasantzas, S.A. Koch, J.T.M. De Hosson, *Rev. Adv. Mater. Sci.* **5** (2003) 57.

[109] G. Palasantzas, S.A. Koch, J.T.M. de Hosson, *Appl. Phys. Lett.* **81** (2002) 1089.

[110] R. Buzio, E. Gnecco, C. Boragno, U. Valbusa, P. Piseri, E. Barborini, P. Milani, *Surf. Sci.* **444** (2000) L1.

[111] Z.J. Jiang, C.Y. Liu, L.W. Sun, *J. Phys. Chem. B* **109** (2005) 1730.

[112] M. Guzman, J. Dille, S. Godet, *Nanomedicine* **8** (2012) 37.

[113] T.H. Lee, C.R. Hladik, R.M. Dickson, *Appl Phys. Lett.* **84** (2004) 118.

[114] F.J. Beck, A. Polman, K.R. Catchpole, *J. Appl. Phys.* **105** (2009) 114310.

[115] C. An, S. Wang, Y.Sun, Q. Zhang, J. Zhang, C. Wang, J. Fang, *J. Mat. Chem. A* **4** (2016) 4336.

[116] E.C. Tyo, S. Vajda, *Nature Nanotechnology* **10** (2015) 577.

[117] H. Tsunoyama, Y. Yamano, C. Zhang, M. Komari, T. Eguchi, A. Nakajima, *Topics in Catalysis* **61** (2018) 126.

[118] D. Biswas, S. Mondal, A. Rakshit, A. Bose, S.R. Bhattacharyya, S. Chakraborty, *Mat. Sci. Semicon. Proc.* **63** (2017) 1.

[119] T. Ressler, B.L. Kniep, I. Kasatkin, R. Schlogl, *Angew. Chem. Int. Ed.* **44** (2005) 4704.

[120] A. Murugadoss, E. Sorek, M. Asscher, *Top. Catal.* **57** (2014) 1007.

[121] N. Cioffi, L. Torsi, N. Ditaranto, G. Tantillo, L. Ghibelli, L. Sabbatini, T. Bleve-Zacheo, M. D'Alessio, P. Giorgio Zambonin, E. Traversa, *Chem. Mater.* **17** (2005) 5255.

[122] F. Family, T. Vicsek, *J. Phys. A* **18** (1985) L75.

[123] Y.P. Zhao, G.C. Wang, T.M. Lu, *Characterization of Amorphous and Crystalline Rough Surfaces: Principles and Applications*, First ed., Academic Press, San Diego, 2000.

[124] D. Bhowmik, D. Chowdhury, P. Karmakar, *Surf. Sci.* **679** (2019) 86.

[125] J.J. Ramasco, J.M. Lpez, M.A. Rodrguez, *Phys. Rev. Lett.* **84** (2000) 2199.

[126] Y. Jianguo, J.G. Amar, *Phys. Rev. E* **66** (2002) 021603.

[127] D.N.E Buchanan, *Phys. Rev. B* **33** (1986) 5384.

[128] V. Vijayakrishnan, A. Chainani, D.D. Sarma, C.N.R. Rao, *J. Phys. Chem.* **96** (1992) 8679.

[129] H.H. Huang, X.P. Ni, G.L. Loy, C.H. Chew, K.L. Tan, F.C. Loh, J.F. Deng, G.Q. Xu, *Langmuir* **12** (1996) 909.

[130] H.S. Shin, H.C. Choi, Y. Jung, S.B. Kim, H.J. Song, H.J. Shin, *Chem. Phys. Lett.* **383** (2004) 418.

[131] J.J. Yang, K.W. Xu, *J. Appl. Phys.* **101** (2007) 104902.

[132] T. Karabacak, *J. Nanophotonics* **5** (2011) 052501.

[133] J.H. Yao, H. Guo, *Phys. Rev. E* **47** (1993) 1007.

[134] T. Karabacak, H. Guclu, M. Yuksel, *Phys. Rev. B* **79** (2009) 195418.

[135] J.T. Drotar, Y.P. Zhao, T.M. Lu, G.C. Wang, *Phys. Rev. B* **62** (2000) 2118.

[136] M. Pelliccione, T. Karabacak, T.M. Lu, *Phys. Rev. Lett.* **96** (2006) 146105.

[137] F. Guinea, J.S. Dehesa, F. Flores, *J. Phys. C: Solid State Phys.* **16** (1983) 6499.

[138] S.L. Lai, J.Y.Guo, V. Petrova, G. Ramanath, L.H. Allen, *Phys. Rev. Lett.* **77** (1996) 99.

[139] J.P. Schmidt, S. E. Cross, S. K. Buratto, *J. Chem. Phys.* **121** (2004) 10657.

[140] C. Leung, R.E. Palmer, *Interfacing Cluster Physics With Biology*, Edited by: P. Jena, Jr.A. Castleman, First ed., *Nanoclusters: A Bridge Across Discipline*, Elsevier, 2010, pp 517-556.

[141] Y. Bai, J. Wang, Z. Yin, N. Chen, X. Zhang, Z. Fu, J. Yao, N. Li, H. He, M. Guli, *Science China Technological Sciences* **56** (2013) 109.

[142] Y. Bai, Z. Gao, N. Chen, H. Liu, J. Yao, S. Ma, X. Shi, *Appl. Surf. Sci.* **315** (2014) 1.

[143] A. Deka, P. Barman, G. Bhattacharjee, S.R. Bhattacharyya *Appl. Surf. Sci.* **526** (2020) 146645.

[144] S.Mondal, D. Chowdhury, P. Barman, S.R. Bhattacharyya, *Eur. Phys. J. D* **71** (2017) 327.

[145] P. Barman, A. Deka, S.Mondal, D. Chowdhury, S.R. Bhattacharyya, *J. Phys. D: Appl. Phys* **53** (2020) 325302.

[146] J.M. Li, L. Lu, Y. Su, M.O. Lai, *Appl. Surf. Sci.* **161** (2000) 187.

[147] D. Raoufi, *Appl. Surf. Sci.* **255** (2009) 3682.

[148] D. Dallaeva, S. Talu, S. Stach, P. Skarvada, P. Tomanek, L. Grmela, *Appl. Surf. Sci.* **312** (2014) 81.

[149] A. Arman, S. Talu, C. Luna, A. Ahmadpourian, M. Naseri, M. Molamohammadi, *J Mater Sci: Mater Electron* **26** (2015) 9630.

[150] F.M. Mwema, O.P. Oladijo, T. S. Sathiaraj, E.T. Akinlabi, *Mater. Res. Express* **5** (2018) 046416.

[151] R.P. Yadav, T. Kumar, V. Baranwal, Vandana, M. Kumar, P.K. Priya, S.N. Pandey, A.K. Mittal *J. Appl. Phys* **121** (2017) 055301.

[152] T. Onda, S. Shibuichi, N. Satoh, K. Tsujii, *Langmuir* **12** (1996) 2125.

[153] Y.L. Zhang, H. Xia, E. Kim, H.B. Sun, *Soft Matter* **8** (2012) 11217.

[154] T. Sun, L. Feng,X. Gao, L. Jiang, *Acc. Chem. Res.* **38** (2005) 644.

[155] O.U. Nimittrakoolchai, S. Supothina, *J. Eur. Ceram. Soc.* **28** (2008) 947.

[156] M. Pelliccione, T. M. Lu, *Evolution of thin film morphology Modeling and Simulations*, First ed., Springer-Verlag, New York, 2008.

[157] V.L. Sougleridis, V. Constantoudis, M. Alexe, R. Scholz, G. Vellianitis, A. Dimoulas, *Thin Solid Films* **468** (2004) 303.

[158] U.B. Singh, R.P. Yadav, R.K.Pandey, D.C. Agarwal, C. Pannu, *J. Phys. Chem. C* **120** (2016) 5755.

[159] T. Young, *R. Soc. Lond.* **95** (1805) 65.

[160] R. Wenzel, *Ind. Eng. Chem.* **28** (1936) 988.

[161] A.B.D. Cassie, S. Baxter, *Trans. Farady Soc.* **40** (1944) 546.

[162] B.M. Smirnov, *Phys. Rep.* **188** (1990) 1.

[163] J.F. Weaver, G.B. Hoflund, *J.Phys. Chem.* **98** (1994) 8519.

[164] S.R. Bhattacharyya, T.K. Chini, D. Datta, R. Hipler, I. Shyjumon, B.M. Smirnov, *J. Exp. Theor. Phys.* **107** (2008) 1009.

[165] S.R. Bhattacharyya, D. Datta, T.K. Chini, D. Ghose, I. Shyjumon, R. Hipler, *Nucl. Instrum. Meth. B* **267** (2009) 1432.

[166] S.R. Bhattacharyya, D. Datta, I. Shyjumon, B. M. Smirnov, T.K. Chini, D. Ghose, R. Hipler, *J. Phys. D: Appl. Phys.* **42** (2009) 035306.

[167] Y. Bai, L. Yan, J. Wang, Z. Yin,N. Chen, F. Wang, Z. Tan, *Mater. Des.* **103** (2016) 315.

[168] P. Prieto, V. Nistor, K. Nouneh, M. Oyama, M.A. Lefdii, R. Diaz, *Appl. Surf. Sci* **258** (2012) 8807.

[169] J.G. Kang, Y. Sohn, *J. Mater. Sci.* **47** (2012) 824.

[170] I.L. Salido, D.C. Lim, Y.D. Kim, *Surf. Sci.* **588** (2005) 6.

[171] P. Dutheil, A.L. Thomann, T. Lecas, P. Brault, M. Vayer, *Appl. Surf. Sci.* **347** (2015) 101.

[172] B.S. Kim, S. Shin, S.J. Shin, K.M. Kim, H. H. Cho, *Nanoscale Res. Lett.* **6** (2011) 1.

[173] A.K. Gupta, M. Gupta, *Biomaterials* **26** (2005) 3995.

[174] C.J. Murphy, T.K. Sau, A.M. Gole, C.J. Orendorff, J. Gao, L. Gou, S.E. Hunyadi, T. Li, *J. Phys. Chem. B* **109** (2005) 13857.

[175] K.K. Kefeni, T.A. Msagati, B.B. Mamba, *Mat. Sci. Eng.: B.* **215** (2017) 37.

[176] J. Kudr, Y. Haddad, L. Richtera, Z. Heger, M. Cernak, V. Adam, O. Zitka, *Nanomaterials* **7** (2017) 243.

[177] S.K. Sardana, V.S. Chava, V.K. Komarala, *Appl. Surf. Sci.* **347** (2015) 651.

[178] C.N. Lok, C.M. Ho, R. Chen, Q.Y. He, W.Y. Yu, H. Sun, P.K. Tam, J.F. Chiu, C.M. Che, *J. Biol. Inorg. Chem.* **12** (2007) 527.

[179] Z. Zhao, M.A. Carpenter, *J. Phys. Chem. C* **117** (2013) 11124.

[180] M. Haruta, *Cattech* **6** (2002) 102.

[181] M. Sharifi, F. Attar, A.A. Saboury, K. Akhtari, N. Hooshmand, A. Hasan, M.E. Sayed, M. Falahati, *J. Control. Release* **311** (2019) 170.

[182] S. Zhou, H. Yin, V. Schwartz, Z. Wu, D. Mullins, B. Eichhorn, S.H. Overbury, S. Dai, *Chem. Phys. Chem.* **9** (2008) 2475.

[183] G. Nocerino, K.E. Singer, *J. Vac. Sci. Technol.* **16** (1979) 147.

[184] H. Lee, Y.K. Lee, E. Hwang, J.Y. Park, *J. Phys. Chem. C* **118** (2014) 5650.

[185] R. Sellappan, M.G. Nielsen, F.G. Posada, P.C. Vesborg, I. Chorkendorff, D. Chakarov, *J. Catal.* **307** (2013) 214.

[186] W. Li, F. Chen, *J. Alloys Compd.* **632** (2015) 845.

[187] N.N. Kariuki, J. Luo, M.M. Maye, S.A. Hassan, T. Menard, H.R. Naslund, Y. Lin, C. Wang, M.H. Engelhard, C.J. Zhong, *Langmuir* **20** (2004) 11240.

[188] G. Battaglin, E. Cattaruzza, F. Gonella, G. Mattei, P. Mazzoldi, C. Sada, X. Zhang, *Nucl. Instrum. Meth. B* **166** (2000) 857.

[189] R.K. Roy, S.K. Mandal, A.K. Pal, *Eur. Phys. J. B* **33** (2003) 109.

[190] S. Xu, B. Zhao, W. Xu, Y. Fan, *Colloid. Surface. A* **257** (2005) 313.

[191] C.L. Tan, S.K. Lee, Y.T. Lee, *Optics Express* **23** (2015) 6254.

[192] N. Kumar, F. Alam, V. Dutta, *J. Alloys Compd.* **585** (2014) 312.

[193] S. Ristig, O. Prymak, K. Loza, M. Gocyla, W.M. Zaika, M. Heggen, D. Raabe, M. Epple, *J. Mater. Chem. B* **3** (2015) 4654.

[194] Y. Oh, J. Lee, M. Lee, *Appl. Surf. Sci.* **434** (2018) 1293.

[195] A.Q. Wang, J.H. Liu, S.D. Lin, T.S. Lin, C.Y. Mou, *J. Catal.* **233** (2005) 186.

[196] S. Verma, B.T. Rao, V. Sathe, S. Bhartiya, H.S. Patel, R. Kaul, B. Singh, *J. Alloys Compd.* **753** (2018) 395.

[197] D. Llamosa, M. Ruano, L. Martnez, A. Mayoral, E. Roman, M. Garca-Hernndez, Y. Huttel, *Nanoscale* **6** (2014) 13483.

[198] L. Martinez, M. Diaz, E. Roman, M. Ruano, D. Llamosa P., Y. Huttel, *Langmuir* **28** (2012) 11241.

[199] S. Mondal, B. Satpati, S. R. Bhattacharyya *J. Nanosci & Nanotechnol.* **15** (2015) 611.

[200] P.V. Kashtanov, R. Hippler, B.M. Smirnov, S.R. Bhattacharyya, *Eur. Phys. Lett.* **90** (2010) 16001.

[201] P.V. Kashtanov, R. Hippler, B.M. Smirnov, S.R. Bhattacharyya, *J. Theor. & Expt. Phys.* **110** (2010) 521.

[202] F.A. Shunk, *Constitution of Binary Alloys*, First ed., McGraw-Hill Company, New York, 1969.

[203] A.K. Green, E. Bauer, *J. Appl. Phys.* **47** (1976) 1284.

[204] H. Arslan, M.H. Guven, *New J. Phys.* **7** (2005) 60.

[205] J.H. Shim, B.J. Lee, Y.W. Cho, *Surf. Sci.* **512** (2002) 262.

[206] S. Zhao, S. Wang, H. Ye, *J. Phys. Soc. Jpn.* **70** (2001) 2953.

[207] C. D. Wanger, W. M. Riggs, L. E. Davis, J. F. Moulder, G.E. Muilenberg, *Handbook of X-ray Photoelectron Spectroscopy*, First ed., Perkin-Elmer Corporation, Minnesota, USA, 1978.

[208] V.I. Bukhtiyarov, V.V. Kaichev, I.P. Prosvirin, *J. Chem. Phys.* **111** (1999) 2169.

[209] T.C. Kaspar, T. Droubay, S.A. Chambers, P.S. Bagus, *J. Phys. Chem. C* **114** (2010) 21562.

[210] E. Sumesh, M.S. Bootharaju, Anshup, T. Pradeep, *J. Hazard. Mater.* **189** (2011) 450.

[211] P. Sangpour, O. Akhavan, A.Z. Moshfegh, M. Roozbehi, *Appl. Surf. Sci.* **254** (2007) 286.

[212] P. Sangpour, O. Akhavan, A.Z. Moshfegh, *J. Alloys Compd.* **486** (2009) 22.

[213] J.J. Pireaux, M. Liehr, P.A. Thiry, J.P. Delrue, R. Caudano, *Surf. Sci.* **141** (1984) 221.

[214] R. Wang, Z. Wu, C. Chen, Z. Qin, H. Zhu, G. Wang, H. Wang, C. Wu, W. Dong, W. Fan, J. Wang, *Chem. Comm.* **49** (2013) 8250.

[215] J. Li, C.Y. Liu, Y. Liu, *J. Mater. Chem.* **22** (2012) 8426.

[216] M.P. Casaletto, A. Longo, A. Martorana, A. Prestianni, A.M. Venezia, *Surf. Interface Anal.* **38** (2006) 215.

[217] O.G. Ashkhotov, S.A. Khubezhov, M.A. Aleroev, I.B. Ashkhotova, T.T. Magkoev, A.P. Bliev, E.N. Kozirev, *J. Synch. Investig.* **12** (2018) 513.

[218] D.M. Bastidas, E. Cano, A.G. Gonzlez, S. Fajardo, R. Lleras-Prez, E. Campo-Montero, F.J. Belzunce-Varela, J.M. Bastidas, *Corros Sci* **50** (2008) 1785.

[219] R. Alfonsetti, G.D. Simone, L. Lozzi, M. Passacantando, P. Picozzi, S. Santucci, *Surf. Interface Anal.* **22** (1994) 89.

Thesis Highlight

Name of the student: PINTU BARMAN

Name of the CI/OCC: SAHA INSTITUTE OF NUCLEAR PHYSICS

Enrolment No.: PHYS05201604020

Discipline: Physical Sciences **Sub-Area of Discipline:** Nanotechnology

Thesis Title: Nanostructuring on solid surfaces using low energy atomic and cluster ions

Date of Viva Voce: 11/08/2021

Fabrication and deposition of metal nanocluster is one of the latest trends in the field of nanomaterial research because of their unique and size-dependent properties. In order to produce size-selected metal nanoclusters and their soft-landing deposition on a substrate, a low energy cluster beam production instrument (Model: Nanodep60, Oxford Applied Research, UK) has been used the schematic diagram of which is shown in Fig. 1(a). The morphology of thin films plays an important role to contol many of its properties for various applications in nanotechnology therefore, the fundamental understanding of film growth on a certain substrate is essential. The insight information of growth phenomena of a cluster in the form of thin-films can be understood by analyzing some of the surface statistical parameters utilizing the scaling theory. The thesis work mainly focuses on the study of growth behaviour of size-selected metal nanoclusters at various experimental conditions. In one of the works, the growth behaviour of size-selected Ag nanocluster films deposited on Si (100) substrates for various deposition times are studied under the framework of dynamic scaling theory. The non-normal deposition of nanoclusters and the effects of shadowing and re-emission process can be seen in Fig. 1(b). From the growth dynamics study of the films two types of growth variation can be observed that are separated by a crossover deposition time of 20 min as shown in Fig. 1(c). The obtained films are found to be self-affine in nature. From the study, the initial stage of surface growth is found to follow pre-existed conventional growth model known as Kardar-Parisi-Zhang (KPZ) model, while the later growth stage of the films is found to follow non-local growth model where the shadowing effects dominates over the re-emission effect.

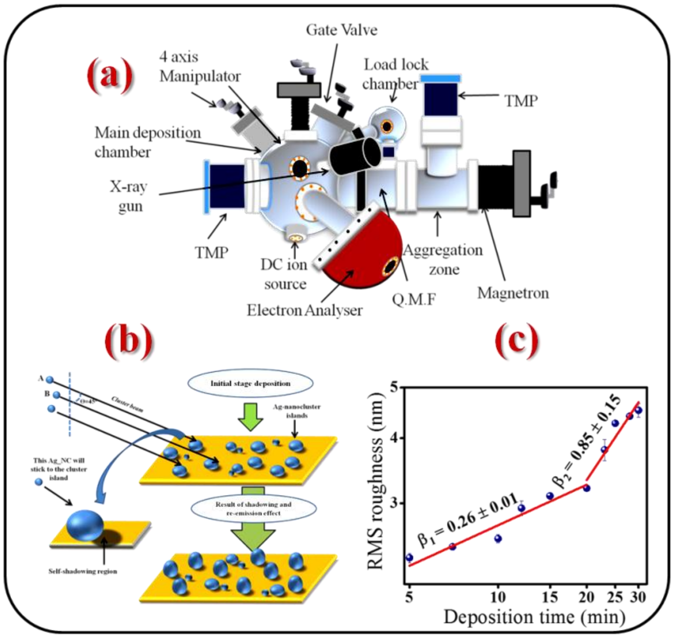

Figure 1: (a) Schematic diagram of nanocluster deposition system; (b) Schematic representation of shadowing effect on film growth; (c) Nanocluster deposited films shows two types of growth variation with increasing time.